SPLICE TESTS OF PLAIN STEEL BARS IN CONCRETE

A Thesis

Submitted to the College of Graduate Studies and Research

In Partial Fulfillment of the Requirements

for the

Degree of Master of Science

in the

Department of Civil & Geological Engineering

University of Saskatchewan

Saskatoon

By

MD NAZMUL HASSAN

PERMISSION TO USE

In presenting this thesis in partial fulfilment of the requirements for a Postgraduate degree from the University of Saskatchewan, I agree that the Libraries of this University may make it freely available for inspection. I further agree that permission for copying of this thesis in any manner, in whole or in part, for scholarly purposes may be granted by the professor or professors who supervised my thesis work or, in their absence, by the Head of the Department or the Dean of the College in which my thesis work was done. It is understood that any copying or publication or use of this thesis or parts thereof for financial gain shall not be allowed without my written permission. It is also understood that due recognition shall be given to me and to the University of Saskatchewan in any scholarly use which may be made of any material in my thesis.

Requests for permission to copy or to make other use of material in this thesis in whole or part should be addressed to:

Head of the Department of Civil & Geological Engineering
University of Saskatchewan
Engineering Building
57 Campus Drive
Saskatoon, Saskatchewan, S7N 5A9
Canada

ABSTRACT

Fifteen splice specimens reinforced with plain steel bars, including three specimens instrumented with both steel and concrete strain gauges, were tested under monotonically applied four-point loading to develop a database of reliable bond test results and contribute to the development of a reliability based bond provision for plain steel bars to evaluate historical concrete structures. The maximum applied load for the specimens and their observed failure behaviour are reported. In addition to that, a strain compatibility analysis, average bond stress distribution, and flexural section analysis within the lap splice length of the instrumented specimens are also reported.

All of the specimens failed in bond within the lap splice length. The load capacity of two specimens reinforced with plain steel bars was 60% of the reported load resistance of specimens with identical geometry and reinforced with deformed bars. The CEB-FIP Model Code provisions for average bond stress of plain steel bars underestimated the maximum applied load recorded for the tested specimens by 16% on average. An empirically derived equation to predict the bond capacity of plain steel bars was determined to be proportional to both the splice length and the nominal bar diameter.

Observed cracks in the shear spans remained vertical and suggest the development of arch action within this region. The formation of a large crack at one end of the lap splice length and a review of the load versus deflection behaviour indicated a sudden bond failure of the specimens. Removal of concrete cover at the ends of the lap splice length following testing of the specimens showed evidence of slip of the lapped bars.

Instrumented splice specimens provided evidence of bond loss within the lap splice region. As-measured steel strains were higher than those measured for the surrounding concrete due to a loss of strain compatibility. The average bond stress distribution within the lap splice length became more uniform as the applied load approached the maximum applied load. The flexural analysis calculated based on concrete strains above the neutral axis and steel strain provided a reasonable estimate of specimen capacity.

CO-AUTHORSHIP

All of the experimental work presented in this thesis was conducted by M. N. Hassan and reviewed by Dr. L. R. Feldman. The results of a select number of specimens contained within the experimental program were published in the proceedings of the 2009 CSCE Annual General Conference in St. John's, Newfoundland, Canada. A manuscript summarizing the findings of the entire research program was submitted to ACI Structural Journal on April 7, 2010, with a revised version of the manuscript submitted on November 5, 2010.

ACKNOWLEDGEMENTS

The author would like to recall the mercy of Allah who has blessed him with the patience to overcome all the challenges throughout this research work.

The author's profound appreciation goes to his supervisor, Dr. Lisa Feldman, for her guidance, mentorship and suggestions. Dr. Feldman's commitment as a research advisor and mentor exceeds all expectations.

The author acknowledges his advisory committee members: Dr. Bruce F. Sparling, and Dr. Leon D. Wegner for their suggestions and guidance. The author also acknowledges Dr. Allan T. Dolovich and Dr. Jian Peng for their suggestions in the preparation of the thesis.

The author gratefully acknowledges Brennan Pokoyoway, Structural Laboratory Technician for his assistance with specimen preparation and testing, and Dale Pavier, Structural Laboratory Technician, for his technical assistance. The author's profound appreciation also goes to fellow graduate students and undergraduate research assistants for their assistance in specimen preparation and testing.

Scholarships from the University of Saskatchewan and the American Concrete Institute are also acknowledged along with additional financial support provided by the University of Saskatchewan. Concrete for the research project as donated by Lafarge is also acknowledged.

Finally, the author acknowledges the supports and encouragement of his family and friends.

TABLE OF CONTENTS

CHAPTER 4
LOAD RESISTANCE AND OBSERVED BEHAVIOUR OF TESTED SPECIMENS

LIST OF TABLES

LIST OF FIGURES

LIST OF SYMBOLS

a	Shear span
A_{sr}	Cross-sectional area of the reinforcing steel bar at the location of the steel strain gauges
c	Depth of the neutral axis from the extreme compression fibre
C_c	Concrete compressive force
c_b	Bottom cover
c_{so}	Side cover
c_{si}	One half of the clear spacing between the spliced bars
c_{min}	Nominal minimum concrete cover
d	Effective depth of the specimen
d_b	Nominal diameter of the reinforcing bar
d_b'	Reduced diameter of the reinforcing bar
E_c	Modulus of elasticity of the concrete
E_s	Modulus of elasticity of the reinforcing steel
f_c'	Concrete compressive strength
f_{ck}	Characteristic concrete compressive strength
f_{ctd}	Design value of tensile strength of concrete
$f_{ctk,min}$	Minimum characteristic tensile strength of concrete
f_{ctm}	Average tensile strength of concrete
f_d	Vertical tensile stress due to dowel shear
f_s	Reinforcing steel stress

f_y Reinforcing steel yield strength

f_{yd} Dynamic yield strength of reinforcing steel bars

f_{ys} Static yield strength of reinforcing steel bars

f_u Ultimate strength of reinforcing steel bars

I_{cr} Cracked moment of inertia

I_e Effective moment of inertia

I_g Gross moment of inertia

jd Moment arm

L Clear span length

L_{cm} Length of the constant moment zone

L_s Lap splice length

L_{sr} Reduced bonded length

l Length of the reinforcing steel measured from the reaction

M Bending moment

M_a Moment due to the applied service load

M_{cr} Cracking moment

$\sum O$ Sum of the perimeter of all of the longitudinal reinforcing bars

P Applied load

P_{max} Maximum applied load

$P_{CEB-FIP}$ Maximum applied load calculated in accordance with the CEB-FIP Model Code (1993)

R Support reaction

R_y Maximum height of profile

S_u Standard deviation of average bond stress

$S_{\varepsilon c}$ Standard deviation of concrete strain gauge reading at $P/P_{max} = 0$

$S_{\varepsilon s}$ Standard deviation of steel strain gauge reading at $P/P_{max} = 0$

$S_{\Delta\varepsilon s}$ Standard deviation of the difference of steel strain between two strain gauge locations at $P/P_{max} = 0$

$S_{\varepsilon s-\varepsilon c}$ Standard deviation of difference between steel and concrete strain at a given strain gauge location

T Tensile force

T_s Tensile force in the reinforcing steel

u Actual bond stress

u_d Design bond stress

u_{avg} Average bond stress

V Shear force

v_a Shear stress due to aggregate interlock

v_b Bond induced shear stress

V_d Dowel shear

x Distance with respect to a datum at the support

Δx Distance between two adjacent strain gauges

α, β Concrete stress block factors for $0.1 \leq \varepsilon_c / \varepsilon_o \leq 2$

Δ_x Deflection at a section located a distance x from the support

$\dot{\varepsilon}$ Strain rate

ε_c Concrete strain

ε_o Strain in concrete at f_c'

ε_s Steel strain

$\Delta\varepsilon_s$ Difference in the readings of two adjacent strain gauges

η_1 Factor for reinforcing bar type

η_2 Factor for bond conditions

η_3 Factor for reinforcing bar size

CHAPTER 1
INTRODUCTION

1.1 Background

More than 40% of the operating bridges in Canada and the United States of America were built over forty years ago (Lounis 2007; Stewart and Val 1999). Many of the historical bridges are concrete structures reinforced with steel bars that do not conform to the current specifications (Loov 1991). Service loads on the aging structures have increased over time while their structural capacity has likely decreased due to different types of damage as they are exposed to harsh environments (Arrien et al. 2001; Baldwin and Clark 1995). Therefore, aging structures, including historical reinforced concrete structures, require evaluation and potential rehabilitation to ensure their safe operation (Feldman and Bartlett 2005). The evaluation of the anchorage requirements for aging concrete structures reinforced with historical reinforcing bars is a challenge for practicing engineers, as current editions of the Canadian and American design standards (CSA 2004a; CSA 2006; AASHTO 2009; ACI Committee 318 2008) do not include provisions for historical reinforcing bars (Feldman et al. 2003).

Reinforcing steel bars have evolved markedly since the wide-scale introduction of reinforced concrete construction in the late nineteenth century (Loov 1991). Figure 1.1 presents some examples of historical deformed reinforcing steel bars that were used, in addition to plain bars (i.e. no surface deformation), in historical reinforced concrete construction (Abrams 1913). Deformed bars produced at that time were proprietary. Different shapes and surface deformation patterns such as round or square bars with lugs, corrugations, or threads and twisted bars were therefore used in historical reinforced concrete structures, and improved their bond capacity as compared to plain steel bars (Loov 1991).

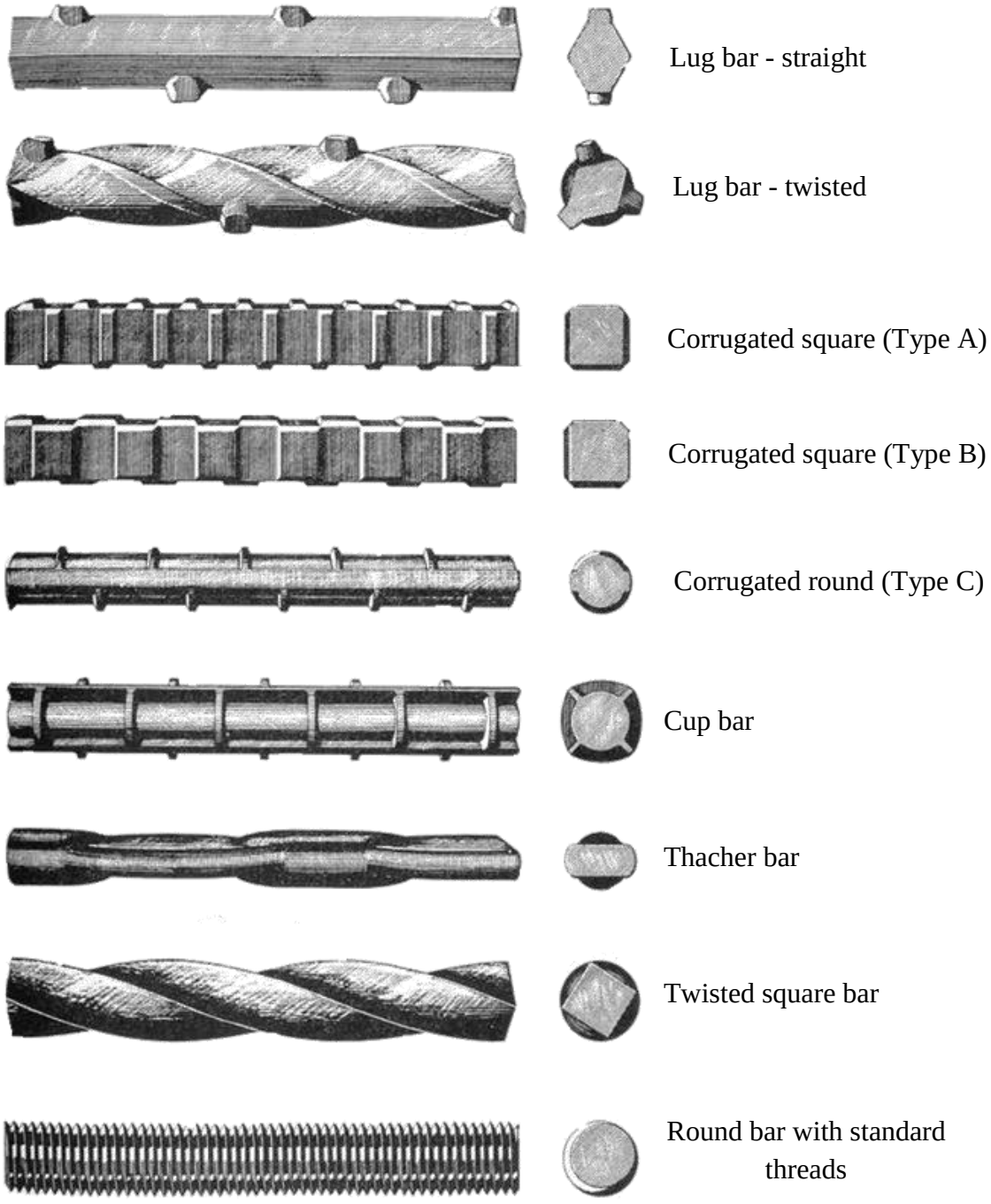

Figure 1.1. Deformed bars used in historical concrete structures (Abrams 1913).

This thesis addresses the evaluation of bond capacity of plain steel bars in historical concrete structures.

The bond characteristic of plain steel bars in flexural members is markedly different than that of deformed bars (MacGregor and Bartlett 2000). Plain reinforcement does not possess lugs or other surface deformations. Two mechanisms of bond are therefore available: adhesion between the bars and the surrounding concrete, and sliding friction between the bars and the surrounding concrete once bar slip initiates. The bond capacity of plain steel bars is reportedly lower than that of modern deformed bars (Abrams 1913; Mylrea 1948; Baldwin and Clark 1995) and their bond failure mode is also different (MacGregor and Bartlett 2000). Current editions of the Canadian and American design standards (CSA 2004a; CSA 2006; AASHTO 2009; ACI Committee 318 2008) do not provide provisions to evaluate the bond of plain steel bars. An unfortunate legacy has therefore been created: there are many historical concrete structures reinforced with plain bars that are still in service, yet the evaluation of their structural capacity poses a challenge for practicing engineers (Baldwin and Clark 1995; Feldman and Bartlett 2005).

Much of the existing research related to the bond of plain reinforcement has focused on bond stress distributions in either pullout or tension specimens (Abrams 1913, Mylrea 1948, Feldman & Bartlett 2005, Feldman & Bartlett 2007). Such work provides valuable insight into bond behaviour and bond strength variability. However, current Canadian and American design provisions (CSA 2004a, CSA 2006, AASHTO 2009, ACI Committee 318 2008) for deformed bars express bond in terms of development length rather than definable bond stresses (Winter 1982). Development length is defined as the length of embedment of the reinforcing steel necessary to develop the design strength at a given section (MacGregor and Bartlett 2000). These development length provisions are based largely on observed behaviour of splice specimens (details presented in Chapter 2) that simulated a realistic stress state in the reinforcing steel and its surrounding concrete for flexural members (ACI Committee 408 2003). The development of new provisions to evaluate the bond of plain steel bars in historical

concrete structures requires a similar approach as that followed by researchers (Orangun et al. 1977) to develop bond provisions for deformed bars. The development of a database of reliable test results for plain steel bars in flexural specimens, including their observed failure behaviour is therefore required.

1.2 Objectives

The primary objective of this study was to contribute to the development of reliability-based bond provisions for the evaluation of historical concrete structures reinforced with plain steel bars by creating a database of splice specimen test results with a supporting analysis of their failure behaviour. Fifteen splice specimens were tested in the current research program to achieve the following sub-objectives:

1. To develop a preliminary equation to express maximum applied load attained from the testing of specimens with plain bars as a function of bar size and lap splice length;

2. To compare the load-carrying capacity of specimens reinforced with plain steel bars with that predicted theoretically and to specimens with similar geometry reinforced with deformed bars;

3. To report the observed failure behaviour of the splice specimens including observed crack patterns and load versus deflection behaviour;

4. To analyze the strain compatibility and average bond stress distribution along the lap splice length to study the bond behaviour of plain steel bars; and

5. To study the effects of bond loss on the internal force distribution within the lap splice length for the instrumented specimens.

1.3 Scope and Methodology

Fifteen splice specimens were tested under monotonically applied four-point static loading to fulfill the objectives of the current study. The testing program was limited to the investigation of two relevant parameters (bar diameter and splice length) to maintain a reasonable limit on the number of specimens tested. The experimental program was designed such that it can serve as a guideline for future research to further refine a development length equation for evaluation and rehabilitation of historical concrete structures reinforced with plain steel bars. Replicate specimens were not tested within this investigation. Three of the specimens were instrumented with steel and concrete strain gauges to study the strain compatibility and bond stress distribution along the lap splice length. Strain gauges were not installed along the shear spans. Despite the limitations, the current study provides valuable information regarding the bond behaviour of plain steel bars and contributes to the development of new design provisions to evaluate the bond of plain steel bars in historical concrete structures.

1.4 Thesis Outline

Chapter 1 presented the research background, stated the objectives, and scope of the current study.

Chapter 2 presents a brief discussion of bond mechanics and describes experimental specimens used to establish such data. A literature review of relevant previous studies is also presented.

Chapter 3 presents details of the experimental program including specimen geometry, specified material properties, specimen preparation, and testing methods.

The reported load-carrying capacity and observed failure behaviour of the tested specimens is presented in Chapter 4. The first three sub-objectives stated in Section 1.2 are addressed in this chapter.

Chapter 5 presents a detailed analysis of the strain gauge data, including apparent strain compatibility, the bond stress distribution in the longitudinal reinforcement along the lap splice length as a function of the applied load, and a flexural section analysis at the instrumented locations. Fourth and fifth sub-objectives of the study, as stated in Section 1.2, are addressed in this chapter.

Chapter 6 summarizes the research and restates the significant findings of the study.

CHAPTER 2
LITERATURE REVIEW

2.1 General

This chapter presents the background information related to the bond of plain steel reinforcing bars in concrete. A brief discussion of the mechanics of bond is followed by a discussion of different bond test specimens. A critical review of the previous studies of the bond of plain steel bars is also presented in this chapter.

2.2 Bond of Steel Reinforcement

The behaviour of a reinforced concrete flexural member depends upon the bond between the longitudinal reinforcing steel and its surrounding concrete (e.g. MacGregor and Bartlett 2000). One of the fundamental assumptions used for the analysis of reinforced concrete members is that perfect bond exists between the longitudinal reinforcing bars and the surrounding concrete. In other words, the strain in the concrete at the level of the longitudinal reinforcing steel is the same as in the reinforcing steel. Bond allows for forces to transfer between the reinforcing bars and the surrounding concrete and dictates the expected failure mode of reinforced concrete members.

As discussed in the previous chapter, plain steel reinforcement has been used as reinforcement in historical concrete structures (Loov 1991). Plain bars do not have lugs (otherwise known as deformations) and so cannot transfer forces by bearing of these lugs against the surrounding concrete once the bar slips. Bond transfer mechanisms of plain steel reinforcement are therefore different than those of modern deformed bars (ACI Committee 408 2003). Chemical adhesion between reinforcing steel bars and the surrounding concrete is the primary bond transfer mechanism for plain steel bars prior to the slip of the reinforcing steel (Abrams 1913). Even a small amount of localized slip

destroys this adhesion, and frictional forces resulting from the surface roughness of the bar then becomes the only remaining bond mechanism (Abrams 1913). The bond capacity of deformed bars is therefore greater than historical plain steel reinforcement (ACI Committee 408 2003).

Figure 2.1 shows a simply-supported reinforced concrete beam to illustrate the fundamental mechanics of force transfer between the concrete and the longitudinal reinforcement. In Figure 2.1 (a), the applied load and the resulting support reactions are denoted by P and R, respectively. The shear spans are denoted by a, and L_{cm} is the length of the constant moment region. Tensile strains and stresses are developed at the bottom face of the member due to the applied load, and flexural cracks form in the midspan beam region where the tensile stress of the concrete exceeds its modulus of rupture (e.g. MacGregor and Bartlett 2000).

Figure 2.1 (b) shows the tensile stress distribution in the concrete surrounding the reinforcing bar. Complete loss of bond between the steel reinforcement and the surrounding concrete occurs at crack locations. The steel tension force, T, at the crack locations can then be calculated from the following equation if perfect bond between the longitudinal reinforcement and the surrounding concrete exists:

$$T = \frac{M}{jd} \qquad [2.1]$$

where M is the bending moment acting at the location of crack, and jd is the moment arm between the tensile force in the longitudinal reinforcement and centroid of the compressive force in the concrete. Figure 2.1 (b) also shows that the concrete surrounding the reinforcing steel in between two cracks carries a portion of the tensile force due to the existence of bond and thus reduces the stress in the longitudinal reinforcement in these regions (e.g. MacGregor and Bartlett 2000). This phenomenon is commonly referred to as “tension stiffening”.

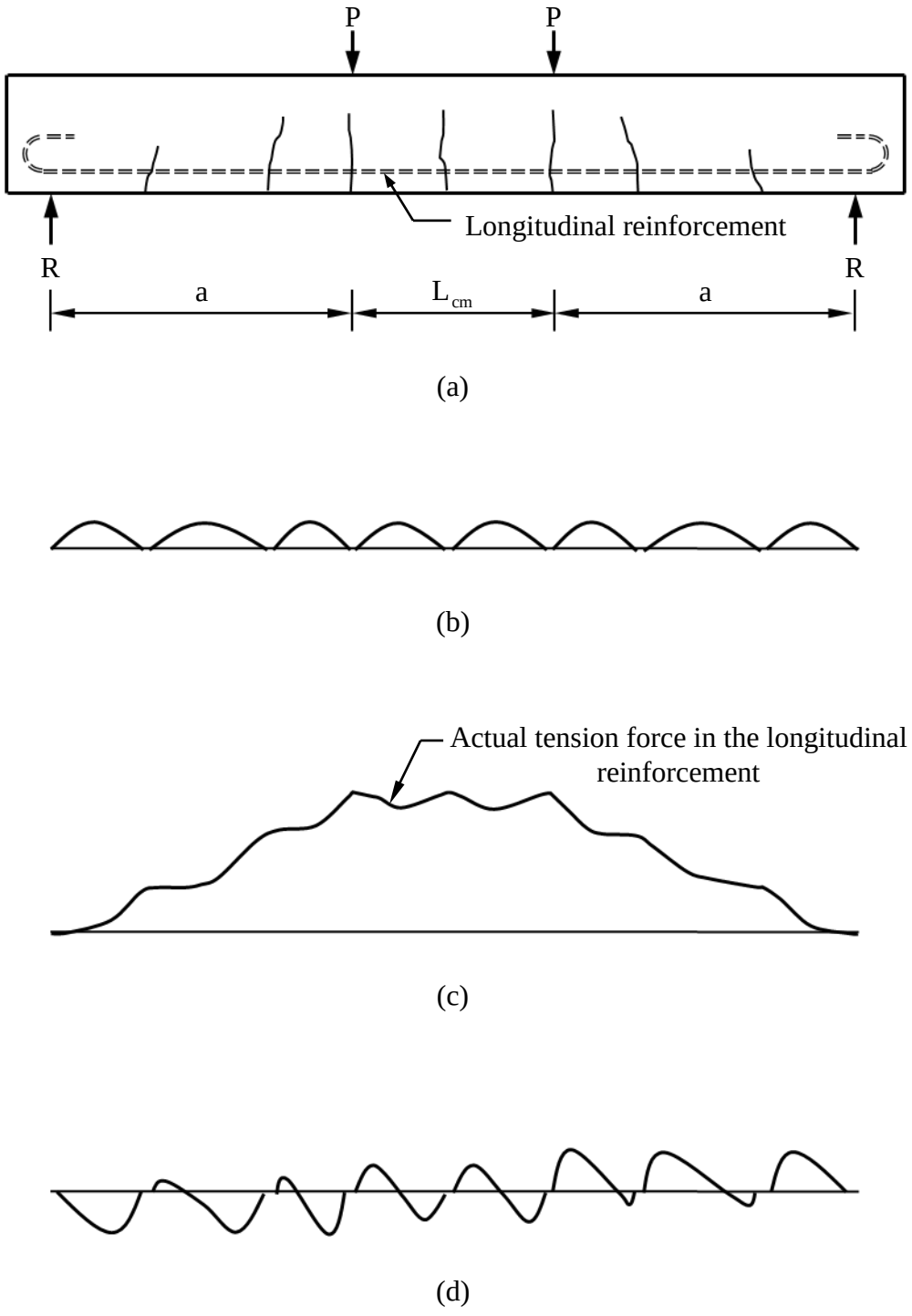

Figure 2.1: Steel force and bond stress variation in a reinforced concrete member (after MacGregor and Bartlett 2000): (a) reinforced concrete beam; (b) tensile stress in concrete; (c) variation of tension force in the reinforcing steel; (d) bond stress distribution along the longitudinal reinforcement.

Figure 2.1(c) shows the actual tension force developed in the longitudinal reinforcement as a result tension stiffening in the beam. Bond between the reinforcing steel and the concrete causes the variation in the tension force over the length of the longitudinal reinforcement. This variation in tension force over the length of the reinforcing bar is known as the shear flow and can be calculated from the following equation (e.g. MacGregor and Bartlett 2000):

$$\frac{dT}{dx} = u \sum O \qquad [2.2]$$

where, u is the bond stress, and $\sum O$ is the sum of the perimeters of all of the longitudinal reinforcing bars. Complete loss of bond would cause a uniform tension force over the length of the longitudinal reinforcement. Shear flow therefore reduces to zero if bond between reinforcing steel and concrete is lost.

Figure 2.1 (d) shows the variation in the bond stress along the length of the reinforcing bar. The bond stress, u, depends upon the location of cracks and tension carried by the concrete and is proportional to the shear flow, $\frac{dT}{dx}$ (ACI Committee 408 2003). Due to the complex nature of the actual bond stress distribution, a uniform average bond stress distribution over the length of the reinforcing bar was often considered for design purposes (ACI Committee 408 2003). The average bond stress, u_{avg}, between two points of a reinforcing bar can be calculated from the following equation (e.g. MacGregor and Bartlett 2000):

$$u_{avg.} = \frac{\Delta f_s \, d_b}{4 \Delta x} \qquad [2.3]$$

where d_b is the diameter of the reinforcing steel bar and Δf_s is the difference in stress in the reinforcing steel between two points located a distance Δx apart.

The shear carrying mechanism of flexural members is also affected by the bond between the reinforcing steel and the concrete. The shear force, V, acting on a section of a flexural member can be expressed as (e.g. MacGregor and Bartlett 2000):

$$V = \frac{dT}{dx}(jd) + \frac{d(jd)}{dx}T \qquad [2.4]$$

The first term on the right hand side of Equation 2.4 relates to normal elastic beam theory, for which the moment arm, jd, remains constant while the tension force in the longitudinal reinforcement changes over the length of the beam (e.g. MacGregor and Bartlett 2000). This term reduces to zero if the bond, and hence the shear flow, between the longitudinal reinforcement and the surrounding concrete is destroyed. This term relates to what is commonly referred to as "beam action".

Complete loss of bond will cause the tensile force in the reinforcing steel to remain constant while the moment arm, jd, varies along the length of the beam as is reflected in the second term on the right hand side of the Equation 2.4. This phenomenon is commonly referred as "arch action" (e.g. MacGregor and Bartlett 2000). Tremendous stresses at the anchorage adjacent to the beam ends would therefore be required to develop the required force in the longitudinal reinforcement if a member resists shear exclusively by arch action. A combination of "beam action" and "arch action" resists the shear effects in typical reinforced concrete beams. However the contribution of these effects is a function of the beam geometry. Beams with shear span-to-depth ratios greater than six that are reinforced with deformed bars primarily transfer forces by beam action (MacGregor and Bartlett 2000). Arch action is the primary shear-carrying mechanism for beams with shear span-to-depth ratios ranging from 0.5 to 2 (MacGregor and Bartlett 2000).

Leonhardt and Walther (1962) reported test results of flexural specimens reinforced with plain steel longitudinal bars and no shear reinforcement and found that shear failure did not govern the failure behaviour. They concluded, based in part on the observed crack patterns, that the shear was carried by arch action which formed as a result of bond loss.

2.3 Factors Affecting Bond

2.3.1 Structural Characteristics

Structural characteristics including: concrete cover, bar spacing, development length, the amount of transverse reinforcement, bar casting orientation, and the transverse spacing between two bars in a splice affect the bond between the longitudinal reinforcing steel and the surrounding concrete (ACI Committee 408 2003).

Increased concrete cover and bar spacing provides additional resistance against slip of the reinforcing steel in concrete members, increasing the bond strength and influencing the mode of bond failure (ACI Committee 408 2003). Bond capacity also increases with the increase of development length or splice length. However bond capacity does not vary proportionally with the development length or splice length for deformed bars (ACI Committee 408 2003). Transverse reinforcement, confining either the developed or spliced bars, also increases the bond capacity and controls the mode of bond failure (ACI Committee 408 2003). Tensile bond capacity increases with the development length. However, the non-uniformity of the bond force distribution along the length of the reinforcement influences the effectiveness of the development length (ACI Committee 408 2003).

The bond capacity also depends upon the casting position of the reinforcing steel. ACI Committee 318 (2008) recommends that the development length for the top reinforcement, defined as those bars that have more than 300 mm of fresh concrete cast below them, should be increased by 30% for deformed bars. The settlement of fresh concrete and the accumulation of bleed water below the reinforcing steel bars are the reasons for the lower bond capacity of the top cast bars (ACI Committee 408 2003).

The use of non-contact lap splices influences the bond capacity of the reinforcing steel bars. An unreinforced section might be created if the transverse spacing of the bars in a noncontact lap splice is high (ACI Committee 408 2003). Therefore, to reduce the effect of transverse spacing of bars in a noncontact splice, a transverse spacing equal to one fifth of the splice length but not more than 150 mm is allowed by American and Canadian design standards (ACI Committee 318 2008; CSA 2004a) for deformed bars.

2.3.2 Bar Properties

Different properties of the reinforcing steel such as the bar size, geometry of the bars, the steel stress and the yield strength, and the bar surface condition affect bond (ACI 408 Committee 2003).

Bond strength depends upon the size of the reinforcing steel bars. The rate of increase of bar area with diameter is higher than that of the bar perimeter. ACI Committee 408 (2003) reported that larger bars require longer development or splice lengths than the smaller bars to develop their failure load as the rate of increase of bar area with diameter is higher than that of the bar perimeter. The effectiveness of transverse reinforcement also increases with the increasing bar size for deformed bars (ACI Committee 408 2003).

Another important factor that influences bond is the geometry of the reinforcing steel. Reinforcing steel bars with different shapes and deformation patterns were used in the construction of historical reinforced concrete structures (Loov 1991). Researchers have shown that the bond capacity of deformed bars is higher than that of the plain steel bars (ACI Committee 408 2003).

Orungun et al. (1977) reported that a lap splice length longer than that required to attain yielding of the reinforcing steel bars does not increase the anchorage capacity. The bar surface condition also influences the bond capacity of the reinforcing steel bars since the magnitude of the frictional forces between the concrete and the reinforcing bars depends

upon the roughness of the bar surface (Abrams 1913). The presence of mud, oil and other non-metallic coatings on the bar surface decreases bond capacity (ACI Committee 408 2003).

2.3.3 Concrete Properties

Concrete properties that affect bond include the concrete compressive strength, aggregate type and quality, tensile strength and fracture energy, concrete density, concrete slump, admixtures, fibre reinforcement, and consolidation (ACI Committee 408 2003).

Bond strength increases with the concrete compressive strength. ACI Committee 408 (2003) reported that the square root of concrete compressive strength, $\sqrt{f'_c}$, represents the contribution of concrete strength to the bond strength for $f'_c < 55$ MPa.

High strength coarse aggregate produces a high fracture energy that reduces crack propagation and thus increases bond strength (ACI Committee 408 2003). Lightweight concrete produces a lower tensile strength, fracture energy, and local bearing capacity, and therefore reduces the bond capacity when compared to the normal-weight concrete (ACI Committee 408 2003). Fibre reinforced concrete increases bond capacity by increasing the tensile strength of the concrete and resisting the propagation of concrete splitting cracks (ACI Committee 408 2003).

Slump, which is the measure of concrete workability, is inversely proportional to bond resistance and is more significant for top-cast bars (ACI Committee 408 2003). Different workability admixtures and chemical admixtures also have adverse effects on bond capacity (ACI Committee 408 2003).

2.4 Bond Test Specimens

2.4.1 General

A wide variety of test specimens have been used to investigate bond in reinforced concrete members. The following sections presents a brief description of the most common specimen types.

2.4.2 Pullout Specimens

Pullout specimens are one of the most widely used bond test specimens due to their ease of construction and testing (ACI Committee 408 2003). Figure 2.2 shows the typical test setup for a pullout specimen. The test bar in a typical pullout specimen is embedded either concentrically or eccentrically in a concrete cylinder or prism (ACI Committee 408 1966). The pullout specimen rests on a rigid base plate. The reinforcing steel is typically loaded monotonically until failure (Feldman and Bartlett 2005) though some cyclic load tests have been performed (Perry and Jundi 1969; Rehm and Eligehusen 1979). Generally, the slip of the reinforcing bar at the unloaded end of the specimen is measured as the test progresses. The average bond stress at various load levels is then typically reported.

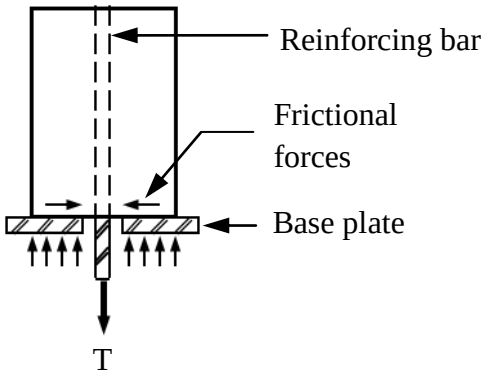

Figure 2.2. Pullout specimen (after MacGregor & Bartlett 2000).

Pullout specimens do not generally represent the true stress state of most reinforced concrete members and therefore test results reported for these specimens are suspect. During the testing of pullout specimens, a tensile force is applied to the reinforcing steel while the concrete surrounding the bar is in compression (ACI Committee 408 2003). The frictional forces that develop between the specimen and the base plate, as shown in Figure 2.2, induce additional compression in the lower portion of the specimen and affect the reported average bond stress (MacGregor and Bartlett 2000). In contrast with the pullout specimens, both the reinforcing steel and the surrounding concrete are in tension in flexural members. Pullout specimens were often fabricated with spiral wire cages to prevent an explosive splitting during testing (Chamberlin 1952). Additional confinement provided by the spiral wire cages generally enhanced the bond capacity (ACI Committee 408 2003). The use of pullout test results to develop development length provisions for reinforcing bars is therefore not recommended.

2.4.3 Beam-End Specimens

A beam-end specimen, also called as modified cantilever beam, is shown in Figure 2.3 and can simulate the stress state of reinforced concrete members that are subject to flexure (ACI Committee 408 2003). The specimen consists of a test bar which is cast in a block of reinforced concrete (ASTM A944 2005). A portion of the test bar near the loading side face of the specimen is left unbonded to avoid the formation of a conical failure surface (ACI Committee 408 2003). The specimen contains stirrups to provide shear resistance. However, the stirrups are oriented parallel to the sides of the specimen to reduce their effects on bond failure. The specimen also contains reinforcing bars to serve as auxiliary flexural reinforcement and facilitate fabrication and testing of the specimen (ASTM A944 2005). Only the test bar and the test setup are shown in Figure 2.3.

The beam-end specimen typically rests on a pedestal. A tension force, T, is applied to the test bar. A reaction plate, which is placed at the end of the specimen that contains

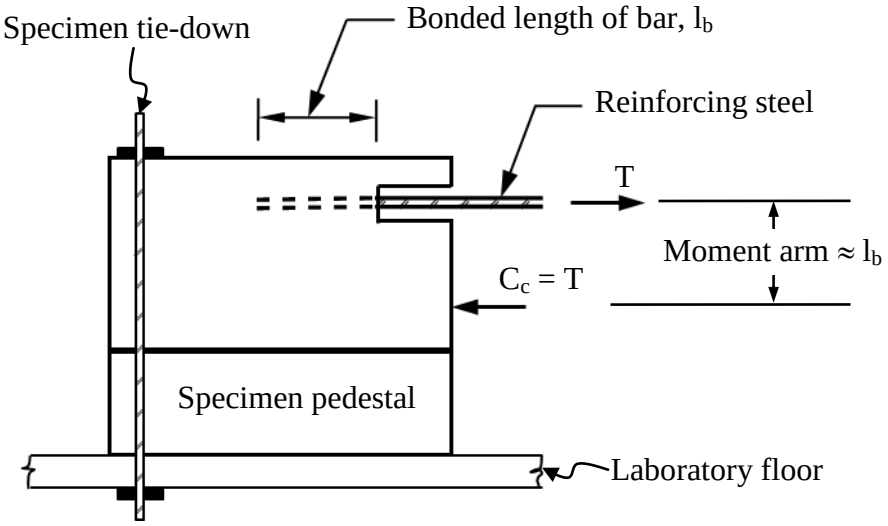

Figure 2.3. Beam-end specimens (after ASTM A944 2005)

reinforcing steel, exerts a compression force, C_c, on the concrete. The location of the reaction plate is such that the distance between the reaction of the plate and the tension in the steel test bar is approximately equal to the bonded length of the reinforcing test bar (ACI Committee 408 2003). The specimen is tied at the other end. The reaction from the specimen tie-down and the specimen pedestal counter the moment produced by the couple resulting from the tension force in the test bar and the compression force in concrete. ASTM A944 (2005) recommended beam-end test specimens to determine the effects of the surface condition on the bond strength of deformed bars.

2.4.4 Conventional Flexural Specimens

Figure 2.4 shows a conventional flexural specimen, often called a beam specimen, which provides a full-scale bond test. Longitudinal reinforcing bars used in the specimens are developed at the beam supports. These specimens are typically simply supported and tested under four-point loading so that the bond behaviour of the reinforcing steel within the constant moment region and in the constant shear regions can be studied using a single specimen (ACI Committee 408 2003). Conventional flexural specimens contain adequate shear reinforcement to resist shear failure. Note that the top bars and the transverse reinforcement are not shown in Figure 2.4 for clarity.

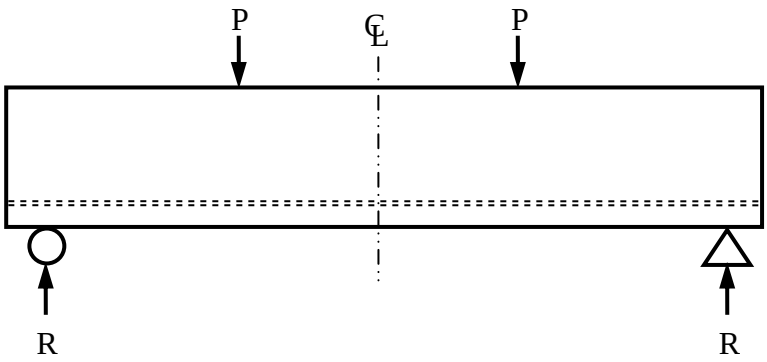

Figure 2.4. Conventional flexural specimen (after ACI Committee 408 2003).

Beam specimens have a significant flaw: the bond capacity of the bars developed at the supports is enhanced due to the high compressive stress developed in that region (Zwicky and Vogel 2006). Test results obtained from these specimens might not truly represent the bond capacity of the longitudinal reinforcement.

2.4.5 Splice Specimens

Figure 2.5 shows a splice specimen which can capture the true stress-state in concrete in the vicinity of the reinforcing bars (ACI Committee 408 2003). This type of specimen is typically simply supported and tested under four-point loading so that the bond behaviour of the reinforcing steel within the constant moment region and in the constant shear regions can be studied using a single specimen.

Figure 2.5 shows that the longitudinal reinforcing bars in these specimens are spliced in the constant moment region. The length of the splice is denoted by L_s, and may vary for testing purposes. The longitudinal reinforcing bars are anchored at the supports to ensure that failure occurs within the midspan splice region. Splice specimens contain adequate transverse reinforcement to resist shear failure and may also contain transverse reinforcement in the midspan splice region. The top bars and the transverse reinforcement are not shown in Figure 2.5 for clarity.

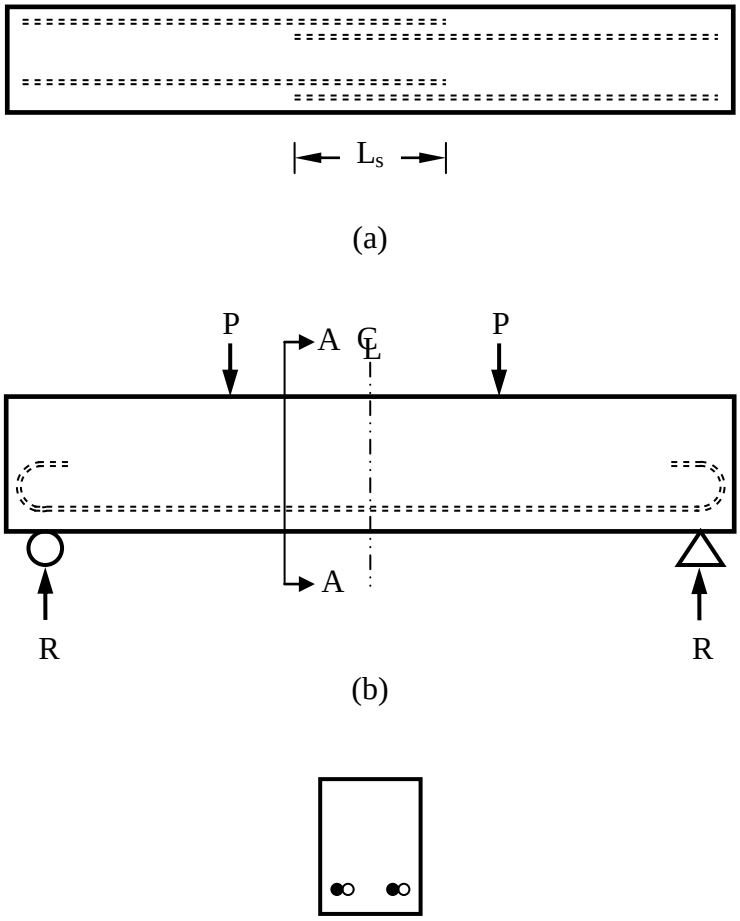

Figure 2.5. Splice specimen: (a) plan view, (b) elevation, and (c) section A-A (after ACI Committee 408 2003).

Splice specimens have been used extensively to study the bond capacity of deformed bars since 1955 (Chinn et al. 1955) and have produced the bulk of the data used to develop the current American and Canadian design provisions for development length (ACI Committee 408 2003; CSA 2004a). Even though splice specimens are widely used to study the bond of deformed bars, they have not been used to study the bond of plain steel bars. Most of the research related to the bond of plain reinforcing bars was conducted at the beginning of the twentieth century when provisions for the bond of the reinforcing bars were specified in terms of average bond stress as determined using relatively simple bond specimens (i.e. pullout).

2.5 Previous Studies

Abrams' (1913) historic research program conducted at the University of Illinois included the testing of both pullout and flexural specimens reinforced with plain steel bars. Figure 2.6 shows the generalized bond stress-slip relationship for pullout specimens with plain round bars that was established from Abrams' (1913) investigation. The established bond stress-slip relationship is independent of bar size and development length. A considerable bond stress develops before the initiation of a measureable slip at the unloaded end of the reinforcement. As unloaded end of the bar starts to slip with increased loading, a rapid increase of bond stress is observed until the maximum bond stress is reached. The bond stress then gradually decreases with increasing slip. Abrams' (1913) observed that first slip begins at the loaded end of the reinforcing bar and gradually extends to the unloaded end. Abrams (1913) therefore proposed that the bond stress distribution along the length of the bar was non-uniform.

Abrams (1913) also tested flexural specimens with span to depth ratios ranging from 1.5 to 3.5 containing plain round and square steel bars. The concrete compressive strength used in the specimens ranged from 9.8 MPa to 28.4 MPa. Specimens were tested under four-point loading. Ames gauges were installed at different locations along the beam specimens to measure the slip of the reinforcing steel with increasing applied load. Most

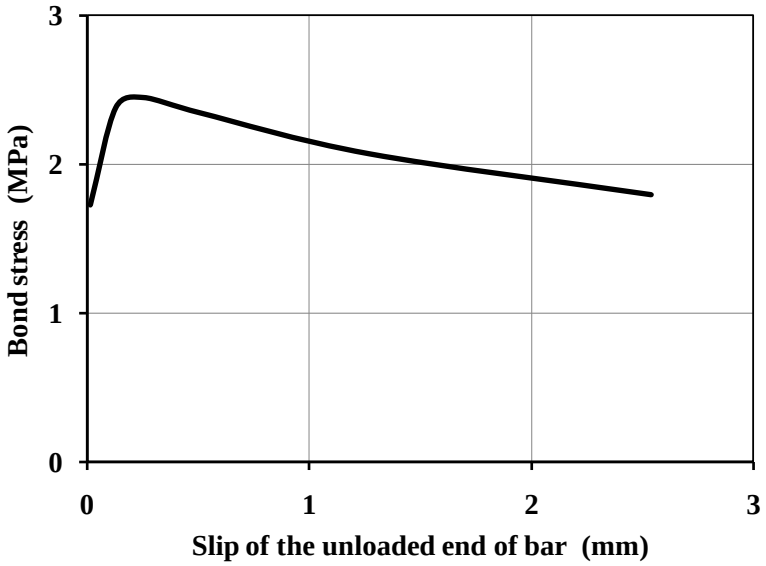

Figure 2.6. Abrams' bond stress-slip model (after Abrams 1913)

of the specimens contained transverse reinforcement in the shear spans to resist shear failure. Abrams (1913) reported that slip of the reinforcing steel first occurs in the constant moment region and then progresses into the shear span. Based on the test results, Abrams (1913) recommended an allowable maximum bond stress of $0.04\,f_c'$ for plain reinforcement. This equation was included in the early editions of American and Canadian reinforced concrete design standards (ACI 1920; Canadian Engineering Standards Association 1929).

Gilkey et al. (1938) reviewed the studies of different researchers (Gilkey and Ernst 1936; Gilkey et al. 1937; and Wernisch 1937) and reported that the average bond stress of plain steel bars does not vary proportionally with the concrete compressive strength when the strength exceeds 13.8 MPa (2000 psi). Pullout test results of 6.5 mm and 19 mm diameter plain steel bars reported by Gilkey and Ernst (1936) and Gilkey et al. (1937) showed that the average bond stress is not proportional to the development length (Gilkey et al. 1938). Rather, the average bond stress increases with development length up to 24 times the bar diameter. Beyond that limit, the average bond stress remains relatively constant with increasing development length. However, Gilkey et al.

(1938) did not present any relationships between the average bond stress, the concrete compressive strength, and the development length.

Mylrea (1948) reviewed Abrams' (1913) study and proposed a multi-step bond-stress distribution for plain steel reinforcement in both pullout and flexural specimens. Figure 2.7 shows Mylrea's bond model for flexural members. In the figure, l is the length of the reinforcing steel measured from the support, and d_b is the diameter of the plain steel reinforcing bar. The allowable bond stress proposed by Mylrea (1948) ranges

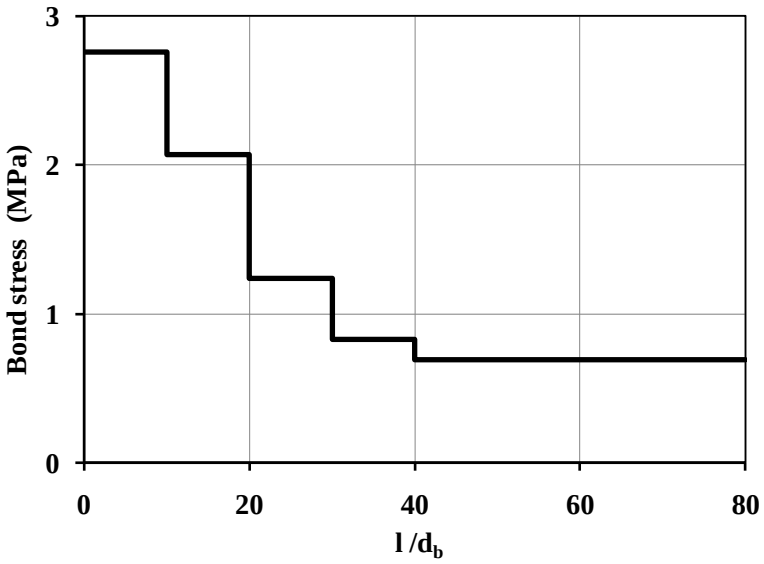

Figure 2.7. Mylrea's bond model for flexural members (after Mylrea 1948)

from 2.8 MPa within $10d_b$ from the end support to 0.7 MPa beyond $40d_b$ from the end support. However, the bond stress model proposed by Mylrea (1948) does not generally equilibrate the forces in the reinforced concrete section; in addition, the effects of the relative slip between the reinforcing steel and the surrounding concrete were not considered in the formulation of this model (Feldman and Bartlett 2008).

The 1963 edition of ACI 318 (1963) was the last to include provisions for the bond of plain steel bars. The allowable bond stress for plain steel reinforcement was one half

that of deformed bars. The code also stated that allowable bond stress is inversely proportional to the reinforcing bar diameter. A thirty percent reduction in allowable bond stress for all top bars was prescribed by ACI 318 (1963) even though the bond of plain bars might be more affected by bar casting orientation (Feldman and Bartlett 2004). The effects of having greater depth of fresh concrete below the reinforcing bar might be more significant for plain steel bars since the bond force transfer of plain steel bars relies solely on the formation of adhesion and friction between concrete and the bars (Feldman and Bartlett 2004).

Bond stress distribution in a flexural member is highly variable and therefore use of a maximum allowable bond stress as a design guideline is unsafe (Winter 1982). The 1971 edition of ACI 318 (ACI 318 Committee 1971) adopted the concept of development length for deformed bars to eliminate the uncertainties in the computation of bond stress in a reinforced concrete flexural member (ACI Committee 318 1971). These new provisions for the development length of plain steel bars were based on the allowable bond stress that was specified in the 1963 version of ACI 318 (Orangun et al. 1977). Provisions for plain reinforcing bars did not appear in this edition of the ACI code, or in more recent code editions.

Research to develop more reliable development length provisions for deformed bars continued and bond provisions for deformed bars have been updated as the test result database increased (ACI Committee 408 2003). Orangun et al. (1977) used splice test results of deformed bars to develop an empirical equation for development length. This equation was presented in the 1995 edition of ACI 318 (ACI Committee 318 1995). Current Canadian and American design provisions (CSA 2004a; CSA 2006; AASHTO 2009; and ACI Committee 318 2008) continue to provide bond provisions for deformed bars in terms of development length. In contrast, limited research is available to develop a reliability-based development length provisions for plain steel bars to aid in the structural evaluation and rehabilitation of historical concrete structures reinforced with plain steel bars (Feldman and Bartlett 2005).

The current CEB-FIP Model Code (CEB-FIP 1993) includes design guidelines for plain steel reinforcement. The CEB-FIP Model Code (CEB-FIP 1993) states that the design value for the allowable bond stress of plain steel bars is 44% of deformed bars provided that all other factors affecting bond are held constant. In contrast to the ACI 318 (1963) design recommendation, the CEB-FIP Model Code (1993) provides a single bar size factor for reinforcing bars with diameter not exceeding 32 mm. A single reduction factor for both plain and deformed bars to account for the effect of top bars is also prescribed. An empirical relationship between the bond stress of plain steel bars, the concrete compressive strength, and the slip of the reinforcing steel is also included. However, the bond model assumes that the bond stress remains constant once 0.1 mm slip in the reinforcing steel is attained. This assumption contradicts the results of Abrams' (1913) work.

Baldwin and Clark (1995) reported test results of beam-end specimens with 8 mm diameter plain steel bars. The test bar was embedded in a prismatic concrete specimen. Specimens were tested such that the stress in the reinforcing steel and concrete matched the true stress state of reinforced concrete members that are subject to flexure. The development length of the reinforcing bars varied from 2.5 to 30 bar diameters and the concrete cover of the specimens ranged from 2 to 6 bar diameters. Rust and mill scale was cleaned from the bar surface and a degreasing agent was used so that a similar bar surface was achieved for all of the specimens. The authors failed to present any data qualifying surface roughness of the bars. They reported that the ultimate failure load of the specimens with plain steel bars varied linearly with the development length and was unaffected by the concrete cover.

Kankam (1997) tested prismatic double pullout specimens with 25 mm diameter instrumented plain steel bars. The test bar was embedded in a square concrete specimen. The length of embedment of the specimens was 200 mm and the bars were anchored at the centre line of the length of the embedment to attain zero slip at halfway between loaded ends. Both ends of the test bar were loaded monotonically to attain the maximum working stress of the reinforcing bars. The author did not present any data qualifying the

surface roughness of the bars. An empirical equation was developed based on the test results to express the bond stress of plain steel bars in terms of steel stress and slip in the reinforcing steel. However, the equation was developed based on the assumption that the bond stress increases with increasing slip which is inconsistent with the findings of Abrams' work (Feldman and Bartlett 2008).

Abrams' (1913) work did not provide enough statistical data to develop new reliability-based bond code provisions to evaluate historical reinforced concrete structures with plain bars (Feldman and Bartlett 2005). Furthermore, the bond behaviour of plain steel bars was not well established in the literature (Abrams 1913; CEB-FIP Model Code 1993; Kankam 1997): different researchers present contradictory relationships between bond stress and slip. Feldman and Bartlett (2005, 2007 and 2008) therefore designed an experimental program at the University of Western Ontario to provide a foundation for the development of reliability-based design provisions for the evaluation of historical concrete structures reinforced with plain bars.

Feldman and Bartlett (2004) reviewed Abrams (1913) historic work and recommended a short list of parameters affecting bond between concrete and plain bars. The list included concrete compressive strength, bar surface roughness, development and splice length, bar size and shape, concrete cover, top bar effects, and bar casting orientation. A total of 252 pullout specimens with plain steel reinforcing bars were tested to investigate all of the previously mentioned parameters with the exceptions of bar casting orientation and top bar effect. Material properties were selected to match historical reinforced concrete structures and other parameters were chosen such that Abrams' (1913) work could be reproduced. Feldman and Bartlett (2005) used a sandblasting technique to produce different surface roughnesses of the plain steel bars used in their study to compare the surface roughness of the modern plain bars with that of the historical plain bars. The surface roughness of the bars were measured in terms of maximum height of profile, R_y, which is the distance between the highest peak and the deepest valley on the bar surface. Feldman and Bartlett (2005) compared their preliminary test results with that of the Abrams (1913) and found that the test results of their sandblasted (R_y = 11.3 μm) and

heavily sandblasted (R_y = 24.7 μm) plain bars provided upper and lower bounds for the test results of Abrams' as-received plain bars.

Feldman and Bartlett (2005) observed a characteristic load-slip curve for all of the specimens: the maximum applied tensile force was observed at a very small slip and then the load dropped asymptotically with increasing slip. This finding verified the bond model proposed by Abrams (1913). Feldman and Bartlett (2005) also reported that the maximum average bond stress and the residual average bond stress were proportional to the square root of the concrete compressive strength, which is inconsistent with Abrams' (1913) reported relationship. Feldman and Bartlett (2005) also reported a quadratic relationship between maximum reinforcing steel tension developed through bond and development length, with a zero intercept. This finding confirms that the relationship between maximum load and development length for plain bars is different than that for deformed bars and prestressing strands (Feldman and Bartlett 2005). Smaller bars also produced a slightly higher bond resistance than larger bars with the same development length. This finding was consistent with Abrams' (1913) historic work. They have also reported that the maximum average bond stress did not vary with the concrete cover.

Feldman and Bartlett (2007) presented a mechanics-based relationship between bond stress, bar force, slip at the loaded end of the bar, and relative slip along the length of the bar in pullout specimens. The analysis of two 200 mm diameter by 800 mm long pullout specimens reinforced with instrumented hollow plain steel bars showed both analytically and experimentally that the bond stress along the length of the bar is non-uniform at all applied loads and is more non-uniform than the model suggested by Mylrea (Feldman and Bartlett 2007). The peak bond stress shifts from the loaded end towards the unloaded end of the specimen with increasing applied load (Feldman and Bartlett 2007).

Feldman and Bartlett (2008) tested two concrete T-beams with shear span to depth ratios of 7.5 to investigate the bond behaviour of flexural specimens. Specimens were reinforced with instrumented built-up hollow plain bars and reinforcement ratios (ratio

of the effective area of the longitudinal reinforcement to the effective area of the concrete) of 0.33% and 0.98%. The specimen with a reinforcement ratio of 0.98% indicated that arch action was the primary force transfer mechanism when the applied load reached 60% of the failure load. The load-deflection behaviour of this beam showed evidence of specimen stiffness reduction. Feldman and Bartlett (2008) concluded that the flexural cracks developed during testing of the specimen might have caused bond loss within its shear span and resulted shift of specimen load carrying mechanism from beam action to arch action. Feldman and Bartlett (2008) compared their results with Mylrea's (1948) proposed bond model and reported that the model is suitable for beams where arch action is the primary shear carrying mechanism.

Bischoff and Johnson (2008) reported test results of four flexural specimens to compare the bond behaviour of plain steel bars and deformed steel bars within the service load range. The shear span-to-depth ratio and the reinforcement ratio of the beams were 3.97 and 1.3%, respectively. The surface roughness of the plain reinforcing steel was approximately 15.5 μm. The longitudinal reinforcement in all of the specimens yielded. The specimens with deformed bars showed a larger yield plateau before failure while the specimens with plain bars exhibited a complete loss of bond once the reinforcing steel yielded and failed immediately without any significant yield plateau. However, identical load-deflection behaviour within the service load range was observed for the two kinds of reinforcement used.

Bond code provisions for deformed bars have evolved markedly over time. Current American and Canadian bond provisions (ACI Committee 408 2003) for flexural members with deformed bars are developed based on the behaviour observed in splice specimens. A similar approach should be followed to develop new bond provisions for plain steel bars to aid in the structural evaluation and rehabilitation of historical concrete structures. Feldman and Bartlett (2005, 2007 and 2008) provided a foundation for the development of a reliability based bond provisions for plain bars. The development of a database of reliable splice test results is the next step towards the development of reliability-based development length provisions for plain steel bars.

CHAPTER 3
EXPERIMENTAL PROGRAM

3.1 General

Fifteen splice specimens were tested in this investigation. This chapter presents details of the specimens including their geometry, instrumentation, and specified material properties. Fabrication of the specimens, including reinforcing cage assembly, concrete placement, and curing of the specimens is also presented with the testing methods used. The details of the concrete and reinforcing steel companion specimen preparation and testing are also described.

3.2 Test Parameters

The current study investigates the effects of bar size and splice length on the bond of plain steel reinforcement. All specimens had identical cross-sectional dimensions and span lengths, but were reinforced with three different sizes of longitudinal bars: 19 mm, 25 mm and 32 mm diameter. The lap splice lengths ranged from 12.8 to 32.4 times the longitudinal bar diameter.

3.3 Test Specimens

3.3.1 Selection of Specimen Geometry

Splice specimens were used for the current study due to their advantages over other bond test specimens as described in Section 2.4.5. One of the sub-objectives of the study was to compare the capacity of the specimens with plain steel bars with that of the deformed bars. Therefore, the specimen geometry was selected such that test results from the program could be compared with specimens with identical geometry that were reinforced with deformed bars as reported by Idun and Darwin (1995).

Idun and Darwin (1995) tested 54 splice specimens containing 25 mm diameter deformed steel longitudinal bars to investigate the effects of: bar deformation patterns, splice length, concrete cover and bar spacing, concrete strength, transverse reinforcement, and epoxy coating on the bond strength of deformed bars. The clear span length of the specimens was either 3.66 m or 4.57 m with 1.22 m or 1.37 m long shear spans, respectively. The height and width of the specimens varied from 390 mm to 440 mm and 305 mm to 610 mm, respectively, to control the concrete cover and longitudinal bar spacing. The specimen lap splice lengths ranged from $16\,d_b$ to $28\,d_b$. No. 10 deformed closed stirrups were provided in the shear spans at 150 mm on centre. Stirrups were also provided in the lap splice region, but their number and bar size were varied to investigate the effects of transverse reinforcement on the bond capacity of the specimens. Stirrups were not provided in the constant moment region outside the lap splice length. The concrete compressive strength obtained from companion cylinder tests at the corresponding splice specimen test date ranged from 28.2 MPa to 37.5 MPa. Specimens were tested in an inverted position under monotonically increasing four-point loading.

Two of the specimens reported by Idun and Darwin (1995) contained 410 mm and 610 mm lap splices of 25 mm deformed bars. The nominal width and height of the specimens were 305 mm and 410 mm, respectively, with clear bottom and side covers to the deformed longitudinal steel bars equal to 50 mm. The specimen clear span was 4.57 m and the shear span-to-depth ratio, a/d, was 3.9. The as-tested concrete compressive strengths were 26.4 MPa and 29.2 MPa for the specimens with 410 mm and 610 mm lap splice lengths, respectively, which represents the upper limit of the concrete compressive strengths used in Abrams' (1913) study of flexural specimens. New North Star deformed bars with a nominal yield strength of 560 MPa and average rib spacings and heights of 12.4 mm and 1.73 mm, respectively, were used as longitudinal reinforcement. These bars comply with ASTM A1035M (2009) specifications for the deformation requirements for deformed bars. No. 10 deformed bars with a yield strength of 445 MPa were used as stirrups. Stirrups were placed at 0.25 L_s from both ends of the lap splice length, where L_s is the length of the lap splice. Both of the specimens failed

due to the loss of bond in the splice region and attained total load equal to 155 kN and 199 kN for the specimen with 410 and 610 mm lap splice lengths, respectively. The geometry of the specimens for the current study was selected such that test results could be compared with the specimens reported by Idun and Darwin (1995).

3.3.2 Specimen Geometry Used in the Experimental Program

Figure 3.1 shows the geometry of the specimens tested in the current investigation. Figure 3.1(a) shows the cross-section of the splice specimens. The nominal width and height of the specimens were 305 mm and 410 mm, respectively. The nominal bottom cover, c_b, and side cover, c_{so}, to the longitudinal plain steel bars was 50 mm for all of the specimens while the clear spacing of the spliced bars varied as the width of the specimen was kept constant. The bottom and side cover of the specimens were lower than one half of the clear spacing between the spliced longitudinal bars, c_{si}, for all of the specimens. Therefore, the 50 mm bottom and side cover would be the governing concrete cover dimension and was constant for all of the specimens. The overall cross-sectional dimensions, including clear concrete cover to the longitudinal reinforcement, were identical to those used by Idun and Darwin (2005) as described in the previous section. The effective depths of the specimens with 19 mm, 25 mm and 32 mm plain longitudinal bars were 351 mm, 347 mm and 344 mm, respectively.

Figure 3.1(b) shows an elevation view of the splice specimens, including splice length, loading, and reinforcing steel arrangement. All of the specimens were 4.87 m long with a clear span between the supports equal to 4.57 m. The shear span of the specimens, a, was 1.37 m and the length of the constant moment zone, L_{cm}, was 1.83 m. The shear span-to-depth ratio, a/d, was 3.91, 3.94 and 3.98 for the specimens with 19, 25 and 32 mm plain longitudinal bars, respectively. The reinforcement ratios, A_s/bd, for the specimens with 19, 25 and 32 mm bars were 0.53%, 0.95%, and 1.51%, respectively.

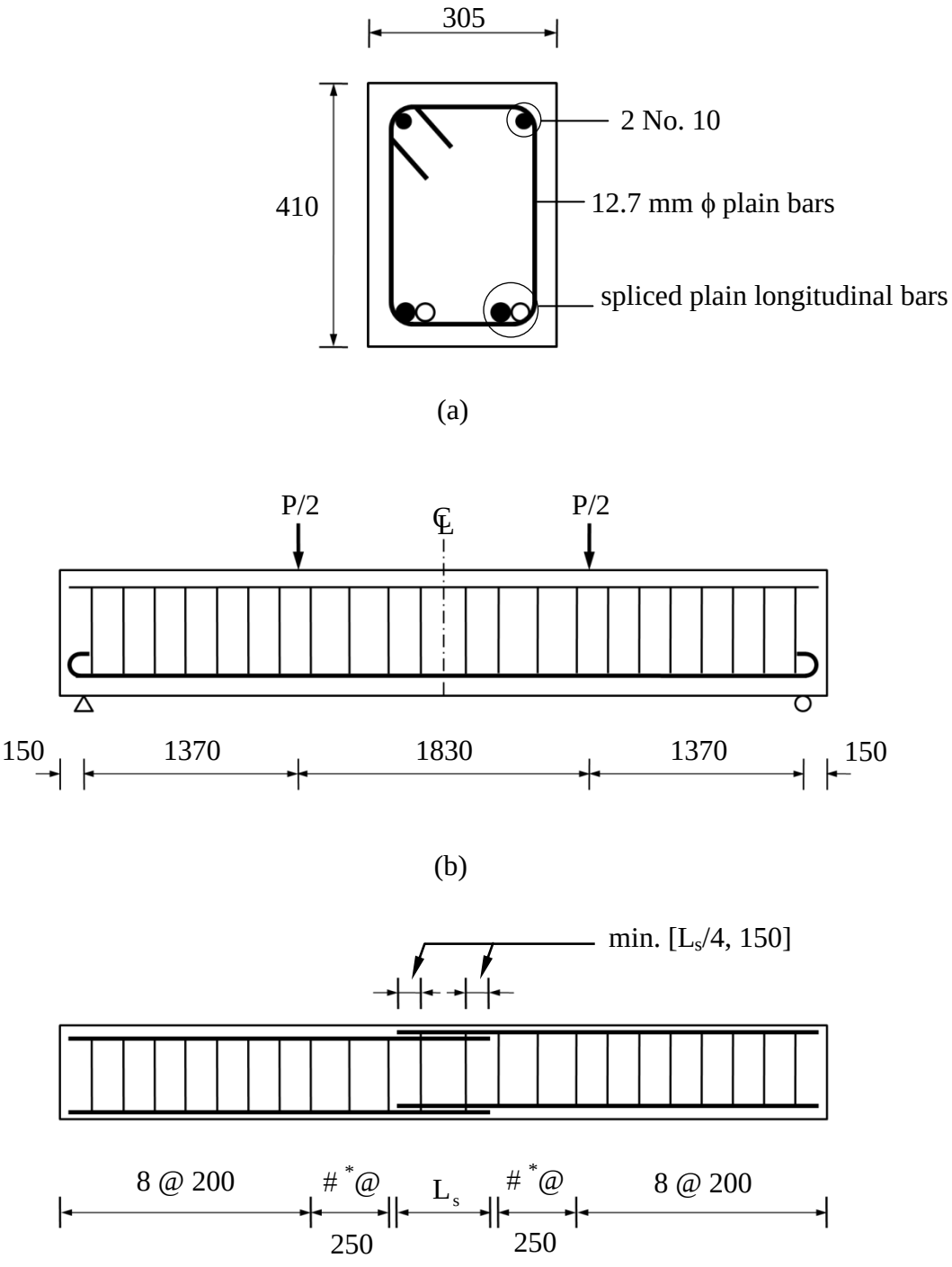

* Note: 2 spaces for $L_s < 810$ mm; 1 space for $L_s \geq 810$ mm

Figure 3.1. Specimen geometry: (a) cross section, (b) elevation and (c) plan view.

Figure 3.1(c) shows a plan view of the specimens and illustrates the arrangement of the spliced longitudinal bars. The lap splices were located in the constant moment region, as shown in the Figure 3.1(c). The other ends of the spliced bars adjacent to the support locations were anchored by means of 180° hooks to ensure that failure occurred within the lap splice length. The diameter of the semicircular bend of the hooks for 19, 25 and 32 mm plain longitudinal steel bars was 6.3, 6.0 and 9.4, respectively, as expressed as multipliers of the respective bar diameter. All hooks also had a straight extension equal to the greater of 4 times the diameter of the bar or 60 mm. The hooks dimensions were selected such that the bars could be bent by a local reinforcing steel supplier. The selected values of bend diameter and extension of the hooks comply with ACI Committee 318 (1963) recommendations for standard hooks for plain steel bars.

The lap splice lengths were selected such that all specimens would fail in bond. CEB-FIP Model Code (CEB-FIP 1993) provisions for bond of plain steel bars, as presented in Appendix 3A, were used to predict the minimum lap splice lengths required to attain yielding of the longitudinal reinforcing steel. The resulting splice lengths were equal to 640 mm, 840 mm and 1080 mm for the specimens with 19 mm, 25 mm and 32 mm plain longitudinal bars, respectively. The specified material properties presented in Section 3.4 were used in these predictions. In contrast, the predicted failure loads for the specimens tested were calculated in accordance with CEB-FIP Model Code (1993) considering actual material properties. These failure loads are reported in Section 4.3.

Specimens were designed for shear in accordance with CSA A23.3-04 (CSA 2004a). Closed 12.7 mm (1/2 inch) diameter plain steel stirrups were provided at a spacing of 200 mm on-centre within the shear spans. The inside diameter of the 90° bends and 135° hooks of the stirrups was 4.7 times their diameter. The 135° hooks had a straight extension of 110 mm (8.66 times diameter of the stirrup bars). The bend diameter and straight extension comply with ACI Committee 318 (1963) recommendations for stirrups with plain steel bars. In contrast with the specimens tested by Idun and Darwin (1995), specimens tested in the current study contained stirrups in the constant moment region outside the lap splice length at a spacing of 250 mm on-centre. These additional

stirrups were provided to prevent failure of the specimens that might otherwise occur due to the cracks that usually appear at the end of the lap splice length as a result of the abrupt change in specimen stiffness at these locations (Aly et al. 2006). Two additional stirrups were provided within the lap splice length at a distance of one quarter of the splice length but not more than 150 mm from the end of the splice to resist prying action (Lukose et al. 1982). The upper limit of the spacing of the stirrups in the lap splice length was set to ensure that the stirrups were located close to the end of the lap splice length regardless of the lap splice length used.

The diameter of the transverse reinforcing bars used in the current investigation was slightly larger than that used by Idun and Darwin (1995). The bar size selection was governed by commercial availability. The slight difference in bar diameter was not expected to cause any significant influence in the bond capacity of the specimens as the bond failure mode for plain steel bars is different than that of the deformed bars, as discussed in the Section 2.5.

Table 3.1 presents specimen details including the as-measured longitudinal bar diameter, lap splice length and casting and testing dates. Details of the bar diameter measurement and preparation of specimens are presented in Sections 3.4 and 3.5, respectively. Twelve out of fifteen specimens longitudinally reinforced with 19, 25 and 32 mm bars were fabricated without any internal instrumentation. Lap splice lengths were selected such that the effects of bar diameter and lap splice length on the maximum load carrying capacity of the specimens and their failure behaviour could be studied when other parameters affecting bond of plain steel bars were held constant. The maximum load carrying capacity of the specimens was normalized by the square root of the concrete compressive strength, $\sqrt{f'_c}$, to facilitate direct comparison as it represents the concrete contribution to the bond strength of plain steel bars, as discussed in Section 2.5. Four

Table 3.1. Specimens details

Specimen ID*	Bar Diameter d_b (mm)	Lap Splice Length L_s (mm)	Date Cast	Date Tested	Specimens stripped from forms (Days)	Age at test (Days)
19-305	19.0	305 (16.1 d_b)	February 10, 2009	April 3, 2009	11	52
19-410	19.0	410 (21.6 d_b)	February 10, 2009	April 3, 2009	11	52
19-510	19.0	510 (26.8 d_b)	February 10, 2009	March 31, 2009	11	49
19-610	19.0	610 (32.1 d_b)	March 25, 2009	May 19, 2009	8	55
25-410	25.3	410 (16.4 d_b)	July 21, 2008	November 24, 2008	11	126
25-510	25.2	510 (20.4 d_b)	July 21, 2008	November 27, 2008	11	129
25-610	25.3	610 (24.4 d_b)	July 21, 2008	November 17, 2008	11	119
25-810	25.3	810 (32.4 d_b)	March 25, 2009	May 22, 2009	8	58
32-410	31.7	410 (12.8 d_b)	February 10, 2009	April 1, 2009	11	50
32-610	31.7	610 (19.1 d_b)	February 10, 2009	April 1, 2009	11	50
32-810	31.7	810 (25.3 d_b)	February 10, 2009	March 20, 2009	11	38
32-910	31.8	910 (28.4 d_b)	March 25, 2009	April 30, 2009	8	36
25-410I	25.3	410 (16.4 d_b)	March 25, 2009	June 10, 2009	8	77
25-510I	25.3	510 (20.4 d_b)	March 25, 2009	June 11, 2009	8	78
25-610I	25.3	610 (24.4 d_b)	March 25, 2009	June 10, 2009	8	77

* The first number in the specimen designation refers to the size of the longitudinal reinforcing bars and the second number refers to the splice length provided. An 'I' following the specimen designation identifies the specimens that were instrumented with strain gauges.

different lap splice lengths were selected for each longitudinal bar size so that a relationship between the maximum attained load versus lap splice length could be determined. Specimens that were longitudinally reinforced with 25 mm diameter bars and had lap splice lengths of 410 and 610 mm were intentionally cast to provide a comparison with specimens having identical geometry and reinforced with deformed bars as reported by Idun and Darwin (1995).

Three identical specimens, longitudinally reinforced with 25 mm diameter bars, and containing lap splice lengths of 410, 510 and 610 mm were instrumented with both concrete and steel strain gauges. The steel and concrete strain gauges used in the study were manufactured by the Tokyo Sokki Kenkyujo Company Limited, Tokyo, Japan and were supplied by Hoskin Scientific Limited, Vancouver, Canada. The steel strain gauges (manufacturer designation FLA-6-11-3LT) were 12.5 mm long and 4.3 mm wide with a gauge length and width of 6 mm and 2.2 mm, respectively. The concrete strain gauges (manufacturer designation PFL-30-11) were 40 mm long and 7 mm wide and had a gauge length of 30 mm and width of 2.3 mm.

Figure 3.2(a) shows the plan view of the instrumented specimen and illustrates the location of the steel strain gauges. Each segment of the spliced bars in the lap splice length for Specimens 25-410I and 25-510I was instrumented with two steel strain gauges: one at the loaded end of the lap splice length and the other at the centreline of the splice. Each segment of the spliced bars in the lap splice length for Specimen 25-610I was instrumented with four steel strain gauges: at 0, 0.25 L_s, 0.5 L_s and 0.75 L_s, from the loaded end of the splice, where L_s is the lap splice length. Steel strain gauges were used to determine strain compatibility and bond-stress distribution along the lap splice length. They were also used for flexural sectional analysis within the lap splice length.

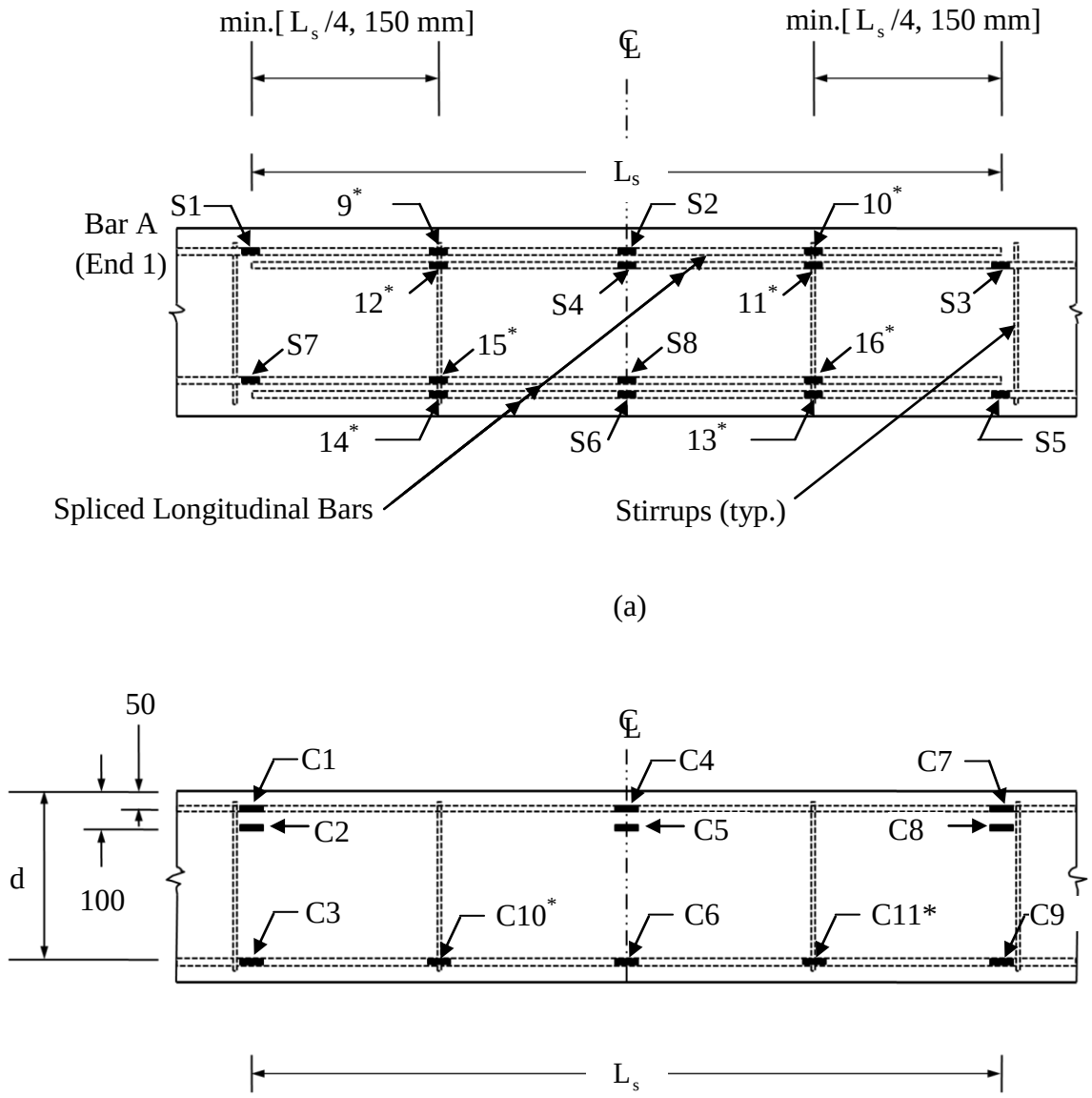

* Specimen 25-610I only

Figure 3.2: Strain gauge arrangements in instrumented specimens: (a) steel strain gauges shown on a plan view; (b) concrete strain gauges shown on an elevation.

Figure 3.2(b) shows the locations of the concrete strain gauges that were installed along the lap splice length on one side face of the instrumented specimens. Nine concrete strain gauges, three at each end of the lap splice length and three at the centreline of the lap splice length, were installed on Specimens 25-410I and 25-510I. Concrete strain gauges were located at depths of 50 mm, 100 mm and the effective depth, d, from the top of the specimens. Strains recorded by the three concrete strain gauges at the different depths facilitated a flexural sectional analysis of the specimens. The concrete strain gauges at the effective depth, d, were also used for strain compatibility analyses at these locations. Two additional concrete strain gauges were installed on Specimen 25-610I at the effective depth, d, from the top of the specimen at $0.25\,L_s$ from each end of the lap splice length to facilitate a strain compatibility analysis at these locations.

3.4 Material Properties

3.4.1 Concrete

The concrete specifications were selected such that the final product would be reasonably representative of historical concrete. The target 28 day concrete compressive strength was 20 MPa, which represents the average concrete strength used in Abrams' (1913) flexural specimens. General purpose (type GU) Portland cement without admixtures or air entrainment and normal weight coarse aggregate with a maximum size of 20 mm were used. Concrete was supplied by local ready-mix concrete suppliers. The concrete slump was measured for each batch as per CSA A23.2-00 (CSA 2000) and presented in Section 4.2.1.

Seventy five millimetre diameter by 150 mm long concrete companion cylinders were cast from each batch of concrete supplied. Dimensions of the companion cylinders comply with CSA A23.2-00 (CSA 2000) and were selected such that the stress versus strain relationship of concrete could be established using equipment available in the Structural Laboratory. Companion cylinders were cast in two equal layers with 20 rods per layer. Companion cylinders were capped with a sulphur-based compound to obtain level top and bottom surfaces during testing. Three companion cylinders were tested on

the day of each specimen test to obtain the concrete compressive strength and the stress-strain relationship. A compressometer, available in the Structural Laboratory, was attached to the concrete cylinder to measure its axial deformation with applied load. The Baldwin Concrete Compression machine was used to test the cylinders with a loading rate ranging from 0.17 MPa/s to 0.35 MPa/s. The loading rate complied with the specified rate prescribed by CSA A23.2-00 (CSA 2000). Dial gauge readings at different levels of applied load were recorded manually for the compressometer and used to obtain the axial strain. The results of the concrete companion cylinder tests are reported in Section 4.2.1.

3.4.2 Reinforcing Steel

Historical reinforcing bars had lower nominal yield strengths than those produced today (Erlemann 1999). Reinforcing bars produced between 1910 to 1927, and 1928 to 1963 had approximate average yield strengths of 230 MPa and 300 MPa respectively (Erlemann 1999). CSA G40.21 300W (CSA 2004b) hot-rolled plain steel reinforcing bars with a nominal minimum yield strength of 300 MPa were therefore selected for use in this investigation.

Material properties of the longitudinal bars were established from coupons obtained from the excess length of bars used in the splice specimens. Three steel coupons were prepared and tested in accordance with ASTM A370 (ASTM 2008) for each heat batch and size of longitudinal plain bars. The longitudinal plain steel bars for Specimens 25-410, 25-510 and 25-610 were supplied from one batch, whereas the longitudinal bars for the remainder of specimens with 25 mm bars were supplied from another batch. The longitudinal bars for the specimens with 19 mm and 32 mm bars were obtained from one heat batch each. The steel coupons were tested using a Universal Testing Machine manufactured by SATEC and were stressed at a rate of 1.73 MPa/s to 6.76 MPa/s. Extensometers with a gauge length of 50.8 mm were attached to the coupons to measure the axial deformation of the steel. A data acquisition system, manufactured by National Instruments, automatically logged the time, applied load, and corresponding

deformation during testing, and sampled data at a rate of 5 times per second. The static yield strength, f_{ys}, of the reinforcement was calculated in accordance with Rao et al. (1966) since it is known to be function of the loading rate:

$$f_{yd} - f_{ys} = 6.9 + 0.007\dot{\varepsilon} \qquad [3.1]$$

where f_{yd} is the dynamic yield strength in MPa, and $\dot{\varepsilon}$ is the strain rate within the plastic range in μ mm/mm/s. Equation 3.1 is valid for the strain rates ranging from 200 to 1600μ mm/mm/s. The results of the steel coupon tests are presented in Section 4.2.2.

The surface roughness of the plain steel bars, measured as the distance between the highest peak and deepest valley on the bar surface, was 3.1μ m for bars as-received from the manufacturer. Figure 3.3 shows a surface roughness tester manufactured by Mitutoyo that was used to measure the surface roughness of the bars using a single stroke length of 0.25 mm. The surface roughness of the historical plain steel bars was higher than the modern plain bars, as described in the Section 2.5. Feldman and Bartlett's (2005) pullout test results suggested that the surface roughness of their sandblasted bars (R_y = 11.3 μm) is the lower bound of the surface roughness of Abrams (1913) as-received bars. All longitudinal reinforcement was therefore sandblasted using 220 grit aluminum oxide, a nozzle distance of 125 mm, and a 698 kPa blast pressure to obtain a surface roughness that would result in a measured maximum height of profile, R_y, that approximated the lower bound of the surface roughness of the longitudinal bars used in the Abrams' (1913) investigation.

A total of thirty surface roughness measurements were made on each length of longitudinal reinforcing bar received from the sandblaster. Readings were taken at approximately 200 mm intervals along the length of the bar starting at the end that would be spliced. Three readings were taken around the bar perimeter at each interval.

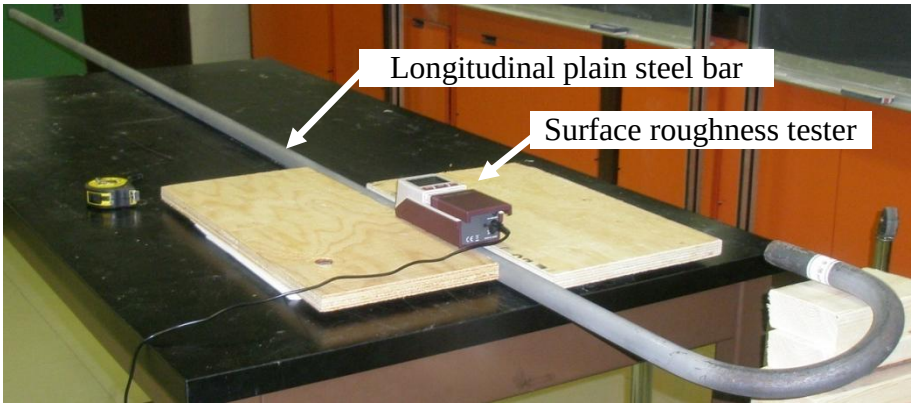

Figure 3.3. Surface roughness measurements.

The bar diameter was also measured using slide callipers at each location of the surface roughness measurements. The surface roughness and bar diameter measurement results are reported in Section 4.2.2.

Shear reinforcement was bent in the laboratory from 12.7 mm (1/2 inch) diameter hot-rolled CSA G40.21 300W (CSA 2004b) steel with a nominal minimum yield strength of 300 MPa. No. 10 Grade 400 deformed reinforcing bars were used as the top bars to facilitate the assembly of the reinforcing steel cage.

3.5 Specimen Preparation

Six meter long bar lengths to be used as the longitudinal reinforcement were received from local suppliers. The bars were then cut to suit using a band saw in the Structural Laboratory and sent to the local sandblasting company. Bars were then transported to a local reinforcing steel supplier to fabricate the 180° hooks described in Section 3.3. Any excess lengths of the sandblasted hooked bars were cut from the splice end using the band saw in the Structural Laboratory to obtain the final desired bar length. Surface roughness and bar diameter measurements were taken as described in Section 3.4.2 and then the bars were covered with plastic sheets and stored in the laboratory to keep them dry and prevent rusting until the reinforcing steel cages were assembled.

The surface of the longitudinal plain bars used in the instrumented specimens was abraded at the strain gauge locations to obtain a flat surface long enough to accept the 12.5 mm long by 4.3 mm wide steel strain gauges. This surface treatment caused a 1% localized reduction of the cross-sectional area of the plain steel bars. The prepared surface was then cleaned with a cloth dampened with isopropyl alcohol to ensure proper adhesion of the steel strain gauges. The strain gauges were installed on the treated surface of the bars using the manufacturer specified adhesives (adhesive type CN as supplied by the strain gauge supplier).

Figure 3.4(a) shows an example of steel strain gauges installed on a reinforcing bar. The steel strain gauges were wrapped with teflon tape and another layer of ordinary tape, as shown in the Figure 3.4(b), to prevent them from being damaged during the fabrication of reinforcement cage and concrete placement operations. The protective seal covered approximately 19.4%, 12.3% and 24.5% of the splice length of Specimens 25-410I, 25-510I and 25-610I, respectively. A reduction in the load-carrying capacity of the instrumented specimens may therefore have resulted due to the reduction in surface area of the reinforcing bars to be bonded with concrete along the lap splice length (Nilson 1971). Steel strain gauges were designated as shown in the Figure 3.2(a); tags containing steel strain gauges designations were attached to the wires connected to the respective strain gauges. Connection wires for the strain gauges were bundled and tied with the stirrups outside of the splice region and brought out from the wooden forms.

All of the stirrups were fabricated in the Structural Laboratory. The out-to-out dimensions of the stirrups were 230 mm wide by 335 mm high. Lifting hooks made from No. 10 deformed bars were bent and tied into the reinforcing cage at a distance of approximately 700 mm from each end of the specimen to facilitate specimen handling using the overhead crane. The utmost care was taken while tying the reinforcing cages, particularly within the lap splice length. Steel tie wires were used to attach stirrups within the lap splice length to the lapped longitudinal bars. The stirrup locations were verified to ensure that they were placed in their specified locations. Additional tie wires were used to fasten the lapped longitudinal bars to prevent them from shifting during the

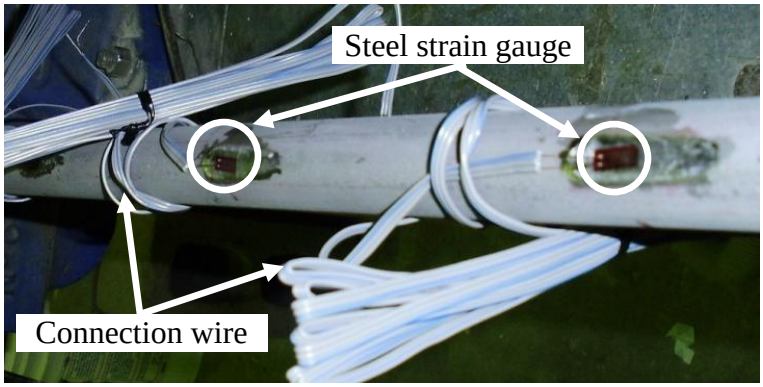

(a)

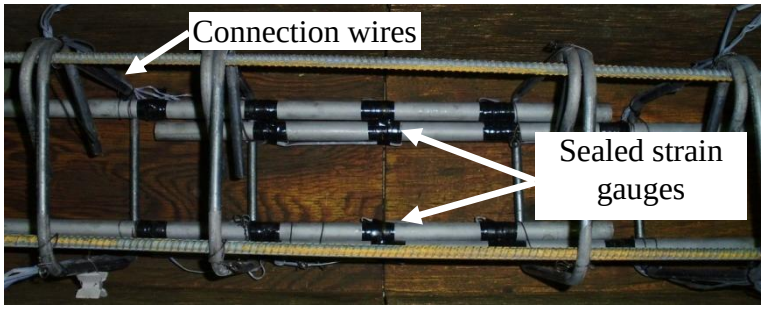

(b)

Figure 3.4. Installation of steel strain gauges: (a) steel strain gauge on the surface of the plain longitudinal bar and (b) complete instrumentation of the lap splice length for specimen 25-610I.

handling of the reinforcing cages. The reinforcing cages used for the instrumented specimens were fabricated with additional caution to protect the installed steel strain gauges from any possible damage.

A form release agent was applied to the walls and base of the wooden forms prior to the placement of the reinforcement cages to ensure that the forms could be easily removed once the concrete was placed and had cured. The form release agent was also applied to plastic moulds used for casting of the companion concrete cylinders.

Fifty millimetre plastic chairs were placed on the base of the wooden forms to maintain the desired bottom clear concrete cover for the longitudinal bars. Plastic chairs of the same dimension were also used to maintain the prescribed side cover for the longitudinal reinforcement. Chairs might locally affect the concrete consolidation and might affect the bond of the longitudinal plain reinforcement at the locations where the bar resting on the chair. Chairs were therefore not placed within the lap splice length.

The reinforcing cages were transported using the overhead crane from the locations where they were fabricated to the wooden forms. Proper caution was taken when the cages were lowered into the forms to avoid contact between cages and the walls and the base of the forms that had been previously coated with the form releasing agent. Necessary adjustments were made to ensure that the specimen geometry and splice details were maintained as required once the reinforcing cages had been placed in the forms. Additional steel ties that were previously used to secure the spliced longitudinal bars were removed. The specimen designation, centreline and outside edge of the hooked reinforcement were marked on the formwork. The forms were then covered with plastic sheets to prevent intrusion of any foreign material in the form prior to concrete placement operations.

The plastic sheeting was removed from the forms prior to concrete placement. Concrete was offloaded from the truck and placed into a hopper. Figure 3.5(a) shows that the

(a)

(b)

Figure 3.5. Concrete placement: (a) specimens and (b) preparation of companion cylinders

hopper was then lifted using the overhead crane and taken as close as possible to top of the required form. The concrete was dropped vertically into the forms and was first placed in the lap splice length to encapsulate it, and then placed in remaining portion of each form. All specimens were placed in two horizontal lifts. An electric internal vibrator was used to compact the concrete between lifts and after the second lift. Wooden screeds were then used to obtain the desired depth of concrete in the form. The top surfaces of the specimens were then finished with a hand trowel. Special care was taken to ensure that the steel lifting hooks that projected vertically from the top face of the specimen remained vertical. The formation of plastic shrinkage cracks on the top surface of the specimen was observed after completion of concrete casting. Companion concrete cylinders were cast as shown in the Figure 3.5(b). The concrete slump was determined in accordance with CSA-A23.2 (CSA 2000) during concrete placement operations.

Figures 3.6(a) and (b) show that the specimens were cured using wet burlap and plastic sheets. Specimens were cured for seven days. The burlap was checked every 24 hours during specimen curing and rewetted as necessary. Concrete companion cylinders were covered with plastic sheets as shown in the Figure 3.6(c) and were cured for seven days

(a)

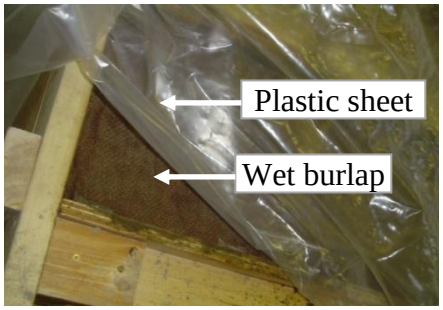

(b)

(c)

Figure 3.6: Concrete curing: (a) specimens, (b) close-up of burlap and plastic sheeting, and (c) companion cylinders

following casting. The specimens were stripped from the forms after 8 to 11 days. The concrete companion cylinders were also stripped out of their respective moulds on the same date. Splice specimens and their companion concrete cylinders were then stored in the Structure Laboratory until testing. The average temperature and humidity of the laboratory were 22° C and 15%, respectively.

As described in Section 3.3, concrete strain gauges were installed on the side face of the instrumented specimens at different depths. The concrete strain gauge locations were marked on the specimen surface, and those surfaces were then abraded to attain a smooth base for bonding of the surface precoating agent. The surface precoating agent (type PS adhesive, supplied by the manufacturer) was applied locally to the surface of

the concrete to approximately achieve a 1 mm thick coating. These areas were covered by a plastic sheet supplied by the manufacturer, and the surface precoating adhesive layer was allowed to cure for 24 hours. The plastic cover was then removed from the surface and the concrete strain gauges were installed using the same precoating agent. The second layer of adhesive with the concrete strain gauges was cured for another 24 hour period. Tags labelled with the concrete strain gauge identification numbers, as shown in the Figure 3.2(b), were attached to the connection wires of the respective gauges.

Specimens were painted white to aid in the identification of cracks during testing. The locations of supports, specimen centreline, the end of the lap splice lengths, and load points were marked on the specimens. The stirrup locations were also marked on the specimens to facilitate the identification of the crack locations observed during testing.

3.6 Test Setup and Procedures

Figure 3.7(a) shows the typical test setup for the specimens. Specimens were simply supported and tested under static four-point loading. The Amsler testing machine supports were removed from the machine located in the Structural Laboratory and fixed to the built-up steel box sections that rested on the laboratory strong floor as shown in Figure 3.7(b). The supports were adjusted to obtain a roller support at one end of the specimen and a pin support at the other end. The bearing area between the specimens and the supports was increased by placing a 150 mm steel plate in between them to prevent a concrete bearing failure at the supports. Specimens were placed on the supports and necessary adjustments were made to ensure that the specimens were level prior to testing.

A 2.3 m long wide flange spreader beam (W310×52) transferred load from the loading frame to the specimen as shown in the Figure 3.7(a). The spreader beam was oriented

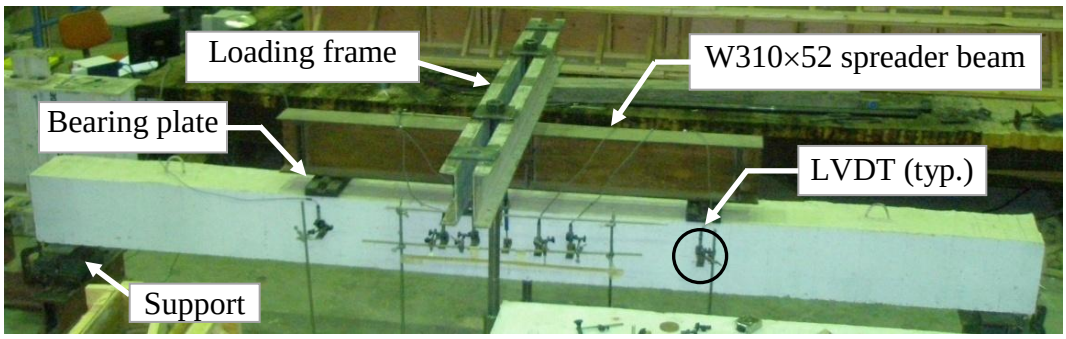

(a)

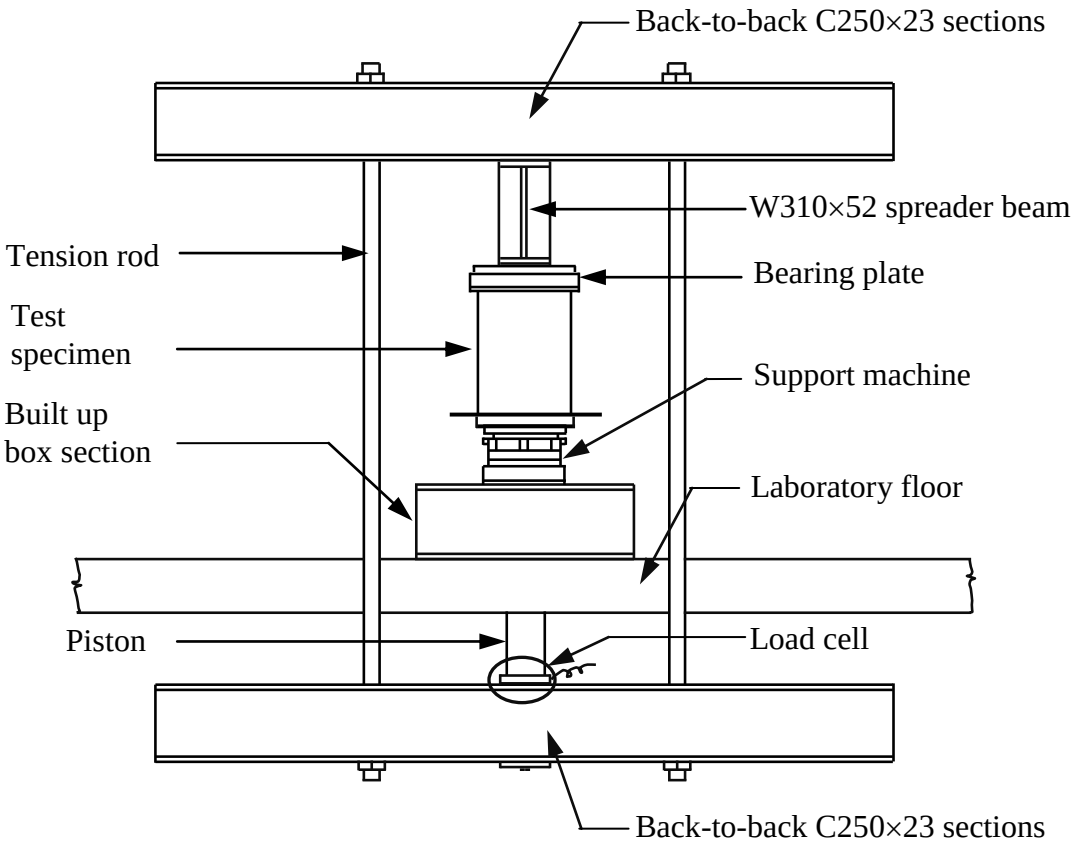

(b)

Figure 3.7: Test setup: (a) typical testing setup, and (b) details of the test set-up

parallel to the specimen with its centreline aligned with that of the specimen. Two 160 mm wide bearing plates were then placed on the top face of the specimen at the location of the applied loads to ensure uniform distribution of the loads from the spreader beam to the specimen. The spreader beam transferred load to the bearing plates via rollers placed in between them. The top face of the specimen at the locations of the applied loads was levelled and compressible plywood was placed between the bearing plates and the specimen to allow uniform transfer of the load over the bearing area.

The loading frame that facilitated transfer of load to the specimens through the wide flange spreader beam is shown in the Figure 3.7(b). Two 2.4 m long steel beams consisting of back-to-back C250×23 channels connected by two tension rods served as the loading frame for the testing. The tension rods were 50 mm in diameter and their centre-to-centre spacing was 1 m. The loading frame was oriented perpendicular to the specimens at midspan. The assembly of the frame was such that one of the steel beams was located beneath the floor of the laboratory and attached to the hydraulic jack piston manufactured by Enpack. A load cell manufactured by Interface Incorporated and capable of measuring loads up to 220 kN was placed in between the hydraulic jack and the spreader beam of the frame to measure the applied load. The other spreader beam was located above the floor such that it could transfer the load applied by the hydraulic jack to the wide flange spreader beam.

The hydraulic jack controlled the stroke rate during testing and supported the loading frame. The specimens were therefore supporting their self-weight and the weight of the wide flange spreader beam and the bearing plates prior to the application of load from the loading frame. The self-weight of the wide flange spreader beam and the bearing plates was measured using the Universal Testing Machine in the Structural Engineering Lab and were equal to 1.29 kN and 0.24 kN, respectively. The capacity of the wide flange spreader beam and the frame was checked in accordance with CAN/CSA S16-01 (CISC 2006) to ensure that they would have adequate capacity to transfer the load to the specimens over the anticipated entire test load range.

Figure 3.8 shows that seven linear variable differential transformers (LVDTs) were used to measure the deflection within the constant moment region for each specimen. Two of the LVDTs were located at each point of applied load, and the remaining five LVDTs were evenly distributed along the lap splice length. The midspan LVDT was manufactured by Curtiss-Wright Company and had a range of 300 mm. All other LVDTs were manufactured by Measurement Group Incorporated and had a range of 50 mm. Steel angles attached at the specimen mid-height were used as reference points for the LVDTs. Figure 3.8 shows the LVDT numbering system.

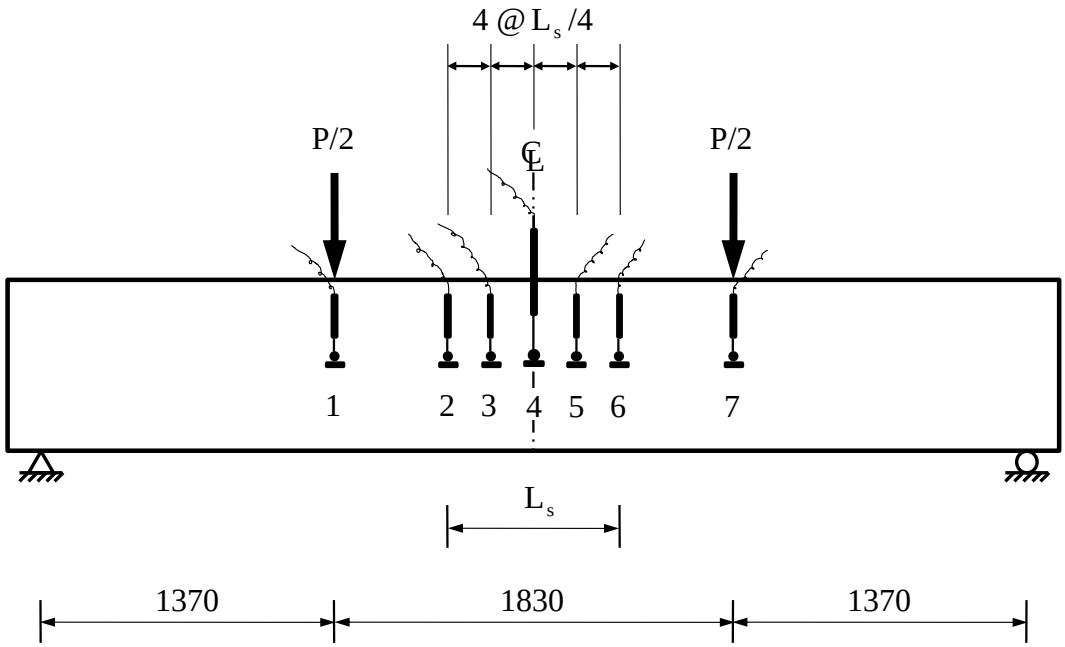

Figure 3.8: Arrangements of the LVDT's.

Figure 3.9 shows the system that was used to control the testing of the specimens. The Labview computer program developed by National Instruments controlled the two-component data acquisition system (DAQ) which was manufactured by the same company. The first DAQ component was an output control module that maintained a monotonic stroke rate of 0.015 mm/s for the hydraulic jack throughout the specimen testing. The second component was the data logger that recorded the load cell, LVDT, and strain gauge readings twice per second. A gap existed between the top steel beam of

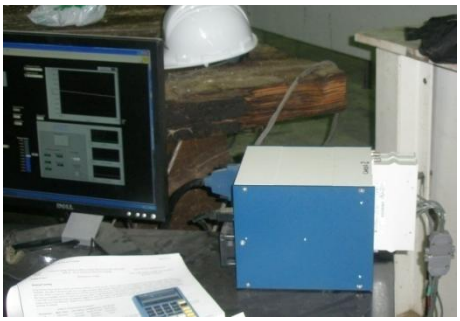

(a)

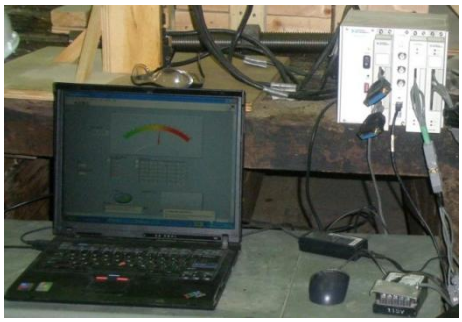

(b)

Figure 3.9: Data acquisition system: (a) system controlling the hydraulic jack and (b) system collecting readings from the load cells, LVDTs and strain gauges.

the test frame and the wide flange spreader beam at the start of the testing. This was done to allow the data acquisition system to log readings for the LVDTs and strain gauges when the applied load was zero and facilitated the calculation of noise in these instruments.

Cracks were marked on the specimens throughout testing. Testing was terminated once the applied load reduced from its maximum recorded value and the critical crack that appeared adjacent to the end of the lap splice length (further discussed in Section 4.4) approximately reached the extreme compression face of the specimen. The concrete cover at the end of the splices was removed after testing to check whether the ends of the spliced steel bars slipped from their initial positions.

This chapter presented details of the experimental program. Fifteen splice specimens were fabricated and tested to fulfill the objectives of the study stated in Section 1.2. A detailed data analysis and discussion of the test results are presented in Chapter 4 and Chapter 5.

CHAPTER 4
LOAD RESISTANCE AND OBSERVED BEHAVIOUR OF TESTED SPECIMENS

4.1 Background

Test results are presented and discussed in this chapter. A comparison of the actual maximum applied loads as recorded for the specimens with the theoretically predicted values is made and results are also compared to similar specimens reinforced with deformed bars as tested by others (Idun and Darwin 1995). A preliminary development length equation for the plain steel bars, developed using a non-linear regression analysis of the test results, is included. Observed specimen behaviour, including typical observed crack patterns and load-deflection response, is reported and discussed.

4.2 Material Properties

4.2.1 Concrete

Table 4.1 presents the age of concrete at the test date, the measured concrete slump, the average concrete compressive strength, f'_c, and the concrete modulus of elasticity, E_c, for all specimens. Concrete slump was measured during specimen casting as discussed in Section 3.5. The average concrete compressive strength, f'_c, and modulus of elasticity of the concrete, E_c, were obtained from testing of the companion cylinders using the construction and testing methods as discussed in Section 3.4.1. The stress-strain relationships for the concrete obtained from concrete companion cylinder testing are presented in Appendix 4A. The concrete modulus of elasticity, E_c, was obtained by performing a linear regression analysis of concrete companion cylinders test data from zero to $0.45 f'_c$.

Table 4.1: Concrete and longitudinal reinforcing steel material properties

Specimen ID*	Concrete				Longitudinal Reinforcing Steel					
	Age of Concrete at Test Date (Days)	Slump of Concrete (mm)	Compressive Strength f'_c (MPa)	Modulus of Elasticity E_c MPa	Bar Diameter d_b mm	Surface Roughness R_y μm	Dynamic Yield Strength f_{yd} MPa	Static Yield Strength f_{ys} MPa	Ultimate Strength f_u MPa	Modulus of Elasticity E_s MPa
19-305	52	95	17.4	18800	19.0	9.54	355	326	520	203000
19-410	52		17.4	18800	19.0	9.67				
19-510	49		18.7	22700	19.0	9.86				
19-610	55	86	21.0	23300	19.0	9.44				
25-410	126	110	23.7	25300	25.3	8.88	346	322	534	196000
25-510	129		24.0	25000	25.2	8.43				
25-610	119		22.8	23800	25.3	8.71				
32-410	50	95	19.8	19000	31.7	9.92	348	318	504	204000
32-610	50		19.8	19000	31.7	9.72				
32-810	38		15.8	19800	31.7	10.1				
32-910	36	86	19.7	22400	31.8	10.0				
25-810	58		19.2	20300	25.3	9.60	346	316	504	206000
25-410I	77		21.5	24200	25.3	9.68				
25-510I	78		20.8	23500	25.3	9.75				
25-610I	77		21.5	24200	25.3	9.94				

* The first number in the specimen designation refers to the diameter of the longitudinal reinforcing bars and the second number refers to the splice length provided. An 'I' following the specimen designation identifies the specimens with internal instrumentation.

An average stress versus strain curve for the concrete at the test date for all specimens was also derived by taking the average of the concrete strain readings obtained from companion cylinder tests at a given stress level, and is presented in Appendix 4A. A regression analysis of average of stress versus strain data for the companion specimens coinciding with each lap splice specimen up to the concrete compressive strength, f'_c, was performed to obtain an equation for the stress-strain relationship to be used in the theoretical load prediction.

4.2.2 Reinforcing Steel

Table 4.1 shows the properties of the longitudinal reinforcing steel including: the as-measured longitudinal bar diameter, the surface roughness, the dynamic yield strength, the static yield strength, the ultimate strength, and the elastic modulus of elasticity. The bar diameter and the surface roughness were measured prior to the assembly of the reinforcing cage as discussed in Section 3.4.2. The dynamic yield strength and the ultimate yield strength were obtained directly from the steel coupon tests as discussed in Section 3.4.2. The stress versus strain relationships for the longitudinal reinforcing steel bars are presented in Appendix 4B. The static yield strength for the longitudinal reinforcement was determined in accordance with Rao et al. (1966) as discussed in Section 3.4.2. The material properties of the transverse reinforcing steel were not established from coupon tests but instead were assumed to be equal to the nominal properties provided for CSA G40.21 300W (CSA 2004b) steel as discussed in Section 3.4.2.

4.3 Maximum Applied Load

4.3.1 Comparison of Actual and Predicted Loads

Table 4.2 presents the maximum applied loads recorded for the specimens and those determined theoretically. The applied loads were recorded directly from the load-cell data as discussed in Section 3.6. Maximum applied loads were normalized by the square

Table 4.2. Comparison of actual and predicted maximum applied loads

Specimen ID	Splice Length as a Multiplier of Bar Diameter, d_b	Normalized Maximum Load $P_{max} / \sqrt{f'_c}$ (kN / √MPa)	Midspan Deflection Corresponding to the Maximum Applied Load (mm)	Predicted Normalized Maximum Load, $P_{max} / \sqrt{f'_c}$ (kN / √MPa)			
				Using average bond stress provisions from CEB-FIP Model Code (1993)	Onset of Steel Yielding, $f_s = f_{ys}$ at $\varepsilon_s = \varepsilon_{ys}$	Strain Hardening Neglected, $f_s = f_{ys}$	Considering Strain Hardening, $f_s = f_u$
19-305	16.0	8.50	7.38	5.06	16.8	18.1	29.5
19-410	21.6	9.14	7.80	7.88	16.8	18.2	29.5
19-510	26.8	9.58	9.17	10.7	16.4	17.6	28.8
19-610	32.1	17.8	17.5	14.0	15.7	16.7	27.3
25-410	16.4	16.2	12.0	12.4	27.0	28.2	45.7
25-510	20.4	18.4	11.0	16.0	26.8	28.1	45.5
25-610	24.4	20.6	14.0	19.4	27.5	28.8	46.5
25-810	32.4	29.7	17.7	25.1	29.0	30.3	46.8
32-410	12.8	15.6	7.81	14.6	43.6	45.5	66.0
32-610	19.1	25.1	10.6	22.3	43.6	45.5	66.0
32-810	25.3	31.8	11.2	28.8	48.2	48.6	68.2
32-910[+]	28.4	34.5	18.6	35.1	45.2	45.8	66.3
25-410I	16.4	14.5	8.41	12.0	27.0	28.6	44.6
25-510I	20.4	17.8	9.59	15.2	27.7	29.1	45.2
25-610I	24.4	15.4	10.5	18.7	27.0	28.7	44.7

[+] Specimen has been identified as outlier

root of the concrete compressive strength, $\sqrt{f'_c}$, as discussed in Section 3.3.2 to provide a direct comparison between the maximum applied loads recorded for different specimens. Table 4.2 also shows the normalized maximum applied loads predicted theoretically. The applied bending moment due to the self-weight of the specimen (2.94 kN/m), and that of the spreader beam and bearing plates (1.29 and 0.24 kN, respectively) used for the test setup were subtracted from the theoretically predicted values of the moment capacity to provide a direct comparison with the test results. The specimen self-weight was calculated assuming normal weight concrete with a density of 2400 kg/m^3 while the weights of the spreader beam and bearing plates were measured directly as discussed in Section 3.6. Table 4.2 also presents the recorded midspan deflection of the specimens corresponding to the maximum applied load.

Specimen 32-910 (i.e. the specimen longitudinally reinforced with 32 mm diameter bars and a lap splice length of 910 mm) has been identified as an outlier as a result of technical difficulties encountered during testing. The specimen required unloading and reloading twice prior to failure and resulted in a total 5.8 mm plastic deflection at the specimen midspan between the initial and final load cycles. This loading and unloading might have affected the bond of the longitudinal plain bars in the specimen and its resulting maximum applied load. The results obtained for this specimen have been excluded from the subsequent analysis.

Table 4.2 presents the normalized maximum applied load calculated in accordance with the CEB-FIP Model Code (1993). The code provisions outlined in Section 3.3.2 and Appendix 3A were used to determine the steel stress that can be developed by the plain longitudinal bars as a function of the lap splice length provided. The concrete compressive strain at the extreme compression fibre and the location of neutral axis corresponding to the calculated longitudinal reinforcing steel stress at the section analyzed were determined assuming perfect bond between reinforcing steel and concrete and equilibrium of internal forces at the section analyzed and following an iterative process. The average stress-strain relationship obtained from the companion concrete

cylinders, as presented in Appendix 4A, was used to obtain the resulting concrete compressive force and its line of action. The moment capacity of the section was determined and adjusted to subtract the specimen self-weight and that of the spreader beam and the bearing plates. The corresponding normalized applied load was then calculated from statics considering the four-point loading arrangement applied.

The normalized applied load required to initiate yielding of the longitudinal reinforcing steel was also calculated and presented in Table 4.2, with the longitudinal steel strain set equal to the steel strain corresponding to the static yield stress. The normalized applied load was then calculated following similar steps as discussed in the previous paragraph.

The normalized maximum load assuming elasto-plastic behaviour of the reinforcing steel was calculated in accordance with CAN/CSA-A23.3 (CSA 2004a) code provisions with the partial material resistance factors set equal to unity and the stress in the longitudinal reinforcement set equal to static yield strength, f_{ys}. The maximum applied load considering strain hardening of the specimens was also calculated by setting the maximum useable compressive strain in concrete equal to 0.0035 and the stress in the longitudinal reinforcing steel equal to its ultimate strength, f_u. The partial material resistance factors were once again set equal to unity. The concrete compressive force and its line of action were determined using Whitney's stress block parameters. The moment capacity of the section calculated neglecting and considering strain hardening of the reinforcing steel was adjusted to subtract the moment due to the self-weight of the specimen and that of the spreader beam and bearing plates. The resulting normalized applied load calculated from statics considering the four-point loading arrangement applied to the specimens is presented in Table 4.2.

The comparison of the actual and theoretical normalized maximum applied loads indicates that all but two specimens failed in bond at loads well below the theoretical values predicted assuming elasto-plastic behaviour of the longitudinal reinforcement. Specimens 19-610 and 25-810 attained loads equal to 106% and 98%, respectively, of

their theoretically calculated maximum loads determined neglecting strain hardening of the reinforcing steel, and 65.2% and 63.5%, respectively, of their theoretically calculated loads considering strain hardening of the longitudinal reinforcement. A more detailed review of the specimen behaviour, as provided by observed crack patterns and load-deflection response, is therefore required to establish the likely failure mode of these two specimens and is discussed in Sections 4.4 and 4.5.

A comparison of the actual maximum normalized applied load with that predicted neglecting strain hardening of the reinforcing steel indicates that the lap splice length required to initiate flexural failure is a function of the longitudinal bar diameter. Specimens with 610 mm lap splice lengths longitudinally reinforced with 25 mm and 32 mm plain steel bars attained 71% and 55%, respectively, of their maximum theoretical applied loads. However, the specimen with the identical lap splice length longitudinally reinforced with 19 mm bars attained an actual load slightly greater than the theoretical maximum applied load predicted neglecting strain hardening of the reinforcing steel. Similarly, Specimen 32-810 attained 68% of its theoretical maximum load predicted neglecting strain hardening of the reinforcing steel, even though Specimen 25-810 attained loads approximately equal to its theoretical yielded load. Longer lap splice lengths are therefore required for larger diameter plain steel bars as compared to smaller diameter bars in order to initiate flexural failure, a finding that is in agreement with the available literature for bond of deformed bars (ACI Committee 408 2003). The tension force that develops in the longitudinal reinforcing steel bar at flexural failure is proportional to the bar area while the bond force is proportional to the surface area of the bar (e.g. MacGregor and Bartlett 2000). The rate of increase of bar area with diameter is higher than that of the bar perimeter as discussed in Section 2.3.2. Larger bars therefore require a longer splice length to develop the desired bar stress at flexural failure (ACI Committee 408 2003).

The normalized maximum loads attained by Specimens 25-410 and 25-610 were compared with identical specimens reinforced with deformed bars as reported by Idun and Darwin (1995). Details of the specimens reported by Idun and Darwin (1995) are

available in Section 3.3.1. The specimen self-weight and that of the spreader beam and bearing plates used in the current study were deducted from the failure loads reported for Idun and Darwin's (1995) specimens to compensate for the fact that the specimens in this earlier study were tested in an inverted position. The resulting maximum loads were normalized by the square root of the reported concrete compressive strength to facilitate a direct comparison and were equal to 27.6 kN/√MPa and 34.4 kN/√MPa for the specimen with 410 and 610 mm lap splice lengths, respectively. The splice specimens reinforced with plain steel bars were capable of resisting peak loads that are approximately 60% of those recorded for identical specimens reinforced with deformed bars with the same nominal diameter.

Instrumented specimens with 410 mm, 510 mm, and 610 mm lap splice lengths attained normalized maximum applied loads equal to 89.5%, 96.6%, and 74.9% of their respective identical specimens without internal instrumentation. The tape used to protect the steel strain gauges affected bond as discussed in Section 3.5 and reduced the load carrying capacity of the instrumented specimens. The load carrying capacity of Specimen 25-610I was 1.06 and 0.87 times the capacity of Specimens 25-410I and 25-510I, respectively, indicating that the load carrying capacity of Specimen 25-610I was affected significantly due to the installation of additional steel strain gauges at the quarter points along the lap splice length for this specimen only. The instrumented specimens were therefore only used to describe bond behaviour as inferred from strain compatibility, bond stress distributions along the lap splice length and flexural section analysis based on strain gauge data. These results are presented in Chapter 5.

CEB-FIP Model Code (1993) provisions for average bond stress underestimated the prediction of the maximum load by 16% on average. A comparison of the maximum applied loads with CEB-FIP Model Code (1993) predictions for specimens that were not instrumented with strain gauges is presented in Figure 4.1. The vertical axis of the figure presents the actual-to-CEB-FIP predicted load ratio and the horizontal axis presents the lap splice length as a function of bar diameter. Figure 4.1 indicates that the CEB-FIP

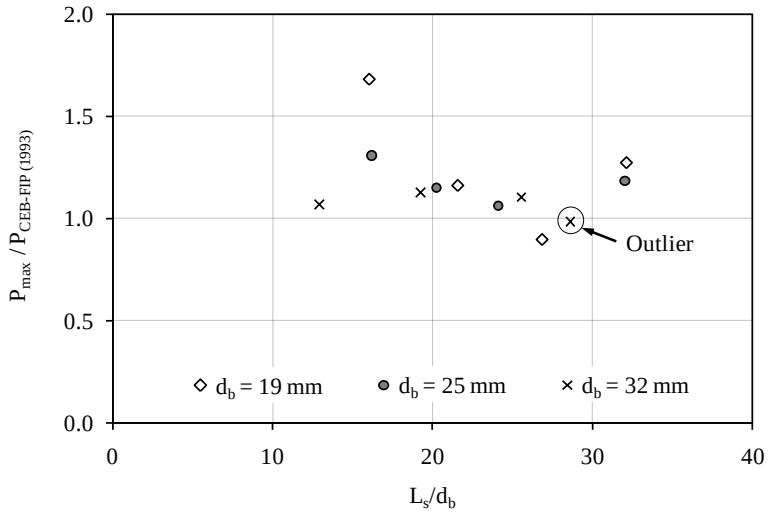

Figure 4.1. Comparison of maximum applied load with CEB-FIP Model Code (1993) predictions.

Model Code (1993) underestimated the maximum applied load by 10% for specimens with 32 mm plain steel bars, in comparison to 21% on average for specimens with 19 mm and 25 mm plain steel bars. It may be noted that the CEB-FIP Model Code (1993) recommended a single bar size factor for bars with diameters less than or equal to 32 mm, which likely contributed to these findings. Figure 4.1 also suggests that the actual-to-predicted load ratio for specimens longitudinally reinforced with 19 mm and 25 mm bars decreased with increasing lap splice length provided that the normalized applied load did not reach that corresponding to the theoretical maximum applied load predicted neglecting longitudinal reinforcing steel strain hardening for the specimen.

4.3.2 Load Capacity as a Function of the Tested Parameters

An empirical equation for the normalized maximum applied load excluding the specimen self-weight and that of the spreader beam and the bearing plates used for the test setup was developed as a function of the splice length and the longitudinal bar diameter. A nonlinear regression analysis of the 11 splice specimens without internal instrumentation yields:

$$\frac{P_{max}}{\sqrt{f'_c}} = 1.37 \times 10^{-4} R_y L_s d_b \quad [4.1]$$

where L_s is the lap splice length in mm, d_b is the longitudinal bar diameter in mm, and R_y is the maximum height of profile as a measure of the bar surface roughness in μm. All parameters in Equation 4.1 are significantly different from zero, and the root mean square error (RMSE) is 2.81 kN/√MPa. Substituting the mean value of 9.44 μm for R_y into Equation 4.1 provides the simplified relationship:

$$\frac{P_{max}}{\sqrt{f'_c}} = 1.29 \times 10^{-3} L_s d_b \quad [4.2]$$

The root mean square error for Equation 4.2 is 2.08 kN/√MPa. Equations 4.1 and 4.2 are valid only for the range of lap splice lengths and bar diameters used in the current investigation. Equation 4.2 suggests that the normalized applied load is proportional to the total surface area of the bar within the lap splice length.

Figure 4.2 shows the fit of Equation 4.2 with the experimental data. A linear and proportional relationship between normalized maximum applied load and lap splice length, with $P_{max}/\sqrt{f'_c} = 0$ at $L_s = 0$, is the best fit. This finding differs from the linear, but not proportional, relationships for deformed bars (ACI Committee 408 2003) and prestressing strands (Barnes et al. 2000). It also differs from Feldman and Bartlett's (2005) suggested quadratic relationship with zero intercept developed for plain steel bars in pullout specimens; however this may be a function of the limited scope of the current study. An expanded study that includes the testing of additional splice specimens with different lap splice lengths and longitudinal bar sizes is required to refine this relationship but is outside of the scope of the current research program.

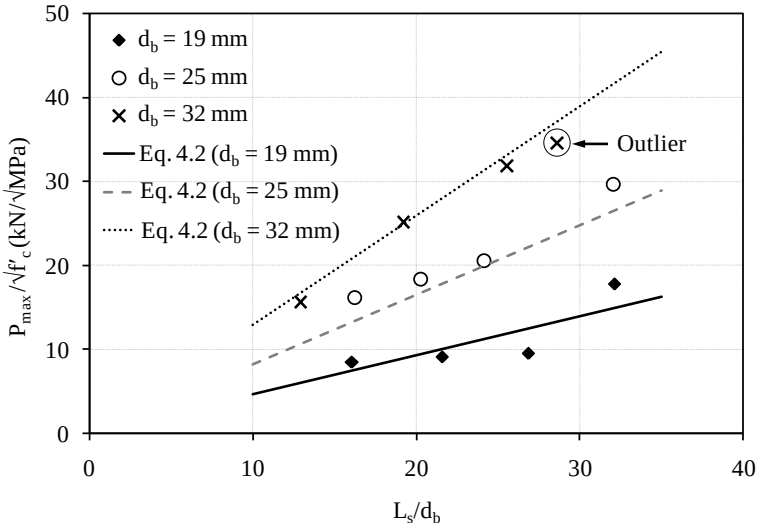

Figure 4.2. Normalized maximum applied load versus development length as a function of bar diameter

4.4 Observed Crack Patterns

4.4.1 General

All specimens exhibited similar crack patterns during testing. Flexural tensile cracks were not observed prior to the testing of the specimens but developed as testing progressed. These flexural cracks first initiated within the constant moment region and were followed by cracks in the shear spans. The average spacing of the cracks was approximately 200 mm and 250 mm on centre within the shear spans and constant moment region outside the splice length, respectively, and roughly coincided with the stirrup locations. Flexural cracks in the lap splice length generally developed near the lap splice length ends, possibly due to the reduced stiffness in these locations (Aly et al. 2006). The development of cracks along the lap splice length was also observed and was more common for specimens with lap splice length greater than $32\,d_b$.

Shear cracks were not observed which might, therefore, indicate bond loss (Leonhardt and Walther 1962). The mechanics of inclined shear crack formation as reported by Leonhardt and Walther (1962), based on their study of flexural specimens reinforced

.

with plain steel bars, can be used to interpret the orientation of the cracks within the shear spans as observed. Figure 4.3(a) shows a cracked reinforced concrete beam subject to four-point loading. Figure 4.3(b) shows that concrete adjacent to the flexural crack within the shear span experiences shear stress due to aggregate interlock, v_a and bond induced shear stress, v_b (Kim 1987). It also experiences a tensile stress, f_d, resulted from the dowel shear, V_d, of the longitudinal reinforcement (Kim 1987). Figure 4.3(b) also shows that the tension in the longitudinal reinforcement, T, varies along its length due to the existence of bond between reinforcing steel and concrete. A concrete element in the shear span adjacent to a crack is identified, with its free body diagram shown in Figure 4.3(c). The shear stress acting on the faces of the element comprises a bond induced shear stress, v_b, and shear stress due to aggregate interlock, v_a (Kim 1987). The tensile stress acting on the element's horizontal faces is a result of dowel shear of the longitudinal reinforcement, f_d (Kim 1987). Kim and White (1999) reported that a localized concentrated bond induced shear stress, v_b, develops soon after the onset of flexural cracking within the shear span of a beam reinforced with deformed bars, and accounts for the formation of inclined shear cracks. The absence of inclined shear cracking within the shear span of the tested specimens therefore indicates that the bond induced shear stress for the specimens was absent or relatively low. This was expected as the bond capacity of plain steel bars depends solely on adhesion and sliding friction between concrete and the bars (Abrams 1913) and reduces when flexural cracks form (Lutz and Gergely 1967). Such a crack pattern also indicates that a specimen's load carrying mechanism shifts towards that of a tied arch (Leonhardt and Walther 1962).

The height and width of one of the cracks in the lap splice length increased suddenly, typically with an audible noise, and the applied load then dropped markedly indicating specimen failure. No splitting cracks were observed during testing of the specimens. Concrete surrounding the longitudinal reinforcing steel at the ends of the splice was removed after testing revealing bar slip. This evidence of bar slip, combined with the absence of splitting cracks and the development of the crack at the ends of the lap splice length at failure suggests a sudden pullout bond failure occurred.

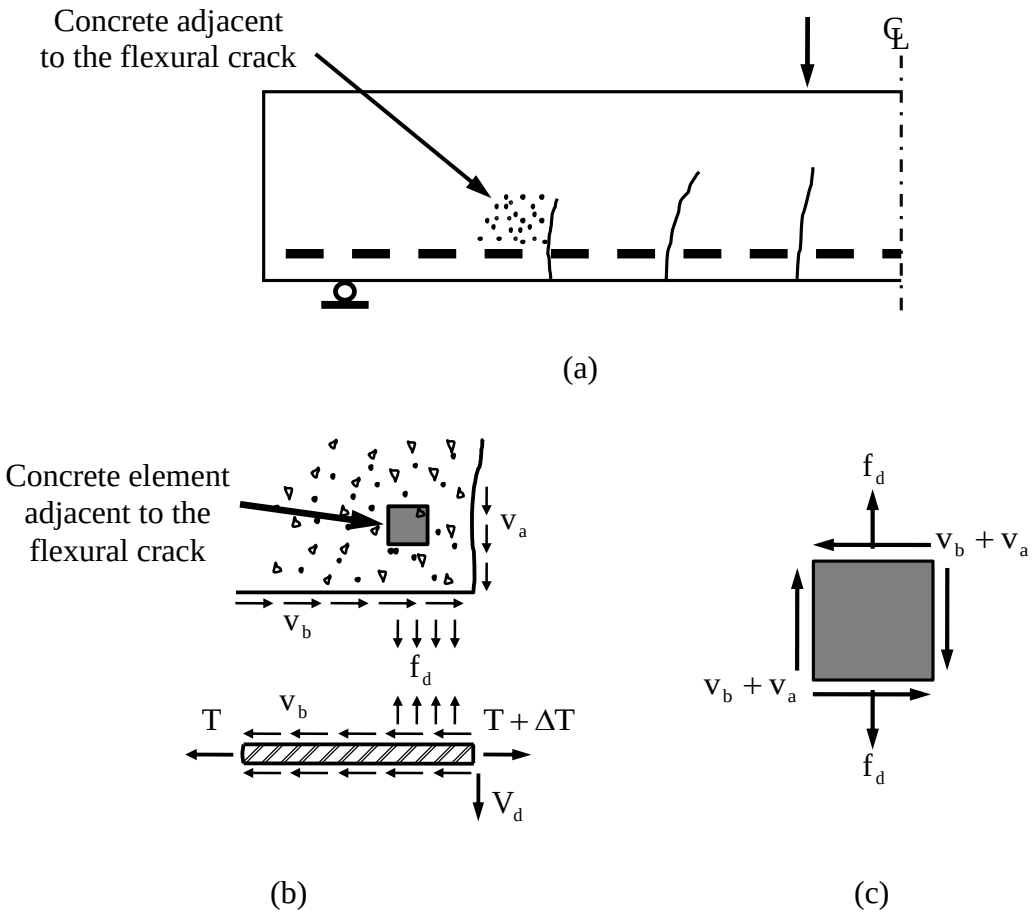

Figure 4.3. Stress state adjacent to a flexural crack in a shear span: (a) reinforced concrte flexural member subjected to four-point loading, (b) stresses on concrete and the reinforcing steel adjacent to a flexural crack, and (c) stress state of a concrete element adjacent to the flexural crack (after Kim 1987).

The following subsections present the specific crack patterns and assessment of girder damage during testing using destructive techniques for four representative specimens: 25-410, 25-610, 25-810, and 19-610. Specimens 25-410 and 25-610 are shown to illustrate the typical damage incurred by a specimen with lap splice length lower than $32d_b$ and to compare their failure behaviour with similar specimens reinforced with deformed bars as reported by Idun and Darwin (1995). Specimens 25-810 and 19-610 are shown to illustrate the typical damage incurred by a specimen that attained or exceeded the maximum applied load predicted theoretically, neglecting strain hardening of the reinforcing steel. Crack patterns and photos of longitudinal bar end slip for all other specimens are presented in Appendices 4C and 4D, respectively.

4.4.2 Specimen 25-410

Figure 4.4 shows the observed crack pattern for Specimen 25-410 at different load levels to illustrate the general cracking behaviour of specimens with lap splice lengths less than $32d_b$. Crack width measurements were not taken and therefore a single line width was used to present all but the large crack that developed at the maximum applied load at the right end of the lap splice length. The formation of the first flexural crack was random and hard to detect with bare eyes. Therefore, the lowest load level presented, $P = 0.6\ P_{max}$, represents the applied load at which the flexural crack first crossed the level of the longitudinal reinforcement.

Figure 4.4(a) shows the crack pattern at $P/P_{max} = 0.6$ and indicates that cracks appeared at the stirrup locations outside of the lap splice length and at the right end of the lap splice length. Figure 4.4(a) also shows that the crack adjacent to the point of applied load on the right-hand side of the specimen midspan crossed the longitudinal reinforcement at this load level. Bond loss was therefore likely adjacent to this crack (Lutz and Gergely 1967) and might cause a shift of the load carrying mechanism from beam action to arch action (e.g. MacGregor and Bartlett 2000).

Figure 4.4(b) shows that previously developed cracks extended to cross the longitudinal reinforcement level at $P/P_{max} = 0.75$, and might signify more widespread bond loss in the specimen. Figure 4.4(c) shows that typical cracks extended to 100 mm from the bottom face of the member when the applied load reached $P/P_{max} = 0.9$.

Figure 4.4(d) shows the observed crack pattern at $P/P_{max} = 1$. The height and width of the crack at the right end of the lap splice length increased suddenly with an audible noise as the maximum load was attained. A marked drop of applied load, indicating sudden failure of the specimen, quickly followed. This crack extended to the mid-height of the specimen while the height of the other cracks generally remained unchanged. No inclined shear cracks were observed. The resulting crack pattern is in contrast with that

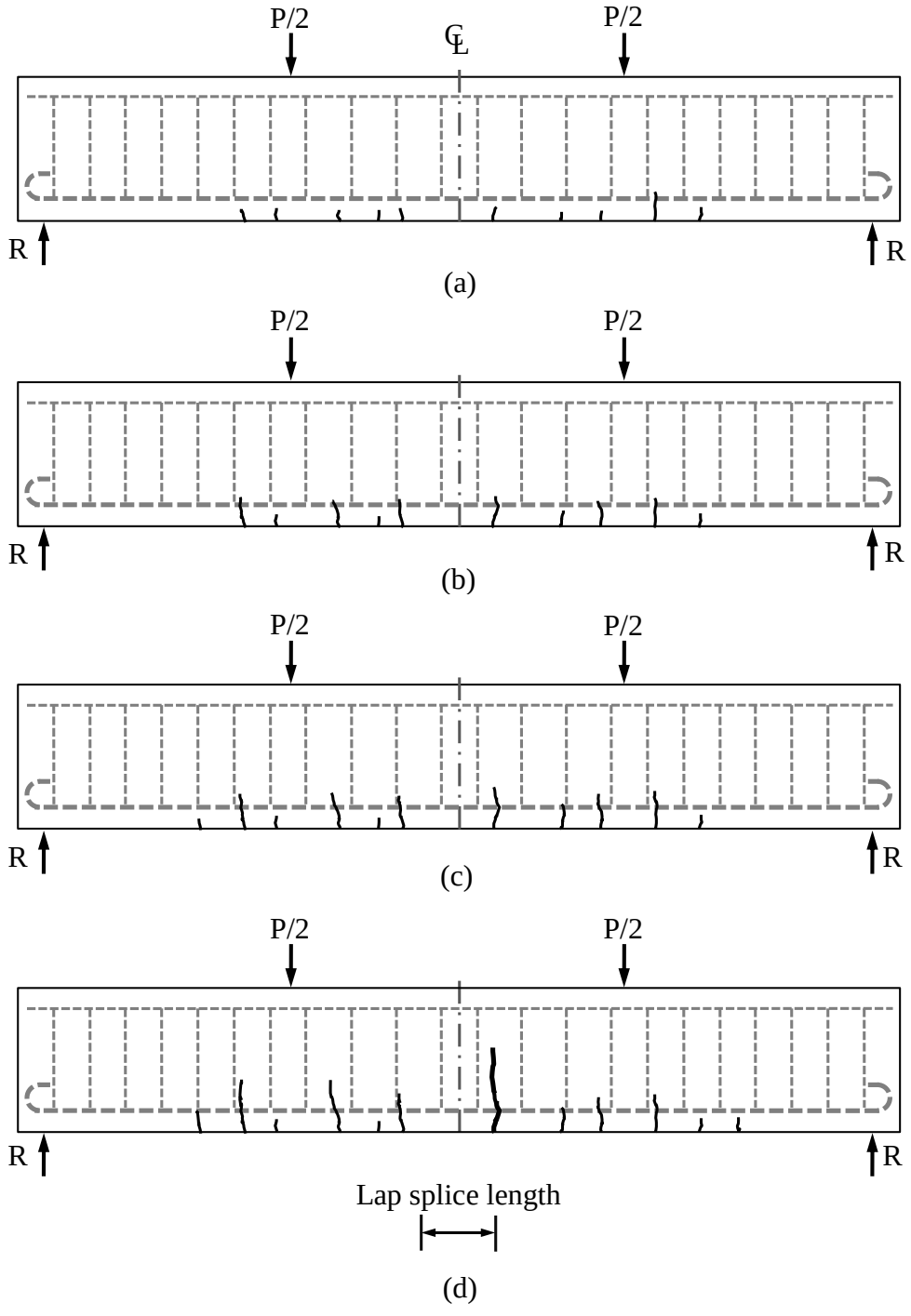

Figure 4.4. Observed crack pattern - Specimen 25-410: (a) P = 0.6P_{max}, (b) P = 0.75P_{max}, (c) P = 0.9 P_{max}, and (d) P = P_{max}.

observed for specimens with deformed bars as reported by Idun and Darwin (1995), in which splitting cracks and shear cracks were identified.

The concrete cover at the ends of the lap splice length was removed after testing. Figure 4.5 shows the resulting end slip. This end slip confirms that specimen failure occurred as a result of bar pullout in the lap splice length and therefore confirms that it failed as per its intended design (see Section 3.3.2).

Figure 4.5. End slip of the lapped longitudinal reinforcing bars - Specimen 25-410.

4.4.3 Specimen 25-610

Figure 4.6 shows the observed crack pattern for Specimen 25-610 at the maximum applied load. Cracking of this specimen was not recorded as the test progressed and so is not available for presentation. Figure 4.6 shows that the general crack pattern for this specimen is similar to that observed for Specimen 25-410, while significant differences exist in their load versus deflection behaviour, as will be presented in Section 4.5.3.

Figure 4.6 shows that cracks formed at the ends of the lap splice length. The width and height of the crack at the left end of the lap splice length increased suddenly at the maximum applied load and extended approximately 300 mm from the bottom face of the specimen. The cracking behaviour of this specimen otherwise coincided with the typically observed crack pattern for Specimen 25-410 as described in Section 4.4.2.

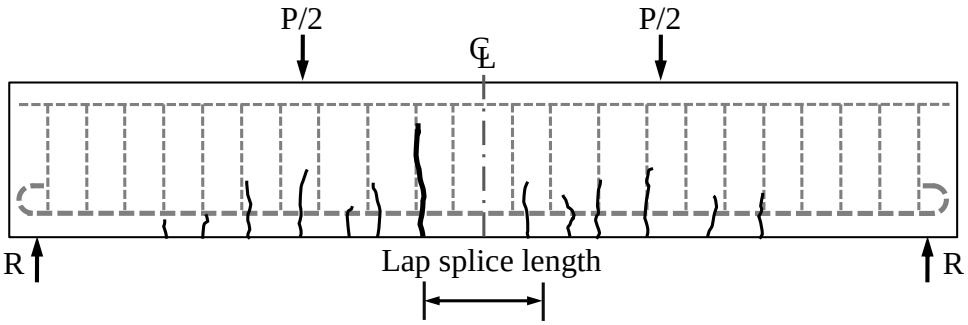

Figure 4.6. Observed crack pattern - Specimen 25-610.

The concrete surrounding the longitudinal reinforcement adjacent to both ends of the lap splice length was removed after testing was terminated and revealed end slip of the longitudinal reinforcement. Figure 4.7 shows this end slip and suggests that failure of this specimen resulted from longitudinal bar pullout caused by bond loss.

Figure 4.7. End slip of the lapped longitudinal reinforcing bars - Specimen 25-610.

4.4.4 Specimen 25-810

Figure 4.8 shows the observed crack pattern for Specimen 25-810 and illustrates the general cracking behaviour of a specimen with a lap splice length greater than $32d_b$ that attained 98% of its theoretical maximum applied load predicted neglecting strain hardening. Though the overall crack pattern matches the general description provided in Section 4.4.1, the loads at which significant crack pattern stages were identified differs from that of specimens with shorter lap splice lengths.

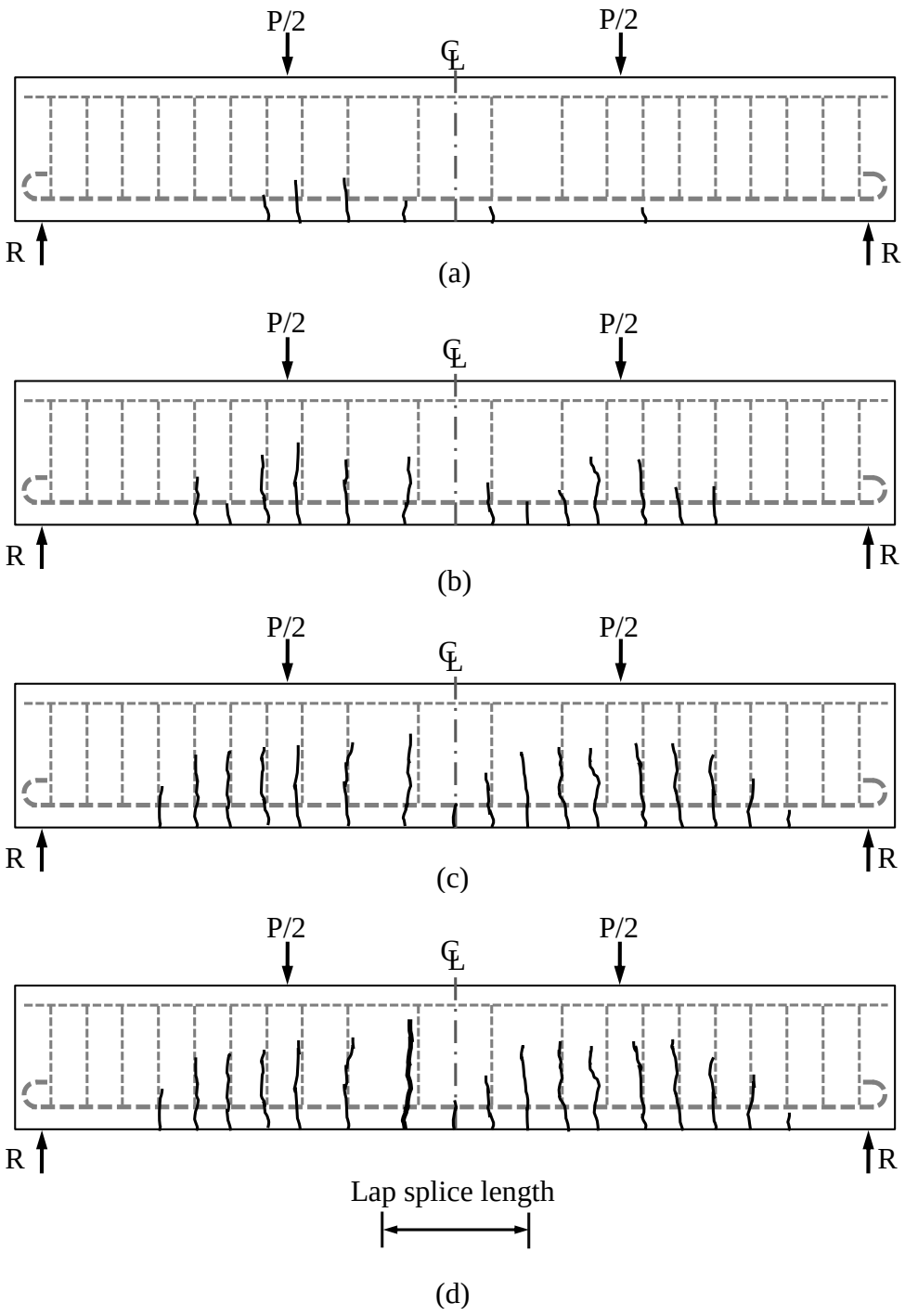

Figure 4.8. Observed crack pattern - Specimen 25-810: (a) P = 0.25P_{max}, (b) P = 0.4P_{max}, (c) P = 0.9 P_{max}, and (d) P = P_{max}.

Figure 4.8(a) shows the observed crack pattern at P/P_{max} = 0.25. Cracks were generally confined to the constant moment region at this load level, with all cracks generally crossing the longitudinal reinforcement. Figure 4.8(b) shows that cracking extended into the shear spans at P/P_{max} = 0.4, with the formation of new cracks, both within the constant moment region and the shear spans. Figure 4.8(c) shows that new cracks formed at the centreline of the lap splice length and within the shear spans of the specimen as the applied load increased to P/P_{max} = 0.9. Figure 4.8(d) shows that the crack adjacent to the left end of the lap splice length lengthened and widened considerably at P/P_{max} = 1, followed by a marked reduction in the applied load.

Figure 4.9 shows the condition at each end of the lap splice length once the concrete surrounding the longitudinal reinforcement was removed following testing. Slip of the bars at both ends of the lap splice length is noted. This end slip confirms that specimen failure occurred as a result of bar pullout in the lap splice region rather than yielding of the longitudinal reinforcing steel.

Figure 4.9. End slip of the lapped longitudinal reinforcing bars – Specimen 25-810.

4.4.5 Specimen 19-610

Figure 4.10 shows the observed cracking behaviour of Specimen 19-610. This specimen also attained its theoretical maximum applied load predicted neglecting strain hardening. Figure 4.10(a) shows that cracks were generally confined within the constant moment

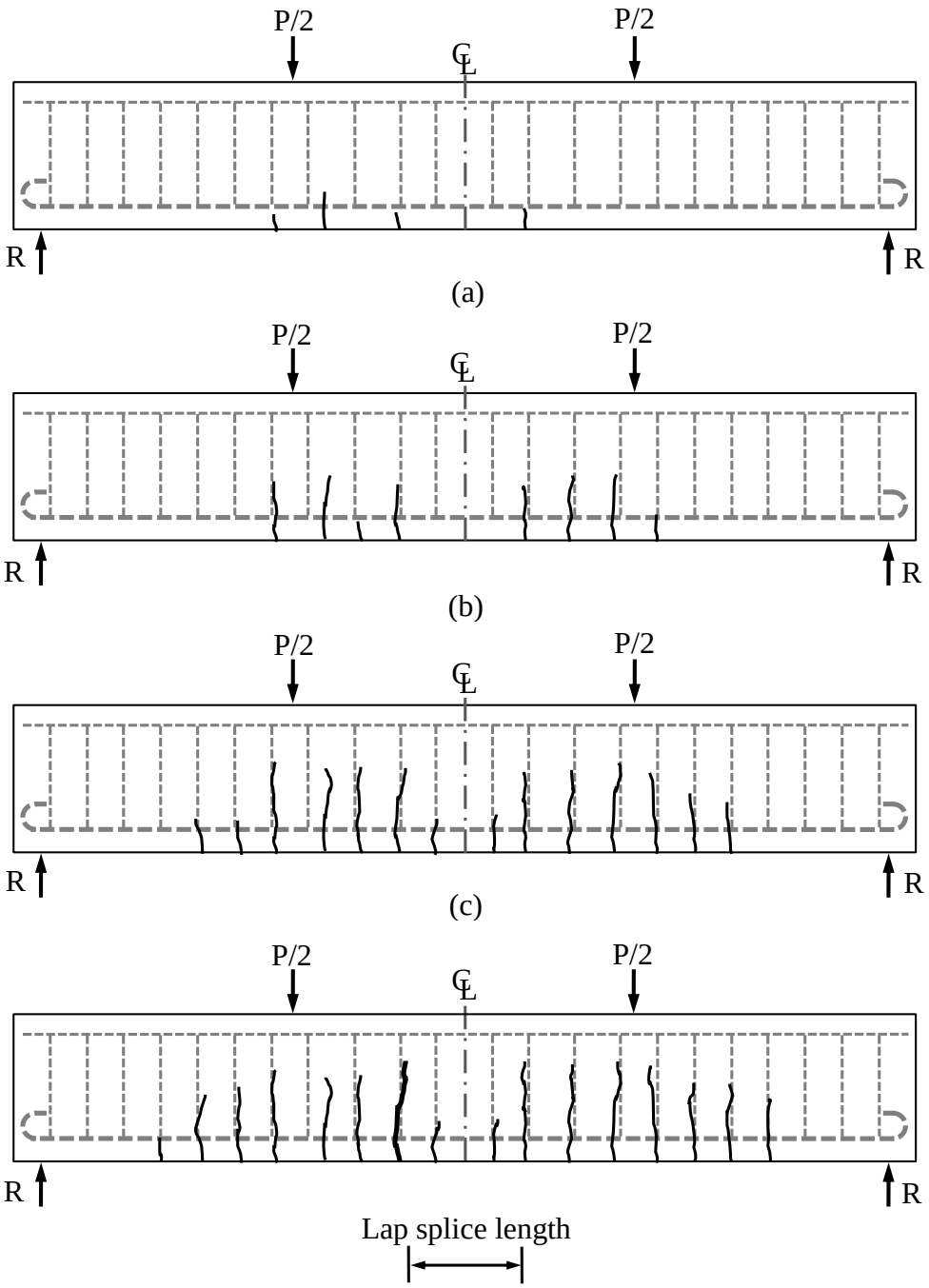

Figure 4.10. Observed crack pattern - Specimen 19-610: (a) P = 0.25P_{max}, (b) P = 0.37P_{max}, (c) P = 0.6 P_{max}, and (d) P = P_{max}.

region at P/P_{max} = 0.25 and that the crack pattern was similar to that identified for Specimen 25-810 at this same level. However, Figure 4.10(b) shows that the lengths of the cracks extended to the specimen midheight when the applied load reached P/P_{max} = 0.37. Figure 4.10(c) shows that new cracks within both the constant moment region and the shear spans developed as P/P_{max} increases to 0.6. Though further increase in the applied load did not result in any observable increases in crack height, slight widening of previously developed cracks in the constant moment region was observed as P/P_{max} increased to 0.9. Figure 4.10(d) then shows that the crack at the left end of the lap splice length widened considerably at P/P_{max} = 1.0, though no corresponding noise was detected. The applied load then markedly decreased.

Concrete cover surrounding the longitudinal reinforcement at the ends of the splice was removed after testing was completed. Figure 4.11 shows that the reinforcing steel at the right end of the splice slipped from its initial position while the left end of the splice did not slip. A bond failure due to pullout of the longitudinal reinforcement therefore accounted for the failure of the specimen.

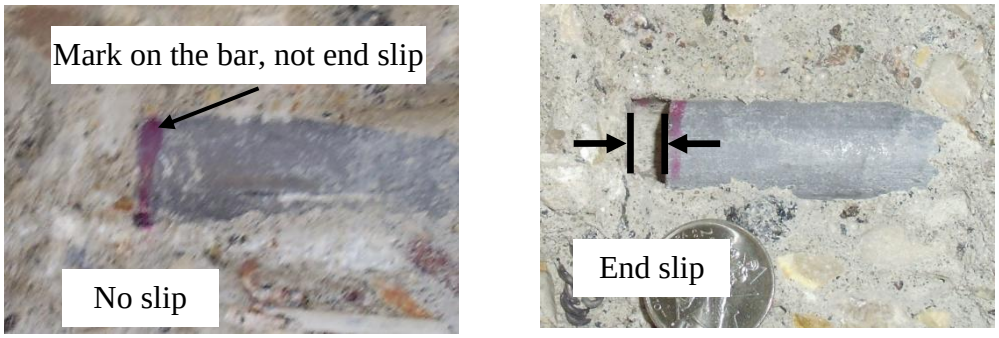

(a) (b)

Figure 4.11. End slip of the lapped longitudinal reinforcing bars - Specimen 19-610: (a) left end, and (b) right end.

4.4.6 Summary – Observed Crack Pattern

The typically observed crack patterns as described provide a useful means to identify the failure behaviour of the tested specimens. Specimens 19-610 and 25-810 exhibited a characteristic crack pattern similar to that observed for other specimens: even though their maximum applied loads were approximately equal to their respective theoretical maximum load calculated neglecting strain hardening (i.e. $f_s = f_{ys}$).The observed crack patterns and evidence of longitudinal bar end slip suggest that all specimens failed in bond due to pullout of the longitudinal reinforcement. Inclined shear cracks did not form within the shear spans of the specimens due to loss of bond and suggested that the load carrying mechanism of the specimen shifted towards that of a tied arch. The length and width of one of the cracks at the ends of the lap splice length increased suddenly indicating bond failure of the specimen occurred due to the pullout of the bars within the lap splice length. The following section presents the load-deflection behaviour for the specimens to provide confirmation of the failure mechanisms.

4.5 Load-Deflection Behaviour

4.5.1 General

Load versus deflection behaviour for the specimens was determined from the LVDT and load cell data. The theoretical load-deflection behaviour was also established to provide a comparison with the actual specimen behaviour. The theoretical specimen deflection at specific locations within the specimen's constant moment region, Δ_x, was calculated for flexural members subjected to four-point loading:

$$\Delta_x\left(a < x < L - a\right) = \frac{Pa}{12E_cI_e}\left(3Lx - 3x^2 - a^2\right) \qquad [4.4]$$

where P is the sum of the two equal point loads applied to the specimens, L is the specimen clear span length, a is the shear span length, x is the distance between the support and the section under investigation, E_c is the modulus of elasticity of the

concrete as presented in the Table 4.1, and I_e is the effective moment of inertia of the member.

The effective moment of inertia, I_e, was calculated from the equation reported by Bischoff (2005):

$$I_e = \frac{I_{cr}}{\left[1-\left(1-\frac{I_{cr}}{I_g}\right)\left(\frac{M_{cr}}{M_a}\right)^2\right]} \leq I_g \qquad [4.5]$$

where I_{cr} is the cracked transformed moment of inertia, I_g is the uncracked gross moment of inertia, M_{cr} is the cracking moment calculated in accordance with CAN/CSA-S6-06 (CSA 2006), and M_a is the moment induced by the applied load. Bischoff's (2005) equation is more accurate than Branson's (1963) equation for members with reinforcement ratios less than 1% (Bischoff and Scanlon 2007). Differences between these two methods reduce with increasing applied load due to the reducing effects of tension stiffening (Bischoff 2005).

The load versus midspan deflection curve for the specimens exhibited a characteristic pattern: the slope of the curve was at its maximum between zero load and that corresponding to first cracking of the section, followed by a reduction in the slope of the curve due to the reduction in the stiffness of the specimen after cracking. Further reduction in the slope of the load versus deflection curve prior to the maximum applied load was also observed for specimens with lap splice lengths greater than $20d_b$ which might be an indication of bond loss (Feldman and Bartlett 2008). The applied load drops markedly with an additional midspan deflection once the maximum load was attained indicating sudden failure of the specimen occurred. No load plateau was observed prior to the failure of the specimen. Observed load versus deflection behaviour of the specimens along with their observed crack patterns and end slip of the longitudinal

reinforcing steel suggests bond failure of the specimens due to longitudinal bar pullout in the lap splice length.

The following subsections present the load versus deflection behaviour at: the specimen centreline (LVDT 4), quarter points along the lap splice length (LVDTs 3 and 5), the ends of the lap splice length (LVDTs 2 and 6), and the points of applied load (LVDTs 1 and 7) for four representative Specimens: 25-410, 25-610, 25-810 and 19-610. The locations of the LVDTs are discussed in Section 3.6 and shown in Figure 3.8. Deflection profiles at different applied load levels for the representative specimens are also presented. The load versus deflection curves and deflection profiles for the remainder of the specimens are presented in Appendices 4E and 4F, respectively.

4.5.2 Specimen 25-410

Specimen 25-410 is representative of the typical load-deflection response for specimens with short lap lengths ($L_s < 20d_b$). Figures 4.12(a), (b), (c), and (d) show the normalized applied load versus deflection at: the specimen centreline, the quarter points of the lap splice length, the ends of the lap splice length, and the points of applied load, respectively. Figure 4.12(a) shows that the slope of the curve between the origin and Point "a", the first cracking load, was at its maximum and was equal to 2.67 kN/√MPa/mm, which is approximately 50% of the theoretical load-deflection curve. The formation of plastic shrinkage cracks, as mentioned in Section 3.5, might be accounted for the lower flexural stiffness of the specimen prior to cracking. The first cracking load was equal to 2.57 kN/√MPa (P/P_{max} = 0.16), which is lower than the theoretical cracking load of 2.89 kN/√MPa. This was expected, as the restraint from shrinkage provided by the reinforcement produces tensile stresses in the concrete and tends to reduce the load corresponding to first cracking (Bischoff and Johnson 2007). Figure 4.12(a) also shows that the slope of the midspan load-deflection curve reduced to 1.34 kN/√MPa/mm after cracking and remained relatively constant from Point "a" until the maximum load was attained.

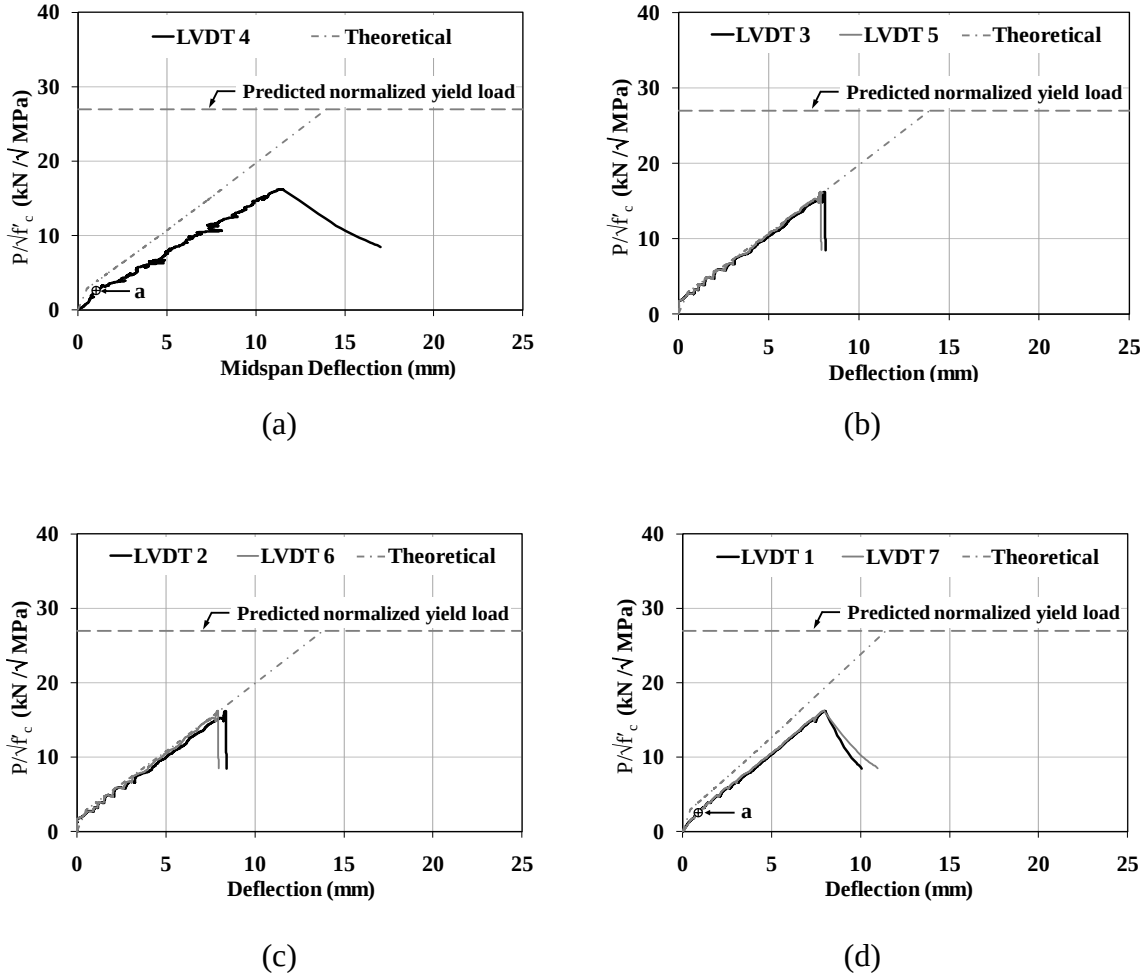

Figure 4.12. Normalized applied load versus deflection - Specimen 25-410: (a) midspan, (b) quarter points along the lap splice length, (c) ends of the lap splice length, and (d) points of applied load.

The failure of Specimen 25-410 occurred suddenly at a midspan deflection of 12.0 mm once the maximum load was attained, as shown in Figure 4.12(a); the load then dropped markedly with an increase in midspan deflection. There was no evidence of a load plateau prior to failure; in addition, the maximum normalized load was well below that required to initiate yielding of the longitudinal reinforcement. This sudden failure of the specimen, as indicated by the load-deflection curve, as well as from the observed crack pattern and evidence of longitudinal bar end slip as discussed in Section 4.4.2, suggests bond failure occurred.

Figures 4.12(b) and (c) show the load-deflection behaviour captured by the LVDTs located at the quarter points and at the ends of the lap splice length, respectively. In contrast with the load deflection behaviour at the specimen midspan, the LVDTs at the lap splice length quarter points and ends showed no significant deflection up until a normalized applied load of 1.8 kN/√MPa (P/P_{max} = 0.11). The slope of the load deflection curve was relatively constant from this point to the normalized maximum applied load and was equal to 1.77 kN/√MPa/mm (approximately equal to the slope of the theoretical load deflection curve at these locations). A rigid body rotation of sections between flexural cracks developed adjacent to the ends of the lap splice length and might have resulted in the lower deflection at these locations. Figure 4.12(d) shows that the deflections at the points of applied load were higher than those predicted theoretically for the entire load range. The slope of the load-deflection curve from the origin to Point "a" was approximately 3.1 kN/√MPa/mm. The slope of the load-deflection curve reduced to 1.91 kN/√MPa/mm after cracking and remains constant until maximum load.

Figure 4.13 shows the deflection profile of Specimen 25-410 at different load levels and provided a comparison with the theoretical deflection profile. The deflected shape at P/P_{max} = 0.16, which corresponds to the theoretical cracking load, indicates that deflection at the load points and midspan deviated from the theoretical deflection. In

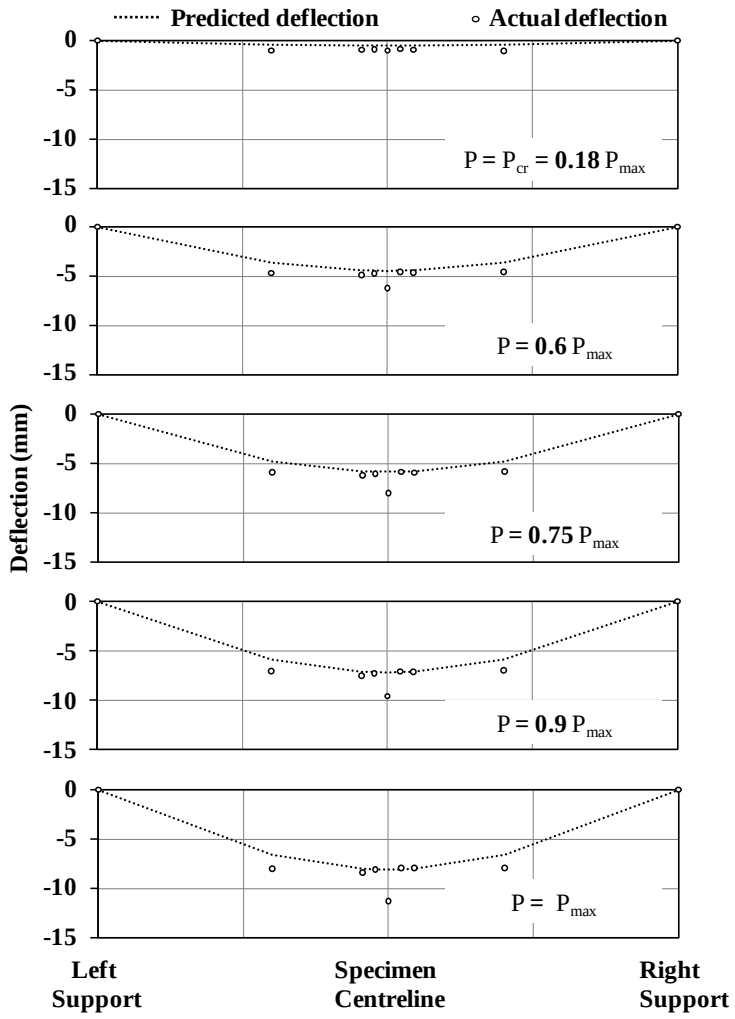

Figure 4.13. Deflected profile at different load levels - Specimen 25-410

contrast with the deflections at the centreline of the lap splice length and at the points of applied load, the deflection at the ends of the lap splice length and at the quarter points along the lap splice length were approximately equal to the theoretical deflection for the entire loading range. Cracks near the end of the splice length influenced the LVDT readings at those locations as discussed earlier and resulted in lower deflections at these locations.

Figure 4.13 shows that the deflected shape of Specimen 25-410 at P/P_{max} = 0.6, 0.75, 0.9 and 1. The observed crack patterns at these load levels were already presented in Section 4.4.2. The deflections at the specimen midspan and at the points of applied load application were consistently approximately 1.4 and 1.2 times the respective theoretical deflections.

4.5.3 Specimen 25-610

Figures 4.14(a), (b), (c), and (d) show the normalized applied load versus deflection at: the specimen centreline, quarter points along the lap splice length, ends of the lap splice length, and the points of applied load for Specimen 25-610 to illustrate the general load-deflection behaviour of specimens with lap splice lengths ranging from $20d_b$ to $32d_b$. The increase in the lap splice length increased the specimen stiffness in addition to its load carrying capacity. LVDT 5 which was located at the quarter point on the right side of the lap splice length centreline did not function properly due to technical difficulties during testing and therefore is not been shown in Figure 4.14(b).

Figure 4.14(a) shows that the load versus deflection curve at the specimen midspan showed an initially steep and linear section between the origin and point "a" similar to that observed for Specimen 25-410. Point "a" corresponds to the normalized applied load at first cracking of the specimen and was equal to 2.67 kN/√MPa (P/P_{max} = 0.13): 7.3% lower than the theoretically predicted normalized cracking load of 2.88 kN/√MPa. The slope of this initial steep portion was equal to 4.13 kN/√MPa/mm which is 15.6%

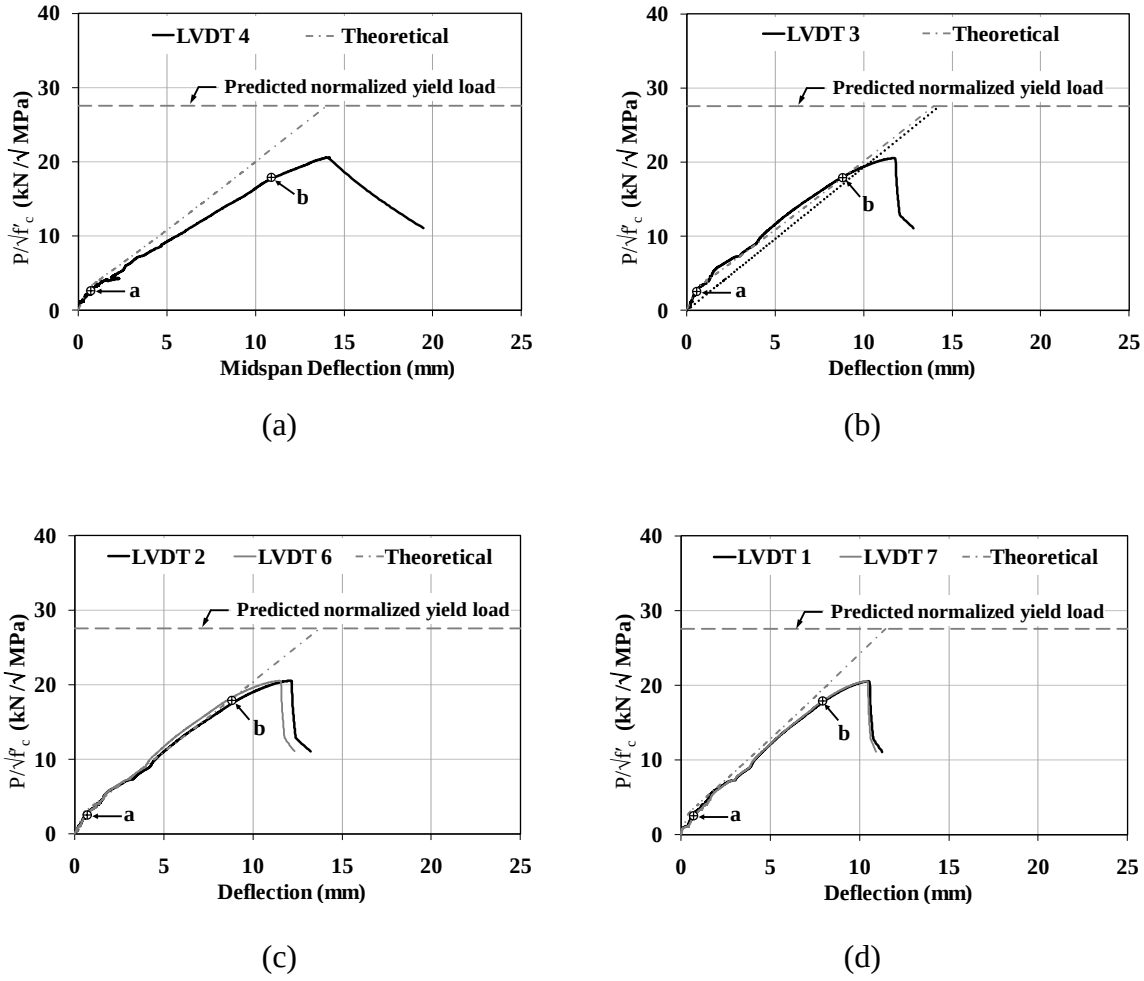

Figure 4.14. Normalized applied load versus deflection - Specimen 25-610: (a) midspan, (b) quarter points along the lap splice length, (c) ends of the lap splice length, and (b) points of applied loads.

lower than that of the theoretical load-deflection curve. This was expected, as the formation of plastic shrinkage cracks as mentioned in Section 3.5 would result in a lower flexural stiffness for the specimen prior to cracking.

Figure 4.14(a) shows that the slope of the midspan load-deflection curve, and hence the flexural stiffness of the specimen, decreased after cracking; however, it did not remain constant between first cracking (Point "a") and the maximum applied load. The slope of this curve, between Points "a" and "b" (P/P_{max}= 0.87) was 1.44 kN/√MPa/mm. The slope of curve then reduced to 0.93 kN/√MPa/mm for P/P_{max} = 0.87 to 1. Significant bond degradation due to the formation of new cracks or the lengthening and widening of previously developed cracks and a comparatively long lap splice length might be the reason for this reduction in the specimen stiffness.

Figure 4.14(a) also shows that the applied load recorded for the specimen dropped markedly with any increase in the midspan deflection once the maximum load was attained, and indicated sudden failure of the specimen. A load plateau suggesting yielding of the longitudinal reinforcement was not evident. This confirms that the sudden failure of the specimen occurred due to a bond failure within the lap splice length.

Figures 4.14(b) and (c) suggest that the load-deflection curves at the quarter points within the lap splice length and at the ends of the lap splice length followed the theoretical load-deflection curve up until P/P_{max} = 0.87 (Point "b'). The slope of the curve was 4.56 kN/√MPa/mm and 3.85 kN/√MPa/mm for P/P_{max} = 0 to 0.13 (Point "a") at the quarter points within the lap splice length and the ends of the lap splice length, respectively. The slope of the curve was approximately equal at the quarter points within the lap splice length and the ends of the lap splice length for P/P_{max} > 0.13 and was 1.9 kN/√MPa/mm and 1.1 kN/√MPa/mm for P/P_{max} = 0.13 to 0.87 and P/P_{max} = 0.87 to 1.0, respectively.

Figure 4.14(d) indicates that the load-deflection behaviour at the points of applied load showed a similar pattern as observed for the lap splice length centreline. The slopes of the load-deflection curve were 3.28 kN/√MPa/mm and 2.18 kN/√MPa/mm for P/P_{max} = 0 to 0.13 and P/P_{max} = 0.13 to 0.87, respectively, which were lower than that of the theoretical load-deflection curve. The slope of the load-deflection curve then reduced to 1.02 kN/√MPa/mm for P/P_{max} = 0.87 to 1.

Figure 4.15 shows the deflection profile for Specimen 25-610 at the load levels corresponding to the crack patterns presented in Section 4.4.3. The deflection profile of Specimen 25-610 was relatively similar to that of Specimen 25-410. Deflections at the midspan and load points were higher than their respective theoretical deflections for the entire loading range, and were 1.25 and 1.95 times the respective theoretical deflections at P/P_{max} = 0.13. In contrast with deflections measured at the midspan and load points, deflections at the ends of the lap splice length and at $0.25L_s$ from the left end of the lap splice length were approximately equal for P/P_{max} <0.9. Deflections at the midspan and load points were approximately 1.25 and 1.1 times that of their respective theoretical deflections for P/P_{max} = 0.5, 0.75 and 0.9. Deflections started to increase significantly for P/P_{max} > 0.87 as discussed earlier and resulted in deflections at P/P_{max} = 1 that are 1.36 and 1.24 times the respective theoretical deflection. Deflections at the ends of the lap splice length and at $0.25L_s$ from the left end were 1.56 times the theoretical deflection at P/P_{max} =1.

4.5.4 Specimen 25-810

Figures 4.16(a), (b), (c), and (d) show the normalized applied load versus deflection at the specimen midspan, quarter points along the lap splice length, both ends of the lap splice length, and at the points of applied load to illustrate the failure behaviour of a specimen that attained the maximum load predicted theoretically neglecting strain hardening. Figure 4.16(a) shows that the midspan load-deflection curve exhibited behaviour similar to Specimen 25-610. The slope of the curve was its maximum between the origin and Point “a” and was equal to 3.67 kN/√MPa/mm, where Point “a”

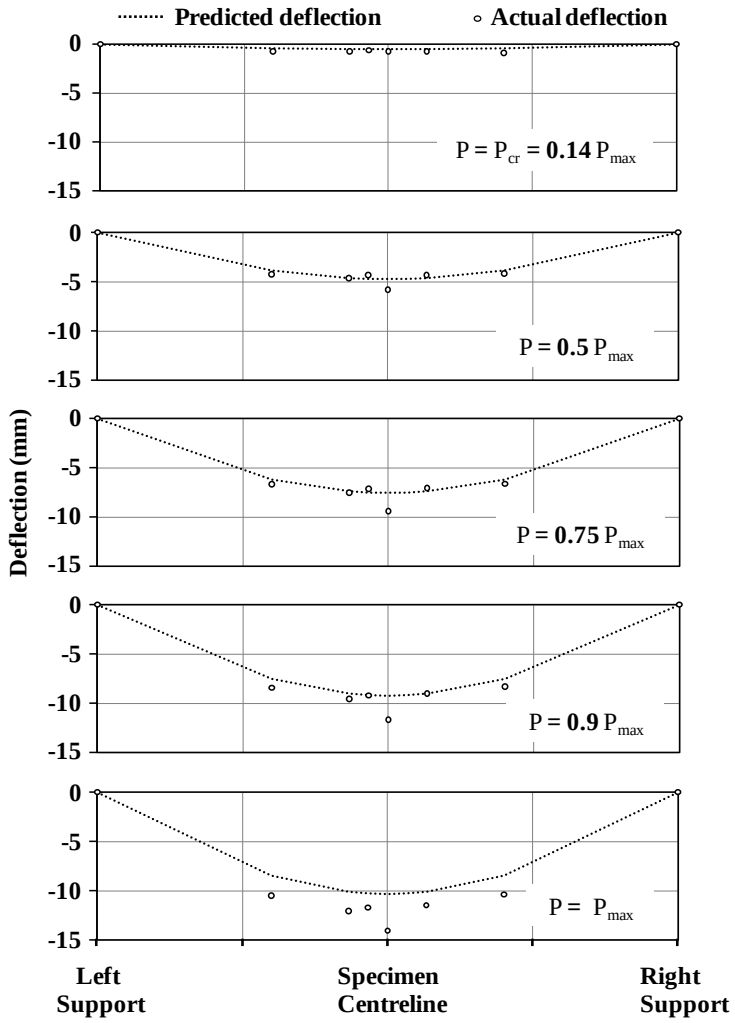

Figure 4.15. Deflected profile at different load levels - Specimen 25-610

.

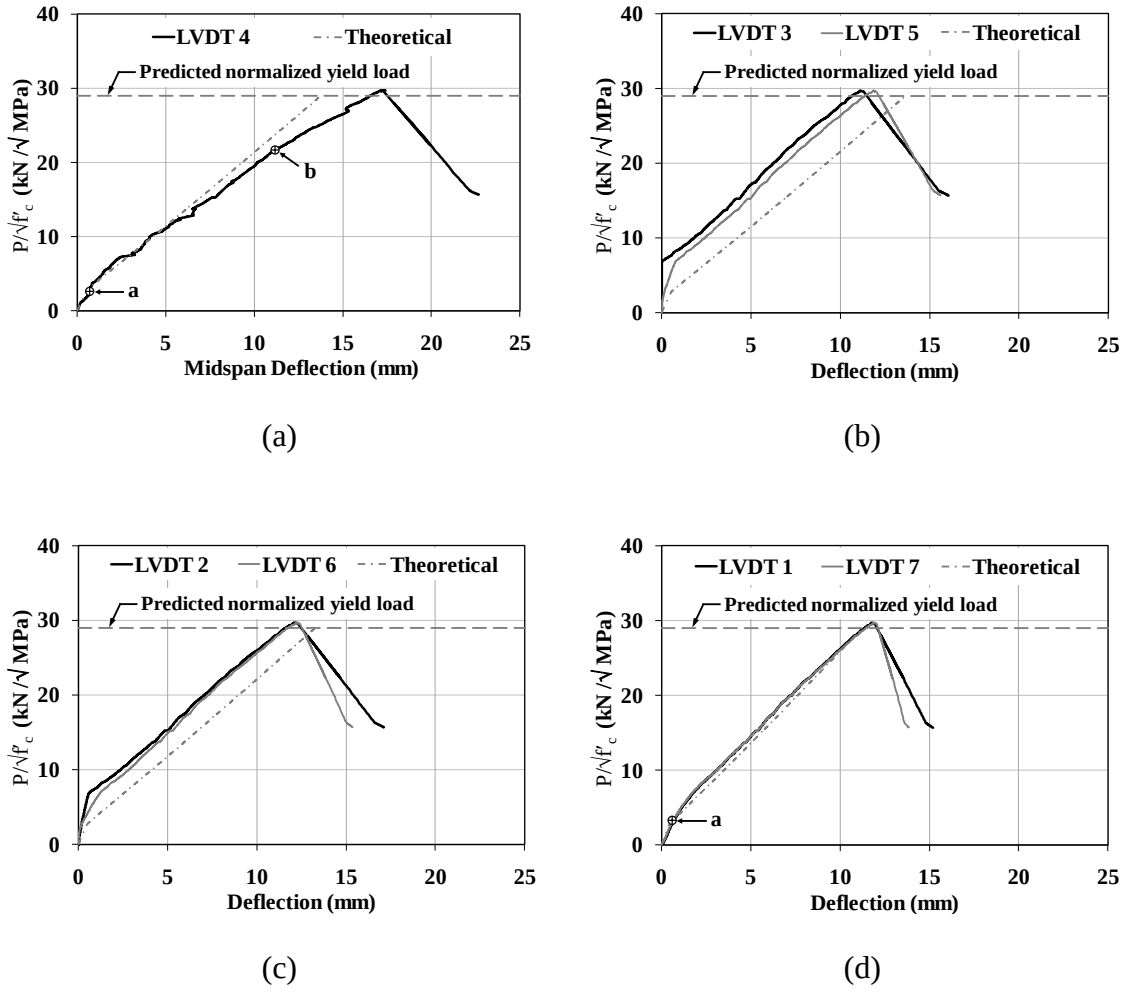

Figure 4.16. Normalized applied load versus deflection - Specimen 25-810: (a) midspan, (b) quarter points along the lap splice length, (c) ends of the lap splice length, and (d) points of applied load.

represents first cracking and corresponds to the normalized applied load of 2.68 kN/√MPa (P/P_{max} = 0.09): 3.9% lower than the theoretical normalized load at first cracking of 2.79 kN/√MPa. The slope of the midspan load-deflection curve then reduced to 1.7 kN/√MPa/mm and remained approximately constant up until Point "b", corresponding to a normalized applied load of 21.8 kN/√MPa (P/P_{max} = 0.73). The midspan deflection was approximately equal to that of the theoretical deflection up until P/P_{max} = 0.42. The observed crack pattern at P/P_{max} = 0.4, presented in the Section 4.4.4, indicates that bond loss might be the reason for this higher midspan deflection. The midspan deflection at Point "b" was approximately 10% higher than the theoretical deflection and suggests that the deflection was comparable to that calculated theoretically under service load conditions and that tension stiffening of plain steel bars for this specimen was similar to specimens reinforced with deformed bars. Longer lap splice lengths therefore appeared to improve the deflection and load-carrying capacity within the typical service level load range. The slope of the load-deflection curve was 1.35 kN/√MPa/mm for P/P_{max} = 0.73 to 1, a 20.6% decrease, suggesting that bond loss might occur due to the formation of new cracks and the increase in crack lengths as discussed in Section 4.4.4.

Failure of the specimen occurred suddenly once the maximum load was attained, as the load dropped markedly with any further increase in the midspan deflection. No yield plateau was evident for this specimen. The observed crack pattern and end slip of the reinforcing steel, as discussed in Section 4.4.4, suggested that the sudden failure of the specimen was, therefore, due to bond failure within the lap splice length.

Figures 4.16(b) and (c) show that similarities existed in the load-deflection behaviour of this specimen with those previously presented (i.e. Specimens 25-410 and 25-610) at the quarter points along the lap splice length. Figure 4.16(b) shows that the deflection at LVDT 3 was approximately zero for $P/P_{max} \leq 0.24$. The slope of the load deflection curve at the quarter points along the lap splice length was higher than that of the theoretical load-deflection curve for $P/P_{max} \leq 0.24$ and ranged between 6.9 to 13

kN/√MPa/mm. The slope of the load-deflection curve then remained approximately constant for P/P_{max} = 0.24 to 1 and was equal to 2.14 kN/√MPa/mm. LVDT readings at these locations might be affected by the cracks that develop within the lap splice length as mentioned earlier and might be the reason for the lower deflection at these locations.

Figure 4.16(d) shows the load-deflection behaviour at the points of applied load for Specimen 25-810. The slope of the load-deflection curve between the origin and Point "a" (P/P_{max} = 0.09) was equal to 4.62 kN/√MPa/mm. This portion of the curve represented the load-deflection behaviour prior to the cracking. The slope of the load-deflection curve then reduced to 2.38 kN/√MPa/mm and remained relatively constant up until the maximum applied load.

Figure 4.17 shows the deflected shape of Specimen 25-810 at the load levels corresponding to those shown for the crack patterns presented in Section 4.4.4. Figure 4.17 indicated that the deflection at the specimen midspan was equal to the theoretical deflection up until P/P_{max} = 0.4. The midspan deflection was 1.1 times its theoretical deflection for P/P_{max} = 0.73 (Point "b") and then was approximately 1.22 times of their theoretical deflection for P/P_{max} = 0.9 and 1. In contrast, the deflections at the points of applied load were roughly equal to the respective theoretical deflections throughout the entire loading range. Deflections at the ends of the lap splice length and at the quarter points were lower than the theoretical deflections as observed for other specimens.

4.5.5 Specimen 19-610

Figures 4.18(a), (b), (c), and (d) show the normalized applied load versus deflection at the midspan, quarter points of the lap splice length, ends of the lap splice length, and load points for Specimen 19-610 to illustrate its failure behaviour. Specimen 19-610 attained a maximum applied load approximately 1.06 times its theoretically calculated maximum applied load neglecting strain hardening as discussed in Section 4.3.

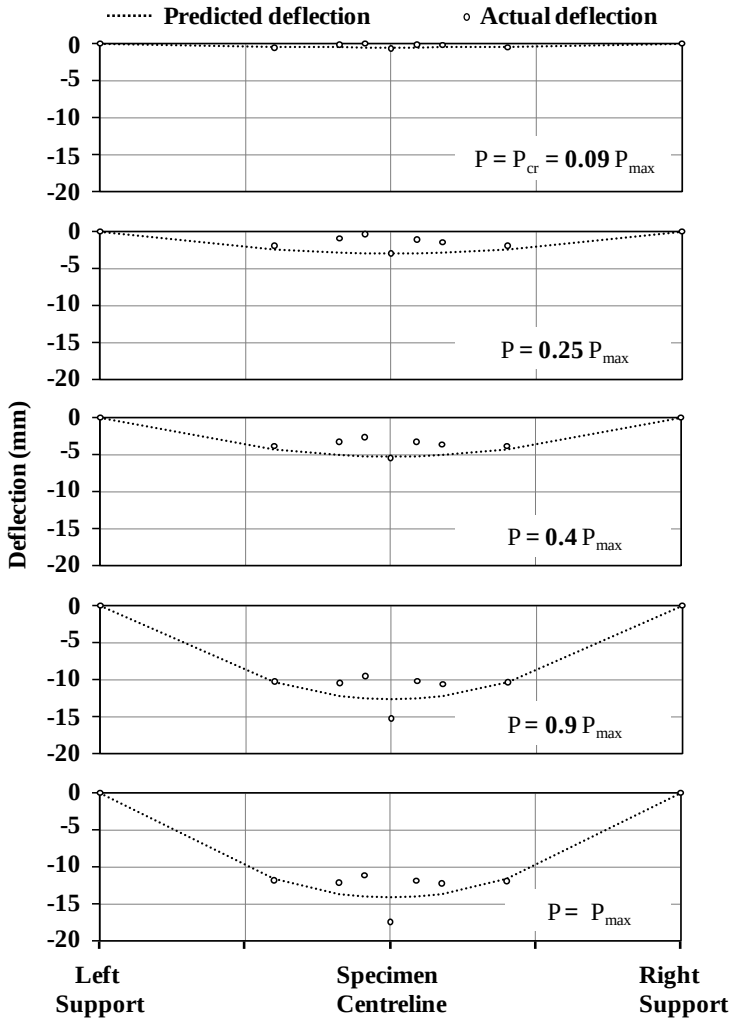

Figure 4.17. Deflected profile at different load levels - Specimen 25-810

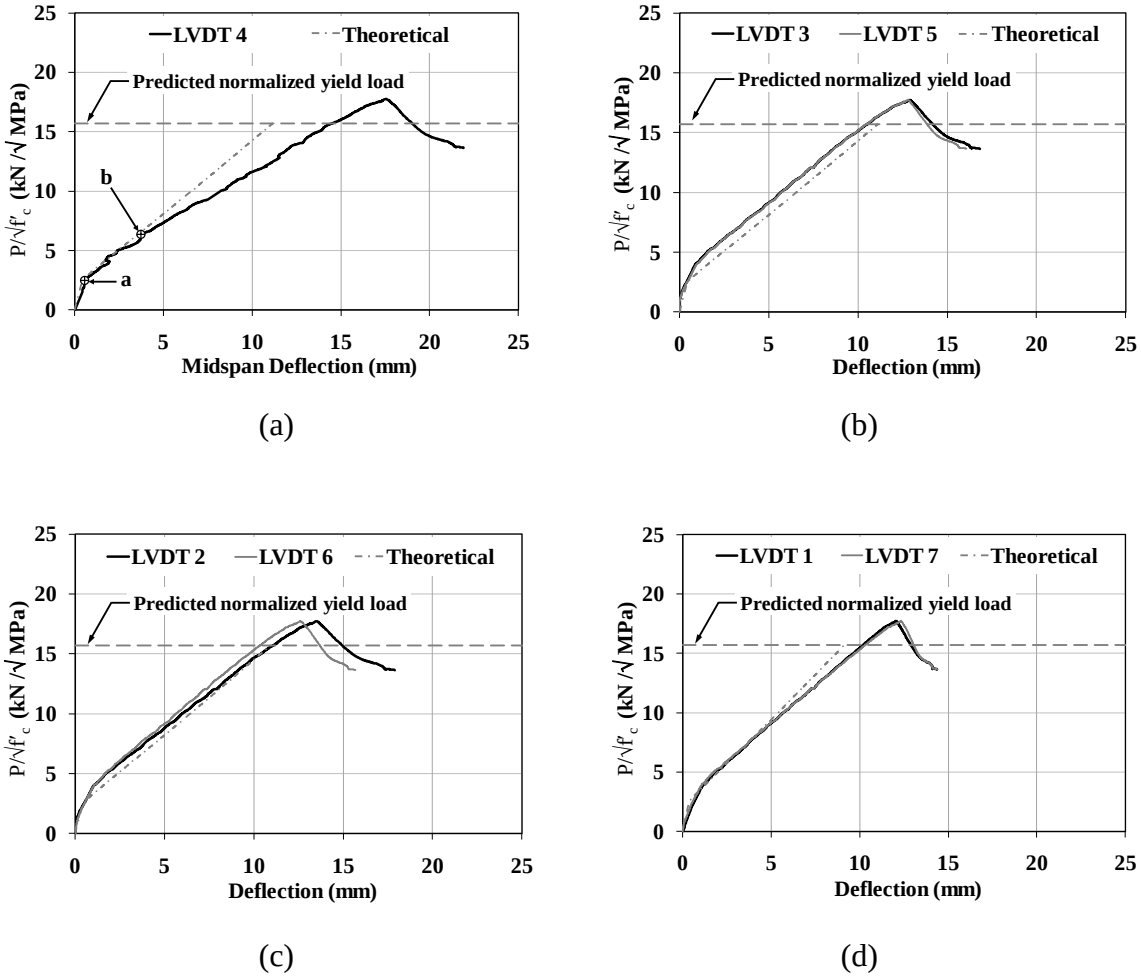

Figure 4.18. Normalized applied load versus deflection - Specimen 19-610: (a) midspan, (b) quarter points of the lap splice length, (c) ends of the lap splice length, and (d) points of applied load.

The midspan deflection for Specimen 19-610 as shown in Figure 4.18(a) shows behaviour similar to Specimen 25-810. The slope of the load-deflection curve was its maximum from the origin to Point 'a' and was equal to 4.54 kN/√MPa/mm: 20% lower than that of the theoretical curve. The formation of plastic shrinkage cracks as mentioned in Section 3.5 was one of the reasons for the lower flexural stiffness of the specimen prior to cracking. Point "a" represented the first cracking of the specimen and corresponds to a normalized applied load of 2.41 kN/√MPa (P/P_{max} = 0.14) which was lower than the theoretical value of 2.53 kN/√MPa.

Figure 4.18(a) shows that the slope of the load deflection curve then reduced to 1.1 kN/√MPa/mm following cracking and remained constant up until Point "b" which corresponds to a normalized applied load of 6.32 kN/√MPa (P/P_{max} = 0.36). The midspan load deflection curve approximately followed the theoretical curve up until Point "b". This specimen showed signs of significant bond loss for $P/P_{max} > 0.4$ as was evident from the crack pattern reported in Section 4.4.5 and was the likely reason for flexural stiffness reduction at loads beyond $P/P_{max} > 0.4$. The slope of the load deflection curve reduced to 0.86 kN/√MPa/mm and remained constant until the maximum load was attained. In contrast with Specimen 25-810, higher midspan deflections under serviceability limit conditions were achieved. Figure 4.18(a) indicates that specimen failure occurred once the maximum load was attained. A load plateau was not evident and thus the behaviour shown was similar to Specimen 25-810 and a sudden bond failure resulted.

Figure 4.18(b) and (c) shows the load-deflection behaviour at the quarter points and the ends of the lap splice length, respectively, and suggested similar behaviour to the previously reported specimens. Deflections at these locations were lower than the theoretical deflections. The formation of cracks close to the lap splice length ends was the likely reason for these reduced deflections. Figure 4.18(d) indicates that the slope of the load deflection curve was 4.2 kN/√MPa/mm for P/P_{max} = 0 to 0.2. The slope of the load deflection curve then reduced to 1.24 kN/√MPa/mm which was 20% lower than the

slope of the theoretical load deflection curve and remained constant for $P/P_{max} \geq 0.2$. It may the noted that the deflections at these locations were approximately equal to the theoretical values up until $P/P_{max}= 0.5$ and then exceeded the theoretical deflection of the specimen.

Figure 4.19 shows the deflection profile at the theoretical cracking load and the load levels reported in Section 4.4.5 for crack pattern development. The deflection profile of the specimen was similar to those reported for other specimens. The deflections at the midspan and the points of applied load were approximately equal to the theoretical values at $P/P_{max} \leq 0.25$. Bond loss due to cracking, as discussed in Section 4.4.4, likely resulted in higher actual deflections at higher applied load levels. In contrast, deflections at the ends of the lap splice length and at the quarter point locations were lower than the theoretical values as was also observed for other specimens.

4.5.6 Summary – Load versus Deflection Behaviour

The load-deflection behaviour of the specimens tested suggests that bond loss resulted for all of the specimens. No load plateau was evident; rather, failure occurred suddenly once the maximum applied load was attained. The increase of the lap splice length increased the stiffness of the specimen tested. Deflections at the lap splice length quarter points and ends were significantly lower than the midspan deflections and suggested that LVDT readings at these locations were affected by the cracks near the lap splice length ends. The installation of additional LVDTs outside the lap splice length was therefore recommended for future tests as they were necessary to obtain an accurate overall deflection profile of the specimens.

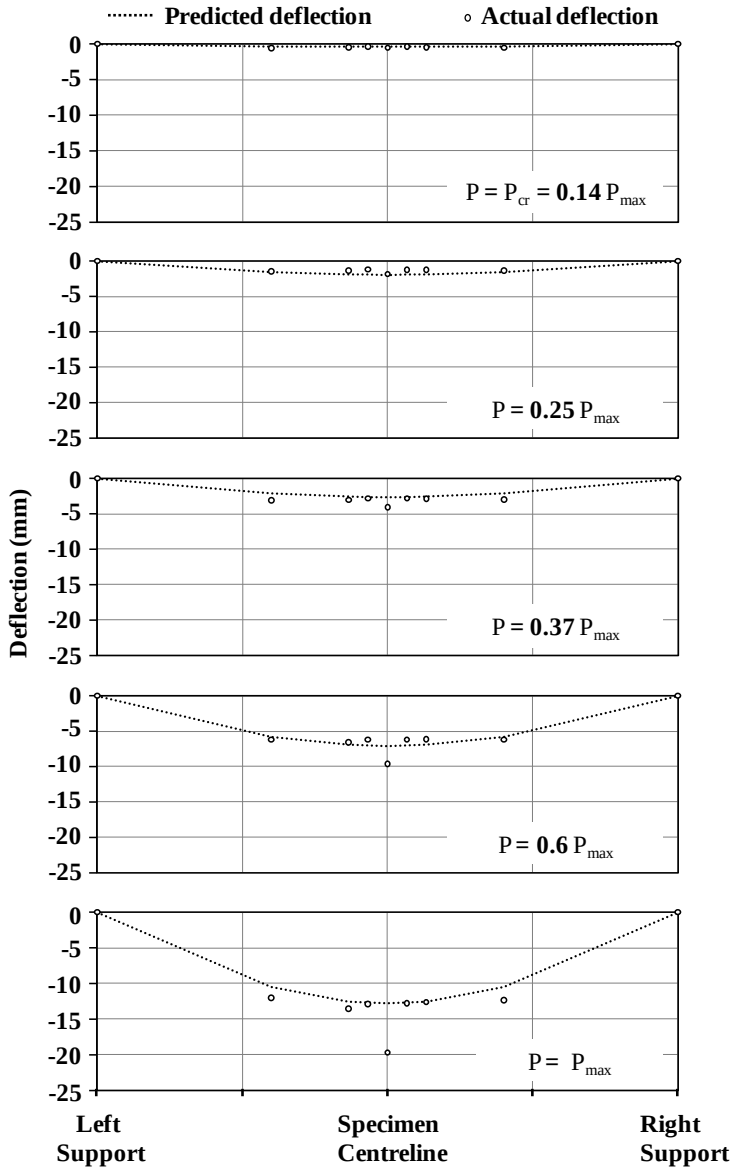

Figure 4.19. Deflected profile at different load levels - Specimen 19-610

4.6 Conclusion

This chapter presented general behaviour for splice specimens with plain steel bars. A preliminary development length equation for plain steel bars to evaluate historical concrete structures was developed. General failure behaviour of the specimens provided by crack patterns and load versus deflection behaviour confirmed evidence of a bond failure in all specimens and suggested that increasing the splice length provided improved load deflection behaviour due to a increase in the specimen stiffness within the region of the lap splice length. The first three sub-objectives of the study were addressed in this chapter.

A detailed analysis of instrumented specimens as presented in Chapter 5 provides additional insight into the bond loss of splice specimens with plain steel bars.

CHAPTER 5
ANALYSIS OF INSTRUMENTED SPECIMENS

5.1 Background

The steel and concrete strain gauges installed on select specimens, as discussed in Chapter 3, provided a useful means to verify strain compatibility within the lap splice length, report average bond stress distribution along the lap splice length, and conduct a flexural analysis at different sections along the lap splice length of these specimens. Other observed failure behaviour for these specimens, including: crack patterns, photographs of longitudinal bar end slip, load-deflection behaviour, and the deflection profiles are presented in Appendices 4C to 4F. The material properties of these specimens are presented in Appendices 4A and 4B. The following sections provide a discussion on the analysis of the instrumented specimens.

5.2 Strain Compatibility

5.2.1 General

The strain in the longitudinal reinforcing steel must be equal to the strain in the surrounding concrete for perfect bond to exist (e.g. MacGregor and Bartlett 2000). Data recorded for the steel and concrete strain gauges located at the effective depth, d, from the top of the specimen showed whether strain compatibility existed in the splice specimens tested. Specimen 25-610I was the most heavily instrumented of the three specimens discussed here, with steel strain gauges located at the loaded ends, the quarter points, and the centreline of the lap splice length. Other specimens were instrumented with steel strain gauges at the loaded ends and centreline of the lap splice length only. The locations of the steel and concrete strain gauges are presented in Figure 3.2. Strain gauge data were recorded for several minutes at the start of testing prior to the application of applied loading as discussed in Section 3.6. This allowed the standard

deviation of the noise in both the steel and concrete strain gauges to be calculated at $P/P_{max} = 0$ and is presented in Appendix 5A. However, the test data did not allow for the determination of standard deviation at other load levels, so this was assumed equal to that calculated at zero applied load.

5.2.2 Specimen 25-610I

Figures 5.1(a) to (e) show the steel and concrete strains at the effective depth, d, from the top of the section versus the normalized applied load for Specimen 25-610I at the following locations along the specimen length: the left end of the lap splice length, the right end of the lap splice length, the specimen centreline, $0.25L_s$ from the left end of the lap splice length, and $0.25L_s$ from the right end of the lap splice length, respectively. A tensile strain in both the reinforcing steel and concrete is considered positive in the figures. It may be noted that the tensile strain in concrete and reinforcing steel bars due to the self-weight of the specimen and the loading equipments (Spreader beam and bearing plates), and shrinkage of concrete were not captured by the strain gauges. Concrete strain gauge C9 at the right end of the lap splice length coincided with a crack that developed at that location and did not function properly. Its response is therefore not shown in Figure 5.1(b). Similarly, steel strain gauge S14 did not function due to the damage that occurred during specimen preparation, as discussed in Section 3.5 and is therefore not shown in Figure 5.1(d).

The standard deviation of the steel strain and the difference between the steel and concrete strains determined at the 95% confidence level was 6.2μ and 13.2μ, respectively, at $P/P_{max} = 0$. Figure 5.1 indicates that the recorded steel strains for $P/P_{max} < 0.05$ were lower than the standard deviation of the strain gauge readings determined at the 95% confidence level and therefore suggests that gauge readings for $P/P_{max} < 0.05$ might not be significant.

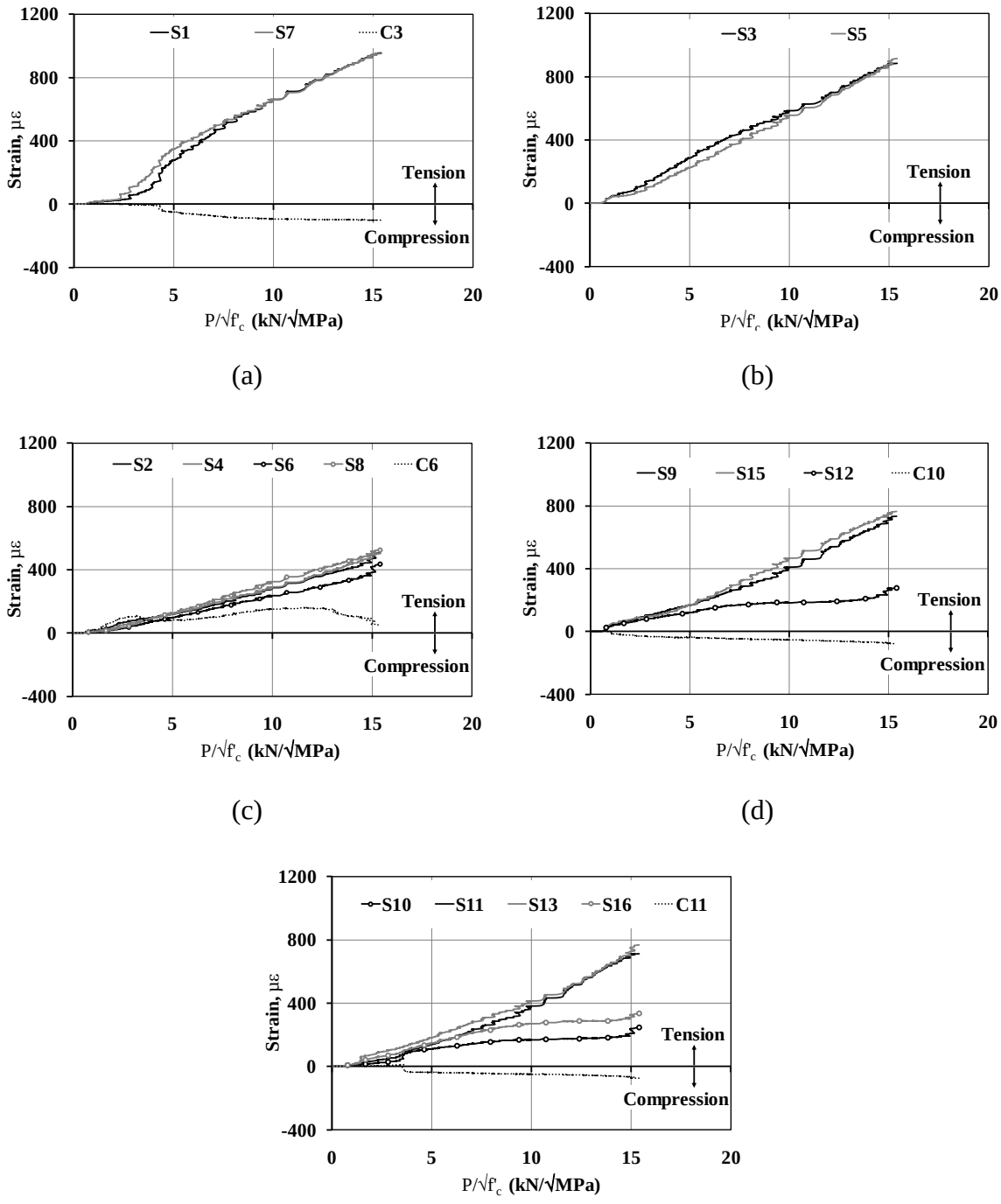

Figure 5.1. Strain in the longitudinal reinforcing steel bars and in the surrounding concrete - Specimen 25-610I: (a) left end of the lap splice length, (b) right end of the lap splice length, (c) centreline of the lap splice length, (d) $0.25L_s$ from the left end of the lap splice length, and (e) $0.25L_s$ from the right end of the lap splice length.

Figure 5.1(a) shows the strain recorded by two steel gauges, S1 and S7, and concrete gauge C3 at the left end of the lap splice length. The development length available for the reinforcing steel at the locations of these two steel strain gauges was equal to the lap splice length provided in the specimen. Figure 5.1(a) shows that steel strains in S1 and S7 were comparable for the entire loading range and indicates that load sharing between reinforcing bars at the left end of the lap splice length was equal. Figure 5.1(a) also indicates that the rate of increase of steel strain was a function of the normalized applied load. The steel strains recorded by gauges S1 and S7 increased at a rate approximately 19.9μ √MPa/kN for P/P_{max} = 0.05 to 0.17, which approximately corresponds to the theoretical specimen cracking load. The steel strains then increased at a rate approximately equal to 90μ √MPa/kN until P/P_{max} = 0.28. Cracking of the specimen caused partial bond loss of the reinforcing steel at this location for P/P_{max} > 0.17 and was the reason for the sudden increase in the steel strain. The steel strain recorded by gauges S1 and S7 then increased at a rate 78.7μ √MPa/kN and 57.3μ √MPa/kN for P/P_{max} = 0.28 to 0.48 and 0.48 to 1.0, respectively.

Figure 5.1(a) shows that the as-measured concrete strain decreased with increasing applied load and the strain in the concrete became compressive for the much of the loading range. This occurs for two reasons. First, the strain in the concrete will reduce once the tensile stress in the concrete exceeds its modulus of rupture and cracks develop. Second, the concrete surrounding the reinforcing steel slips adjacent to these cracks once the adhesion component of bond is overcome. The tension in concrete therefore releases. Figure 5.1(a) also shows that the strains in the concrete were lower than the steel strains. The difference in the steel and concrete strain readings indicates that the reinforcing steel slip locally and suggests partial bond loss at the location of the strain gauges.

The difference in the steel and concrete readings for P/P_{max} > 0.07 was higher than the standard deviation of the difference between steel and concrete strain calculated at the 95% confidence level and indicated that reinforcing steel started to slip from its surrounding concrete at relatively low levels of applied loads. The difference in the steel

and concrete strain gauge readings increased linearly and became 50μ at P/P_{max} =0.17 and 267μ at P/P_{max} = 0.28, respectively. Local bond loss, as discussed earlier, is the reason for this difference in steel and concrete strain readings. The longitudinal bars continued to slip from its surrounding concrete with the increase of applied load and the difference in steel and concrete strain increased to 565μ and 1050μ for P/P_{max} = 0.48 and 1, respectively.

Figure 5.1(b) shows that the steel strain at the right end of the lap splice length was similar to Figure 5.1(a). The longitudinal reinforcing bars shared load reasonably equally for the entire loading range. The steel stress at the right end of the lap splice length increased at a rate of 34.5μ √MPa/kN for P/P_{max} = 0.05 to 0.17 and was approximately 70% higher than that at the other end of the lap splice length, suggesting that bond loss at this end was higher than the other end. The steel strain at the right end of the lap splice length then increased to a rate of 61.8μ √MPa/kN for P/P_{max} = 0.17 to 1, which was approximately equal to the strain increase rate at the left end of the lap splice length for P/P_{max} > 0.28. The steel strains at the ends of the lap splice length therefore increased approximately equally after cracking of the specimen.

Figure 5.1(c) shows the results of the four steel strain gauges and the concrete strain gauge at the centreline of the lap splice length. All four longitudinal reinforcing bars at the lap splice length centreline shared loads reasonably equally for the entire loading range. The strain in the reinforcing steel increased at a rate approximately equal to 23.4μ √MPa/kN for P/P_{max} = 0.05 to 0.17. This rate was approximately 1.2 and 0.7 times that at the left and right end of the lap splice length, respectively, for $P/P_{max} \leq 0.17$, even though the number of longitudinal bars sharing the load at the centreline of the lap splice length was twice that at the ends of the lap splice length. The strain in the longitudinal reinforcing steel along the lap splice length therefore increased approximately equally prior to specimen cracking, and then increased at a rate approximately 32.6μ /kN.√MPa for P/P_{max} = 0.17 to 1.0. This rate was approximately 40 to 60% lower than that at the ends of the lap splice length.

Figure 5.1(c) also shows that the difference between the steel and concrete strain measurements at the centreline of the lap splice length was approximately zero for $P/P_{max} \leq 0.25$. Slip of the reinforcing steel at the loaded ends of the lap splice length posed higher bond demand at the centreline of the lap splice length (Feldman and Bartlett 2007) and therefore slip at the centreline of the splice length initiated when $P/P_{max} \approx 0.25$. The difference in the steel and concrete strain then increased linearly for $0.25 < P/P_{max} \leq 0.85$ with a difference between steel and concrete strain of 250μ at $P/P_{max} = 0.85$. This value was approximately 27% of that at the left end of the lap splice length. A significant increase in the difference in the strain values recorded for the steel and concrete strain gauge measurements was observed for $P/P_{max} > 0.85$, and is an indication of further bond degradation. The difference in the steel and concrete strain at the maximum applied load was 440μ and was approximately 42% that at the left end of the lap splice length.

Figure 5.1(d) shows the strains recorded by the steel and concrete gauges at 0.25 L_s from the left end of the lap splice length. Steel gauges S9 and S15 were 0.75 L_s away from the cut (i.e. unloaded) end of the reinforcing bar extending through the lap splice length from one support, while gauge S12 was located $0.25L_s$ away from the cut end of a reinforcing bar that extend thorough the lap splice length to the other support. Figure 5.1(d) shows that the readings for steel gauges S9 and S15 were comparable for the entire loading range which is an indication of equal load sharing between those two bars, and was expected since both bars had the same development length. Steel strains recorded by gauge S9 and S15 increased relatively linearly at a rate of 31.4μ √MPa/kN for $P/P_{max} \leq 0.37$. Steel strains at this location were therefore higher than that at the left end and centreline of the lap splice length for $P/P_{max} \leq 0.17$. The stirrup at this location affected bond conditions and might be accounted for the higher steel strain at this location. The steel strains then increased at a rate approximately equal to 57.8μ √MPa/kN from $P/P_{max} = 0.37$ to 1, which was approximately equal to that at the left end of the lap splice length.

Figure 5.1(d) also suggests that steel strain gauge S12 shared load approximately equally to that of S9 and S15 up until P/P_{max} = 0.15, even though the available development length of this reinforcing steel at strain gauge was one third that of S9 and S15. This is an indication that the spliced bars at $0.25L_s$ shared load equally for $P/P_{max} \leq$ 0.15. The strain measured by gauge S12 then deviated from those recorded by S9 and S15 and increased at a rate equal to 21.1μ √MPa/kN for P/P_{max} = 0.15 to 0.45. This was 65% of that recorded by gauges S9 and S15 and was a further indication that steel stress was a function of the available development length. The steel strain recorded by gauge S12 then increased at a rate of 4.3μ √MPa/kN for P/P_{max} = 0.45 to 0.85, which was approximately 7% that of gauges S9 and S15. This was expected because the central part of the lap splice length did not experience significant bond loss for $P/P_{max} \leq 0.85$ and therefore developed steel stress effectively, resulting in a lower steel strain increase rate for gauge S12 for P/P_{max} = 0.45 to 0.85. The steel strain then increased at a rate approximately equal to 41.7μ √MPa/kN for P/P_{max} = 0.85 to 1.0. Significant bond loss at the centreline of the lap splice length was observed for $P/P_{max} > 0.85$ and resulted in the elevated steel strain increase rate at gauge S12.

A comparison of the steel and concrete strains at $0.25L_s$ from the left end of the lap splice length as shown in Figure 5.1(d) indicates that the steel strain started to deviate from that measured for the concrete at P/P_{max} = 0.06. The difference in steel and concrete strains at this section increased approximately linearly from zero to 102.5μ for $0.06 < P/P_{max} \leq 0.15$ for all longitudinal bars. The slip of the reinforcing steel at that location then became a function of the available development length of the bars. The difference in steel strain recorded by gauge S9 and S15 and concrete strain recorded by C10 increased approximately linearly for P/P_{max} = 0.15 to 0.37 and P/P_{max} = 0.37 to 1.0. This difference was 240μ at P/P_{max} = 0.37, which was 0.56 and 4.6 times of that at the left end and centreline of the lap splice length, respectively, and 830μ at P/P_{max} = 1.0 which was 0.8 and 1.9 times of that at the left end and centreline of the lap splice length, respectively.

The difference in steel and concrete strains at the location of gauge S12 was somewhat different than that at the gauges S9 and S15 for $P/P_{max} > 0.15$. The difference in steel and concrete strains at gauge S12 increased approximately linearly and became 210μ at $P/P_{max} = 0.45$ which is 0.4 and 2.7 times of that at the left end and centreline of the lap splice length, respectively. This difference then increased to 260μ at $P/P_{max} = 0.85$ and was 0.28 and 1.1 times of that at the left end and centreline of the lap splice length, respectively. The difference in steel and concrete strain at gauge S12 then increased to 352.3μ at the maximum applied load which was 0.33 and 0.8 times of that at the left end and centreline of the lap splice length. Slip of the reinforcing steel along the lap splice length was therefore a function of the development length available at a given location and applied load level.

Figure 5.1(e) shows the strain recorded by the steel and concrete gauges at $0.25L_s$ from the right end of the lap splice length. Steel gauges S11 and S13 were $0.75L_s$ away from the cut end of the reinforcing bar extending through the lap splice length from one support, while gauges S10 and S16 were located $0.25L_s$ away from the unloaded (i.e. cut) end of a reinforcing bar that extend thorough the lap splice length to the other support. The resulting steel strains shown in this figure were similar to those shown in Figure 5.1(d) that were located at $0.25L_s$ from the left end of the lap splice length (i.e. gauges S9, S12, and S15). Steel strain at S11 and S13 were comparable for the entire loading range indicating equal load sharing between the two spliced reinforcing bars. The strain in the reinforcing steel increased at a rate of approximately 27.0μ √MPa/kN for $P/P_{max} = 0.05$ to 0.23. Steel strain then increased at a rate of approximately 44.0μ √MPa/kN and 63.5μ √MPa/kN for $P/P_{max} = 0.23$ to 0.58, and 0.58 to 1, respectively. Bond loss due to cracking of the specimen as discussed earlier was the reason for this higher rate of steel strain increase for gauges S11 and S13.

Figure 5.1(e) also shows that the steel strains recorded by gauges S10 and S16 were comparable to those recorded by S11 and S13 up until $P/P_{max} = 0.23$, which indicates that all of the longitudinal bars at $0.25L_s$ from the right end of the lap splice length shared load reasonably equally for low load levels. Steel strains at S10 and S16 then

deviated from those recorded by S11 and S13 as observed for steel bars at $0.25L_s$ from the left end of the lap splice length. Steel strains recorded by gauges S10 and S16 increased at a rate ranging from 15.7μ √MPa/kN to 30.2μ √MPa/kN for P/P_{max} = 0.23 to 0.58 and were 35 to 70% of those recorded by gauges S11 and S13. The steel strain recorded by gauge S16 was approximately 50% higher than that of gauge S10 which might be accounted for the crack that developed at the right end of the lap splice length at P/P_{max} = 0.28. Steel strains at S10 and S16 then increased at a rate ranging from 3.6μ √MPa/kN to 5.7μ √MPa/kN for P/P_{max} = 0.58 to 0.95 which was approximately 5 to 9% of that at the location of steel gauge S11 and S13. This was expected as the central portion of the lap splice length developed steel stress effectively resulting in a lower steel strain increase rate at the location of gauge S10 and S16 for P/P_{max} = 0.58 to 0.95. The steel strain then increased at a rate approximately equal to those recorded by gauge S11 and S13 for $P/P_{max} > 0.95$.

Figure 5.1(e) also indicates that the concrete strain at $0.25L_s$ from the right end of the lap splice length deviated from the steel strain at P/P_{max}= 0.09, suggesting that slip of the reinforcing steel occurred at a relatively low load level. The difference in the reinforcing steel and concrete strains at that location was approximately 120μ at P/P_{max} = 0.23, even though no bond loss was observed at the centreline of the lap splice length at this load level. The difference in the reinforcing steel and concrete strains at the location of S11 and S13 was 375μ and 815μ for P/P_{max} = 0.58 and 1.0, respectively, indicating slip of the reinforcing steel at these locations was 3.6 to 1.8 times that at the centreline of the lap splice length. The difference in the reinforcing steel and concrete strains at S10 and S16 was 255μ for P/P_{max} = 0.58 and was 2.4 times of that at the centreline of the lap splice. The strain difference was 365μ for P/P_{max} = 1.0 and was 17% lower than that at the centreline of the lap splice length.

The strain compatibility analysis within the lap splice length suggests that cracking and stirrup placement affected bond within the lap splice length for Specimen 25-610I. Steel strains along the lap splice length for Specimen 25-610I indicates that the strain in the longitudinal reinforcing steel was a function of available development length at a given

point: reinforcing steel with a longer development length developed higher steel strain. The slip of the reinforcing steel at the specimen centreline was negligible at lower load levels and started to increase at higher levels of applied loads, while slip at the loaded end was always greater than that at other locations along the lap splice length. The steel strain and strain compatibility analysis yielded similar results for Specimens 25-510I and 25-410I as discussed in the following sections.

5.2.3 Specimen 25-510I

Figures 5.2(a), (b) and (c) show the strains recorded by the steel and concrete gauges versus the normalized load at: the left end, right end, and centreline of the lap splice length, respectively, for Specimen 25-510I. Strain gauges were not installed at the quarter points of the lap splice length for this specimen. Steel strains at all locations indicate equal load sharing between the longitudinal bars as observed for Specimen 25-610I.

Figure 5.2(a) indicates that steel strain at the left end of the lap splice length increased at a rate of 10.5μ √MPa/kN up until P/P_{max} = 0.07. The steel strain then increased at a rate 34.4μ, 67.6μ, and 57.4μ √MPa/kN for P/P_{max} = 0.07 to 0.3, 0.3 to 0.53, and 0.53 to 1, respectively. These steel strain increase rates were comparable to those observed for the reinforcing steel at the left end of the lap splice length for Specimen 25-610I. Figure 5.2(b) shows that the steel strain at the right end of the lap splice length increased at a rate of 21.2μ, 37.5μ, 69.8μ, and 56μ √MPa/kN for $P/P_{max} \leq 0.13$, $0.13 \leq P/P_{max} \leq 0.3$, $0.3 \leq P/P_{max} \leq 0.53$, and $0.53 \leq P/P_{max} \leq 1.0$, respectively. These strains were comparable to those reported for the left end of the lap splice length.

Figure 5.2(c) shows that the steel strain at the centreline of the lap splice length increased at a rate 12.2μ √MPa/kN for P/P_{max} = 0 to 0.75. The rate of increase of steel strain at the centreline of the lap splice length for Specimen 25-510I was approximately

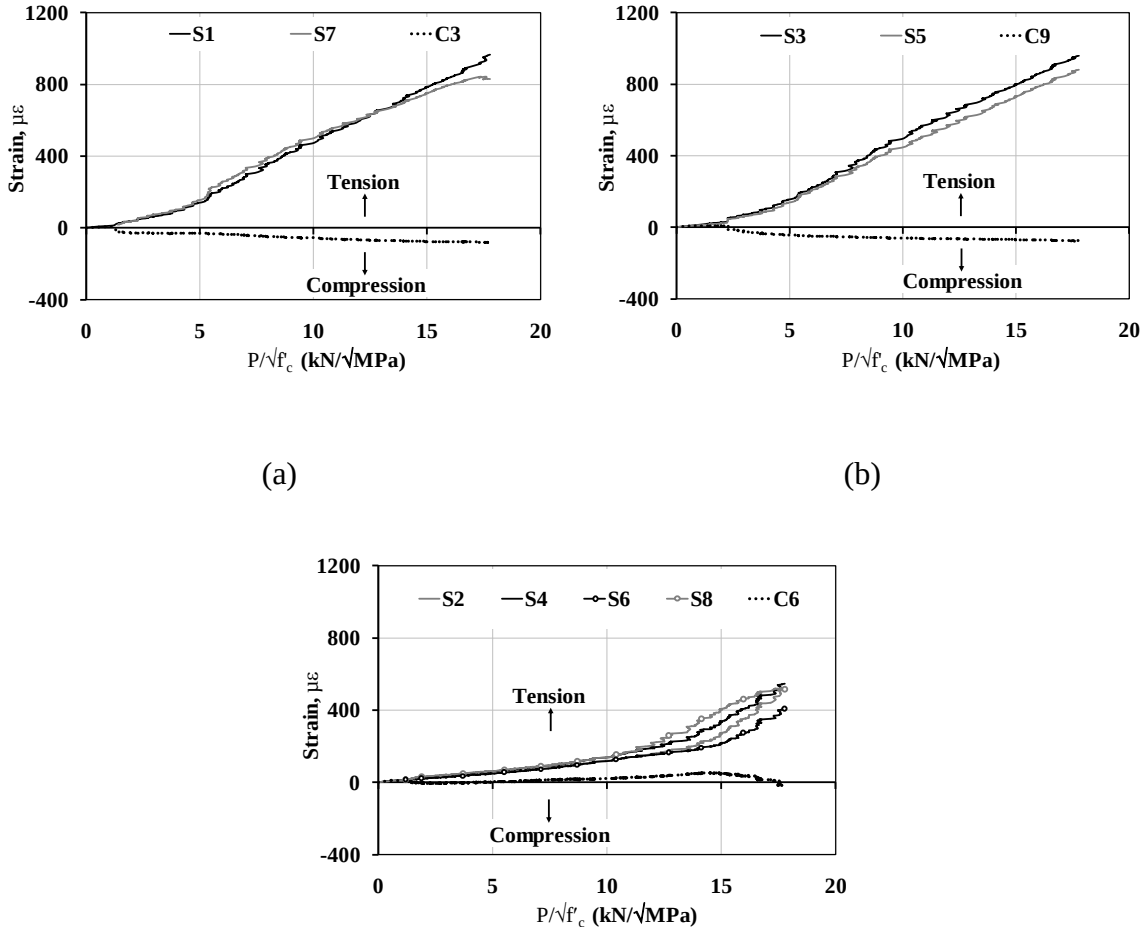

Figure 5.2. Strain in the longitudinal reinforcing steel bars and in the surrounding concrete - Specimen 25-510I: (a) left end of the lap splice length, (b) right end of the lap splice length, and (c) centreline of the lap splice length.

40 to 50% that observed for the centreline of the lap splice length of the Specimen 25-610: this was expected as the bonded length between loaded end and the centreline of the lap splice length was intact for Specimen 25-510I as steel strain gauges were not installed at the quarter points of the lap splice length. The maximum load capacity for Specimen 25-510I, as reported in Table 4.2, was therefore 16% greater than that of Specimen 25-610I, and suggests that a higher bond capacity was available within this shorter lap splice length. The steel strain at the centreline of the lap splice length for Specimen 25-510I for P/P_{max} = 0.75 to 1 increased at a rate approximately 4.5 to 8 times that observed for $P/P_{max} \leq 0.75$. This was expected as the bond loss adjacent to loaded ends of the lap splice length posed higher bond demand at the lap splice length centreline and increased the steel strain at the lap splice length centreline.

The difference in the steel and concrete strains at the ends and centreline of the lap splice length were evident for $P/P_{max} > 0.07$, indicating that reinforcing steel at the strain gauge locations started to slip from their initial position at lower load level. The difference in the steel and concrete strains at the ends of the lap splice length were 480μ and 986μ for P/P_{max} = 0.5 and 1, respectively. In contrast with the loaded ends of the lap splice length, the difference in the steel and concrete strains at the centreline of the lap splice length were approximately 157μ and 480μ for P/P_{max} = 0.75 and 1, respectively. The slip of the reinforcing steel from its surrounding concrete at the centreline of the lap splice length was 0.22 and 0.5 times that at the ends of the lap splice length for P/P_{max} = 0.75 and 1, respectively. The slip of the reinforcing steel along the lap splice length was therefore a function of the available development length for the reinforcing steel. Similar behaviour was observed for Specimen 25-610I.

5.2.4 Specimen 25-410I

Figures 5.3(a), (b) and (c) show the recorded steel and concrete strains versus the normalized load at the left end, right end, and centreline of the lap splice length, respectively, for specimen 25-410I. Steel strains at all instrumented locations indicated

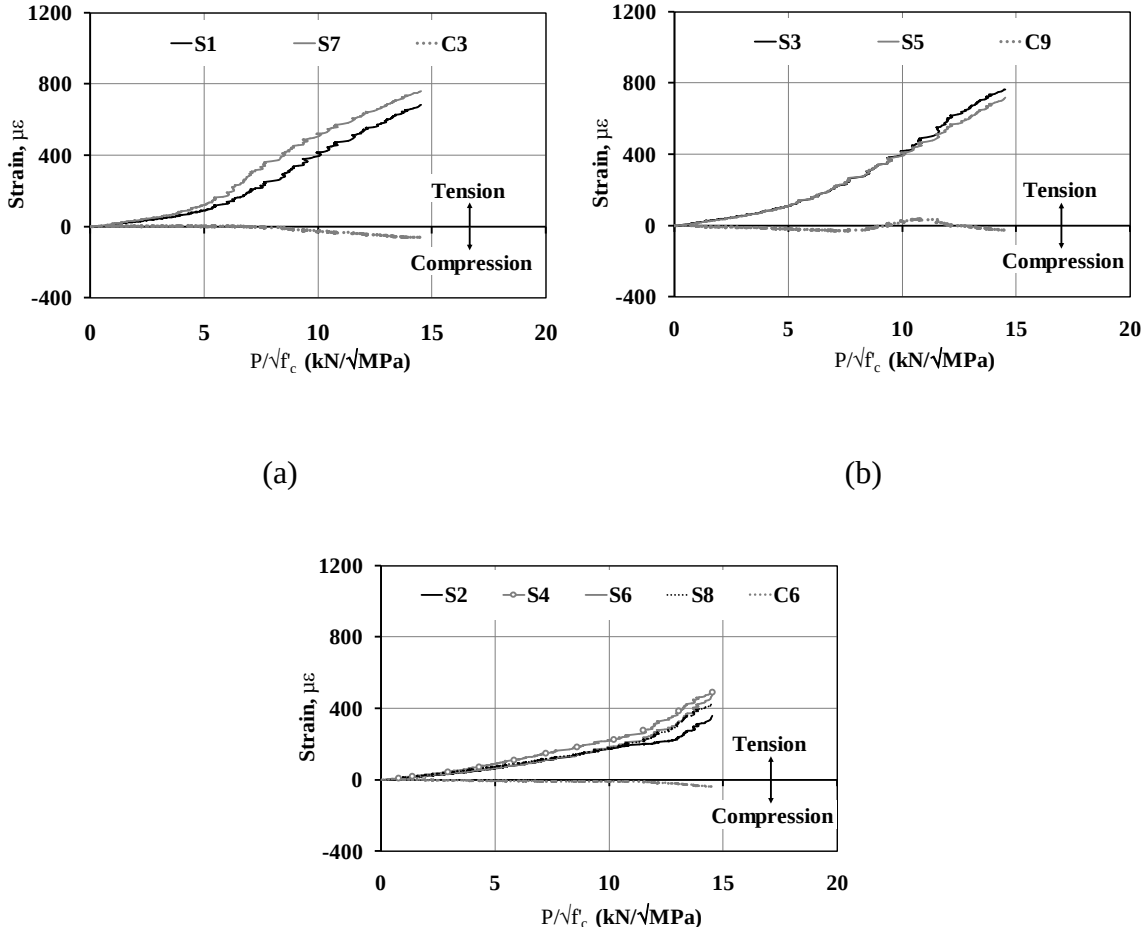

Figure 5.3. Strain in the longitudinal reinforcing steel bars and in the surrounding concrete - Specimen 25-410I: (a) left end of the lap splice length, (b) right end of the lap splice length, and (c) centreline of the lap splice length.

equal load sharing between the longitudinal bars at all load levels. Similar behaviour was observed for the other instrumented specimens.

Figures 5.3(a) and (b) show that the steel strain at the loaded ends of the lap splice length increased at a rate approximately 24.0μ and 68.4μ √MPa/kN for $P/P_{max} \leq 0.4$ and $0.4 \leq P/P_{max} \leq 1.0$, respectively. Bond loss adjacent to the loaded ends of the lap splice length resulted in the increased steel strain rate for $P/P_{max} \geq 0.4$ as was evident from the cracking observed during specimen testing. In contrast with the behaviour observed at the ends of the lap splice length, Figure 5.3(c) shows that the steel strain increase rate at the centreline of the lap splice length was 18.6μ and 74.6μ √MPa/kN for $P/P_{max} \leq 0.83$, and $0.83 < P/P_{max} \leq 1.0$, respectively. The slope observed for $P/P_{max} \leq 0.83$ was 0.6 times that at the centreline of the lap splice length for Specimen 25-610I. This was expected as the bond capacity between the loaded ends and centreline of the lap splice length was not affected by the installation of additional steel strain gauges at the lap splice length quarter points. The strain rate observed for $P/P_{max} > 0.83$ was approximately 4 times the rate observed for lower values of applied load. This is an indication that significant bond loss occurred adjacent to the loaded end of the lap splice length which increased the bond demand for the central portion of the lap splice length.

Figure 5.3 also shows that the steel strain started to deviate from that of the concrete strain at $P/P_{max} = 0.07$ indicating that the reinforcing steel stated to slip from its surrounding concrete at low levels of applied loads as observed for the other instrumented specimens. The difference in the reinforcing steel and concrete strains at the loaded ends of the lap splice length were 156μ and 777μ for $P/P_{max} = 0.4$ and 1, respectively. The difference in the reinforcing steel and concrete strain at the centreline of the lap splice length was equal to 280μ and 478μ for $P/P_{max} = 0.83$ and 1, respectively. The slip of the reinforcing steel from concrete at the centreline of the lap splice length was 0.46 and 0.62 times, that at the ends of the lap splice length for $P/P_{max} = 0.83$ and 1, respectively. The slip of the reinforcing steel was therefore a function of available development as also observed for Specimens 25-610I and 25-510I.

5.2.5 Summary – Strain Compatibility

The strain compatibility analysis of the instrumented specimens indicated that the bond between reinforcing steel and concrete along the lap splice length was affected by the installation of steel strain gauges, development of cracks, available development length at a given point, and the magnitude of applied load. Specimen cracking initiated localized bond loss and resulted in a higher rate of local steel strain. The longitudinal reinforcing steel at the loaded ends of the lap splice length experienced higher slip compared to that at the centreline of the lap splice length.

The average bond stress distribution calculated based on steel strain gauge readings and a flexural sectional analysis at the instrumented sections within the lap splice length at different levels of applied loads are discussed in Sections 5.3 and 5.4, respectively.

5.3 Bond Stress Distribution

5.3.1 General

The bond stress distribution along the lap splice length was derived from the steel strain gauge data. The following equation was used to calculate the average bond stress, u_{avg}, assuming a uniform bond stress between adjacent strain gauges:

$$u_{avg} = \frac{\Delta\varepsilon_s A_{sr} E_s}{\pi d_b \Delta x} \qquad [5.1]$$

where $\Delta\varepsilon_s$ is the difference between two adjacent steel strain gauge readings at a given load level, E_s is the modulus of elasticity of the longitudinal reinforcing bars, A_{sr} is the cross-sectional area of the reinforcing steel bar as reduced due to installation of steel strain gauges as described in Section 3.5, d_b is the measured diameter of the longitudinal reinforcing bars, and Δx is the distance between two adjacent steel strain gauges. Material properties of the longitudinal reinforcing steel are presented in

Appendix 4B. The average bond stress, u_{avg}, was assumed positive from the loaded end of the reinforcing steel to the unloaded (i.e. cut) end of the reinforcing steel along the lap splice length. The average bond stress, u_{avg}, adjacent to the unloaded (i.e. cut) end of the bar was calculated assuming zero steel strain at the cut end of the lap splice length. The standard deviation of the average bond stress calculated was based on the standard deviation of the steel strain gauges readings reported in Section 5.2.1, with detailed information shown in Appendix 5A, ranged between 0.0004 to 0.7 MPa at $P/P_{max} = 0$.

The spliced longitudinal bars were each made from two bar segments: the first segment (i.e. end) of the bar extended from one specimen support through the lap splice at the beam centreline, and the other segment of the bar extended through the lap splice to the other support. Ideally, the bond stress distribution along the lap splice length should be identical for the same end of the two longitudinal reinforcing bars and a mirror image of each other for opposing ends of the same longitudinal bar. However, the actual distribution of bond stress along the lap splice length was more complex than the idealized bond stress distribution. The following sections describe the average bond stress distributions as calculated for the three instrumented specimens.

5.3.2 Specimen 25-610I

Figure 5.4 shows the average bond stress distribution along the lap splice length for Specimen 25-610I. Figure 5.4(a) shows the bond stress distribution for Bar A, which was located on the left hand side of the beam cross-section as shown in Figure 3.2(a). End 1 of Bar A was instrumented with steel gauges S1, S9, S2, and S10, and End 2 of the Bar A was instrumented with steel gauges S3, S11, S4, and S12.

Figure 5.4(b) shows the average bond stress distribution for Bar B, which was located on the right hand side of the beam cross-section. End 1 of Bar B was instrumented with steel gauges S7, S15, S8, and S16 and End 2 of Bar B was instrumented with steel gauges S5, S13, S6, and S14. Steel strain gauge S14 did not function as mentioned in

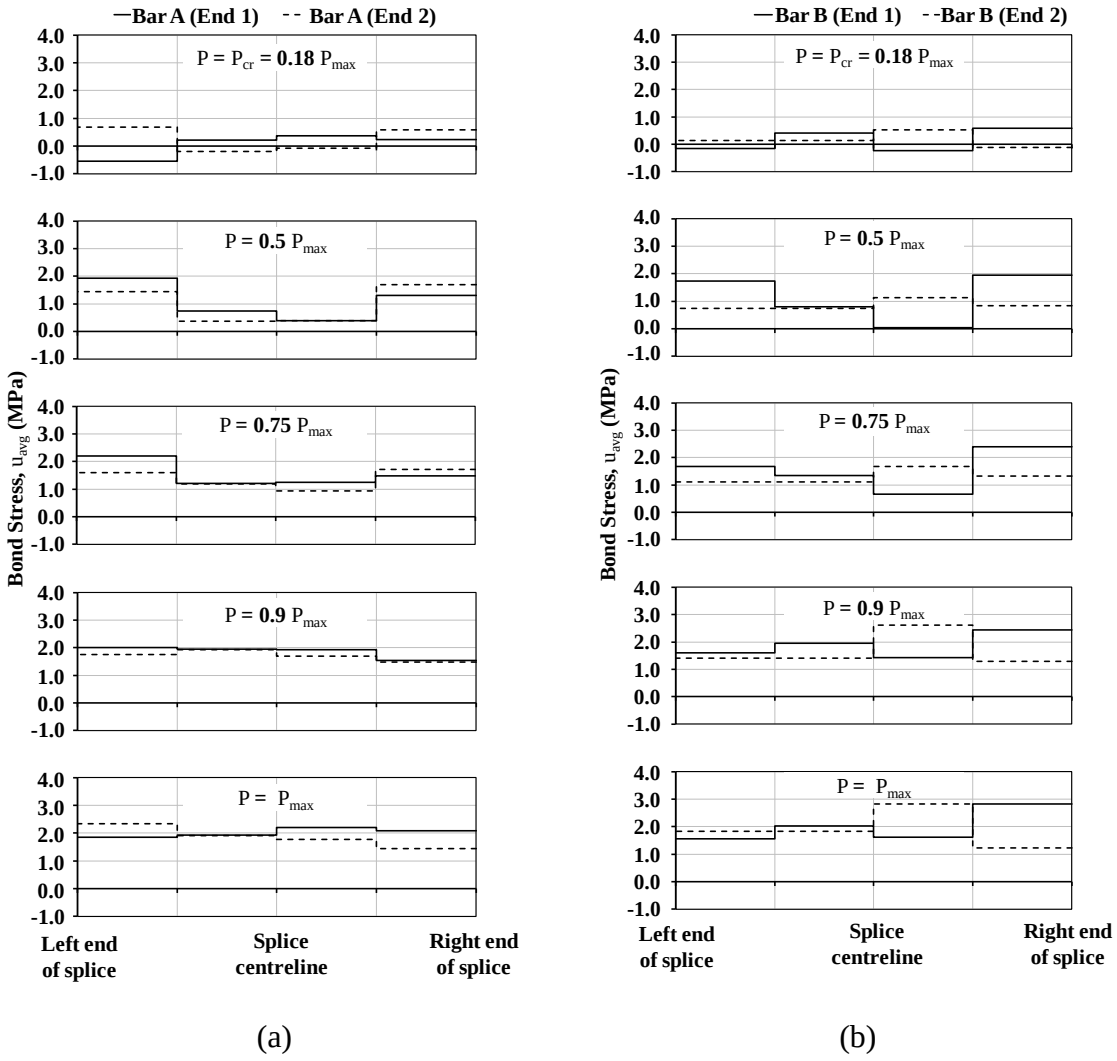

Figure 5.4. Bond stress distribution along the lap splice length - Specimen 25-610I: (a) Bar A, and (b) Bar B.

Section 5.2.2, therefore the average bond stress between gauge S6 and the unloaded (i.e. cut) end of Bar B (End 2) is shown, with no discontinuity at the quarter point along the lap splice length.

Figure 5.4(a) shows that the bond demand along the lap splice length of Bar A was non-uniform at P/P_{max} = 0.18, which corresponds to the theoretical cracking load. The magnitudes of average bond stresses for the four bar segments between adjacent steel strain gauges from the loaded to unloaded end of the lap for End 1 of Bar A were -0.54, 0.22, 0.37, and 0.24 MPa while that for End 2 of the same bar were 0.6, -0.08, -0.20, and 0.68 MPa. The assumption of uniform bond stresses between adjacent steel strain gauges might have resulted in the negative value of average bond stress. The average bond stresses along the central portion of End 1 was approximately 0.55 times of that calculated at the loaded end while that along the region between $0.25\,L_s$ from the cut end of End 1 to its cut end was approximately 0.44 times of that calculated at the loaded end. This is an indication that both the unloaded end and the central portion were equally effective in load transfer. In contrast, the central portion of End 2 of the same bar did not develop significant bond stress compared to the loaded and unloaded ends of the same bar end.

Figure 5.4(b) shows that the bond demand along the lap splice length of Bar B was also non-uniform at P/P_{max} = 0.18. The average bond stresses for the four bar segments between adjacent steel strain gauges from the loaded to unloaded end of the lap for End 1 of Bar B were -0.15, 0.41, -0.23, and 0.59 MPa. The two longitudinal bars at $0.25L_s$ from right end of the lap splice length shared load reasonably equally for $P/P_{max} \leq 0.23$ as discussed in Section 5.2.2 and accounted for the higher bond demand adjacent to the unloaded end of the End 1 of the bar. The average bond stress for the two bar segment between adjacent steel strain gauges from the loaded end to the centreline of the lap splice length of End 2 of the same bar were -0.12 and 0.53MPa and the segment from the centreline (gauge S6) to the cut end the bar was 0.15 MPa.

Figure 5.4 (a) shows that the average bond stress distribution along the lap splice length for Ends 1 and 2 of Bar A were approximately mirror image of each other at P/P_{max} = 0.5. The average bond stresses for the four bar segments between adjacent steel strain gauges from the loaded to unloaded end of the lap for End 1 of Bar A were 1.9, 0.73, 0.39, and 1.3 MPa, while the average bond stresses for the four bar segments between adjacent steel strain gauges from the loaded to unloaded end of the lap for End 2 of the same bar were 1.7, 0.39, 0.37, and 1.5 MPa. Bond demand at this applied load level was therefore higher at the loaded and unloaded ends of the splice length as compared to the central region.

Figure 5.4(b) shows that the bond demand at End 1 was relatively similar for both bars at P/P_{max} = 0.5. The average bond stresses for the four bar segments between adjacent steel strain gauges from the loaded to unloaded end of the lap for End 1 of Bar B were 1.7, 0.79, 0.04, and 2.0 MPa. The average bond stress for two bar segment between adjacent steel strain gauges from the loaded end to the centreline of the lap splice length of End 2 of the same bar were 0.84 and 1.1 MPa and the segment from the centreline (gauge S6) to the cut end the bar was 0.74 MPa.

Figure 5.4(a) shows that the bond demand within the central portion of the lap splice length of Bar A increased significantly compared to those calculated adjacent to the ends as applied load increased from P/P_{max} = 0.5 to 0.75. The increase in bond demand adjacent to both ends of the lap splice length was approximately 13% while increased range from 65 to 220% in the bar segments adjacent to the centreline of the splice length. This increase in bond demand suggests that bond demand shifted to the central region of the lap splice length as a result of bond loss at the loaded ends. A similar trend was observed for Bar A (End 2): the average bond stress at the loaded end remained constant while that at the unloaded end increased by approximately 10% as load increased from P/P_{max} = 0.5 to 0.75. In contrast, the increase of average bond stress along the central portion of Bar A (End 2) was 140 to 220%.

Figure 5.4(b) shows that the average bond stress distribution of Bar B was similar to Bar A at P/P_{max} = 0.75. The bond demand at the loaded end of the lap splice length of Bar B (End 1) remained approximately constant while that at the unloaded end increased by 23% over the values of average bond stress calculated for P/P_{max} = 0.5. The average bond stress within the central regions of this bar segment increased approximately 143% for the same increase in applied load. The average bond stress distribution of Ends 1 and 2 of Bar B differed: for End 2, bond demand increased by 58% and 48% over those values calculated at P/P_{max} = 0.5 for the segments adjacent to the loaded end and central bar segments, respectively. The increase in bond demand for both of these regions was approximately equal and suggests that bond loss experienced by this bar was relatively low at this level of applied load.

Figure 5.4(a) shows that the bond stress distribution for Bar A becomes uniform and average bond stress at the loaded end of the lap splice length approached its maximum value at P/P_{max} = 0.9. The bond demand adjacent to the unloaded end of Bar A increased 4 to 10% while a 8 to 14% decrease at the loaded end occurred as the applied load increased from P/P_{max} = 0.75 to 0.9. This is an indication of significant bond loss. It may be noted that the specimen's load versus deflection curve also showed a slight change in slope at P/P_{max} = 0.85, further substantiating that significant bond loss occurred along the lap splice length.

The bond distribution along Bar B remained non-uniform at P/P_{max} = 0.9, as shown in Figure 5.4(b). The average bond stress at the loaded end of the bar decreased by 4% while that at the unloaded increased approximately 1 to 26% as load increased from P/P_{max} = 0.75 to 0.9. The average bond stress adjacent to the centreline of the lap splice length for Bar B (End 1) was approximately 0.9 to 1.2 times that at the loaded end and 0.6 to 0.8 times that at the unloaded end. The average bond stress adjacent to the centreline of the lap splice length for Bar B (End 2) was approximately 2.0 times that at the loaded and unloaded ends of the bar.

Figure 5.4(a) shows that the average bond stress distribution along the lap splice length of Bar A remained approximately uniform with a 34% increase in average bond stress adjacent to the unloaded end and a 2 to 8% decrease in average bond stress adjacent to the loaded end as the applied load increased from P/P_{max} = 0.9 to 1.0. In contrast, the average bond stress distribution along the lap splice length of Bar B remained non-uniform at P/P_{max} = 1.0. Such a difference in the bond stress distribution along the two bars that made up this lap splice suggests that Bar A failed first with Bar B failing immediately thereafter as it could not resist the applied load on its own.

The average bond stress distribution in the splice region at different levels of applied loads indicated that the stress remains non-uniform for much of the loading range. A gradual loss of bond adjacent to the ends of the lap splice length imposed a higher bond demand in the central region of the lap splice length. The bond stress distribution therefore became uniform as the applied load approaches its maximum value indicating that the peak bond stress shifted from the loaded end to the unloaded end of the bar segment. Similar behaviour was observed for Specimens 25-410I and 25-510I.

5.3.3 Specimen 25-510I

Figure 5.5 shows the average bond stress distribution for Specimen 25-510I. Bar A and Bar B were located on the left hand side and right hand side of the beam cross-section, respectively, as shown in Figure 3.2(a). End 1 of Bar A was instrumented with steel gauges S1 and S2 and End 2 of the Bar A was instrumented with steel gauges S3 and S4. End 1 of the Bar B was instrumented with steel gauges S7 and S8 and End 2 of the Bar B was instrumented with steel gauges S5 and S6.

The average bond stress distribution for Bars A and B were approximately uniform at P/P_{max} = 0.15, but then became non-uniform as shown in the Figures 5.5(a) and (b) at P/P_{max} = 0.5. The average bond stress distribution along the lap splice length of Bars A

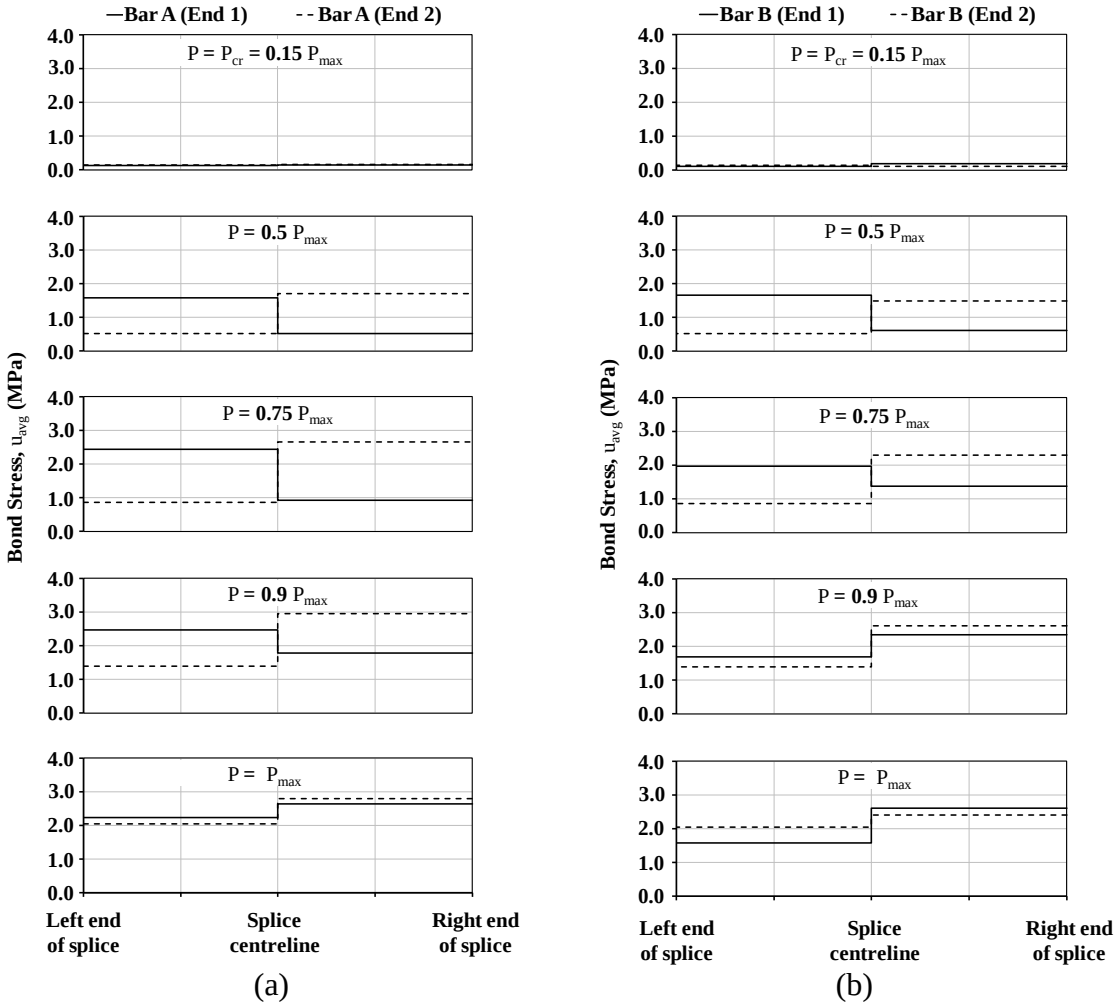

Figure 5.5. Bond stress distribution along the lap splice length - Specimen 25-510I: (a) Bar A, and (b) Bar B.

and B at P/P_{max} = 0.5 were approximately identical for the same end of the two longitudinal reinforcing bars and a mirror image of each other for opposing ends of the same longitudinal bars. The average bond stress at the loaded end of Bars A and B ranged from 1.5 MPa to 1.7 MPa and was approximately 3 times that at their respective unloaded ends.

Figure 5.5(a) shows that the average bond stress distribution for the two ends of Bar A at P/P_{max} = 0.75 were mirror images of each other as observed at P/P_{max} = 0.5. The average bond stress increased by approximately 55% and 75% at the loaded and unloaded ends of Bar A, respectively as the load increased from P/P_{max} = 0.5 to 0.75. The average bond stress adjacent to the loaded end of Bar A (End 1) remained approximately constant while that at the loaded end of Bar A (End 2) increased by 12% as load increased from P/P_{max} = 0.75 to 0.9, indicating that the average bond stress adjacent to the loaded end of the bar approached its maximum value. In contrast with the loaded end of Bar A, the average bond stress adjacent to the unloaded end of the lap splice length of Ends 1 and 2 of Bar A increased approximately 90% and 60%, respectively, indicating that significant bond loss adjacent to the loaded end imposed a higher bond demand in the region adjacent to the unloaded end of the bar.

As P/P_{max} increased from 0.5 to 0.75, the average bond stress increased approximately 20% and 54% at the loaded end of Ends 1 and 2 of Bar B, respectively. In contrast, the average bond stress at the unloaded end increased 125% and 68% for Ends 1 and 2, respectively, of the same bar. The average bond stresses at the loaded end of Bar B (End 1) and Bar B (End 2) were 1.4 times and 2.7 times that of their respective unloaded ends. The average bond stress distribution of Bar B (End 1) at P/P_{max} = 0.9 indicated that the peak of the average bond stress shifts from the loaded end to the unloaded end and was similar to the results for Bar A (End 1). In contrast with End 1 of Bar B, the average bond stress at the loaded end of Bar B (End 2) was 1.9 times of that at the unloaded end of the bar.

The average bond stress distribution at P/P_{max} =1 indicated that the peak average bond stress for End 1 of both bars shifted to the unloaded end of the bar. In contrast, the average bond stress adjacent to the loaded end of the End 2 of Bars A and B were 20% to 40% higher than that at the unloaded end of the bar indicating that a shift in the location of the peak of the average bond stress did not occur for this end of the bars. Higher bond demand adjacent to the unloaded end of End 1 of both Bars A and B initiated pullout of the bars in the lap splice length from their initial position as shown in Figure 5D.5(b).

5.3.4 Specimen 25-410I

Figures 5.6(a) and (b) show the bond stress distribution along the lap splice length for Bars A and B for Specimen 25-410I, respectively. This specimen was instrumented identically to Specimen 25-510I.

Figure 5.6 shows that the average bond stress from the loaded end to the lap splice length centreline for Bars A and B at P/P_{max} = 0.19 were close to the standard deviation of the average bond stress calculated at the 95% confidence level. The average bond stress from the lap splice length centreline to the unloaded end was 0.2 MPa to 0.28 MPa for Bars A and B, respectively, indicating that the average bond stress adjacent to the unloaded end was higher than that adjacent to the loaded end. The bond stress distribution at this low level of applied load was highly non-uniform and the sign of the bond stresses varied along the lap splice length as observed for Specimens 25-510I and 25-610I. The assumption of uniform bond stresses between adjacent steel strain gauges might have resulted in the lower average bond stress adjacent to the loaded end of the lap splice length.

Figure 5.6(a) shows that the average bond stress distribution for Bar A (End 1) was uniform along the length of the bar at P/P_{max} = 0.5 and was approximately equal to 0.67 MPa: 11.5 and 3.5 times of that observed adjacent to the loaded end and unloaded end,

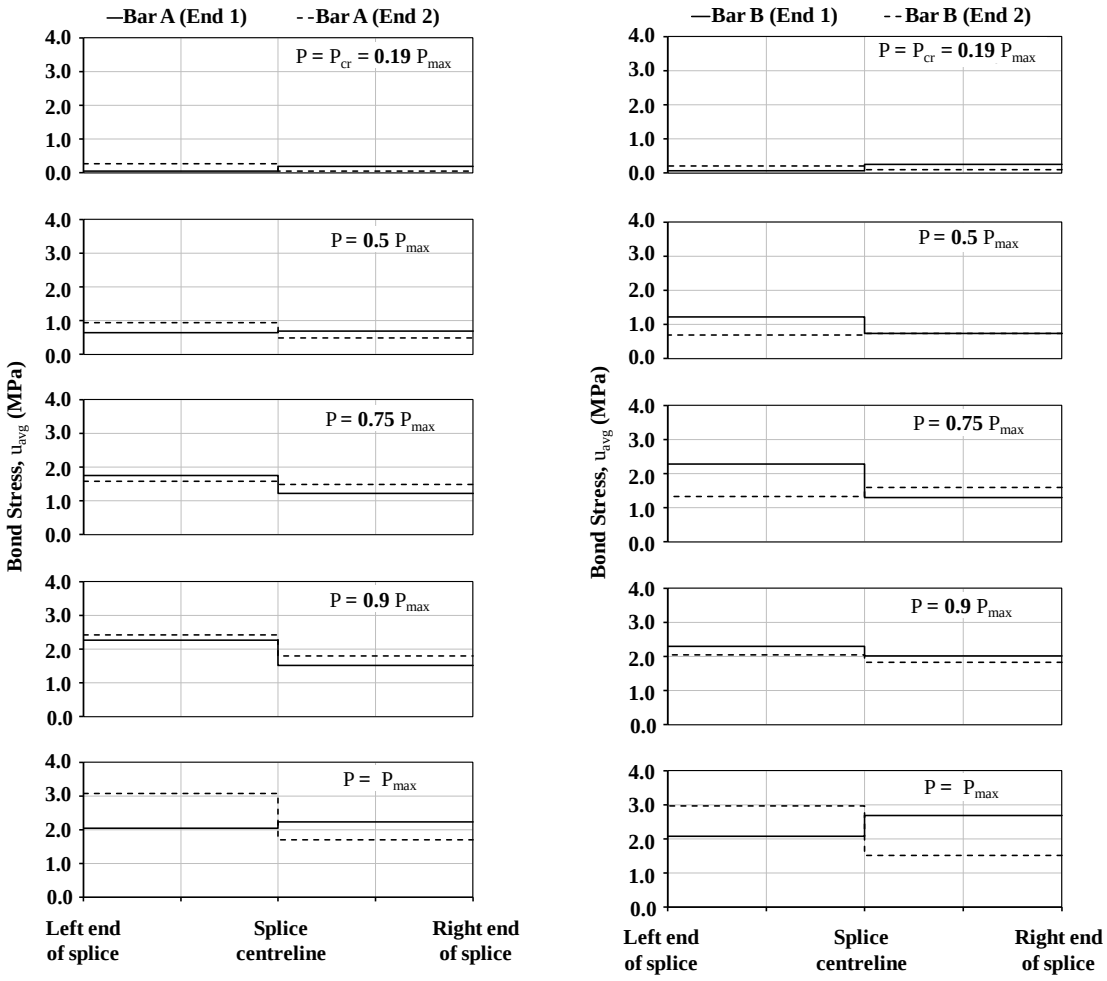

(a) (b)

Figure 5.6. Bond stress distribution along the lap splice length - Specimen 25-410I: (a) Bar A, and (b) Bar B.

respectively, of the same bar at P/P_{max} = 0.19 and suggests partial bond loss adjacent to the loaded end with increased P/P_{max}.

The average bond stress distribution for Bar A (End 1) at P/P_{max} = 0.75 and 0.9 indicates that the bond demand adjacent to the loaded end was approximately 1.5 times that adjacent to the unloaded end. The average bond stresses adjacent to the loaded end and unloaded end, increased approximately 175% and 75%, respectively, with this increase in the applied load and indicates further bond loss from that which occurred at P/P_{max} = 0.5. The average bond demand adjacent to the loaded and unloaded ends then increased approximately 27% as the applied load increased from P/P_{max} = 0.75 to 0.9, indicating that the average bond stress adjacent to the loaded end approached its maximum value.

Figure 5.6(a) shows that the average bond stress for Bar A (End 2) was non-uniform at P/P_{max} = 0.5 and was 0.49 MPa and 0.93 MPa at the loaded and unloaded ends, respectively. The unloaded end of the bar therefore experienced higher bond demand relative to the loaded end. The average bond stress then became uniform at P/P_{max} = 0.75 and was equal to 1.54 MPa along the entire lap splice length. The average bond stress adjacent to the loaded and unloaded ends increased approximately 210% and 70%, respectively, as the applied load increased from P/P_{max}= 0.5 to 0.75, suggesting that significant bond loss occurred adjacent to the loaded end of the bar. The peak average bond stress shifted to the unloaded end of the bar at P/P_{max} = 0.9 due to the significant bond loss adjacent to the loaded end of the bar. The average bond stress at the unloaded end was 2.42 MPa: approximately 1.3 times that at the loaded end of the bar.

Figure 5.6(a) shows the average bond stress distribution for Bar A at P/P_{max} = 1, and indicates that the average bond stress adjacent to the unloaded end was higher than that adjacent to the loaded end. The average bond stress at the loaded end decreased approximately 5% to 10% and that at the unloaded end increased approximately 27% to 48% as load increased from P/P_{max} = 0.9 to 1. The average bond stress adjacent to the

loaded end approached its maximum value and imposed higher bond demand at the unloaded end of the bar, eventually caused bar pullout.

The average bond stress distribution of Bar B (End 1) shows similar behaviour as Bar A (End 1): the average bond demand adjacent to the loaded end was higher than that adjacent to the unloaded end. The average bond stress for the loaded end was 1.6 and 1.8 times higher than that at the unloaded end of the bar for P/P_{max} = 0.5 and 0.75, respectively. Higher bond demand adjacent to the loaded end of the bar was an indication of partial bond loss within this bar segment. In contrast, the average bond stress for Bar B (End 2) was uniform along the lap splice length for P/P_{max} = 0.5 with a magnitude of 0.72 MPa. The average bond stress at the loaded and unloaded ends of Bar B (End 2) then increased approximately 120% and 90% as the load increased from P/P_{max} = 0.5 to 0.75, indicating higher bond loss adjacent to the loaded end.

The average bond stress distribution for Bar B at P/P_{max} = 0.9 became approximately uniform. This is an indication that the average bond stress adjacent to the loaded end approached its maximum value. The average bond stress distribution at P/P_{max} = 1 suggests that the peak average bond stress distribution for both Ends 1 and 2 of Bar B shifted from the loaded to the unloaded end of the bar as observed for the Bar A.

5.3.5 Summary – Bond Stress Distribution

The average bond stress distribution along the lap splice length of instrumented specimens suggests that stresses remained non-uniform for much of the loading range. Gradual loss of bond adjacent to the ends of the lap splice length imposed a higher bond demand in the central region of the lap splice length. The bond stress distribution therefore became uniform as the applied load approached its maximum value indicating that the peak bond stress shifted from the loaded end to the unloaded end of the bar segment. The flexural section analysis of the specimen along the lap splice length was discussed in Section 5.4.

5.4 Flexural Section Analysis

5.4.1 General

A flexural sectional analysis at the sections instrumented with steel and concrete strain gauges was performed. All calculations assumed that plane sections remained plane and therefore the assumption of a linear strain distribution was made. Concrete and longitudinal steel strain values, as measured from testing, were increased by the strains caused by the self-weight of the specimen and that of the spreader beam and the bearing plates. The linear strain distribution was estimated for load increments of $P/P_{max} = 0.05$ using the following two methods: (1) considering data recorded by the concrete strain gauges at 50 mm, 100 mm and the effective depth from the top of the section (Method 1), and (2) considering data recorded by the top two concrete strain gauges and the steel strain gauge on the longitudinal reinforcement (Method 2). A linear regression analysis of strain readings was performed to establish the linear strain distribution at each instrumented section and for each load level. The coefficients of determinations, R^2, of the estimated linear strain distribution for all considered load levels are presented in Appendix 5A and are discussed in the following sections. The neutral axis location and compressive strain in the concrete at the extreme compression (i.e. top) fibre for all load increments were determined from the derived strain distributions. The depth of the neutral axis was compared with the theoretical depth as determined considering force equilibrium at the section and neglecting the tensile strength of the concrete after cracking.

The compressive force in the concrete and its line of action were determined in accordance with procedures developed by ISIS Canada (2007) for modified Whitney stress block factors, α and β, less than the ultimate load level. The calculated concrete compressive force includes the contribution from the self-weight of the specimen and that of the spreader beam and the bearing plates used in the test setup. The calculated compressive force was therefore adjusted to subtract the concrete compressive force due to the self-weight of the specimen and that of the spreader beam and the bearing plates used in the test setup to provide a comparison with the normalized applied load. The

tension force in the longitudinal reinforcement was calculated using the steel strain readings at a given section and considering the reduced cross-sectional area of the reinforcing steel bars at the location of steel strain gauges. The tensile strength of the concrete was neglected in the sectional analysis. The internal moment was then calculated at the section's plastic centroid at different levels of applied normalized load for both analysis methods described. The internal moment due to the applied load was compared to the moment as calculated using statics.

5.4.2 Specimen 25-610I

Figures 5.7(a), (b), and (c) show the neutral axis location at the left end of the lap splice length, centreline of the lap splice length, and right end of the lap splice length, respectively, for Specimen 25-610 at different levels of applied loads. The concrete strain gauge located 50 mm from the top of the section at the right end of the lap splice length was non-responsive and the concrete gauge located at the effective depth from the top of that section coincided with a crack and provided erratic results. The flexural sectional analysis at the right end of the lap splice length was therefore performed considering the concrete strain reading at 100 mm from the top of the section and the steel strain at the effective depth of the section.

The coefficients of determination, R^2, for the concrete strain distributions estimated using the three concrete strain gauge readings (Method 1) ranged from 0.99 to 0.77 for P/P_{max} = 0.05 to 0.80, respectively, and 0.77 to 0.46 for P/P_{max} = 0.80 to 1.0, respectively, at the left end of the lap splice length. In contrast, the coefficients of determination for the established strain distributions calculated using two concrete and one steel strain gauge readings (Method 2) were greater or equal to 0.95 for the entire loading range. A comparison of goodness of fit suggested that the strain distribution estimated using Method 2 fitted well with the measured strains compared to Method 1. The concrete strain recorded by the gauge installed at the effective depth of the section deviated from the steel strain as discussed in Section 5.2.2 and might be accounted for

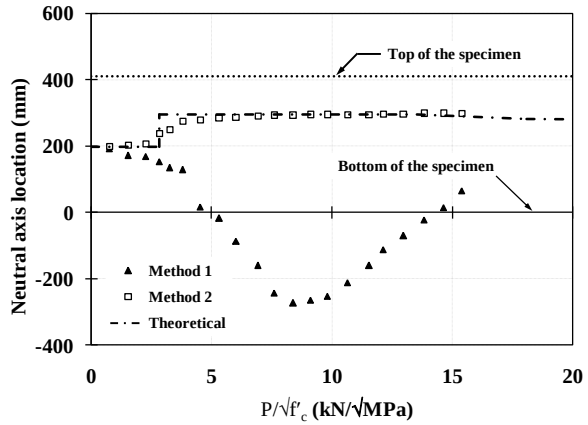

(a)

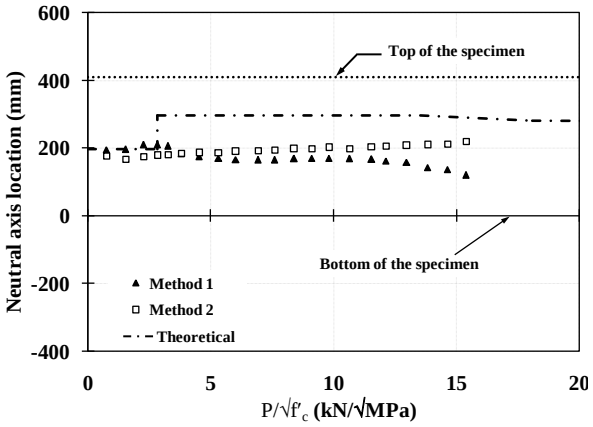

(b)

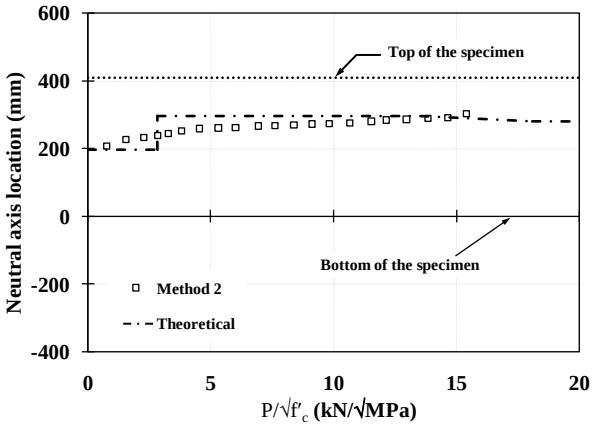

(c)

Figure 5.7. Neutral axis location - Specimen 25-610I: (a) left end of the lap splice length, (b) centreline of the lap splice length, and (c) right end of the lap splice length.

lower coefficients of determinations for estimated strain distribution resulting from Method 1 at the higher load levels. The coefficients of determination for the concrete strain distributions at the midspan of the specimen estimated using both methods were greater than 0.94 for the entire loading range. The coefficients of determination for concrete strain distributions at the right end of the lap splice length were estimated using one method only as discussed earlier and the coefficients of determinations of the estimated strain distributions were equal to 1.0 for the entire loading range.

Figure 5.7(a) shows that the neutral axis locations at the left end of the lap splice length as calculated using Method 2 approximately followed the theoretical neutral axis locations for the entire loading range. However, the transition of the depth of the neutral axis from the uncracked section to the cracked section was gradual, rather than the sudden change as estimated theoretically. The neutral axis location resulting from Method 1 was somewhat more complex than the theoretical neutral axis location. The depth of the neutral axis from the top fibre of this section deviated from that theoretically calculated for $P/P_{max} > 0.10$ and increased from 218 mm to 281 mm for $P/P_{max} = 0.10$ to 0.25, respectively. Bond loss as discussed in Section 5.2.2 was the reason behind the increase of the depth of the neutral axis. The depth of the neutral axis at the left end of the lap splice length then started to increase more rapidly for $P/P_{max} = 0.25$ to 0.55 and reached 270 mm below the bottom (i.e. 680 mm from the top) of the section at $P/P_{max} = 0.55$. The neutral axis location calculated using Method 1 suggested that the entire concrete cross-section at the left end of the lap splice length was in compression for $P/P_{max} > 0.3$. However, the observed crack pattern for Specimen 25-610I as shown in Figure 4C.11 indicated development of a crack adjacent to the left end of the lap splice length for $P/P_{max} \geq 0.42$ and suggested existence of tension in concrete. The established strain distributions resulting from Method 2 also indicated the existence of tension in concrete. Method 1 therefore did not predict the actual strain distribution at the left end of the lap splice length due to the resulting bond loss. Figure 5.7(a) also shows that the depth of the neutral axis resulting from Method 1 started to decrease for $P/P_{max} > 0.55$ and reached 345 mm from the top of the section at $P/P_{max} = 1.0$. A review of observed crack pattern for this specimen indicates that the height of the crack at the

left end of the lap splice length reached mid-height of the section at $P/P_{max} \approx 0.55$ and might caused this reduction in the depth of the neutral axis.

Figure 5.7(b) shows that the neutral axis location at the centreline of the lap splice length followed the theoretical neutral axis location up until $P/P_{max} = 0.18$, which coincided with the theoretical cracking load calculated in accordance with CAN/CSA-S6 (CSA 2006). The depth of the neutral axis from the top of the section calculated using Method 2 decreased with increasing applied load and ranged from 230 mm to 190 mm from top of the section for $P/P_{max} = 0.18$ to 1.0. However, the depth of the neutral axis calculated using this method was higher than the depth of the theoretical neutral axis. The additional stiffness provided by the four partially developed spliced reinforcing bars at the centreline of the lap splice length might be accounted for this difference. The depth of the neutral axis from the top of the section calculated using Method 1 increased with increasing applied load and ranged from 200 mm to 240 mm for $P/P_{max} = 0.18$ to 0.75, respectively, and 240 mm to 290 mm for $P/P_{max} = 0.75$ to 1.0, respectively. Significant increase in bond demand at the central portion of the lap splice length for $P/P_{max} \geq 0.75$, as discussed in Section 5.3.2, might result this increase of the depth of the neutral axis.

Figure 5.7(c) shows that the neutral axis location at the right end of the lap splice length calculated using concrete strain at 100 mm from the top fibre and steel strain at that section matched well with the theoretical neutral axis location. The transition of the depth of the neutral axis from the uncracked section to the cracked section was gradual as observed for the left end of the lap splice length.

A comparison of the depth of the neutral axis calculated using both methods of analysis provided evidence of bond loss within the lap splice length. The neutral axis location resulting from Method 2 matched well with the theoretical neutral axis locations while that resulting from Method 1 deviated from the theoretical neutral axis locations due to the loss of strain compatibility. The depth of the neutral axis calculated using Method 2

indicated that the neutral axis locations remained relatively constant within the lap splice length which was expected within the constant moment region of the specimen.

Figures 5.8(a), (b), and (c) show the concrete compressive force, C_c and steel tension, T_s at the left end of the lap splice length, centreline of the lap splice length, and right end of the lap splice length, respectively, for Specimen 25-610I. Figure 5.8(a) shows that the concrete compressive force at the left end of the lap splice length as calculated using Method 1 was greater than that of the steel tension. In contrast, concrete compressive force at that section calculated using Method 2 was approximately equal to the steel tension. Bond loss at the left end of the lap splice length might result this difference in the internal forces calculated using two methods of analysis. Figure 5.8(b) shows that the concrete compressive forces at the centreline of the specimen calculated using both methods of analysis were greater than the steel tension and suggested that a resultant axial compressive force existed at that section. However, the limited scope of current study did not allow for an explanation of whether this difference in calculated internal forces resulted from loss of strain compatibility or from noise in the strain gauge readings. Figure 5.8(c) shows that the concrete compressive force at the right end of the lap splice length estimated using Method 2 was approximately equal to the steel tension force as observed for the left end of the lap splice length.

Figures 5.9(a), (b), and (c) show the calculated internal moments at the left end of the lap splice length, centreline of the lap splice length, and right end of the lap splice length, respectively for Specimen 25-610I. Figure 5.9(a) shows that the resulting internal moments at the left end of the lap splice length calculated using both methods were approximately equal to the static moment. Figure 5.9(c) shows that the calculated internal moment at the right end of the lap splice length was also equal to the static moment. In contrast, Figure 5.9(b) shows that the internal moment at the midspan of the

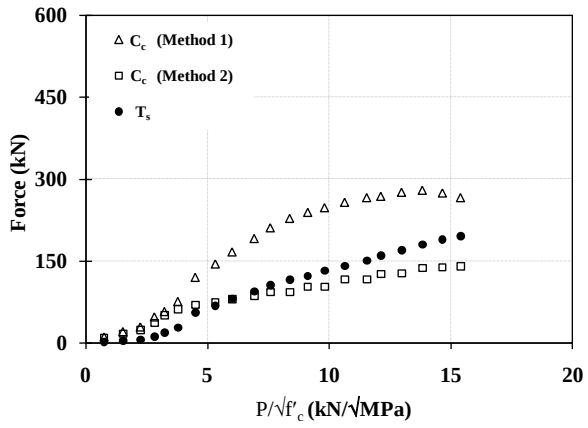

(a)

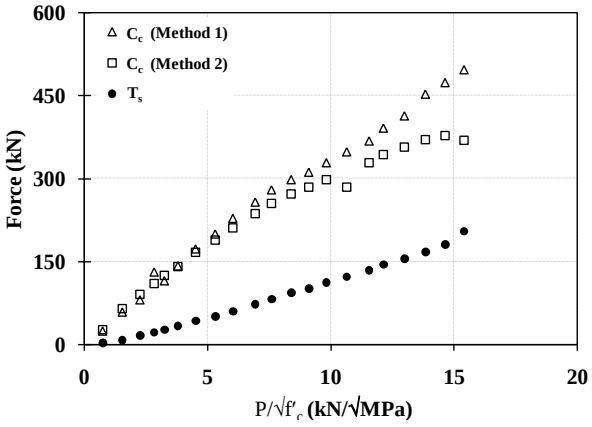

(b)

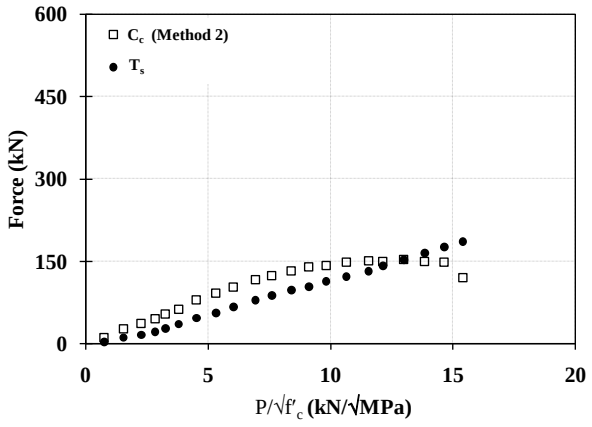

(c)

Figure 5.8. Internal forces - Specimen 25-610I: (a) left end of the lap splice length, (b) centreline of the lap splice length, and (c) right end of the lap splice length.

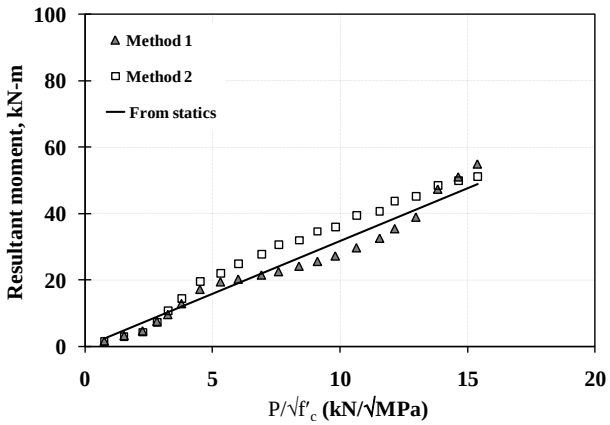

(a)

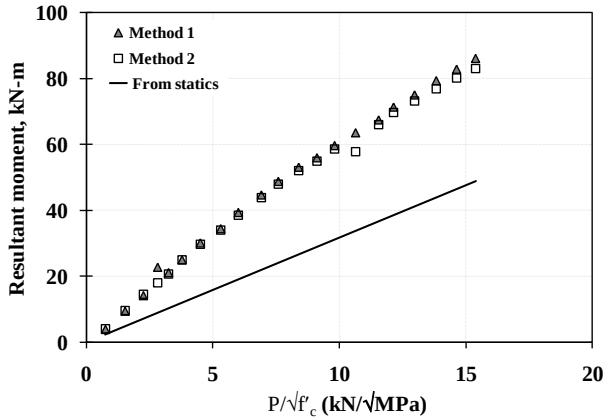

(b)

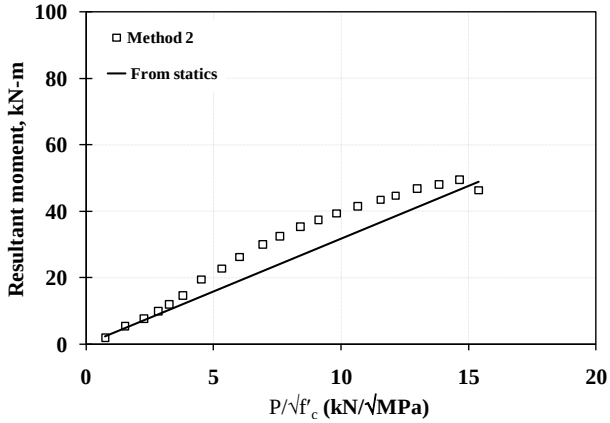

(c)

Figure 5.9. Resultant internal moment- Specimen 25-610I: (a) left end of the lap splice length, (b) centreline of the lap splice length, and (c) right end of the lap splice length.

.

specimen calculated using both methods of analysis was approximately 1.9 times that of the static moment for the entire loading range. The calculated concrete compressive force at this section was higher than the steel tension as discussed earlier and accounted for this higher estimation of the internal moment.

5.4.3 Specimen 25-510I

Figures 5.10(a), (b), and (c) show the neutral axis location at the left end of the lap splice length, centreline of the lap splice length, and right end of the lap splice length, respectively, for Specimen 25-510I. The coefficients of determination for the established strain distributions at the left end of the lap splice length calculated using Method 1 ranged from 1.0 to 0.9 for P/P_{max} = 0.07 to 0.35, respectively, and 0.9 to 0.52 for P/P_{max} = 0.35 to 1, respectively. The coefficients of determination for the established strain distribution at the right end of the lap splice length resulted from Method 1 ranged from 0.99 to 0.63 for P/P_{max} = 0.07 to 0.30, respectively, and 0.63 to 0.35 for P/P_{max} = 0.3 to 1.0, respectively. The observed crack pattern at P/P_{max} = 0.3 as shown in Figure 4C.10 suggested bond loss at the ends of the lap splice length and accounted for the decrease in the coefficients of determination. In contrast, the coefficient of determination for the established strain distributions at the centreline of the lap splice length calculated using Method 1 was higher than 0.99 for the entire loading range. The coefficients of determination for the established linear concrete strain distributions resulting from Method 2 were higher than 0.99 at the ends and centreline of the lap splice length for the entire loading range.

Figures 5.10(a) and (c) show that the neutral axis locations at ends of lap splice length as calculated using Method 2 approximately matched the theoretical values. The transition of the neutral axis depth from the uncracked section to the cracked section was gradual as observed at the ends of the lap splice length for Specimen 25-610I. In contrast, the depth of the neutral axis at the ends of the lap splice length calculated using Method 1

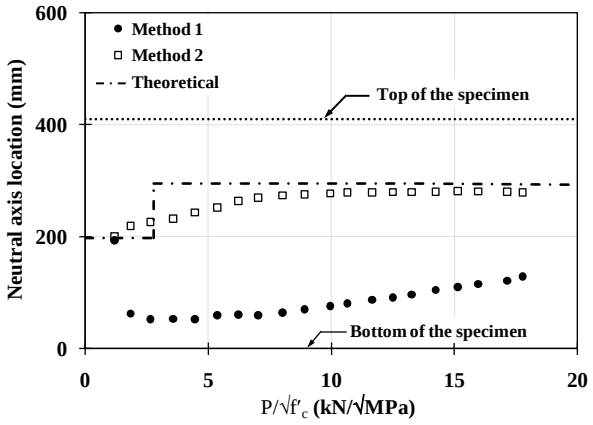

(a)

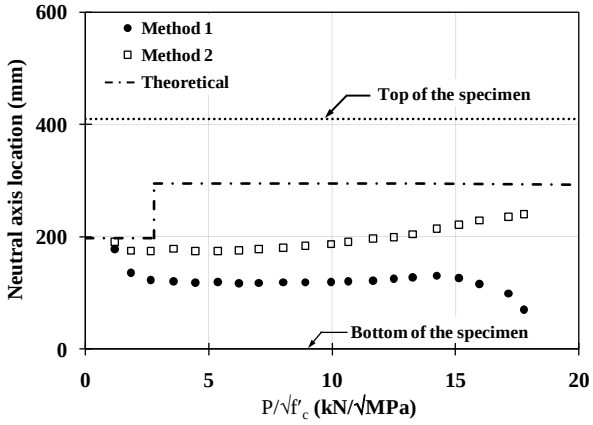

(b)

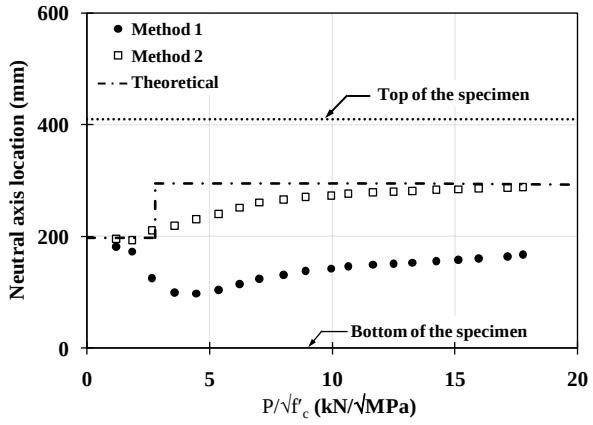

(c)

Figure 5.10. Neutral axis location - Specimen 25-510I: (a) left end of the lap splice length, (b) centreline of the lap splice length, and (c) right of the lap splice length.

deviated from the theoretical neutral axis location for $P/P_{max} > 0.07$. Bond loss as discussed in Section 5.2.3 accounted for this deviation. Figure 5.10(a) shows that the depth of the neutral axis from the top of the section at the left end of the lap splice length as calculated using Method 1 increased from 217 mm to 357 mm for P/P_{max} = 0.07 to 0.15, respectively, and then decreased from 357 mm to 281 mm for $P/P_{max} = 0.15$ to 1.0, respectively. Figure 5.10(c) shows that the depth of the neutral axis from the top of the section at the right end of the lap splice length increased from 228 mm to 312 mm for $P/P_{max} = 0.07$ to 0.25, respectively, and then decreased from 312 mm to 242 mm for $P/P_{max} = 0.25$ to 1.0, respectively. The specimen's observed crack pattern as presented in Figure 4C.10 indicated that the height of the crack at the ends of the lap splice length crossed the level of the longitudinal bars at $P/P_{max} = 0.3$, and then continued to increase with applied load, resulting in the decrease in the depth of the neutral axis at this location.

Figure 5.10(b) shows that the neutral axis location at the centreline of Specimen 25-510I as calculated using Method 1 deviated from the theoretical value for $P/P_{max} > 0.07$. The depth of the neutral axis as calculated using Method 1 increased from 230 mm to 290 mm for $P/P_{max} = 0.07$ to 0.15, respectively, and remained relatively constant for $0.15 \leq P/P_{max} \leq 0.9$. The depth of the neutral axis from the top of the section then increased from 290 mm to 340 mm for $P/P_{max} = 0.9$ to 1.0, respectively. In contrast, the depth of the neutral axis from the top of the section at the centreline of the lap splice length calculated using Method 2 remained relatively constant for $0.07 \leq P/P_{max} \leq 0.55$ and then decreased from 220 mm to 170 mm from for $P/P_{max} = 0.55$ and 1.0, respectively. The depth of the neutral axis from the top of the section resulting from this analysis method was greater than the theoretical value as observed for Specimen 25-610I.

A comparison of the neutral axis depth calculated using both methods of analysis suggestes that Method 1 could not capture the actual location of the neutral axis due to bond loss as observed for Specimen 25-610I. The neutral axis location resulting from Method 2 matched well with theoretical values and suggests that the neutral axis remained relatively constant within the lap splice length as expected.

Figures 5.11(a), (b) and (c) shows the calculated concrete compressive force and steel tension at the left end of the lap splice length, centreline of the lap splice length, and the right end of the lap splice length, respectively, for Specimen 25-510I. Figures 5.11(a) and (c) indicate that the concrete compressive force calculated using Method 2 was approximately equal to the steel tension for the entire loading range. In contrast, the concrete compressive forces at the ends of the lap splice length calculated using Method 1 were not equal to the steel tension and suggested the existence of a resultant compressive force at these sections for the entire loading range. The difference in the concrete compressive force resulting from two different methods of analysis suggested bond loss at the ends of the lap splice length. Figure 5.11(b) shows that the concrete compressive force at the centreline of the lap splice length as calculated using both methods of analysis was not equal to the tension force in the longitudinal reinforcing steel and indicated existence of resultant axial compressive force at this section for the entire loading range. Similar behaviour was observed at the midspan of Specimen 25-610I and requires further investigation to explain such behaviour.

Figures 5.12(a), (b), and (c) show a comparison of the resulting internal moments and the static moments at the left end, centreline, and right end of the lap splice length, respectively, for Specimen 25-510I. Figure 5.12 shows that the internal moments calculated using Method 2 matched well with the static moments at the ends and the centreline of the lap splice length for the entire loading range. However, the internal moments at the left and right end of the lap splice length calculated using Method 1 were approximately 1.2 and 1.3 times, respectively of the static moment for the entire loading range. The difference in the internal moment resulting from two different methods of analysis suggests bond loss at the ends of the lap splice length. The internal moments at the centreline of the lap splice length calculated using Method 1 matched well with the static moments.

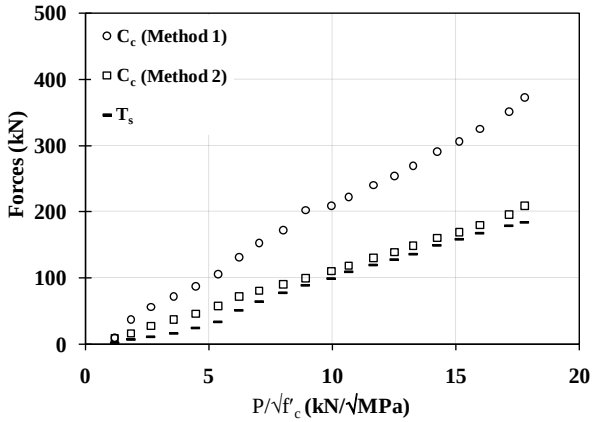

(a)

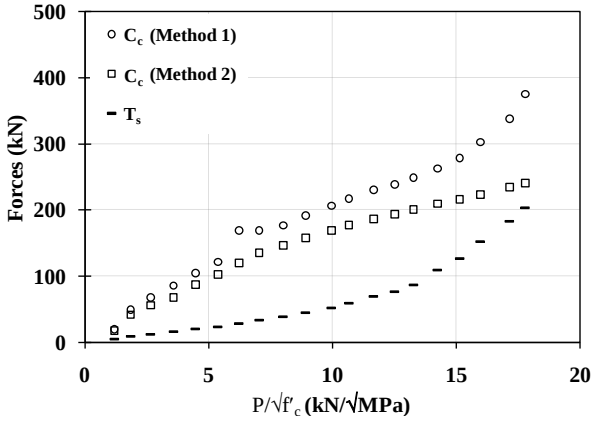

(b)

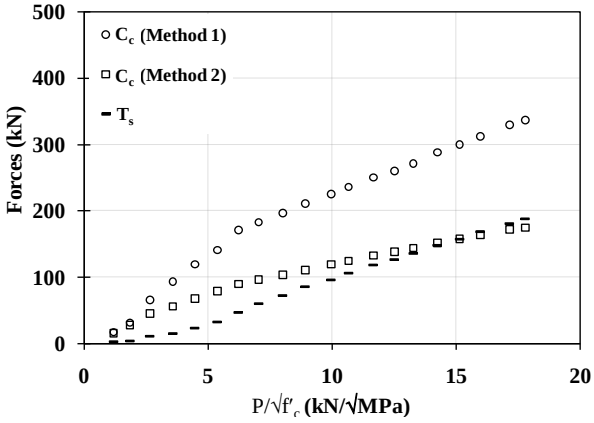

(c)

Figure 5.11. Internal forces- Specimen 25-510I: (a) left end of the lap splice length, (b) centreline of the lap splice length, and (c) right of the lap splice length.

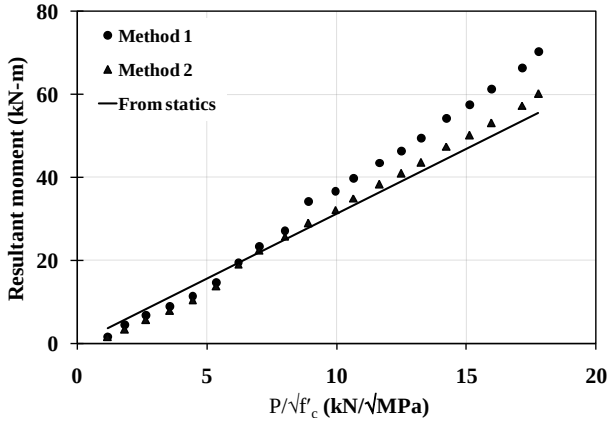

(a)

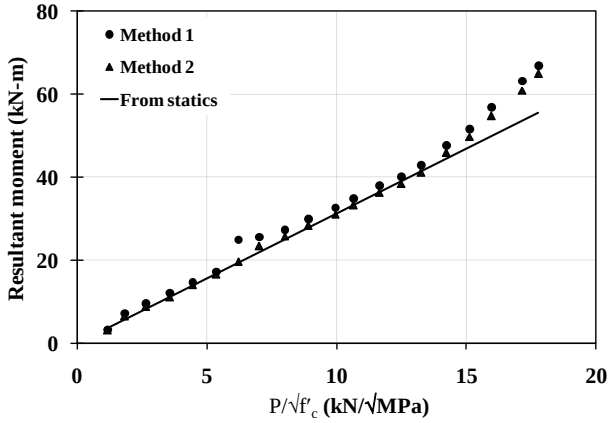

(b)

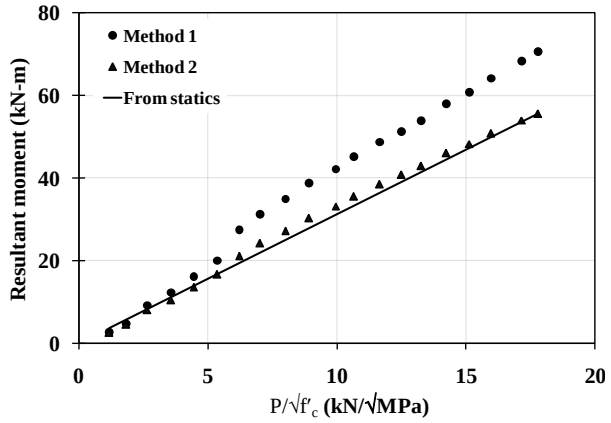

(c)

Figure 5.12. Internal resulting moment- Specimen 25-510I: (a) left end of the lap splice length, (b) centreline of the lap splice length, and (c) right of the lap splice length.

5.4.4 Specimen 25-410I

Figures 5.13(a), (b), and (c) shows the neutral axis locations at the left end, centreline, and right end of the lap splice length, respectively, for Specimen 25-410I. The coefficients of determination of the linear concrete strain distributions at the left end of the lap splice length estimated using Method 1 ranged from 1.0 to 0.84 for P/P_{max} = 0.05 to 0.6, respectively, and 0.84 to 0.64 for P/P_{max} = 0.6 to 1.0, respectively. The coefficients of determination of the concrete strain distributions at the centreline of the lap splice length estimated using Method 1 ranged from 0.99 to 0.86 for P/P_{max} = 0.05 to 0.75, respectively, and 0.86 to 0.75 for P/P_{max} = 0.75 to 1.0, respectively. The coefficients of determination of the concrete strain distributions at the right end of the lap splice length estimated using Method 1 ranged from 0.99 to 0.86 for P/P_{max} = 0.05 to 0.80, respectively, and 0.86 to 0.66 for P/P_{max} = 0.80 to 1.0, respectively. In contrast, the coefficients of determination for the established strain distributions calculated using Method 2 were greater or equal to 0.98 for the entire loading range at the ends and centreline of the lap splice length. An analysis of the goodness of fit suggested that the strain distribution estimated using Method 2 provided a better fit to the measured strains as compared to Method 1.

Figures 5.13(a) and (c) show the neutral axis locations at the ends of the lap splice length resulting from Method 2 approximately matched the theoretical values. The transition of the depth of the neutral axis from the uncracked section to the cracked section was gradual as observed for Specimens 25-610I and 25-510I. In contrast, the depth of the neutral axis calculated using Method 1 at the ends of the lap splice length deviated from the theoretical values for $P/P_{max} > 0.05$. Figure 5.13(a) shows that the depth of the neutral axis from the top of the section at the left end of the lap splice length increased from 214 mm to 301 mm for P/P_{max} = 0.05 to 1.0, respectively. Figure 5.13(c) shows that the depth of the neutral axis from the top of the section at the right end of the lap splice length increased from 221 mm to 314 mm for P/P_{max} = 0.05 to 0.50, respectively, and then decreased from 314 mm to 276 mm from the top of the section for P/P_{max} = 0.5 to 1.0, respectively.

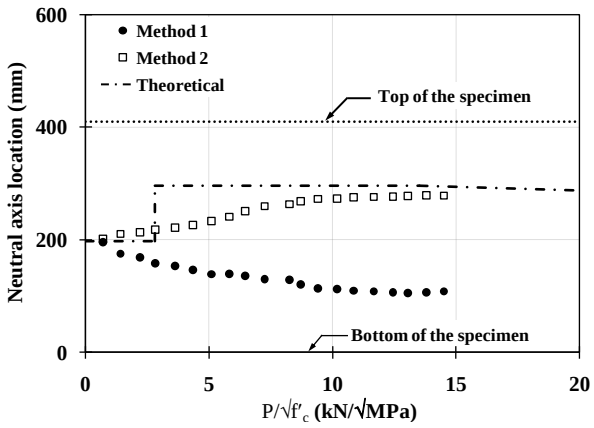

(a)

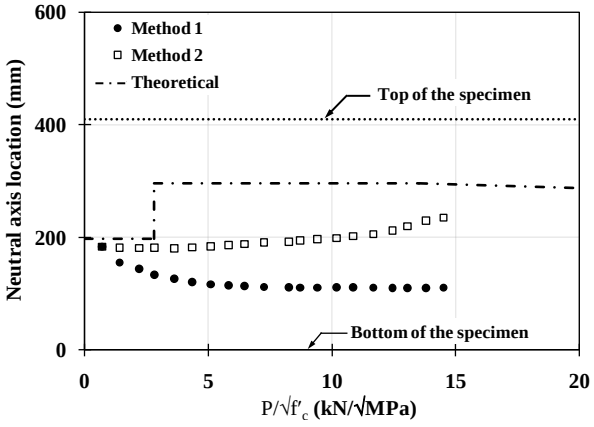

(b)

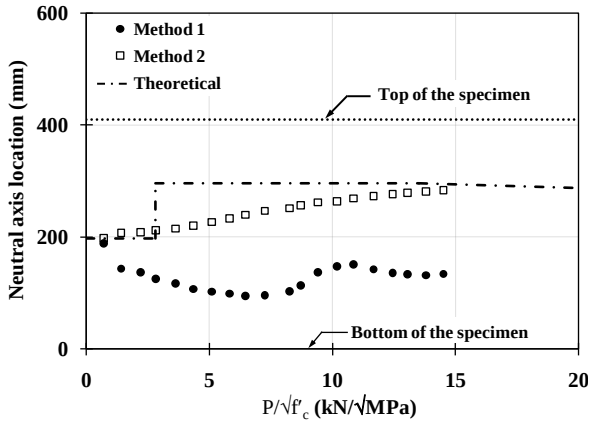

(c)

Figure 5.13. Neutral axis location- Specimen 25-410I: (a) left end of the lap splice length, (b) centreline of the lap splice length, and (c) right of the lap splice length.

Figure 5.13(b) shows that the depth of the neutral axis calculated using Method 2 at the midspan of the lap splice length remained relatively constant for P/P_{max} = 0.05 to 0.35 and then decreased from 225 mm to 175 mm from the top of the section for P/P_{max} = 0.35 to 1.0, respectively. The depth of the neutral axis resulting from this method was higher than the theoretical value as observed for Specimens 25-510I and 25-610I. The depth of the neutral axis calculated using Method 1 increased from 227 mm to 298 mm for P/P_{max} = 0.05 to 0.5, respectively, and then remained relatively constant for P/P_{max} = 0.5 to 1.0.

A comparison of the neutral axis depth calculated using both methods of analysis suggested bond loss within the lap splice length as observed for Specimens 25-510I and 25-610I. The neutral axis location resulting from Method 2 matched well with the theoretical values and suggested that the neutral axis location remained relatively constant within the lap splice length.

Figures 5.14 (a), (b) and (c) show the internal forces at the left end, centreline, and right end of the lap splice length, respectively, for Specimen 25-410I. Figures 5.14(a) and (c) show that the concrete compressive forces calculated using Method 2 were approximately equal to the steel tension force at the ends of the lap splice length, respectively. In contrast, the concrete compressive forces at the ends of the lap splice length calculated using Method 1 were higher than the steel tension forces and suggested that a resultant compressive force existed for the entire loading range. This is an indication of bond loss. Figure 5.14(b) shows that the concrete compressive force at the centreline of the lap splice length calculated using both methods of analysis was not equal to the steel tension and suggested that a resultant compressive force exists. Similar behaviour was observed for Specimens 25-510I and 25-610I and requires further investigation to explain such behaviour.

Figures 5.15(a), (b), and (c) show the comparison of the resultant internal moment with that calculated based on statics at the left end, centreline, and right end of the lap splice

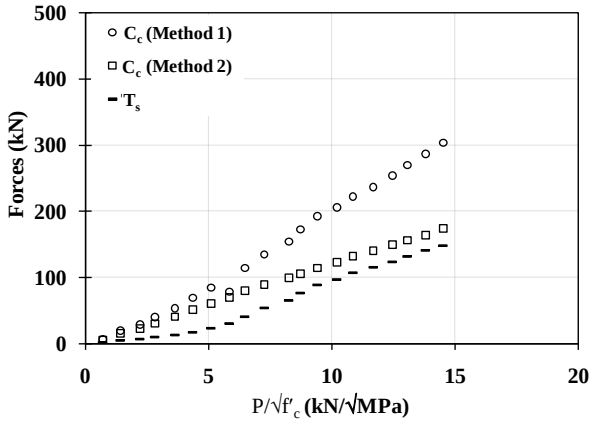

(a)

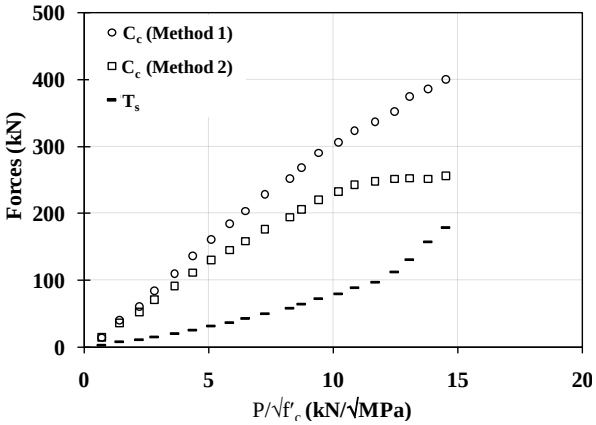

(b)

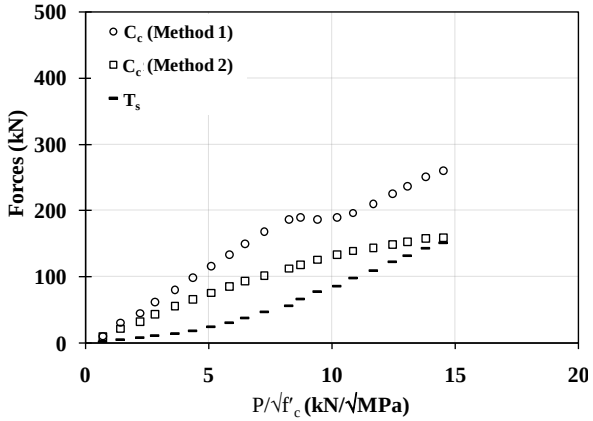

(c)

Figure 5.14. Internal force - Specimen 25-410I: (a) left end of the lap splice length, (b) centreline of the lap splice length, and (c) right of the lap splice length.

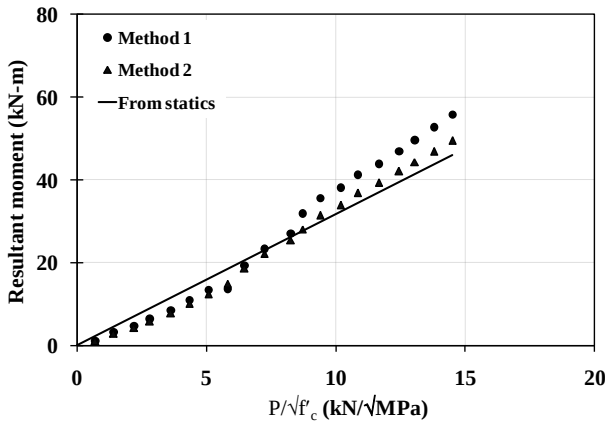

(a)

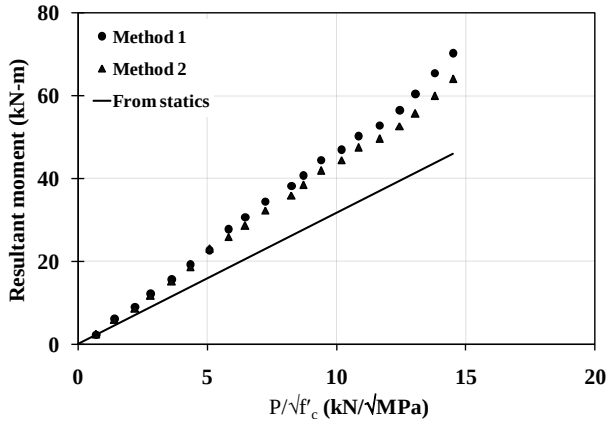

(b)

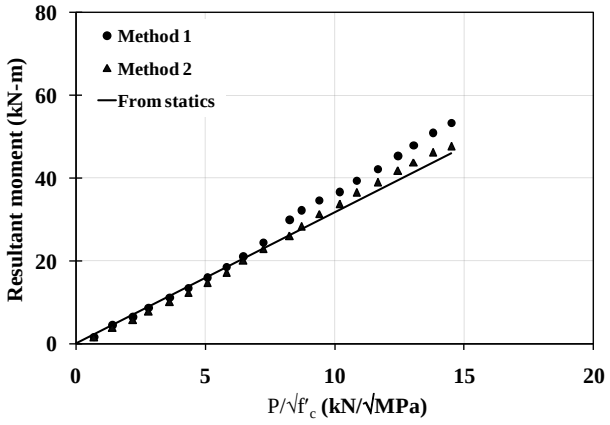

(c)

Figure 5.15. Resultant internal moment - Specimen 25-410I: (a) left end of the lap splice length, (b) centreline of the lap splice length, and (c) right of the lap splice length.

length, respectively, for Specimen 25-410I. Figures 5.15(a) and (c) show that the internal moment at the ends of the lap splice length calculated using both methods were approximately equal to the static moment at all levels of applied load. In contrast, Figure 5.15(b) shows that the internal moment at the centreline of the lap splice length was approximately 1.4 times of that calculated based on statics for the entire loading range. Similar behaviour was observed for Specimen 25-610I.

5.4.5 Summary – Flexural Section Analysis

The flexural section analysis of the instrumented specimens suggested bond loss within the lap splice length. The flexural section analysis resulting from Method 1 deviated from that predicted theoretically as the concrete strain reading at the effective depth of a section was affected by concrete cracking and bond loss. In contrast, the flexural section analysis resulting from Method 2 provided a better prediction of neutral axis locations, internal forces, and resulting internal moments.

The flexural capacity of historical concrete structures reinforced with plain steel bars can be evaluated from the installed strain gauge readings. The flexural capacity of structural elements of historical concrete structures reinforced with plain steel bars can be evaluated from installation concrete strain gauges only as it is not possible to install steel strain gauges on reinforcement post construction. At least three concrete strain gauges should be installed above the approximate neutral axis location as concrete strain readings below the neutral axis were affected by the loss of strain compatibility and concrete cracking. A linear strain distribution at the instrumented sections can be established from a linear regression analysis of as-measured concrete strains. The moment capacity of the existing reinforced concrete structure with plain steel bars can be obtained by calculating the location of the neutral axis and concrete compressive force from the established linear strain distribution.

5.5 Conclusion

The instrumented specimens facilitated the evaluation of the bond behaviour of the plain steel bars along the lap splice length. Strain compatibility within the lap splice length was analyzed and the average bond stress distribution along the lap splice length was reported for all of the instrumented specimens. Results of a flexural section analysis were also presented for all of the instrumented specimens. Bond loss within the lap splice length was evident from: the strain compatibility analysis, reported average bond stress distribution, and flexural section analysis. A method of in-situ instrumentation of historical concrete structures reinforced with plain bars for the purpose of evaluating their flexural capacity was proposed.

Last two sub-objectives of the study, as outlined in Section 1.2, were addressed in Chapter 5. Chapter 6 summarizes the research and restates the major findings of the study.

CHAPTER 6
CONCLUSIONS

6.1 Overview

The current research program was designed to achieve the objectives stated in Chapter 1. Fifteen 4.67 m long splice specimens with a shear span to depth ratio, a/d, approximately equal to 3.94 were tested under monotonically applied four-point loading. The reinforcement ratios were equal to 0.53, 0.95, and 1.51% for specimens longitudinally reinforced with 19 mm, 25 mm and 32 mm diameter bars, respectively. Lap splice lengths ranged from 12.8 to 32.4 times the diameter of the longitudinal reinforcement. Three of the specimens were instrumented with both steel and concrete strain gauges along the lap splice lengths. The following sections summarize the research and restate the major findings of the study.

6.2 Summary of Findings

6.2.1 Bond Capacity as a Function of Tested Parameters

A regression analysis of the test results obtained from the specimens without internal instrumentation was performed and a relationship between the maximum load capacity of the specimens and the tested parameters was derived. It was found that a linear and proportional relationship for maximum load as a function of development length and bar size provides a best fit for the test data.

6.2.2 Comparison of Actual and Predicted Loads

The maximum loads attained by the specimens were compared with the theoretically predicted values and the results reported by others for specimens with identical

geometry reinforced with deformed bars. The following conclusions are drawn from this comparison:

- All but two specimens failed in bond at loads well below those predicted theoretically neglecting strain hardening of the longitudinal reinforcement. A review of the failure behaviour of all specimens, including observed crack patterns and load versus deflection response, confirmed that bond failure occurred in all of the specimens.

- Based upon a limited comparison of two specimens, it appears that splice specimens reinforced with plain steel bars are capable of resisting maximum loads that are approximately 60% of those recorded for similar specimens reinforced with deformed bars with the same nominal diameter.

- Results of an analysis incorporating CEB-FIP Model Code (1993) provisions for the bond stress of plain steel bars underestimate the maximum applied load by 16%, on average for the specimens tested.

6.2.3 Observed Failure Behaviour

The following failure behaviour was observed for the specimens tested:

- Observed crack patterns for the tested specimens showed evidence of bond loss. Cracks in the shear span region remained vertical and therefore did not transform into flexural-shear cracks. Arch action in these specimens is therefore suspected. The formation of a large crack adjacent to one end of the lap splice length at the maximum applied load level was observed for all of the specimens.

- Removal of concrete cover at the ends of the lap splice length following testing revealed end slip of the longitudinal reinforcing bars. All specimens failed due to

pullout of the bars in the lap splice length region as no evidence of longitudinal splitting cracks was observed.

- The load versus deflection behaviour showed no evidence of a load plateau for all specimens tested. Rather, a sudden drop of load with an increase in deflection was observed following the maximum load and indicates that bond failure occurred. The load versus deflection curves for the specimens typically showed a reduction in specimen stiffness compared to the theoretically predicted response and may result from bond loss along the bars within the lap splice length.

6.2.4 Strain Compatibility and Bond Stress Distribution

Three of the specimens were instrumented with steel and concrete strain gauges. The installation of steel strain gauges affected strain compatibility between the longitudinal bars and the surrounding concrete at the location of their installation. However, an analysis of the data obtained provided valuable insight into the strain compatibility and average bond stress distribution within the lap splice length and leads to following conclusions:

- A strain compatibility analysis for the instrumented specimens suggests that perfect bond between the longitudinal reinforcement and the surrounding concrete did not exist for much of the load range.

- A review of the steel strain gauge data along the lap splice length suggests that the magnitude of steel strain is a function of the development length available at instrumented locations.

- The calculated average bond stress distribution along the lap splice length becomes uniform as bond loss adjacent to the loaded end of the lap splice length occurs and poses a higher bond demand in the central region of the lap splice length.

6.2.5 Flexural Section Analysis

A flexural section analysis at different sections along the lap splice length was performed based on the as-measured concrete and steel strains. The results of the flexural section analysis confirm bond loss within the lap splice length. A flexural section analysis based on the two concrete strains above the neutral axis and the steel strain gauge on the longitudinal reinforcement provides a reasonable prediction of the flexural capacity of the specimens. A method to evaluate the flexural capacity of the historical reinforced concrete structures with plain steel bars was also proposed.

6.3 Recommendations for Future Work

The current research program provides valuable insight into the bond failure behaviour of splice specimens longitudinally reinforced with plain steel bars. An expansion of the current research program is required to complete a full parametric study of factors affecting the bond and development of plain steel reinforcing bars. The following are the recommendations for future research related to this study:

- A limited number of splice specimens were tested in the current study to investigate the variation of bond capacity of plain steel bars as a function of splice length and bar size. Square plain steel bars were used in historical concrete structures and should therefore be tested to investigate the effects of bar shape on bond capacity of plain steel bars. Testing of splice specimens with top cast plain round and square steel bars should also be included in future investigation to assess its effects on bond capacity of plain steel bars. The effects of transverse reinforcement on bond of plain steel bars should also be investigated.

- Cyclic and repeated load tests should be conducted to the capture the bond behaviour of longitudinal plain steel bars under repeated service loads.

- Deflection measurements provided by the LVDTs at the ends and quarter points of the lap splice length were affected by crack development at these locations. The

installation of additional LVDTs outside the lap splice length within the constant moment region and shear spans is recommended to better capture the deflection profile of the specimens.

- Instrumented specimens tested in the current study provided valuable insight into strain compatibility within the lap splice length. Future studies should also include instrumentation such that a similar analysis within the shear spans may also be captured. The installation of concrete strain gauges on both sides of the specimens is also recommended as cracking may differ and affect strain readings.

- Future research on bond of plain steel bars should include steel bars with a lower yield strength to represent historical plain steel bars manufactured before 1970.

- The flexural capacity of the existing concrete structures with plain steel bars can be evaluated using readings from installed concrete strain gauges and as measured properties of the concrete. Three or more concrete strain gauges can be installed above the theoretically approximated neutral axis location. The flexural capacity of historical structures then can be reasonably evaluated considering a linear concrete strain distribution using the resulting gauge data.

REFERENCES

Abrams, D.A. 1913. Tests of Bond Between Concrete and Steel. University of Illinois Bulletin No. 71, University of Illinois, Urbana, IL.

Aly, R., Benmokrane, B., and Ebead, U. 2006. Tensile Lap Splicing of Fibre-Reinforced Polymer Reinforcing Bars in Concrete. ACI Structural Journal, **103**(6): 857-864.

American Association of State and Highway Transportation Officials. 2009. AASHTO LRFD Bridge Design Specifications. American Association of State Highway and Transportation Officials, Washington, D.C.

ACI. 1920. Standard Specifications No. 23: Standard Building Regulations for the Use of Reinforced Concrete. American Concrete Institute, Detroit, MI.

ACI Committee 318. 1963. Building Code Requirements for Reinforced Concrete (ACI 318-63). American Concrete Institute, Farmington Hills, MI.

ACI Committee 318. 1971. Building Code Requirements for Reinforced Concrete (ACI 318-71). American Concrete Institute, Farmington Hills, MI.

ACI Committee 318. 1995. Building Code Requirements for Structural Concrete (ACI 318-95) and Commentary (ACI 31R-95). American Concrete Institute, Farmington Hills, MI.

ACI Committee 318. 2008. Building Code Requirements for Structural Concrete and Commentary. American Concrete Institute, Farmington Hills, MI.

ACI Committee 408. 1966. Bond Stress – The State of the Art. Journal of the American Concrete Institute, **63**(11):1161-1188.

ACI Committee 408. 2003. Bond and Development of Straight Reinforcing Bars in Tension. American Concrete Institute, Farmington Hills, MI.

ASTM A944. 2005. Standard Test Method for Comparing Bond Strength of Steel Reinforcing Bars to Concrete Using Beam-End Specimens. ASTM International. West Conshohocken, PA, USA. doi: 10.1520/A0944-05.

ASTM A1035M. 2009. Standard Specifications for Deformed and Plain, Low-Carbon, Chromium, Steel Bars for Concrete Reinforcement. ASTM International. West Conshohocken, PA, USA. doi: 10.1520/A1035_A1035M-09.

ASTM A370. 2008. Standard Test Methods and Definitions for Mechanical Testing of Steel Products. ASTM International. West Conshohocken, PA, USA. doi: 10.1520/A0370-08

Arrien, P., Bastien, J., and Beaulieu, D. 2001. Rehabilitation of Bridges Using Aluminum Decks. Canadian Journal of Civil Engineering, **28**:992-1002.

Baldwin, M.I. and Clark, L.A. 1995. The Assessment of Reinforcing Bars with Inadequate Anchorage, Magazine of Concrete Research, **47**(171): 95-102.

Barnes, R.W., Burns, N.H., and Kreger, M.E. 2000. Development Length of 0.6-Inch Prestressing Strands in Standard I-Shaped Pretensioned Concrete Beams. Research Report 1388-1, Center for Transportation Research, University of Texas at Austin, Austin, Texas, USA.

Bischoff, P.H. 2005. Reevaluation of Deflection Prediction for Concrete Beams Reinforced with Steel and Fibre Reinforced Polymer Bars. Journal of Structural Engineering, ASCE, **131**(5): 752-767.

Bischoff, P.H. and Johnson, R.D. 2007. Effect of Shrinkage on Short-Term Deflection of Reinforced Beam and Slabs. ACI SP 246 Structural Implications of Shrinkage and Creep of Concrete. American Concrete Institute, Farmington Hills, MI, USA, SP 246: 167-180.

Bischoff, P.H. and Johnson, R.D. 2008. Effect of Bond and Cracking on Serviceability Related Behaviour of Concrete Beams Reinforced with Plain (Undeformed) Reinforcing Bars. In the Proceedings of the 37th Annual Conference, Quebec, QC, 10-13 June 2008, Canadian Society for Civil Engineering, QC, Canada, (8 pp. paper in CD-ROM).

Bischoff, P.H. and Scanlon, A. 2007. Effective Moment of Inertia for Calculating Deflections of Concrete Members Containing Steel Reinforcement and Fibre-Reinforced Polymer Reinforcement. ACI Structural Journal, **104**(1): 68-75.

Branson, D.E. 1963. Instantaneous and Time-Dependent Deflections of Simple and Continuous Reinforced Concrete Beams. Report No. 7, Alabama Highway Research Report, Bureau of Public Roads, Montgomery, Ala., USA.

CISC. 2006. Handbook of Steel Construction. 9th Edition, Canadian Institute of Steel Construction, Toronto, Ontario.

Canadian Engineering Standards Association. 1929. Standard Specification for Concrete and Reinforced Concrete. Canadian Engineering Standards Association, Ottawa, Ontario.

CSA. 2000. A23.1-00/A23.2-00: Concrete Materials and Methods of Concrete Construction/Methods of Tests for Concrete. Canadian Standards Association, Toronto, Ontario.

CSA. 2004a. CSA Standard A23.3-2004 - Design of Concrete Structures. Canadian Standards Association, Mississauga, Ontario.

CSA. 2004b. CAN/CSA-G40.20-04/G40.21-04-General Requirements for Rolled or Welded Structural Quality Steel/ Structural Quality Steel. Canadian Standards Association, Mississauga, Ontario.

CSA. 2006. CAN/CSA-S6-2006 - Canadian Highway Bridge Design Code. Canadian Standards Association, Mississauga, Ontario.

CEB-FIP. 1993. CEB-FIP Model Code (1993). Comité Euro-Internationale du Béton (CEB), Thomas Telford Ltd., London.

Chamberlin, S. J. 1952. Spacing of Spliced Bars in Tension Pull-Out Specimens. Journal of the American Concrete Institute, **49**(12): 261-274.

Chinn, J., Ferguson, P.M., and Thompson, J.N. 1955. Lapped Splices in Reinforced Concrete Beams. Journal of the American Concrete Institute, **52**(10): 201-213.

Erlemann, G.G. 1999. Steel Reinforcing Bar Specifications in Old Structures. Concrete International, **21**(4): 49-50.

Feldman, L.R., MacFarlane, D.C., Kroman, J.A., and Bartlett, F.M. 2003. Construction Staging of the Centre Street Bridge Rehabilitation to Accommodate Emergency Vehicle Traffic. In Proceedings of the 31st Annual Conference of the Canadian

Society for Civil Engineering, Moncton, Nouveau-Brunswick, 4-7 June 2003, Canadian Society for Civil Engineers, 10 pp. (CD-ROM).

Feldman, L.R. and Bartlett, F.M. 2004. Design of a Testing Program for Bond of Plain Reinforcement. In the Proceedings of 5th International PhD Symposium in Civil Engineering, June 16-19, Delft, The Netherlands.

Feldman, L.R. and Bartlett, F.M. 2005. Bond Strength Variability in Pullout Specimens with Plain Reinforcement. ACI Structural Journal, **102**(6): 860-867.

Feldman, L.R. and Bartlett, F.M. 2007. Bond Stresses Along Plain Steel Reinforcing Bars in Pullout Specimens. ACI Structures Journal, **104**(6): 685-692.

Feldman, L.R. and Bartlett, F.M. 2008. Bond in Flexural Members with Plain Steel Reinforcement. ACI Structural Journal, **105**(5): 552-560.

Gilkey, H.J. and Ernst, G. C. 1936. Pullout Tests for Bond Resistance of High Elastic Limit Steel Bars. Proceedings of the Highway Research Board, **16**:82-95.

Gilkey, H.J., Chamberlin, S.J., and Beal, R.W. 1937. Bond Resistance of High Elastic Limit Steel Bars, Series of 1937. Proceedings of the Highway Research Board, **17**:149-186.

Gilkey, H.J., Chamberlin, S.J., and Beal, R.W. 1938. The Bond Between Concrete and Steel. Journal of the American Concrete Institute, **35**(9): 1-20.

Idun, E.K. and Darwin, D. 1995. Improving the Development Characteristics of Steel Reinforcing Bars. SM Report No. 41, University of Kansas Center for Research, Lawrence, Kansas, USA.

ISIS. 2007. Reinforcing Concrete Structures with Fibre Reinforced Polymers: Design Manual No. 3. ISIS Canada Network of Centres of Excellence, Winnipeg, Canada.

Kankam, C. K. 1997. Relationship of Bond Stress, Steel Stress, and Slip in Reinforced Concrete. Journal of Structural Engineering, ASCE, **123**(1): 79-85.

Kim, W. 1987. Shear-Critical Cracks in Reinforced Concrete Beams Without Web Reinforcement: Their Initiation and Propagation. PhD Thesis, Structural Engineering Department, Cornell University, Ithaca, New York, USA.

Kim, W. and White, R.N. 1999. Hypothesis for Localized Horizontal Shearing Failure Mechanism of Slender RC Beams. Journal of Structural Engineering, ASCE, **125**(10): 1126-1135.

Leonhardt, F. and Walther, R. 1962. The Stuttgart Shear Tests, 1961 Contributions to the Treatment of the Problems of Shear in Reinforced Concrete Construction. Cement and Concrete Association, London, UK.

Loov, R.E. 1991. Reinforced Concrete at the Turn of the Century. Concrete International, **13**(12): 67-73.

Lounis, Z. 2007. Aging Highway Bridges. Canadian Consulting Engineers, **48**(1): 30-34.

Lukose, K., Gergely, P., and White, R.N. 1982. Behaviour of Reinforced Concrete Lapped Splices for Inelastic Cyclic Loading. Proceedings of American Concrete Institute, **79**(5): 355-365.

Lutz, L.A. and Gergely, P. 1967. Mechanics of Bond and Slip of Deformed Bars in Concrete. Journal of the American Concrete Institute, **64**(11): 711-721.

MacGregor, J.G. and Bartlett, F.M. 2000. Reinforced Concrete: Mechanisms and Design (Canadian Edition), Prentice-Hall Canada Inc., Scarborough, Ontario, Canada.

Mylrea, T.D. 1948. Bond and Anchorage. Journal of the American Concrete Institute, **44**(3): 521-552.

Nilson, A.H. 1971. Bond Stress-Slip Relations in Reinforced Concrete. Research Report No 345. Department of Structural Engineering, Cornell University, Ithaca, NY, USA.

Orangun, C.O., Jirsa, J.O., and Breen, J.E. 1977. A Reevaluation of Test Data on Development Length and Splices. Journal of the American Concrete Institute, **74**(3): 114-122.

Park, R. and Paulay, T. 1975. Reinforced Concrete Structures, John Wiley & Sons Inc., New York, NY, USA.

Perry, E.S. and Jundi, N. 1969. Pullout Bond Stress Distribution Under Static and Dynamic Repeated Loadings. Journal of the American Concrete Institute, **66**(5): 377-380.

Rao, N.R.M., Lohrmann, M., and Tall, L. 1966. Effects of Strain Rate on the Yield Stress of Structural Steels. ASTM Journal of Materials, **1**(1): 241-262.

Rehm, G. and Eligehausen, R. 1979. Bond of Ribbed Bars Under High Cycle Repeated Loads. Proceedings of the American Concrete Institute, **76**(2): 297-309.

Stewart, M. G. and Val, D. V. 1999. Role of Load History in Reliability-Based Decision Analysis of Aging Bridges. Journal of Structural Engineering, ASCE, **125**(7):776-783.

Wernisch, G.R. 1937. Bond Studies of Different Types of Reinforcing Bars. Journal of the American Concrete Institute, **34**(11): 145-164.

Winter, G. 1982. Development of a National Building Code for Reinforced Concrete. Concrete International, **4**(12): 27-37.

Zwicky, D. and Vogel, T. 2006. Critical Inclination of Compression Struts in Concrete Beams. Journal of Structural Engineering, **132**(5): 686 – 693.

APPENDIX 3A: Minimum Splice Length as per CEB-FIP Model Code (1993)

The CEB-FIP Model Code (1993) was used as a guideline to predict the minimum lap splice lengths required for yielding of the longitudinal reinforcement in the specimens and for the maximum applied load for the specimens tested in the current research program, as it provides provisions for the design bond stress for plain reinforcing steel bars, u_d:

$$u_d = \eta_1 \eta_2 \eta_3 f_{ctd} \qquad [3A.1]$$

where f_{ctd} is the design value of concrete tensile strength; η_1 is a factor addressing reinforcement type; η_2 accounts for bond conditions including bar inclination, top bar effect, and the formwork system used; and η_3 accounts for bar size. The CEB-FIP Model Code (1993) equation suggests that the bond of plain bars is 44% of the deformed bars when all other parameters are held constant.

The CEB-FIP Model Code (1993) limits the design value of tensile strength of concrete, f_{ctd}, to two third of the minimum characteristic tensile strength of concrete, $f_{ctk,min}$, to provide a factor of safety against bond failure. Equation 3A.1 was modified to obtain the average value of bond stress, u_{avg}, by replacing f_{ctd} with the mean value of concrete tensile strength, f_{ctm}:

$$u_{avg} = \eta_1 \eta_2 \eta_3 f_{ctm} \qquad [3A.1a]$$

The mean value of concrete tensile strength, f_{ctm}, can be calculated as (CEB-FIP 1993):

$$f_{ctm} = 1.4 \left[\frac{f_{ck}}{10} \right]^{2/3} \qquad [3A.2]$$

where, f_{ck} is the characteristic compressive strength which represents the strength that was determined using the 95% confidence limit. The characteristic compressive strength of concrete, f_{ck}, was considered equal to the specified compressive strength of the concrete, f'_c, to predict the minimum splice length required to yield the reinforcing steel and for the maximum applied load for the specimens tested in the current study.

The CEB-FIP Model Code (1993) states that bond parameters η_1, η_2, and η_3 are all equal to unity for the case of bottom cast plain steel bars with diameters of 19 mm, 25 mm and 32 mm. The average tensile strength, f_{ctm}, is 2.22 MPa from Equation 3A.2 for f'_c = 20 MPa. Equation 3A.1a results in an average bond stress for bottom cast plain steel bars of 2.22 MPa as it is independent of the longitudinal bar diameter within the range used in the test specimens.

The minimum lap length required to develop yielding of the longitudinal tension steel can be determined using following equation (CEB-FIP Model Code 1993):

$$L_s = \frac{d_b f_y}{4 u_{avg}} \qquad [3A.4]$$

where f_y is the nominal yield strength of the longitudinal reinforcement in MPa, and d_b is the diameter of the plain bars in mm. The minimum lap length required to attain yielding of plain steel bars with diameters equal to 19 mm, 25 mm and 32 mm and a nominal yield strength of 300 MPa is 640 mm, 840 mm and 1080 mm, respectively.

The steel stress that can be developed in a specimen with a specific bar size and lap splice length can be found by rearranging Equation 3A.4:

$$f_s = 4 u_{avg} \frac{L_s}{d_b} \qquad [3A.4a]$$

The load carrying capacity of a specimen can then be determined theoretically using the steel stress obtained from the Equation 3A.4a. Details of the calculation procedure are presented in Section 4.3.1.

APPENDIX 4A: Concrete Companion Specimens

The concrete compressive strength, f'_c, modulus of elasticity, E_c, and stress-strain relationship were obtained from testing 75 mm diameter by 100 mm long concrete companion cylinders with the construction and testing methods discussed in Section 3.4.1. Three companion cylinders were tested for each day of specimen testing. Each set of companion specimen tests is therefore representative of the material properties in one of two splice specimens. The concrete companion cylinder test results are summarized in Table 4A.1. Plots of the stress, f_c, versus strain, ε_c, curve are also presented in Figures 4A.1 to 4A.24. The average stress-strain curve obtained for each set companion cylinders and the fit of the curve obtained from the regression analysis are also presented.

Table 4A.1: Concrete companion cylinder test results

Companion cylinder*	Age at Test Date (Days)	Compressive Strength f'_c (MPa)	Strain at f'_c ε_o	Modulus of Elasticity E_c (MPa)	Specimen
C-1-1	126	23.9	0.00187	23200	25-410
C-1-2		23.4	0.00177	27100	
C-1-3		23.9	0.00178	25500	
C-1-4	129	24.9	0.00192	24700	25-510
C-1-5		22.9	0.00172	23800	
C-1.6		23.5	0.00182	26100	
C-1-7	119	23.9	0.00208	24000	25-610
C-1-8		21.0	0.00160	23900	
C-1-9		23.4	0.00175	23600	
C-2-1	52	16.1	0.00258	15700	19-305 and 19-410
C-2-2		17.6	0.00210	20500	
C-2-3		18.5	0.00223	20200	
C-2-4	49	18.0	0.00228	19200	19-510
C-2-5		17.6	0.00233	28000	
C-2-6		20.5	0.00250	20800	
C-2-7	50	19.5	0.00300	18200	32-410 and 32-610
C-2-8		20.0	0.00310	18600	
C-2-9		20.0	0.00230	20300	
C-2-10	38	15.6	0.00170	23500	32-810
C-2-11		16.1	0.00320	16000	
C-2-12		15.6	0.00160	19900	
C-3-1	55	19.5	0.00150	24500	19-610
C-3-2		22.0	0.00190	24200	
C-3-3		21.5	0.00240	21400	
C-3-4		20.0	0.00180	20000	25-810
C-3-5		19.0	0.00200	20900	
C-3-6		18.5	0.00170	19900	
C-3-7	36	19.5	0.00180	21900	32-910
C-3-8		20.5	0.00170	21300	
C3-9		19.0	0.00150	20500	
C-3-10	77	22.4	0.00175	26000	25-410I and 25-610I
C-3-11		21.0	0.00200	20300	
C-3-12		21.0	0.00190	26200	
C-3-13	78	20.5	0.00200	22300	25-510I
C-3-14		19.5	0.00160	22700	
C-3-15		22.4	0.00220	25600	

* "C" in the companion cylinder designation refers to concrete, the first number refers to the concrete batch number and the second number refers to the cylinder serial number.

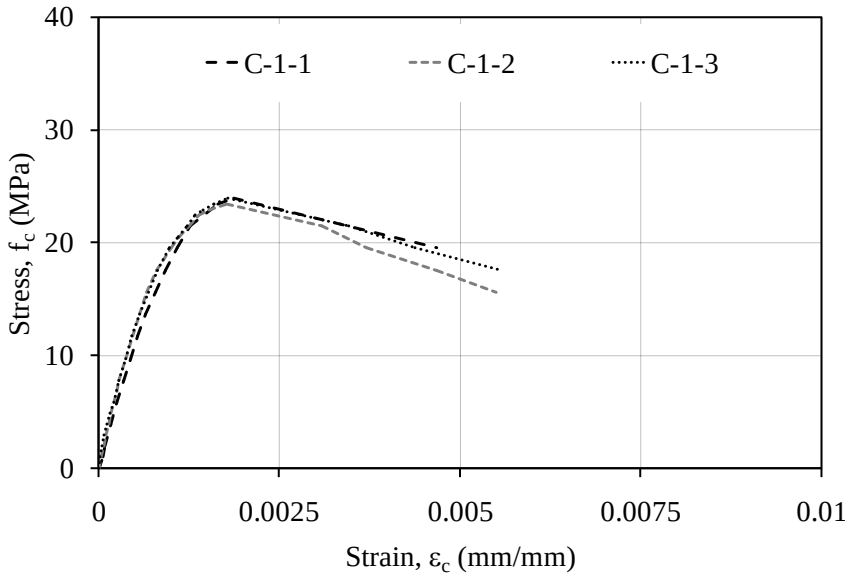

Figure 4A.1: Stress versus strain – Concrete companion cylinder results corresponding to Specimen 25-410.

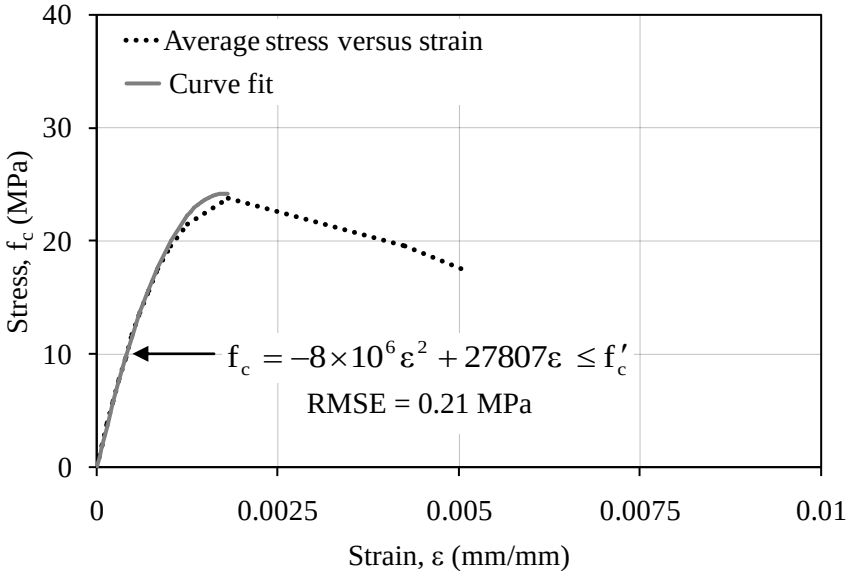

Figure 4A.2. Average stress versus strain - Concrete companion cylinder results corresponding to Specimen 25-410.

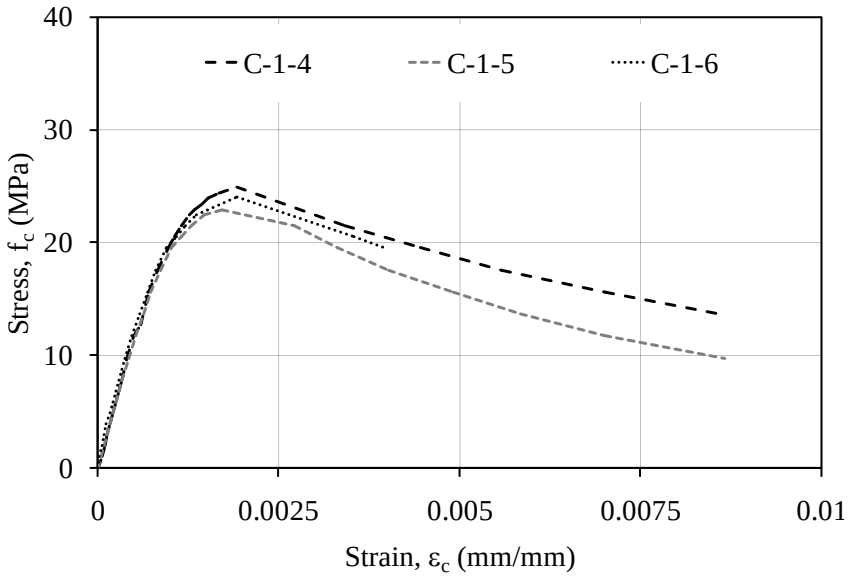

Figure 4A.3: Stress versus strain – Concrete companion cylinder results corresponding to Specimen 25-510.

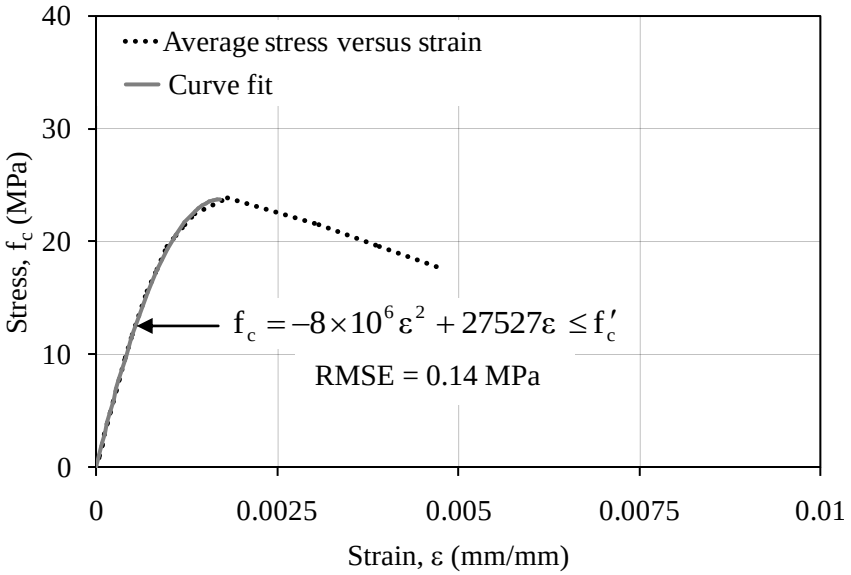

Figure 4A.4. Average stress versus strain - Concrete companion cylinder results corresponding to Specimen 25-510.

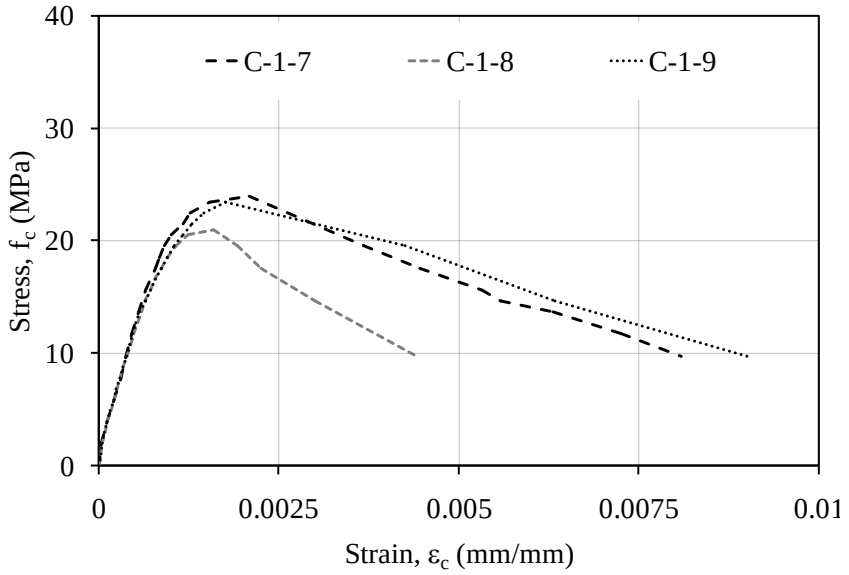

Figure 4A.5: Stress versus strain – Concrete companion cylinder results corresponding to Specimen 25-610.

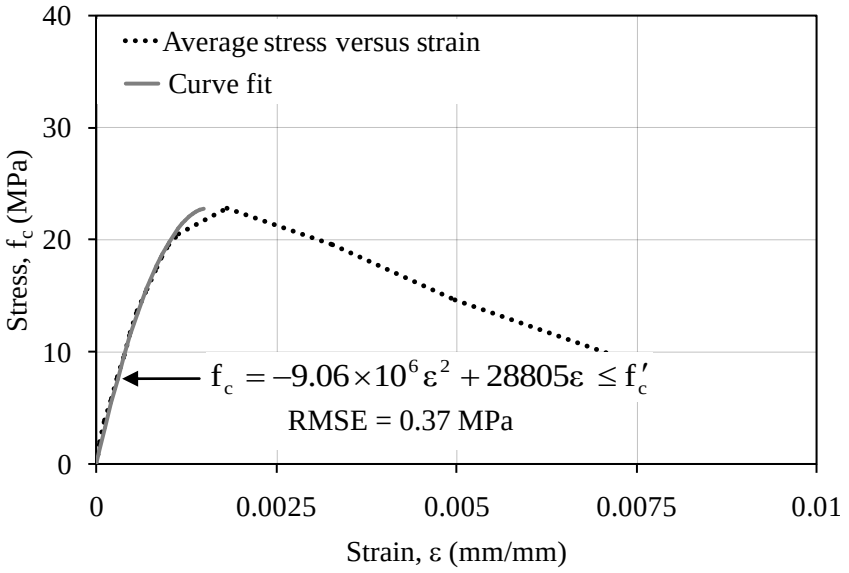

Figure 4A.6. Average stress versus strain - Concrete companion cylinder results corresponding to Specimen 25-610.

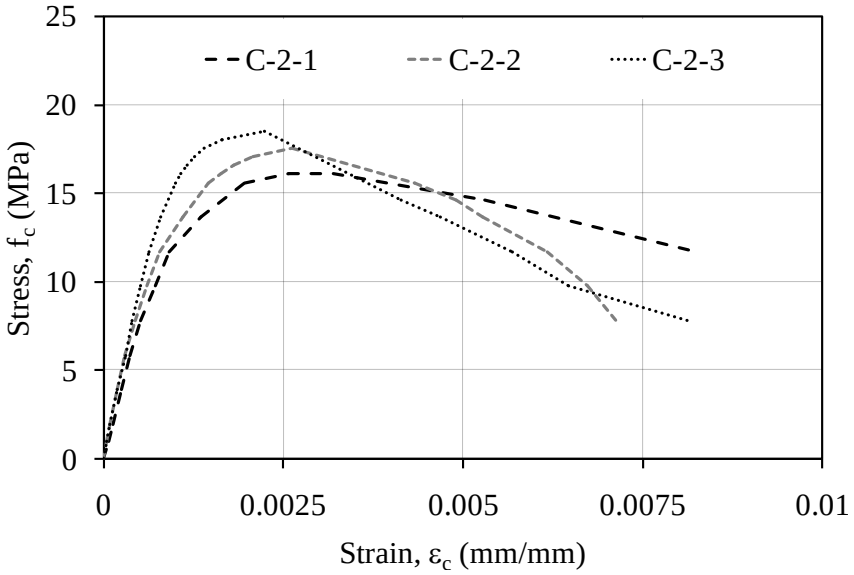

Figure 4A.7: Stress versus strain – Concrete companion cylinder results corresponding to Specimens 19-305 and 19-410.

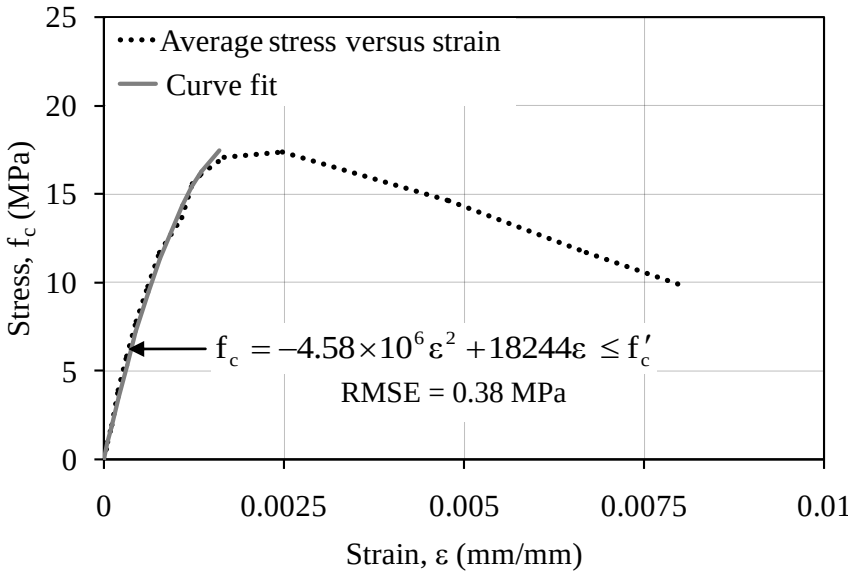

Figure 4A.8. Average stress versus strain - Concrete companion cylinder results corresponding to Specimens 19-305 and 19-410.

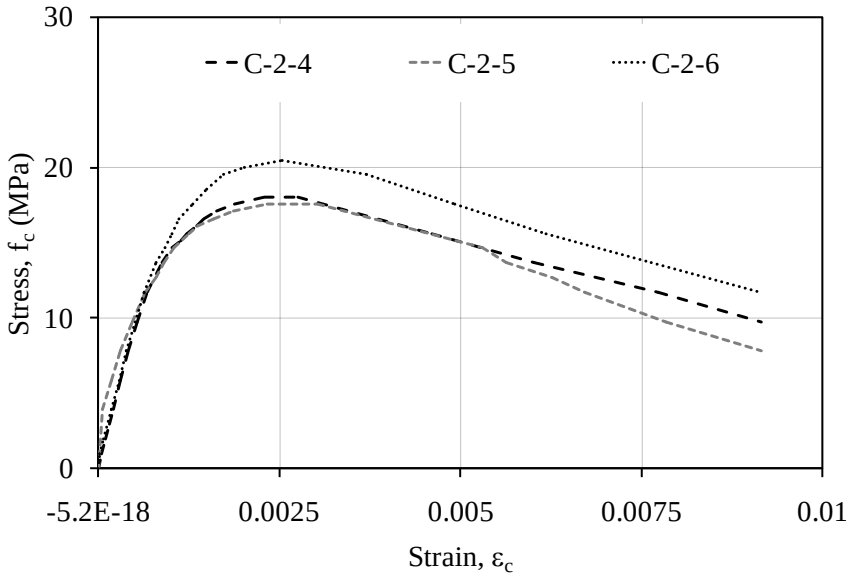

Figure 4A.9: Stress versus strain – Concrete companion cylinder results corresponding to Specimen 19-510.

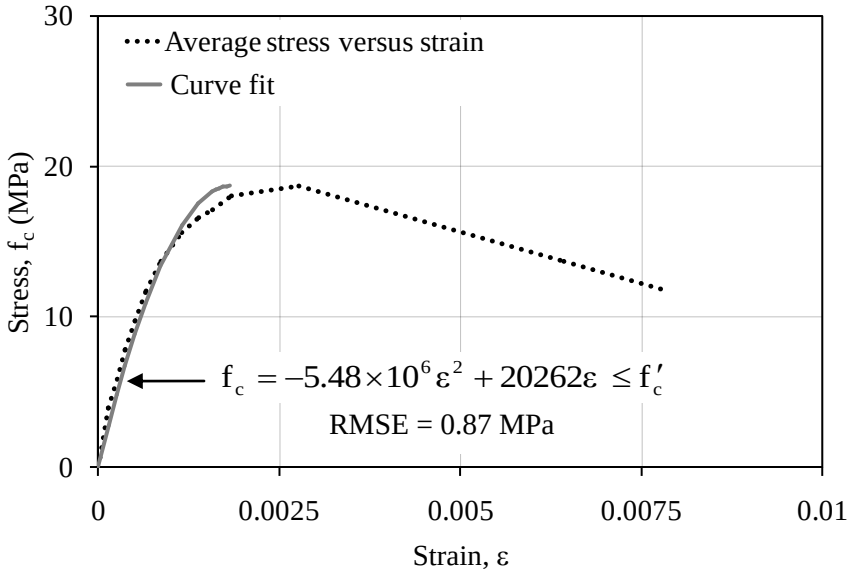

Figure 4A.10. Average stress versus strain - Concrete companion cylinder results corresponding to Specimen 19-510.

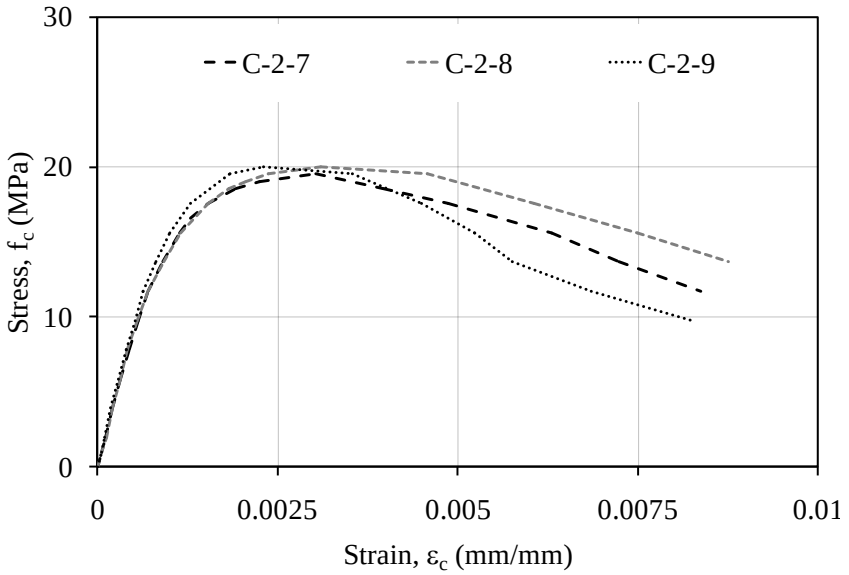

Figure 4A.11: Stress versus strain – Concrete companion cylinder results corresponding to Specimens 32-410 and 32-610.

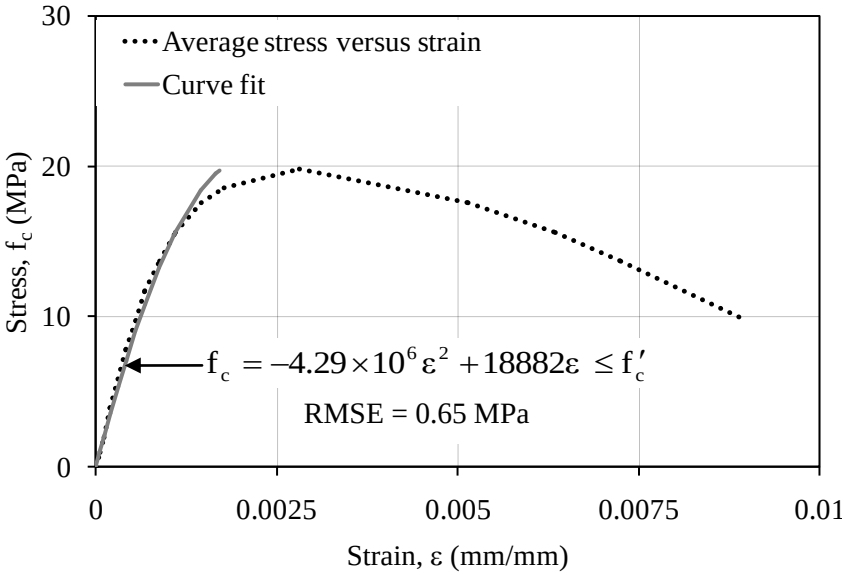

Figure 4A.12. Average stress versus strain - Concrete companion cylinder results corresponding to Specimens 32-410 and 32-610.

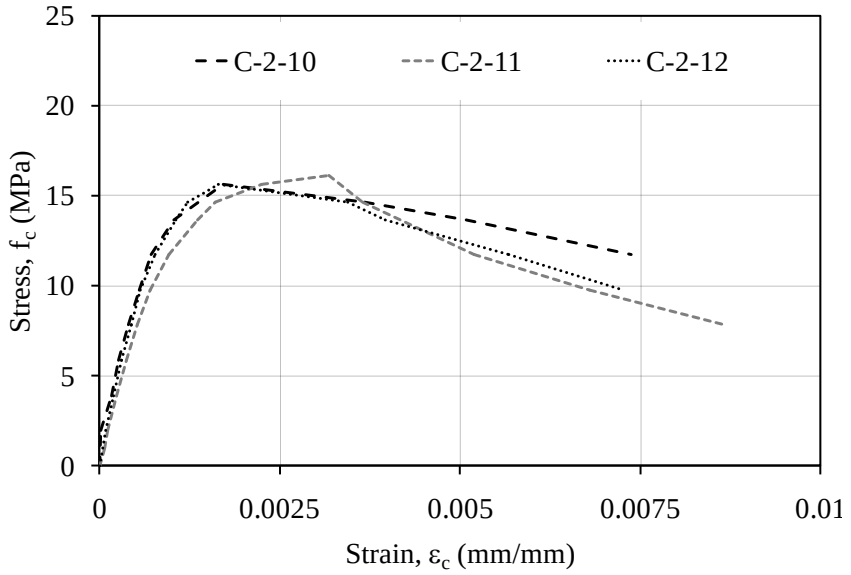

Figure 4A.13: Stress versus strain – Concrete companion cylinder results corresponding to Specimen 32-810.

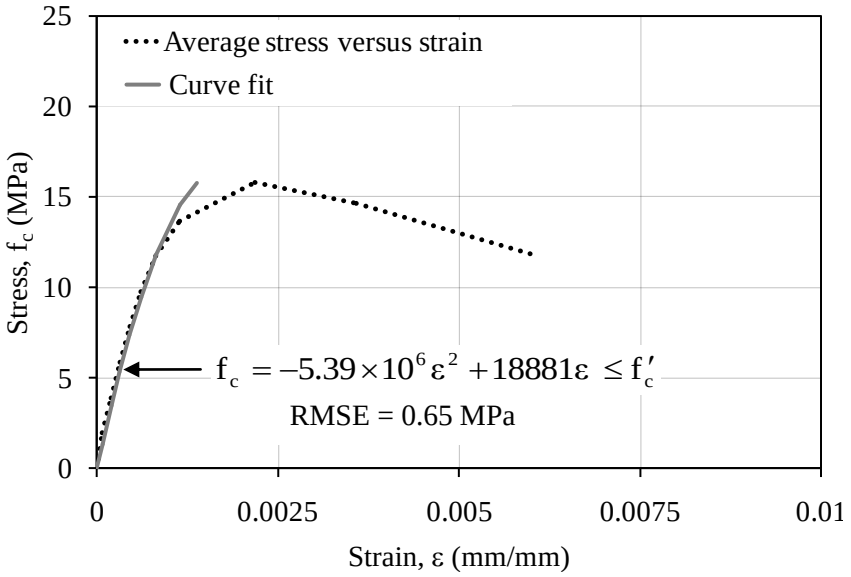

Figure 4A.14. Average stress versus strain - Concrete companion cylinder results corresponding to Specimen 32-810.

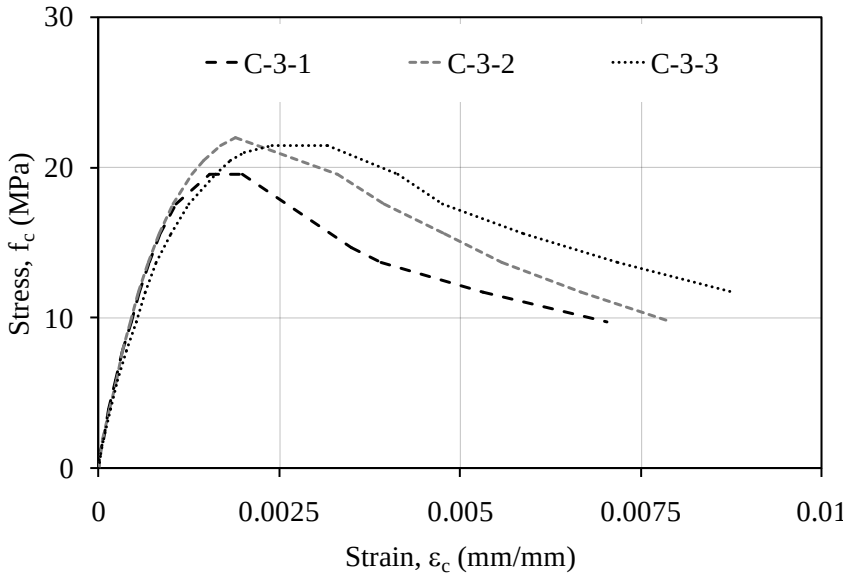

Figure 4A.15: Stress versus strain – Concrete companion cylinder results corresponding to Specimen 19-610.

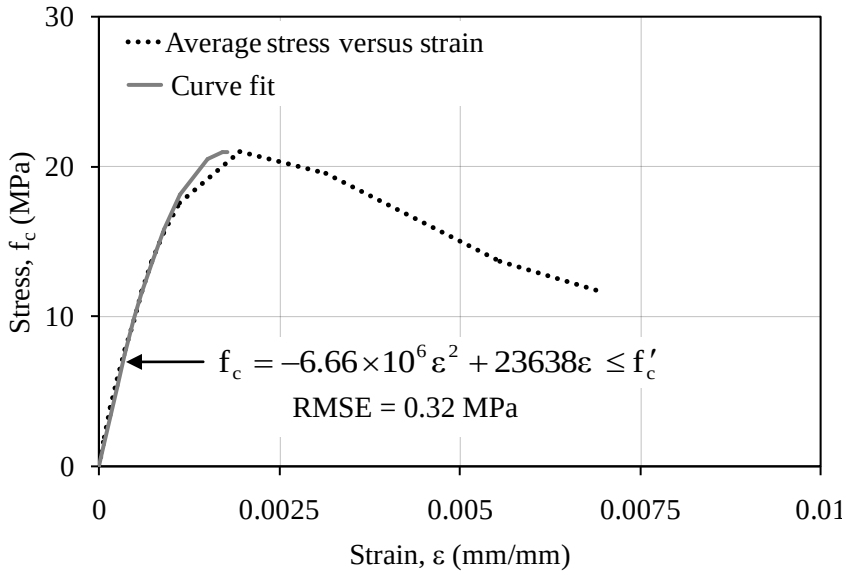

Figure 4A.16. Average stress versus strain - Concrete companion cylinder results corresponding to Specimen 19-610.

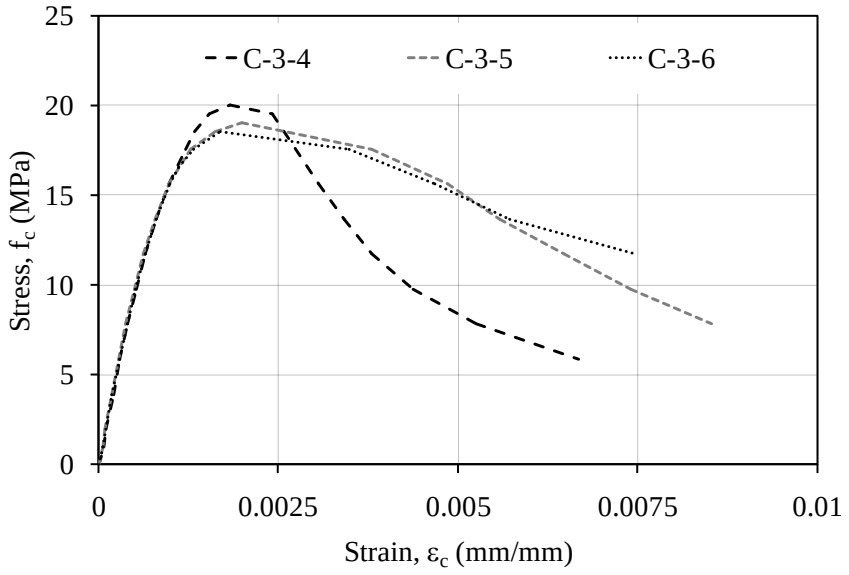

Figure 4A.17: Stress versus strain – Concrete companion cylinder results corresponding to Specimen 25-810.

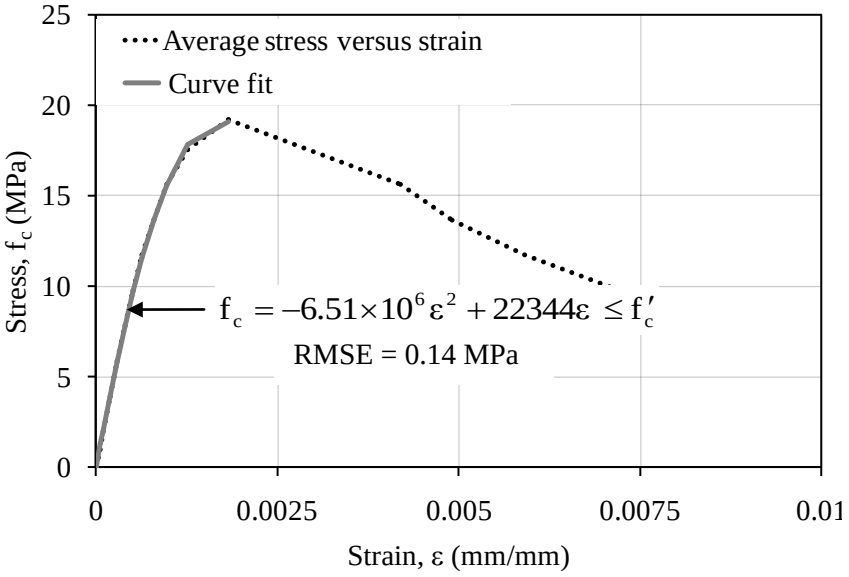

Figure 4A.18. Average stress versus strain - Concrete companion cylinder results corresponding to Specimen 25-810.

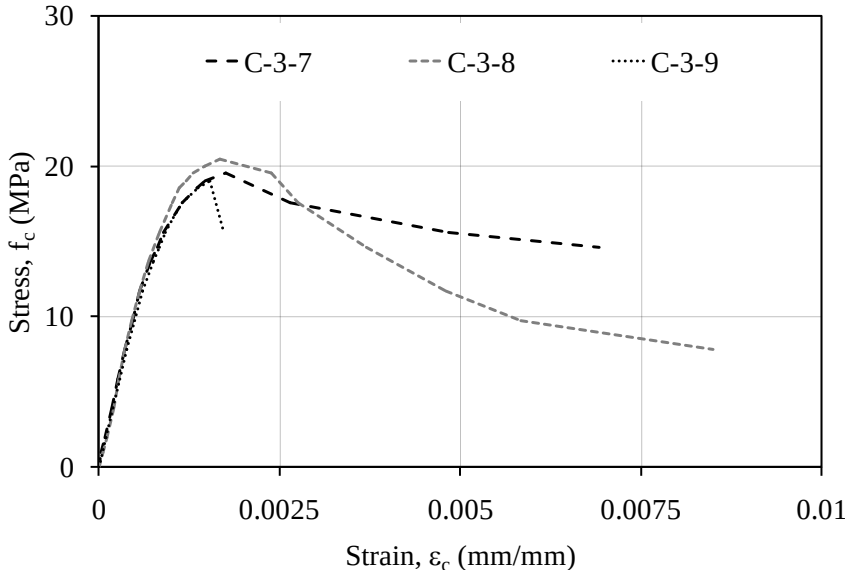

Figure 4A.19: Stress versus strain – Concrete companion cylinder results corresponding to Specimen 32-910.

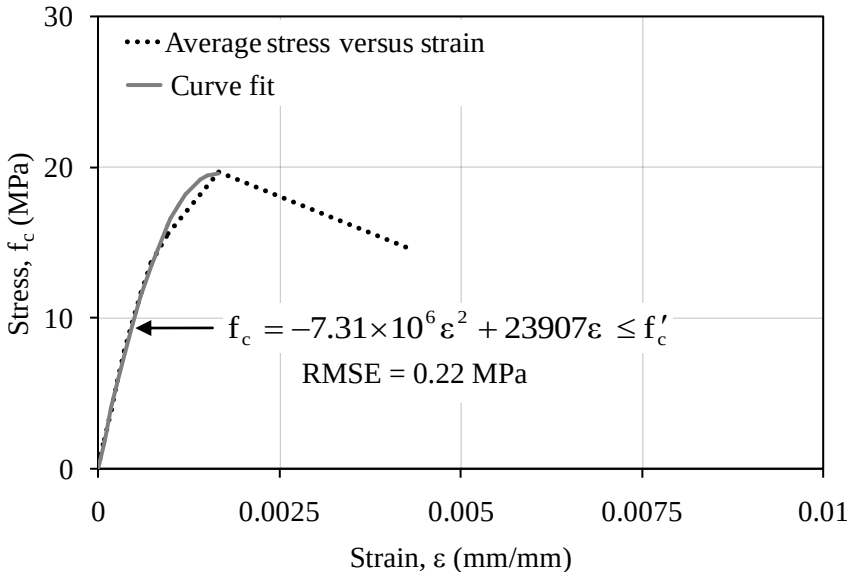

Figure 4A.20. Average stress versus strain - Concrete companion cylinder results corresponding to Specimen 32-910.

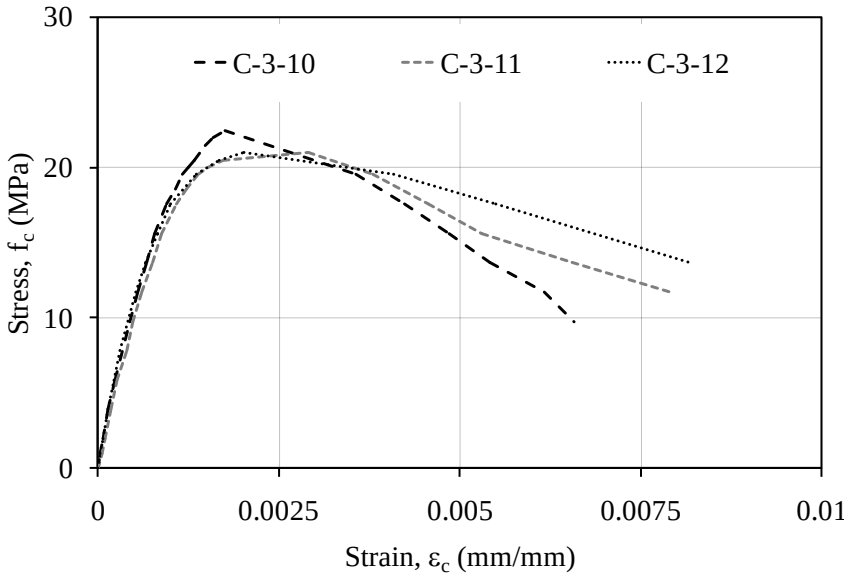

Figure 4A.21: Stress versus strain – Concrete companion cylinder results corresponding to Specimens 25-410I and 25-610I.

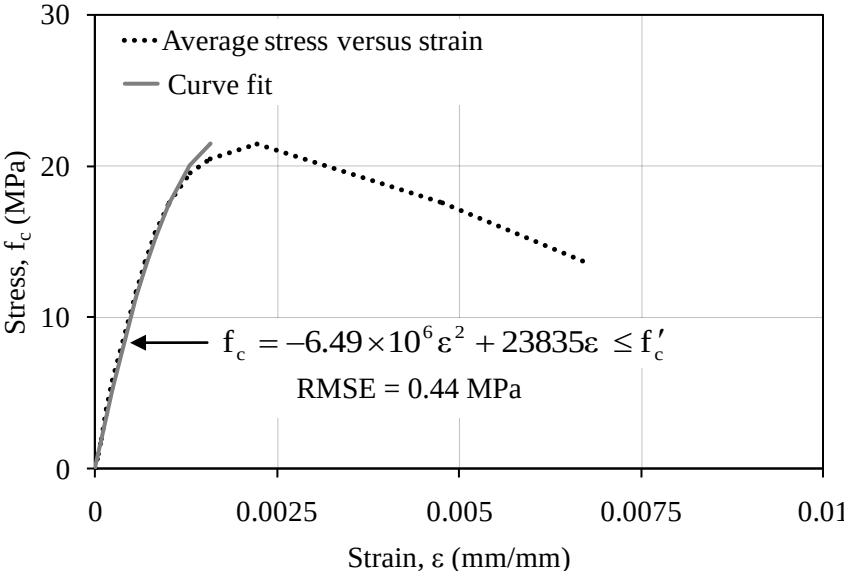

Figure 4A.22. Average stress versus strain - Concrete companion cylinder results corresponding to Specimens 25-410I and 25-610I.

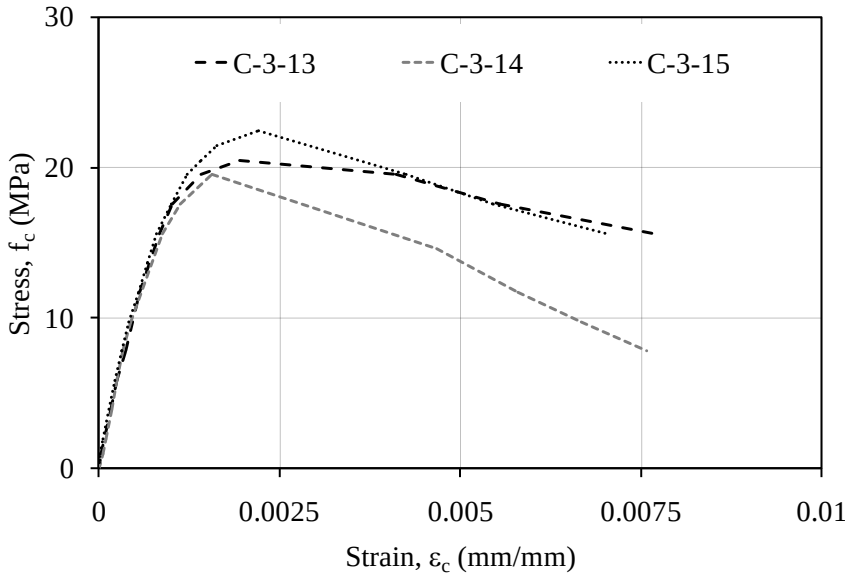

Figure 4A.23: Stress versus strain – Concrete companion cylinder results corresponding to Specimens 25-510I.

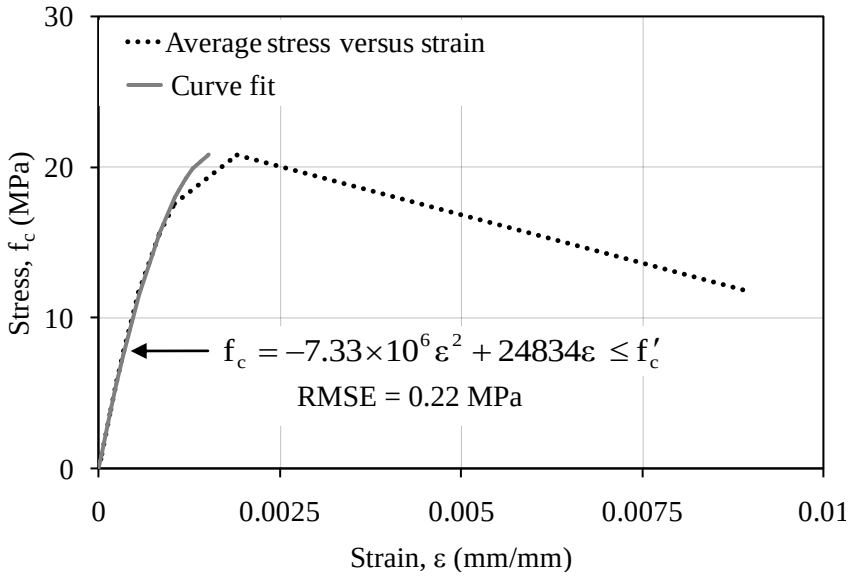

Figure 4A.24. Average stress versus strain - Concrete companion cylinder results corresponding to Specimens 25-510I.

APPENDIX 4B: Properties of the Longitudinal Plain Steel Bars

The diameter of the longitudinal plain steel bars and its surface roughness were measured as discussed in Section 3.4.2. Tables 4B.1 to 4B.15 present the surface roughness measurements and as-measured diameter of the longitudinal plain steel bars. The first number in the bar designation refers to the size of the longitudinal reinforcing bars, the second number refers to the splice length provided and the third number refers to the serial number of the bar.

The installation of steel strain gauges on the reinforcing bars required a local reduction of the bar's cross-sectional area and locally disrupted the bond with the concrete as discussed in Section 3.5. The as measured reduced bonded length, L_{sr}, of the instrumented longitudinal bars are presented in Table 4B.16 and are 80.6%, 87.7%, and 75.5% of the lap splice length for Specimen 25-410I, 25-510I, and 25-610I, respectively. The as-measured nominal diameter, d_b and reduced diameter, d_{br}, (see Figure 4B.1) of the instrumented bars at the instrumentation location are also presented in Table 4B.16. The reduced cross-sectional area, A_{sr}, of the instrumented longitudinal bars at the instrumented locations was calculated using the nominal and reduced bar diameter and are presented in the Table 4B.16.

Steel coupons obtained from the excess length of the longitudinal bars were prepared and tested as per ASTM A370 (ASTM 2008) as discussed in Section 3.4.2. The dynamic yield strength, strain at dynamic yield strength, modulus of elasticity and the ultimate yield strength were obtained directly from the steel coupon tests as discussed in Section 3.4.2 and are presented in Table 4B.17. The table also presents static yield strength for the longitudinal reinforcement which was determined in accordance with Rao et al. (1966) as discussed in Section 3.4.2. The strain at the static yield stress is calculated by dividing the static yield stress by the modulus of elasticity of steel. The stress, f_s, versus strain relationships obtained from coupon testing are also presented in Figures 4B.2 to 4B.5.

Table 4B.1: As-measured surface roughness and bar diameter – Specimen 19-305

Bar Designation	Location	Surface Roughness Readings R_y (μm)			Diameter d_b (mm)
		1	2	3	
19-305-1	1	10.36	8.44	10.64	19.05
	2	9.47	11.50	10.11	19.04
	3	9.58	11.16	11.20	18.92
	4	9.63	10.63	10.47	18.91
	5	9.09	9.61	9.12	18.94
	6	8.76	8.76	10.05	18.93
	7	9.32	9.98	9.35	18.93
	8	10.07	10.82	9.35	18.99
	9	8.65	9.58	11.53	18.96
	10	9.79	9.01	9.03	18.99
19-305-2	1	9.49	8.86	10.22	18.99
	2	8.31	11.29	11.37	18.98
	3	7.21	8.32	10.53	18.97
	4	9.41	9.50	10.48	19.05
	5	11.35	9.57	9.33	19.00
	6	9.38	9.41	8.35	19.07
	7	8.53	8.27	8.37	18.95
	8	11.40	9.20	8.80	19.02
	9	10.39	10.12	9.71	18.94
	10	9.96	10.32	9.08	18.91
19-305-3	1	8.66	9.76	8.50	18.94
	2	9.71	10.10	9.50	18.92
	3	11.30	10.15	9.34	18.92
	4	10.80	10.42	11.01	18.90
	5	8.87	8.69	10.56	18.90
	6	8.11	9.07	8.98	18.91
	7	9.29	9.47	11.22	18.93
	8	8.53	9.47	8.95	18.96
	9	8.28	9.31	9.11	18.95
	10	11.00	8.11	9.05	19.03
19-305-4	1	11.14	10.77	9.18	19.00
	2	7.22	9.31	8.03	18.98
	3	9.16	8.14	9.57	18.93
	4	9.09	8.04	9.87	19.06
	5	8.76	11.02	8.48	19.05
	6	9.23	9.93	9.49	19.03
	7	10.24	9.03	8.68	19.03
	8	7.99	8.92	9.66	18.87
	9	11.14	8.33	9.52	19.02
	10	10.50	8.46	9.28	18.95

Table 4B.2: As-measured surface roughness and bar diameter – Specimen 19-410

Bar Designation	Location	Surface Roughness Readings R_y (μm)			Diameter d_b (mm)
		1	2	3	
19-410-1	1	8.13	9.15	8.16	18.98
	2	10.17	9.09	8.23	18.93
	3	8.72	11.14	8.50	18.93
	4	9.49	10.39	8.21	18.94
	5	10.04	9.71	10.45	19.00
	6	10.68	9.77	9.27	19.07
	7	9.18	8.22	10.76	19.01
	8	10.23	9.33	8.26	18.91
	9	9.98	9.05	9.89	18.92
	10	9.46	9.88	8.12	18.96
19-410-2	1	10.31	10.62	9.98	19.06
	2	9.05	10.57	9.23	19.00
	3	9.77	11.30	11.12	19.02
	4	9.26	10.34	9.64	18.98
	5	9.51	9.74	11.03	19.00
	6	9.05	10.21	10.01	18.98
	7	8.74	11.05	10.70	18.94
	8	10.36	9.13	9.69	18.91
	9	10.87	10.39	8.46	18.96
	10	10.06	9.07	9.93	18.91
19-410-3	1	8.67	11.41	11.13	18.93
	2	8.57	9.66	10.97	18.93
	3	8.19	10.8	11.70	19.08
	4	8.51	9.23	10.84	18.95
	5	9.18	9.40	9.10	18.91
	6	8.96	10.73	11.09	18.95
	7	8.43	9.58	9.34	18.96
	8	8.98	10.49	9.09	18.96
	9	9.54	9.38	8.64	19.03
	10	8.95	11.55	9.82	19.00
19-410-4	1	9.99	8.05	11.21	19.01
	2	9.83	9.06	8.71	19.03
	3	9.06	9.40	9.73	19.02
	4	10.06	8.63	8.70	19.07
	5	8.86	10.8	8.15	19.04
	6	8.82	11.68	9.53	19.05
	7	9.64	9.01	8.61	19.08
	8	10.57	9.94	10.72	19.02
	9	9.06	11.74	8.34	19.02
	10	9.81	9.20	10.56	19.06

Table 4B.3: As-measured surface roughness and bar diameter – Specimen 19-510

Bar Designation	Location	Surface Roughness Readings R_y (μm)			Diameter d_b (mm)
		1	2	3	
19-510-1	1	8.37	9.94	9.69	19.09
	2	8.36	9.92	9.31	18.92
	3	9.99	8.84	8.74	18.96
	4	8.18	9.03	10.68	18.95
	5	9.38	10.99	10.94	18.92
	6	10.25	8.60	10.69	19.02
	7	10.70	9.33	9.56	19.01
	8	8.90	8.58	10.17	18.92
	9	11.20	8.91	9.66	18.98
	10	8.16	11.23	9.75	19.00
19-510-2	1	8.76	11.22	9.37	19.01
	2	9.41	11.37	8.99	18.95
	3	9.48	8.09	9.82	19.10
	4	10.09	8.94	9.22	19.09
	5	8.33	10.42	11.31	19.04
	6	9.99	11.12	10.41	19.06
	7	10.69	11.01	9.90	19.01
	8	9.85	11.13	10.18	19.00
	9	11.41	10.01	9.24	19.04
	10	8.58	9.70	10.82	19.06
19-510-3	1	11.24	9.88	9.55	19.08
	2	10.21	9.05	11.17	18.97
	3	10.27	9.43	10.30	19.06
	4	10.13	10.90	9.93	18.98
	5	9.98	9.72	9.99	19.05
	6	9.68	11.33	8.96	19.01
	7	8.29	8.82	10.17	19.03
	8	9.70	8.79	9.38	19.00
	9	10.52	8.98	11.18	19.01
	10	9.65	10.06	9.07	18.98
19-510-4	1	9.79	10.60	11.00	18.96
	2	9.59	9.03	9.93	19.05
	3	10.76	11.05	11.11	18.99
	4	9.45	9.78	10.09	19.06
	5	9.51	10.03	9.01	19.00
	6	10.15	9.82	9.07	18.95
	7	9.34	9.68	9.61	19.00
	8	10.95	10.84	10.85	19.01
	9	11.29	8.44	10.02	18.98
	10	9.63	9.88	9.65	19.01

Table 4B.4: As-measured surface roughness and bar diameter – Specimen 19-610

Bar Designation	Location	Surface Roughness Readings R_y (μm)			Diameter d_b (mm)
		1	2	3	
19-610-1	1	8.05	8.79	9.47	18.92
	2	8.52	10.43	8.71	18.92
	3	9.68	10.08	10.78	18.87
	4	11.00	8.28	9.96	18.89
	5	8.87	8.43	11.56	18.94
	6	8.06	11.01	8.37	18.99
	7	8.24	8.24	10.8	18.94
	8	10.09	9.14	10.26	18.97
	9	8.34	8.81	8.84	18.98
	10	9.37	9.07	9.09	19.01
19-610-2	1	9.61	10.10	8.09	18.94
	2	8.82	8.51	10.03	18.98
	3	10.30	10.97	8.50	18.92
	4	9.57	8.17	11.47	18.93
	5	8.23	8.50	9.22	19.02
	6	9.64	8.96	9.03	18.94
	7	9.48	10.17	8.20	19.05
	8	8.55	11.11	10.38	18.91
	9	11.08	10.06	7.28	18.94
	10	8.26	10.44	9.72	19.08
19-610-3	1	9.17	9.46	8.87	19.01
	2	8.47	10.23	9.66	18.98
	3	8.24	8.79	10.05	18.89
	4	9.74	8.87	9.48	18.90
	5	9.40	9.03	9.3	18.92
	6	10.25	8.05	9.06	18.96
	7	10.13	8.11	9.16	19.01
	8	10.15	10.51	10.79	19.05
	9	8.40	11.14	8.59	19.01
	10	8.90	8.40	8.32	19.02
19-610-4	1	9.01	11.33	10.24	18.94
	2	9.83	9.31	8.18	19.01
	3	10.45	11.82	10.17	18.97
	4	9.63	9.83	9.80	18.93
	5	9.14	10.82	9.33	18.98
	6	9.41	9.50	8.48	19.02
	7	11.44	9.00	11.02	18.92
	8	9.23	8.64	8.71	18.92
	9	8.33	8.72	8.56	19.06
	10	11.25	9.16	10.79	18.90

Table 4B.5: As-measured surface roughness and bar diameter – Specimen 25-410

Bar Designation	Location	Surface Roughness Readings R_y (μm)			Diameter d_b (mm)
		1	2	3	
25-410-1	1	11.87	10.47	9.67	25.28
	2	9.06	13.18	9.35	25.3
	3	10.15	6.06	10.97	25.32
	4	7.35	6.95	10.46	25.22
	5	7.10	7.18	11.00	25.23
	6	13.58	10.17	8.58	25.23
	7	9.08	11.01	12.11	25.23
	8	12.42	10.7	13.44	25.24
	9	8.72	11.48	11.77	25.20
	10	9.54	7.29	9.58	25.20
25-410-2	1	7.40	8.61	8.78	25.29
	2	6.29	11.83	8.69	25.41
	3	5.78	7.92	6.55	25.51
	4	7.76	6.77	6.18	25.44
	5	11.82	9.77	7.11	25.39
	6	9.21	6.95	7.82	25.26
	7	7.60	10.96	8.70	25.35
	8	9.74	7.15	6.97	25.27
	9	7.44	5.76	12.57	25.29
	10	8.24	7.72	9.34	25.26
25-410-3	1	7.36	9.05	9.14	25.18
	2	7.05	8.52	9.08	25.15
	3	8.03	10.00	8.46	25.21
	4	13.80	10.33	13.16	25.22
	5	8.83	7.01	6.05	25.22
	6	10.01	6.84	6.56	25.17
	7	9.74	7.15	12.15	25.16
	8	7.76	13.36	11.54	25.19
	9	7.07	8.61	7.84	25.21
	10	9.76	7.93	8.78	25.21
25-410-4	1	10.27	9.07	9.19	25.19
	2	8.70	5.75	8.68	25.18
	3	7.98	12.53	7.87	25.19
	4	8.18	7.97	7.56	25.19
	5	8.14	9.37	8.88	25.22
	6	6.83	8.54	5.30	25.34
	7	8.50	8.07	9.05	25.21
	8	6.05	7.20	9.79	25.28
	9	7.91	6.91	7.26	25.22
	10	7.58	8.06	9.30	25.21

Table 4B.6: As-measured surface roughness and bar diameter – Specimen 25-510

Bar Designation	Location	Surface Roughness Readings R_y (μm)			Diameter d_b (mm)
		1	2	3	
25-510-4	1	7.81	8.7	6.62	25.25
	2	10.17	9.95	6.7	25.23
	3	8.23	8.2	10.11	25.24
	4	8.82	12.15	10.63	25.20
	5	6.54	9.25	8.36	25.26
	6	12.02	9.55	7.13	25.18
	7	7.59	6.45	10.08	25.26
	8	8.43	10.45	7.99	25.23
	9	9.42	7.66	6.8	25.21
	10	8.03	10.52	10	25.27
25-510-2	1	9.29	6.02	6.79	25.18
	2	7.77	8.39	7.2	25.23
	3	7.87	7.27	10.08	25.20
	4	9.69	7.51	8.74	25.20
	5	14.32	6.91	6.48	25.20
	6	6.06	6.6	7.87	25.19
	7	7.87	9.34	7.07	25.20
	8	6.20	7.81	13.37	25.21
	9	8.30	7.96	9.5	25.25
	10	8.14	7.63	9.22	25.20
25-510-3	1	12.34	7.32	6.34	25.35
	2	6.93	7.52	10.2	25.38
	3	7.5	6.13	10.68	25.31
	4	9.81	6.62	6.71	25.24
	5	8.64	8.67	10.67	25.24
	6	12.51	10.31	7.84	25.27
	7	8.24	8.53	10.33	25.34
	8	11.58	8.03	9.51	25.31
	9	9.38	6.37	8.71	25.22
	10	12.31	10.22	7.85	25.21
25-510-4	1	8.58	9.43	8.67	25.28
	2	6.46	6.81	9.22	25.21
	3	9.45	6.54	5.82	25.22
	4	8.87	6.52	7.45	25.19
	5	6.75	6.96	6.93	25.26
	6	7.41	7.49	7.2	25.24
	7	8.27	8.53	7.81	25.23
	8	7.43	8.63	5.62	25.20
	9	8.3	7.95	9.2	25.19
	10	8.1	7.78	7.67	25.22

Table 4B.7: As-measured surface roughness and bar diameter – Specimen 25-610

Bar Designation	Location	Surface Roughness Readings R_y (μm)			Diameter d_b (mm)
		1	2	3	
25-610-1	1	7.19	8.13	7.67	25.15
	2	5.98	6.4	6.91	25.18
	3	6.97	8.24	7.71	25.21
	4	10.4	7.18	10.28	25.23
	5	9.27	9.64	8.83	25.31
	6	7.65	11.01	10.75	25.25
	7	10.66	10.86	11.3	25.19
	8	8.96	11.15	11.41	25.20
	9	7.38	10.27	6.74	25.19
	10	8.75	7.08	8.17	25.20
25-610-2	1	7.85	10.05	6.9	25.22
	2	7.47	7.11	10.49	25.23
	3	9.76	11.62	8.38	25.26
	4	11.65	9.76	9.47	25.24
	5	8.24	6.42	6.72	25.40
	6	7.15	9.3	12.87	25.37
	7	6.64	8.12	8.59	25.42
	8	7.15	8.71	7.78	25.42
	9	6.24	9.92	8.13	25.41
	10	7.87	10.17	9.68	25.40
25-610-3	1	6.92	7.21	5.39	25.23
	2	12.21	9.43	10.35	25.23
	3	9.25	7.05	6.82	25.23
	4	7.44	13.18	10.62	25.23
	5	6.17	7.63	13.36	25.32
	6	6.24	7.68	12.86	25.33
	7	6.88	9.82	8.34	25.38
	8	7.75	8.02	8.1	25.34
	9	14.15	8.43	11.24	25.35
	10	10.11	6.43	8.43	25.34
25-610-4	1	8.4	7.8	8.01	25.21
	2	10.99	8.6	8.61	25.20
	3	6.26	7.21	6.51	25.19
	4	7.13	12.25	6.21	25.18
	5	7.68	9.04	7.99	25.19
	6	7.97	8.22	7.96	25.21
	7	8.5	13.38	14.02	25.20
	8	7.1	11.74	8.59	25.20
	9	7.74	6.96	7.35	25.27
	10	7.16	8.54	6.77	25.34

Table 4B.8: As-measured surface roughness and bar diameter – Specimen 25-810

Bar Designation	Location	Surface Roughness Readings R_y (μm)			Diameter d_b (mm)
		1	2	3	
25-810-1	1	8.60	9.68	10.67	25.43
	2	8.24	8.93	8.36	25.42
	3	10.22	8.31	10.55	25.43
	4	8.15	8.73	10.72	25.50
	5	10.45	9.94	10.53	25.53
	6	8.45	10.66	8.14	25.19
	7	8.79	8.40	11.31	25.09
	8	9.25	9.63	8.83	25.22
	9	11.00	9.19	10.68	25.13
	10	8.89	10.54	9.75	25.08
25-810-2	1	9.98	10.94	10.09	25.28
	2	8.83	8.45	8.08	25.27
	3	10.61	10.16	8.33	25.24
	4	8.78	8.62	8.51	25.22
	5	9.63	10.15	9.01	25.23
	6	8.71	9.01	10.10	25.42
	7	8.38	8.06	10.87	25.38
	8	8.38	9.43	11.39	25.38
	9	8.08	9.11	9.21	25.35
	10	10.23	10.04	10.98	25.28
25-810-3	1	9.45	11.10	10.49	25.25
	2	8.68	8.62	9.43	25.30
	3	9.41	8.20	11.00	25.31
	4	9.69	9.03	9.60	25.36
	5	9.14	8.52	9.70	25.33
	6	10.28	10.53	10.73	25.20
	7	8.51	10.33	9.56	25.18
	8	9.38	9.98	11.24	25.23
	9	10.18	8.98	8.37	25.28
	10	10.69	11.51	8.87	25.32
25-810-4	1	8.29	8.32	9.13	25.27
	2	10.05	11.01	10.33	25.28
	3	8.72	9.58	8.32	25.31
	4	10.51	11.23	9.30	25.32
	5	10.93	11.69	11.33	25.35
	6	9.70	8.58	9.98	25.28
	7	8.91	10.38	8.49	25.21
	8	8.22	8.75	10.12	25.31
	9	11.49	10.01	11.18	25.21
	10	9.76	10.38	8.74	25.22

Table 4B.9: As-measured surface roughness and bar diameter – Specimen 25-410I

Bar Designation	Location	Surface Roughness Readings R_y (μm)			Diameter d_b (mm)
		1	2	3	
25-410I-1	1	9.83	8.35	9.69	25.17
	2	9.98	10.12	8.21	25.35
	3	10.45	8.85	8.80	25.30
	4	10.94	10.97	8.64	25.11
	5	10.01	10.58	9.98	25.19
	6	9.38	10.61	8.63	25.36
	7	9.93	9.78	8.66	25.45
	8	9.62	10.77	10.96	25.40
	9	9.32	10.53	9.93	25.46
	10	9.25	10.92	8.38	25.39
25-410I-2	1	10.86	10.71	9.39	25.30
	2	9.31	9.51	9.53	25.38
	3	10.83	8.72	7.91	25.33
	4	10.52	8.59	10.12	25.37
	5	11.77	9.78	9.18	25.29
	6	10.81	11.54	8.71	25.38
	7	10.71	8.43	9.26	25.43
	8	9.43	10.75	9.71	25.26
	9	9.56	11.68	9.48	25.32
	10	11.76	8.66	8.74	25.36
25-410I-3	1	11.34	8.30	9.38	25.30
	2	8.82	8.50	8.66	25.24
	3	9.51	8.68	8.55	25.12
	4	9.77	10.63	8.40	25.11
	5	8.65	8.70	9.02	25.23
	6	10.01	9.77	8.81	25.08
	7	10.03	8.60	10.01	25.06
	8	8.34	9.02	9.43	25.19
	9	8.29	11.85	9.93	25.16
	10	8.49	9.63	11.24	25.20
25-410I-4	1	8.79	9.78	8.21	25.23
	2	9.06	10.20	9.12	25.25
	3	10.19	8.98	9.57	25.21
	4	8.92	8.78	10.01	25.31
	5	9.52	11.88	9.15	25.24
	6	11.76	10.68	8.33	25.34
	7	9.10	11.44	8.40	25.38
	8	10.02	8.95	9.47	25.33
	9	10.80	10.23	11.33	25.36
	10	9.66	9.88	10.57	25.39

Table 4B.10: As-measured surface roughness and bar diameter – Specimen 25-510I

Bar Designation	Location	Surface Roughness Readings R_y (μm)			Diameter d_b (mm)
		1	2	3	
25-510I-1	1	9.76	10.31	9.33	25.50
	2	9.93	8.93	10.38	25.46
	3	9.73	9.89	10.15	25.46
	4	9.65	9.06	10.26	25.50
	5	9.33	9.65	10.46	25.42
	6	9.83	9.12	8.26	25.16
	7	9.74	10.45	8.30	25.21
	8	10.79	10.02	9.83	25.11
	9	10.16	11.30	9.45	25.10
	10	9.40	8.36	10.47	25.17
25-510I-2	1	10.19	9.02	10.58	25.42
	2	10.04	8.52	9.10	25.43
	3	8.41	9.93	9.74	25.42
	4	8.82	8.64	8.97	25.38
	5	9.55	9.11	9.70	25.33
	6	10.13	8.85	10.29	25.14
	7	11.19	9.11	9.16	25.18
	8	10.70	9.41	9.62	25.14
	9	11.08	8.57	11.41	25.16
	10	9.91	12.05	9.34	25.22
25-510I-3	1	9.81	9.51	9.45	25.30
	2	8.91	8.37	8.39	25.19
	3	9.18	11.61	8.98	25.18
	4	9.22	10.11	9.92	25.21
	5	9.37	8.77	11.48	25.48
	6	9.39	9.03	9.97	25.49
	7	8.98	11.49	11.42	25.46
	8	9.00	11.23	8.10	25.42
	9	9.01	11.29	11.37	25.46
	10	9.41	10.27	8.33	25.42
25-510I-4	1	11.39	9.00	10.05	25.44
	2	10.90	8.25	8.26	25.42
	3	10.15	10.90	10.52	25.35
	4	10.78	10.18	9.77	25.45
	5	9.51	9.98	10.13	25.40
	6	8.50	9.55	11.34	25.25
	7	11.06	9.81	9.90	25.25
	8	8.36	7.68	9.11	25.18
	9	8.13	12.03	11.01	25.30
	10	8.70	11.35	8.40	25.22

Table 4B.11: As-measured surface roughness and bar diameter – Specimen 25-610I

Bar Designation	Location	Surface Roughness Readings R_y (μm)			Diameter d_b (mm)
		1	2	3	
25-610I-1	1	10.38	9.58	9.83	25.32
	2	8.45	7.83	11.17	25.35
	3	9.02	10.13	8.35	25.28
	4	9.21	10.65	9.68	25.28
	5	10.36	9.94	10.67	25.28
	6	10.22	8.50	9.01	25.14
	7	11.05	11.39	10.91	25.14
	8	10.78	8.42	8.96	25.04
	9	9.30	10.50	9.57	25.06
	10	9.49	9.83	10.95	25.21
25-610I-2	1	9.67	10.28	8.72	25.40
	2	8.68	8.92	9.29	25.43
	3	10.36	9.73	9.55	25.38
	4	9.01	11.66	10.17	25.33
	5	8.48	8.60	8.53	25.33
	6	8.25	10.57	8.09	25.17
	7	9.77	10.00	9.77	25.21
	8	9.90	10.08	9.12	25.26
	9	9.60	11.48	9.97	25.23
	10	9.56	9.78	11.48	25.23
25-610I-3	1	11.47	11.39	11.37	25.44
	2	11.13	11.46	9.31	25.42
	3	9.56	10.33	9.15	25.46
	4	11.34	10.90	9.42	25.43
	5	12.06	11.44	9.69	25.42
	6	10.72	11.65	9.72	25.3
	7	8.47	9.22	11.75	25.17
	8	12.01	9.14	9.58	25.20
	9	8.93	10.06	9.03	25.20
	10	8.39	11.13	9.87	25.20
25-610I-4	1	11.21	11.22	10.82	25.08
	2	10.89	11.46	8.51	25.11
	3	10.32	9.11	9.27	25.06
	4	8.90	9.97	8.52	25.12
	5	11.36	9.48	11.13	25.16
	6	11.48	10.45	10.77	25.29
	7	9.59	8.22	10.21	25.34
	8	8.53	9.42	8.06	25.32
	9	9.57	11.86	10.69	25.39
	10	10.33	8.72	9.63	25.41

Table 4B.12: As-measured surface roughness and bar diameter – Specimen 32-410

Bar Designation	Location	Surface Roughness Readings R_y (μm)			Diameter d_b (mm)
		1	2	3	
32-410-1	1	9.13	9.29	9.86	31.78
	2	10.07	11.02	9.75	31.70
	3	9.18	11.27	10.40	31.78
	4	10.10	9.00	10.27	31.70
	5	10.42	10.63	9.80	31.68
	6	9.96	9.74	8.52	31.72
	7	9.75	10.56	8.39	31.74
	8	10.69	8.34	10.52	31.75
	9	8.53	11.62	9.93	31.69
	10	10.55	9.78	11.15	31.81
32-410-2	1	9.96	10.70	9.68	31.73
	2	10.73	10.75	9.36	31.74
	3	10.37	11.22	8.90	31.76
	4	9.32	11.04	11.06	31.73
	5	11.46	10.01	8.52	31.76
	6	10.13	10.47	8.48	31.76
	7	9.34	10.60	9.45	31.82
	8	9.83	10.69	10.55	31.83
	9	11.18	9.21	9.74	31.78
	10	9.17	11.02	9.28	31.74
32-410-3	1	9.42	10.38	9.31	31.73
	2	10.25	9.56	10.18	31.70
	3	9.84	10.81	10.67	31.69
	4	10.22	9.73	9.68	31.69
	5	10.62	10.74	8.93	31.62
	6	10.08	9.37	9.00	31.71
	7	11.18	9.02	9.96	31.75
	8	8.45	8.99	10.31	31.69
	9	8.99	9.12	10.00	31.65
	10	10.00	10.03	8.67	31.75
32-410-4	1	10.85	9.99	8.78	31.75
	2	11.16	9.84	10.20	31.68
	3	10.10	9.30	8.87	31.71
	4	9.68	9.13	9.94	31.76
	5	9.54	8.79	10.26	31.74
	6	11.47	10.70	8.96	31.78
	7	11.79	8.77	8.80	31.76
	8	10.36	10.04	8.43	31.75
	9	9.38	10.59	9.63	31.73
	10	10.35	9.51	10.91	31.76

Table 4B.13: As-measured surface roughness and bar diameter – Specimen 32-610

Bar Designation	Location	Surface Roughness Readings R_y (μm)			Diameter d_b (mm)
		1	2	3	
32-610-1	1	9.59	8.32	10.25	31.67
	2	12.65	8.70	10.00	31.70
	3	9.60	8.74	12.12	31.71
	4	10.38	9.00	9.20	31.75
	5	8.59	9.81	9.96	31.69
	6	9.44	12.02	9.28	31.72
	7	8.70	9.13	8.92	31.73
	8	9.50	8.07	9.58	31.74
	9	9.31	9.28	8.47	31.77
	10	8.07	10.80	9.80	31.73
32-610-2	1	10.63	9.06	9.07	31.73
	2	9.91	9.98	10.07	31.74
	3	11.33	9.01	10.91	31.71
	4	9.28	11.11	9.26	31.74
	5	9.08	9.63	8.70	31.75
	6	12.18	10.09	9.94	31.71
	7	11.57	9.42	11.60	31.73
	8	10.46	10.57	9.41	31.70
	9	12.02	9.60	9.15	31.74
	10	11.94	9.58	9.23	31.74
32-610-3	1	9.65	10.08	8.86	31.74
	2	9.21	9.19	11.13	31.78
	3	9.90	9.30	8.75	31.75
	4	10.14	9.56	9.37	31.73
	5	8.92	9.49	8.82	31.82
	6	10.83	9.80	9.49	31.71
	7	10.82	9.24	8.17	31.73
	8	8.31	8.50	9.51	31.70
	9	10.01	11.69	8.93	31.72
	10	8.72	8.03	9.88	31.73
32-610-4	1	9.17	9.01	10.55	31.70
	2	9.31	9.20	8.36	31.70
	3	10.39	9.79	10.86	31.70
	4	10.04	9.81	8.69	31.73
	5	9.35	9.24	10.86	31.70
	6	10.95	10.06	8.04	31.85
	7	9.89	10.71	10.12	31.83
	8	9.26	9.97	8.72	31.90
	9	9.77	10.22	10.53	31.88
	10	9.45	9.07	9.55	31.85

Table 4B.14: As-measured surface roughness and bar diameter – Specimen 32-810

Bar Designation	Location	Surface Roughness Readings R_y (μm)			Diameter d_b (mm)
		1	2	3	
32-810-1	1	9.74	10.46	9.01	31.76
	2	9.32	8.68	12.27	31.75
	3	9.20	10.53	9.60	31.74
	4	11.30	12.50	8.08	31.74
	5	10.68	13.60	11.75	31.78
	6	9.39	11.28	11.38	31.77
	7	9.08	12.07	10.06	31.75
	8	9.77	10.71	10.42	31.81
	9	8.96	12.38	8.00	31.78
	10	11.75	8.43	8.21	31.79
32-810-2	1	10.74	10.62	9.77	31.72
	2	11.74	9.77	10.84	31.71
	3	10.58	10.06	9.55	31.72
	4	9.90	10.49	11.17	31.68
	5	9.43	12.16	11.32	31.68
	6	8.73	11.74	11.06	31.72
	7	9.35	10.36	9.42	31.78
	8	9.84	9.15	11.08	31.71
	9	9.94	9.78	9.13	31.68
	10	10.00	9.88	11.14	31.71
32-810-3	1	10.63	8.41	10.91	31.77
	2	11.12	9.51	11.55	31.67
	3	10.73	9.28	9.59	31.71
	4	8.88	10.04	9.24	31.68
	5	10.68	10.60	10.52	31.72
	6	10.18	10.94	10.19	31.70
	7	8.80	10.48	11.03	31.68
	8	8.89	9.06	8.98	31.73
	9	10.93	10.12	9.22	31.70
	10	8.87	11.46	8.82	31.67
32-810-4	1	10.38	9.66	9.93	31.72
	2	9.89	11.14	9.45	31.70
	3	11.39	11.13	11.23	31.70
	4	9.82	10.14	9.40	31.70
	5	10.58	9.77	9.92	31.69
	6	10.18	10.58	8.13	31.68
	7	10.23	9.02	8.14	31.65
	8	10.04	10.68	10.40	31.72
	9	10.35	9.47	8.55	31.65
	10	9.34	11.20	9.75	31.72

Table 4B.15: As-measured surface roughness and bar diameter – Specimen 32-910

Bar Designation	Location	Surface Roughness Readings R_y (μm)			Diameter d_b (mm)
		1	2	3	
32-910-1	1	9.39	8.95	9.40	31.65
	2	9.97	10.63	11.72	31.69
	3	10.24	9.56	11.71	31.75
	4	10.66	9.43	8.67	31.77
	5	9.89	12.77	8.46	31.67
	6	9.86	10.33	9.80	31.88
	7	11.47	10.39	8.62	31.82
	8	9.42	9.46	8.98	31.82
	9	9.55	9.28	9.25	31.84
	10	8.43	8.35	8.59	31.86
32-910-2	1	8.31	11.49	10.95	31.85
	2	11.36	11.22	9.84	31.83
	3	10.45	9.75	9.80	31.82
	4	8.22	8.97	9.50	31.81
	5	10.36	8.95	9.91	31.80
	6	11.16	11.70	9.67	31.75
	7	9.45	10.79	11.26	31.68
	8	11.01	10.17	11.88	31.64
	9	10.01	11.71	8.36	31.64
	10	11.71	9.33	8.97	31.60
32-910-3	1	11.07	10.29	10.84	31.87
	2	8.16	10.34	10.71	31.88
	3	10.05	11.74	9.91	31.81
	4	8.85	11.19	10.55	31.76
	5	8.43	10.62	8.07	31.78
	6	11.17	8.92	11.12	31.88
	7	11.15	8.60	9.19	31.85
	8	11.88	11.34	9.95	31.88
	9	10.38	10.31	9.14	31.87
	10	10.71	9.59	10.21	32.02
32-910-4	1	8.57	9.06	8.80	31.89
	2	11.66	11.95	9.75	31.89
	3	9.07	10.18	9.04	31.85
	4	10.82	11.60	9.03	31.77
	5	8.59	12.80	11.09	31.79
	6	9.76	10.22	12.41	31.78
	7	9.23	9.79	8.76	31.77
	8	8.35	10.57	9.32	31.76
	9	9.92	9.12	7.99	31.78
	10	11.78	10.84	8.22	31.75

Table 4B.16: Longitudinal reinforcing steel details for the instrumented specimens

Specimen	Lap Splice Length, L_s (mm)	Reduced Bonded Length, L_{sr} (mm)	L_{sr} as a % of L_s	Nominal Diameter, d_b (mm)	Reduced Diameter d_{br} (mm)	Reduced Cross-sectional Area, A_{sr} (mm^2)
25-410I	410	331	80.6	25.3	24.4	496
25-510I	510	448	87.7	25.3	24.5	498
25-610I	610	461	75.5	25.3	24.6	497

Table 4B.17: Reinforcing steel coupon test results

Steel Coupon*	Dynamic Yield Strength f_{yd} (MPa)	Strain at Dynamic Yield Strength $\mu\varepsilon_{yd}$	Modulus of Elasticity E_s (MPa)	Ultimate Strength f_u (MPa)	Static Yield Strength f_{ys} (MPa)	Strain at Static Yield Strength $\mu\varepsilon_{ys}$	Associated Splice Specimen ID
S-19-1	356	2040	191000	520	323	1690	19-305, 19-410, 19-510, and 19-610
S-19-2	354	2040	195000	526	328	1680	
S-19-3	355	1750	222000	524	326	1470	
S-25-1	348	2040	196000	536	326	1660	25-410, 25-510, and 25-610
S-25-2	345	1750	201000	533	321	1600	
S-25-3	345	2040	192000	533	320	1670	
S-25-4	351	2040	207000	507	321	1550	25-810, 25-410I, 25-510I, and 25-610I
S-25-5	333	1750	199000	495	301	1510	
S-25-6	355	2040	211000	510	327	1550	
S-32-1	350	1750	218000	499	323	1480	32-410, 32-610, 32-810, and 32-910
S-32-2	362	2040	201000	515	331	1650	
S-32-3	332	1750	193000	499	300	1550	

*The first letter in the steel coupon designation, S, refers to steel, the first number refers to the size of the longitudinal reinforcing bars and the second number refers to the serial number of the coupon.

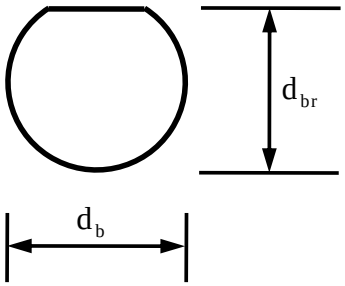

Figure 4B.1. Reduction in the cross-sectional area of the longitudinal reinforcing bars due to the installation of steel strain gauges.

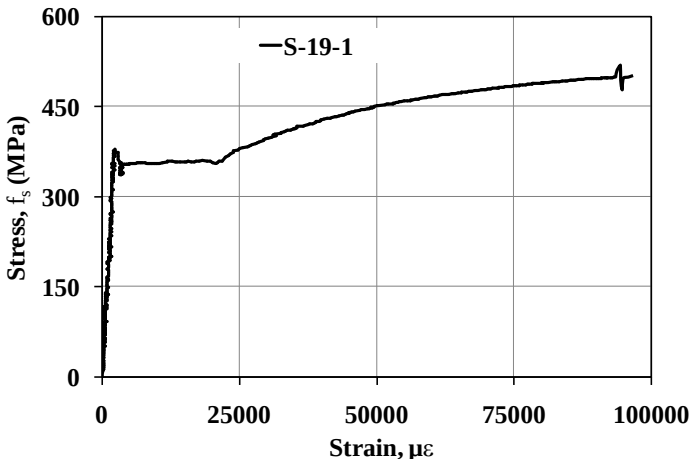

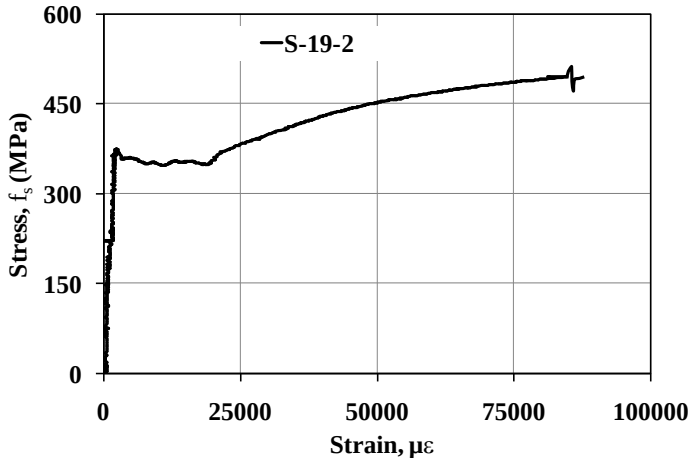

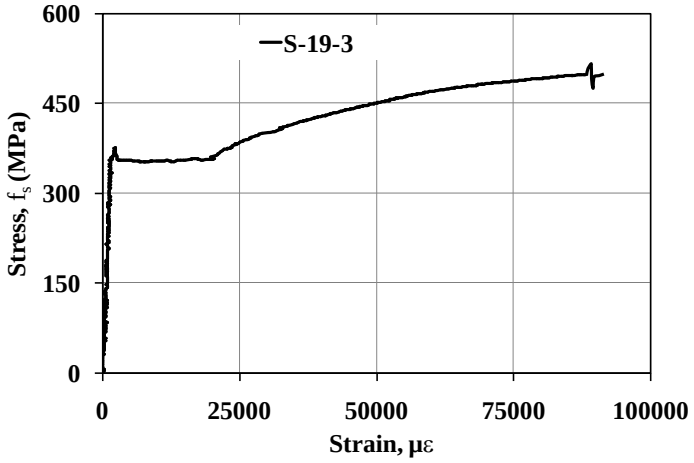

Figure 4B.2. Stress versus strain – Coupons taken from 19 mm diameter bars.

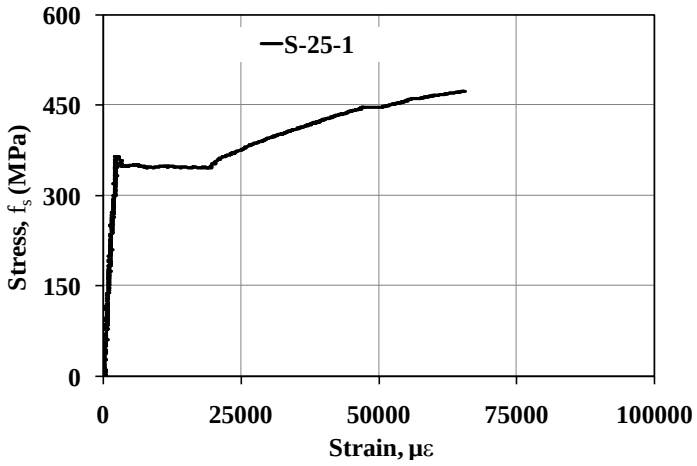

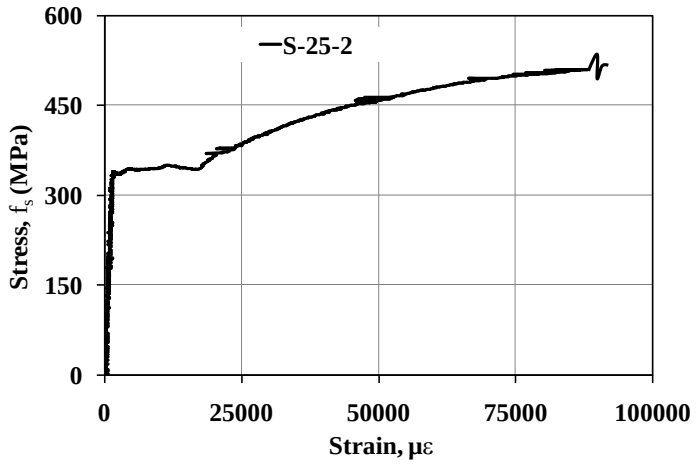

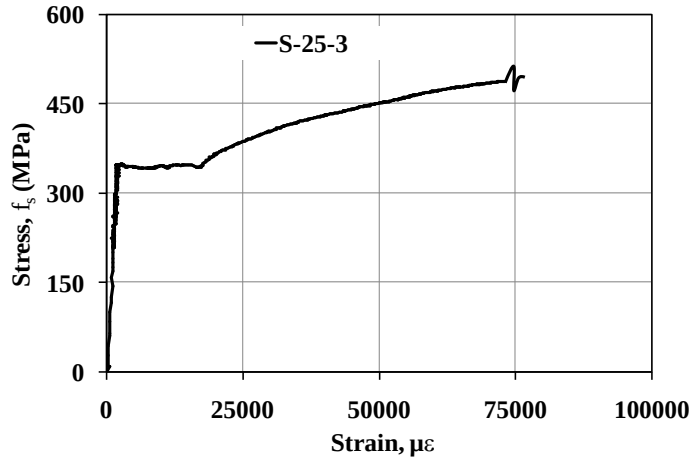

Figure 4B.3. Stress versus strain – Coupons taken from 25 mm diameter bars corresponding to Specimens 25-410, 25-510, and 25-610.

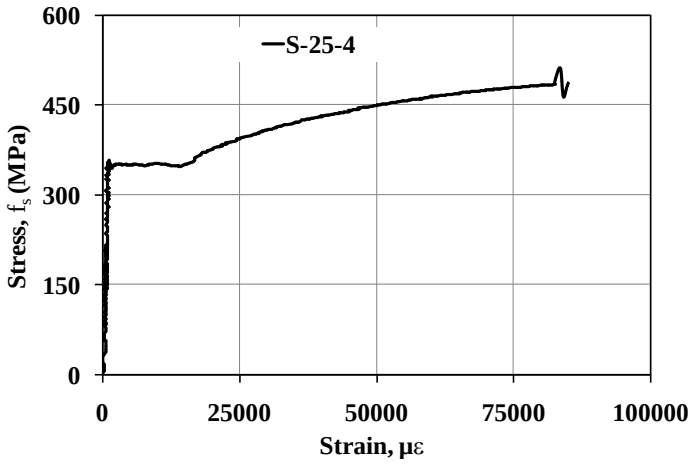

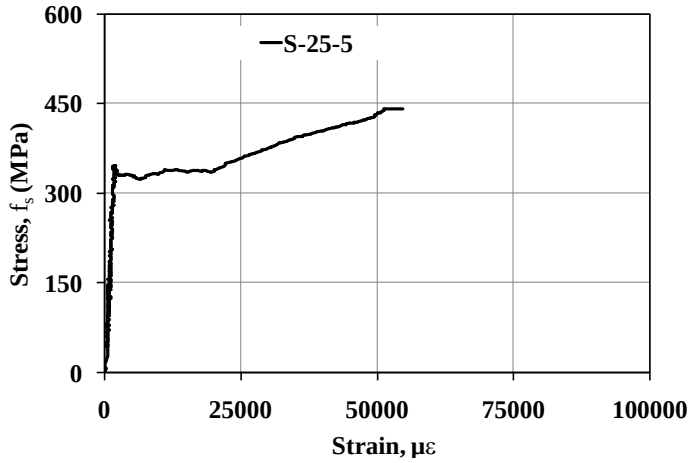

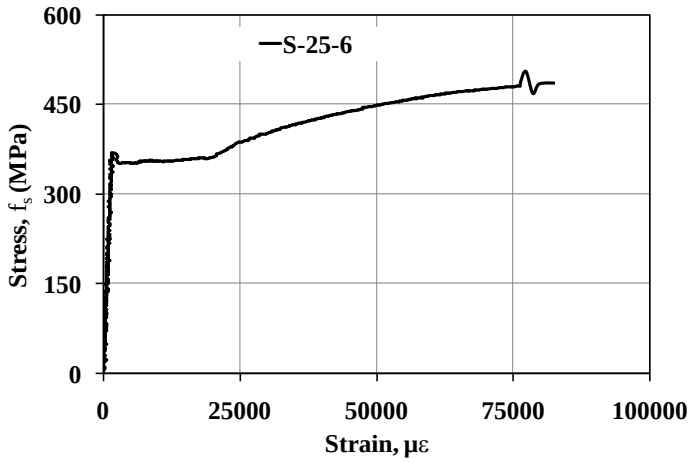

Figure 4B.4. Stress versus strain – Coupons taken from 25 mm diameter bars corresponding Specimen 25-810 and instrumented specimens.

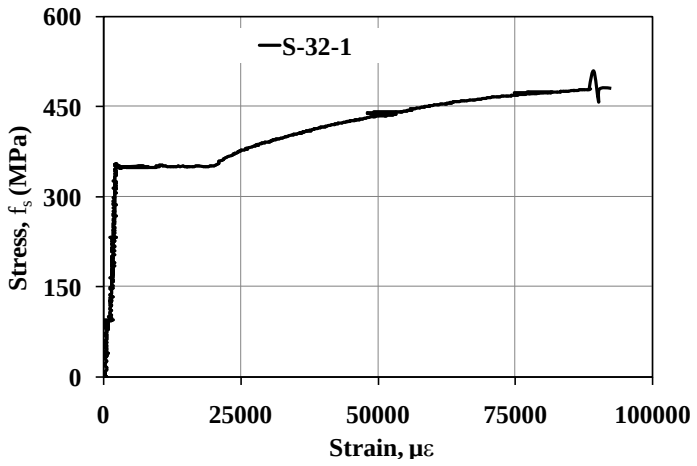

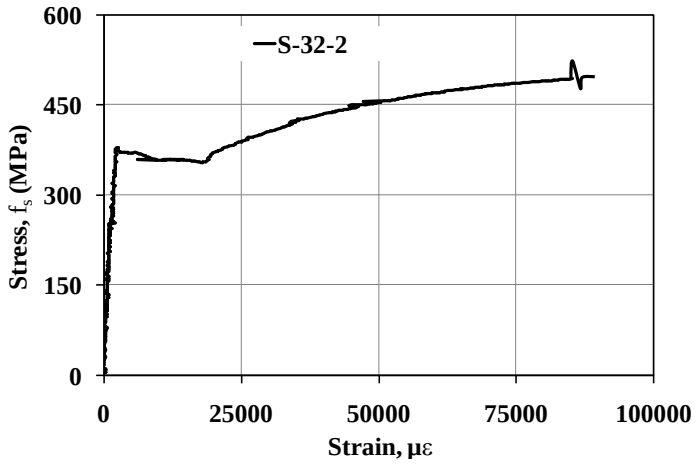

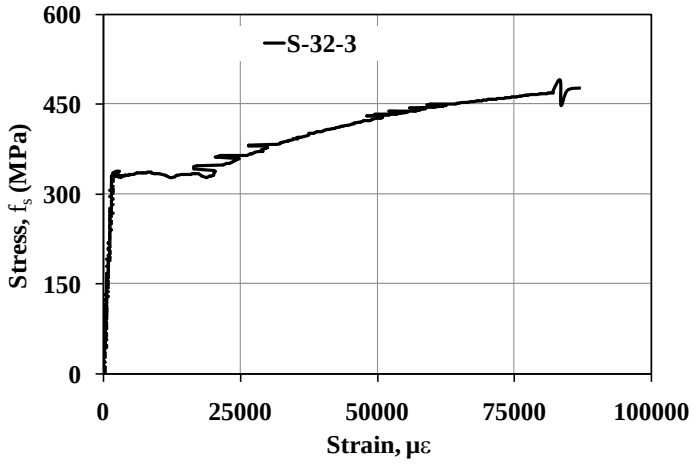

Figure 4B.5. Stress versus strain – Coupons taken from 32 mm diameter bars.

APPENDIX 4C: Observed Cracking Behaviour

Cracks were marked as testing of the specimens progressed. The observed crack patterns at the load level when the crack height first crossed the level of the longitudinal reinforcing steel level is presented as it generally coincides with the initiation of bond loss in the specimen. Crack patterns at load levels when new cracks developed in the lap splice length and outside the lap splice length, and load levels representing significant increases in crack height are also presented. Crack width measurements were not taken and therefore a single line weight is used for all of the cracks except the large crack adjacent to one end of the lap splice length that develops at the maximum applied load level. Observed crack patterns for Specimens 25-410, 25-510, 25-810 and 19-610 are provided in Section 4.4 and are therefore not repeated here.

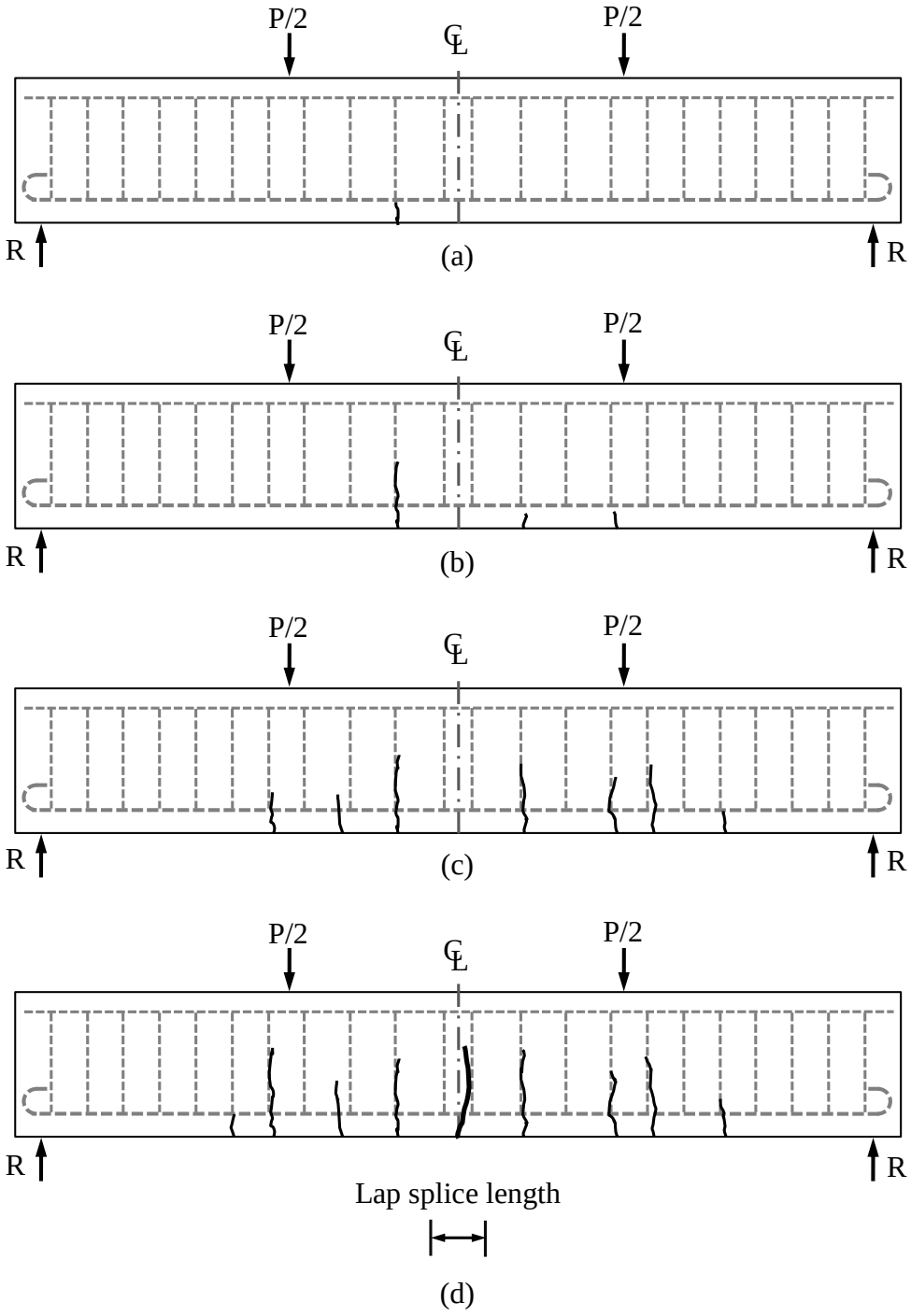

Figure 4C.1. Observed crack pattern - Specimen 19-305: (a) P = 0.3 P_{max}, (b) P = 0.4 P_{max}, (c) P = 0.7 P_{max}, and (d) P = P_{max}

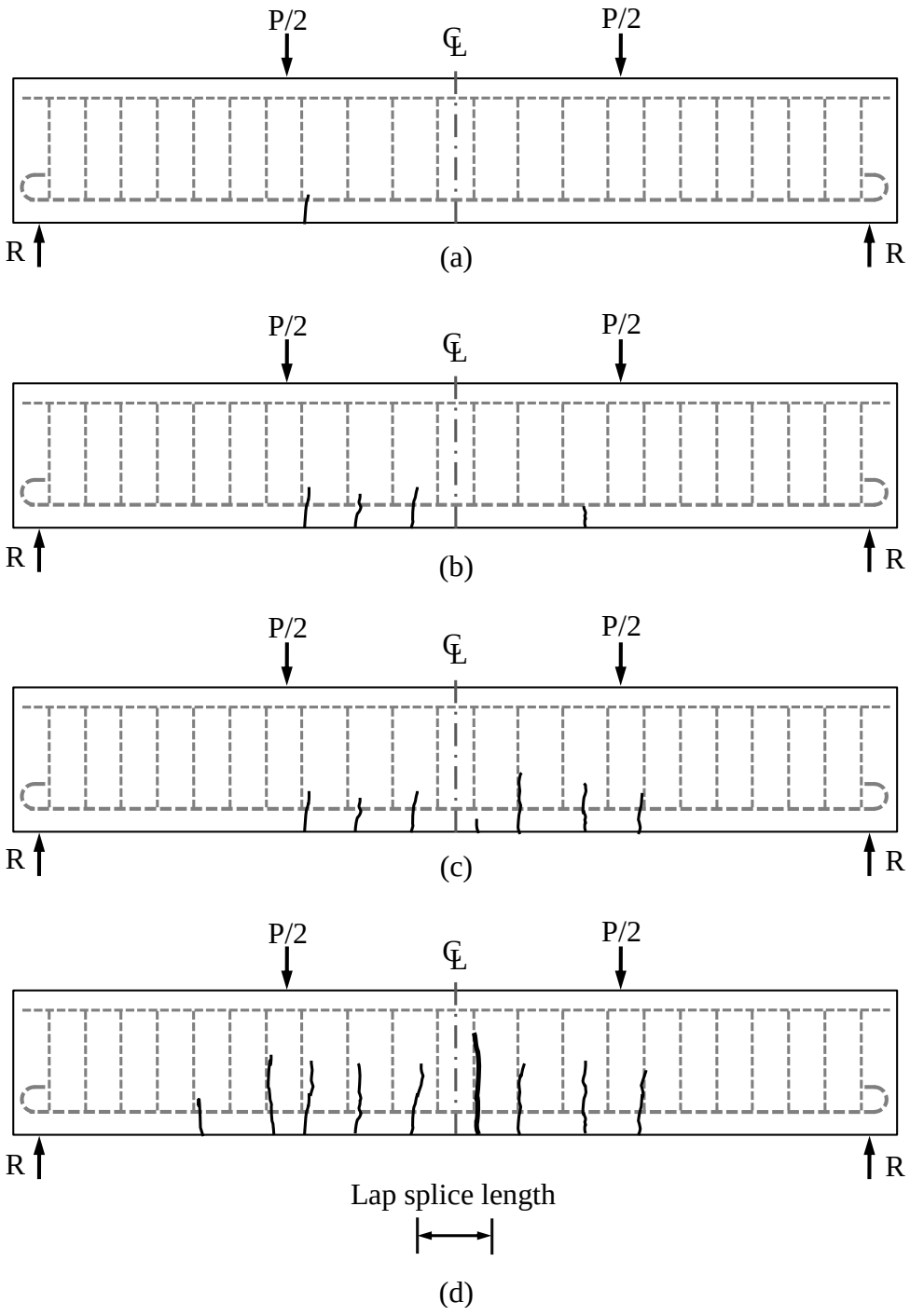

Figure 4C.2. Observed crack pattern - Specimen 19-410: (a) P = 0.4 P_{max}, (b) P = 0.5 P_{max}, (c) P = 0.65 P_{max}, and (d) P = P_{max}

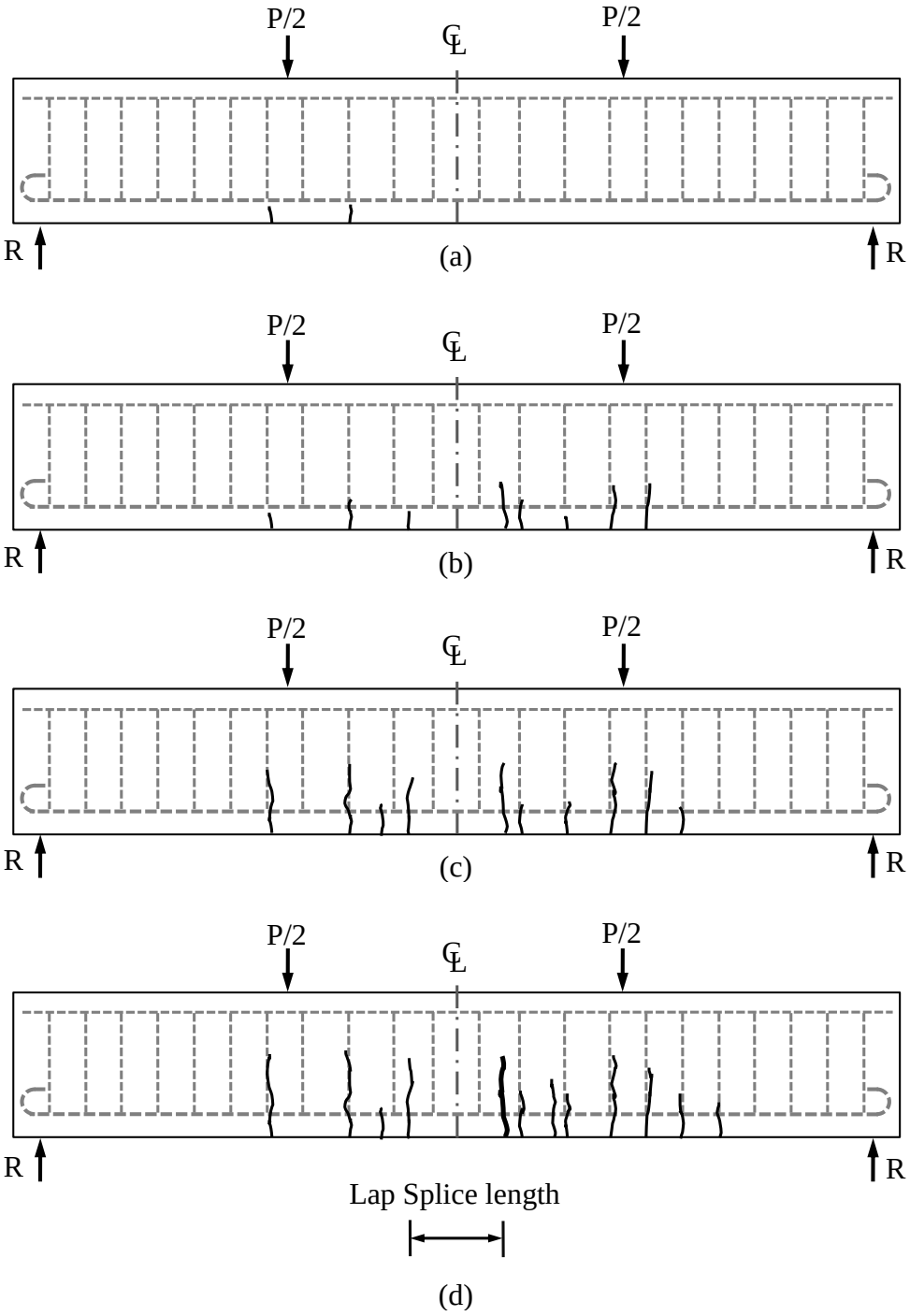

Figure 4C.3. Observed crack pattern - Specimen 19-510: (a) P = 0.5 P_{max}, (b) P = 0.6 P_{max}, (c) P = 0.7 P_{max}, and (d) P = P_{max}

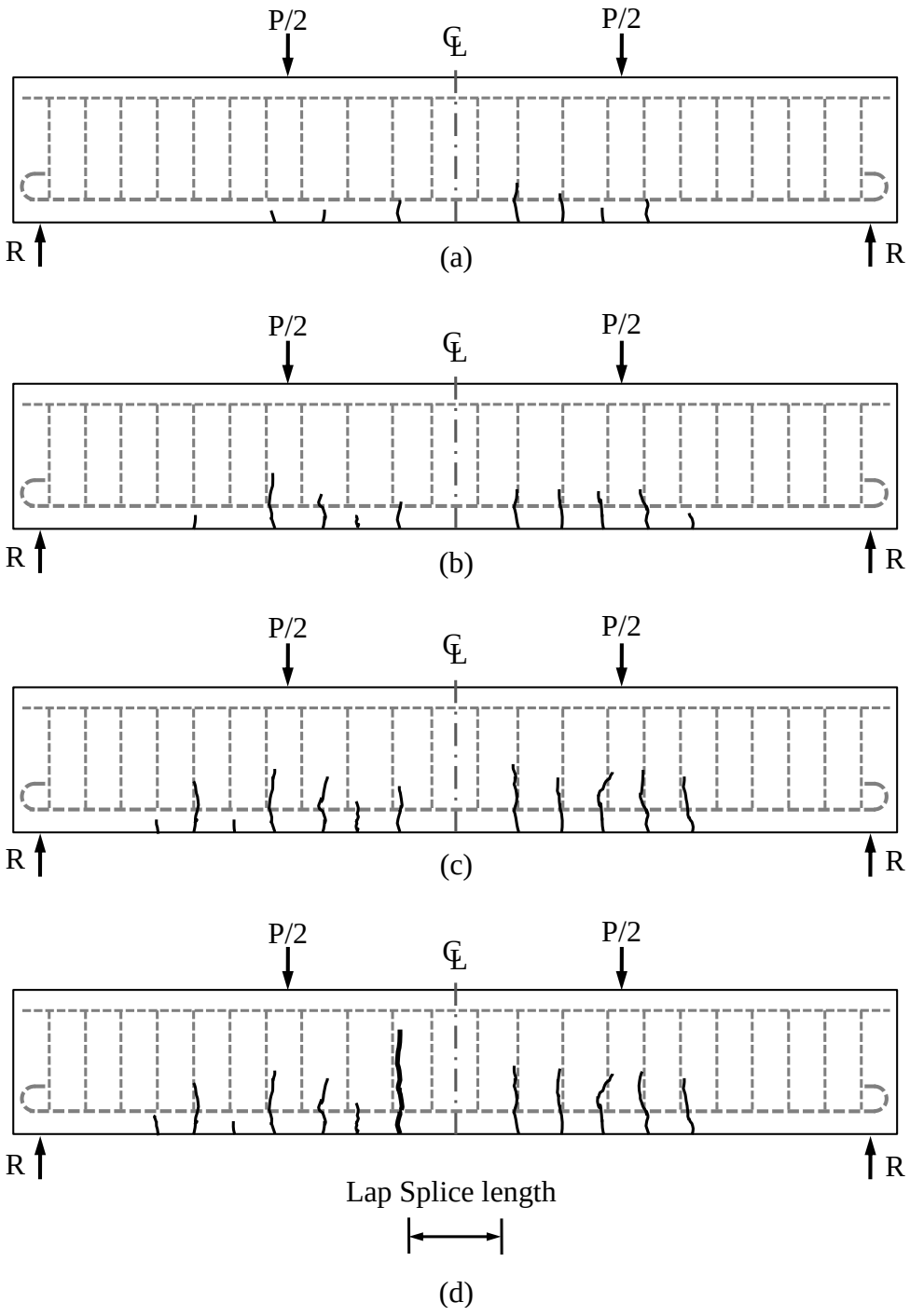

Figure 4C.4. Observed crack pattern - Specimen 25-510: (a) P = 0.4 P_{max}, (b) P = 0.6 P_{max}, (c) P = 0.8 P_{max}, and (d) P = P_{max}

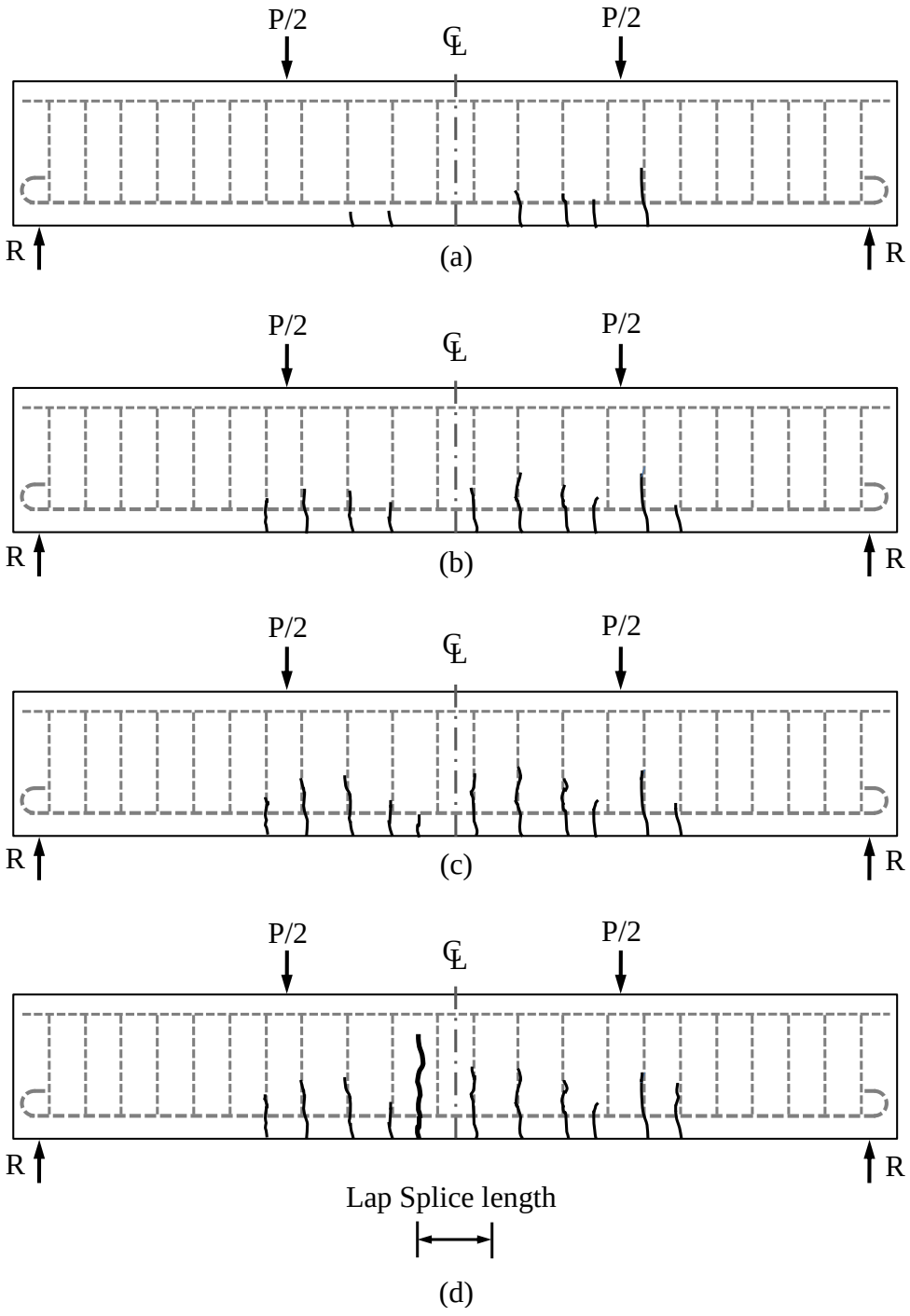

Figure 4C.5. Observed crack pattern - Specimen 32-410: (a) P = 0.6 P_{max}, (b) P = 0.8 P_{max}, (c) P = 0.9 P_{max}, and (d) P = P_{max}

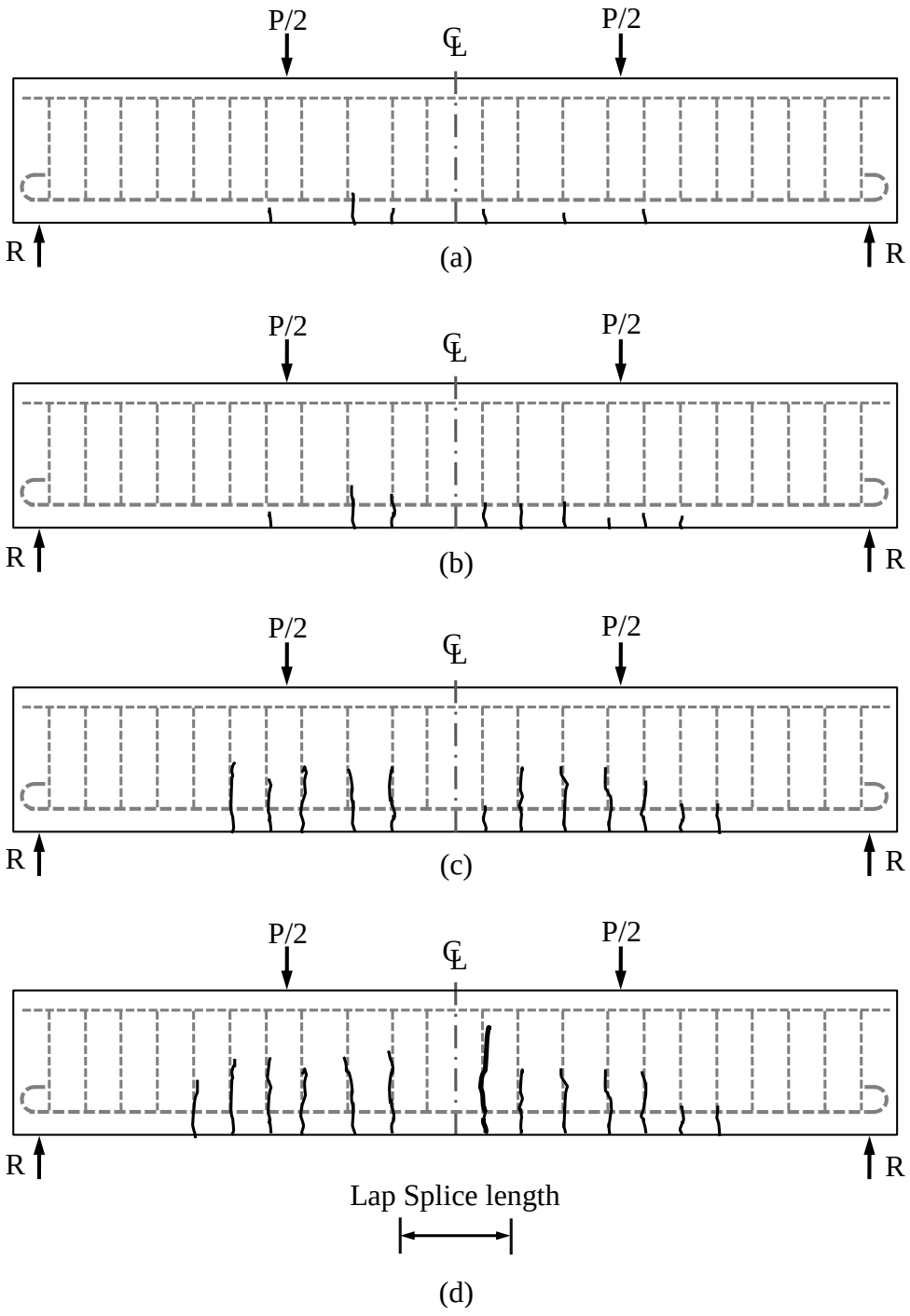

Figure 4C.6. Observed crack pattern - Specimen 32-610: (a) P = 0.3 P_{max}, (b) P = 0.45 P_{max}, (c) P = 0.8 P_{max}, and (d) P = P_{max}

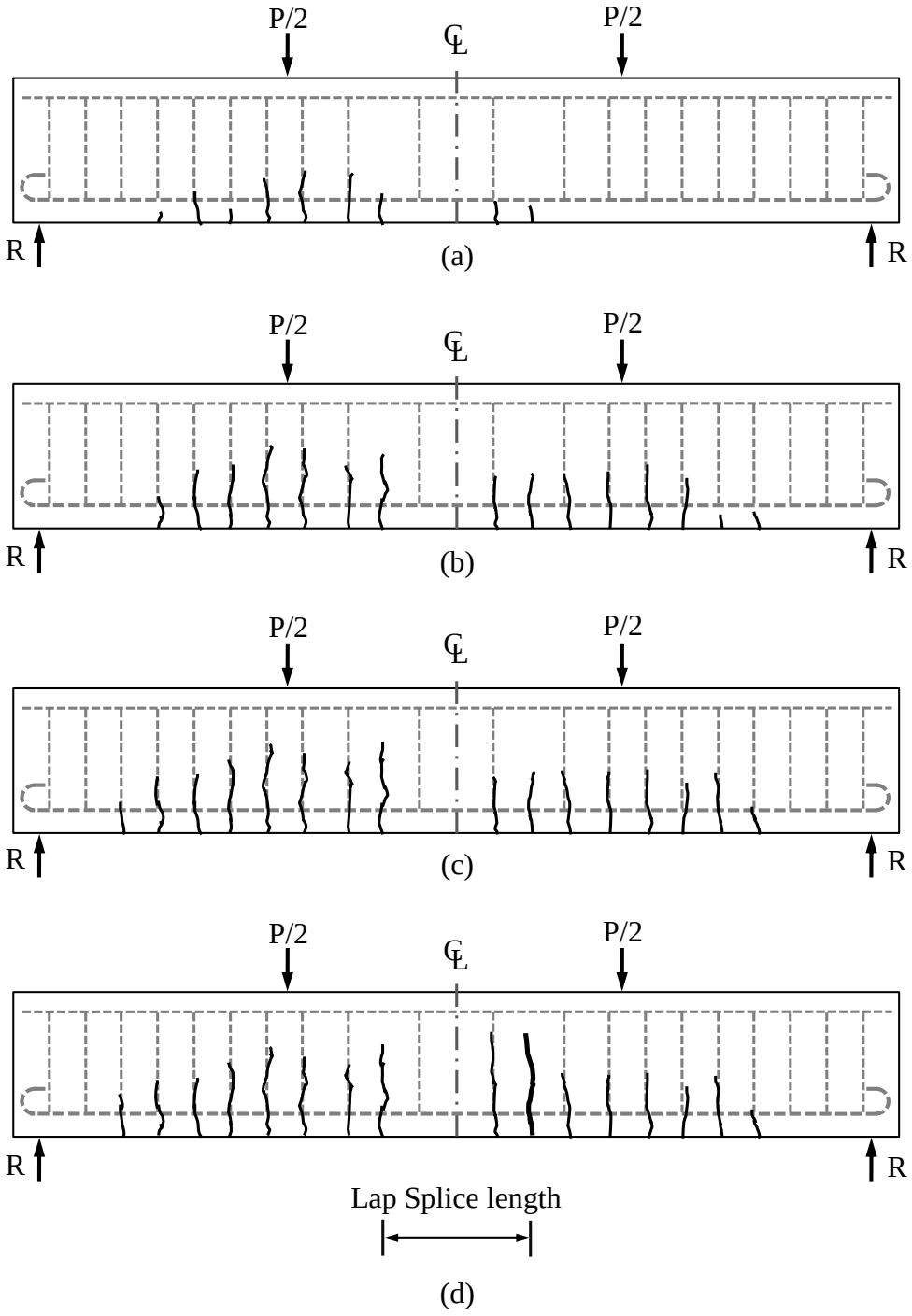

Figure 4C.7. Observed crack pattern - Specimen 32-810: (a) P = 0.4 P_{max}, (b) P = 0.7 P_{max}, (c) P = 0.9 P_{max}, and (d) P = P_{max}

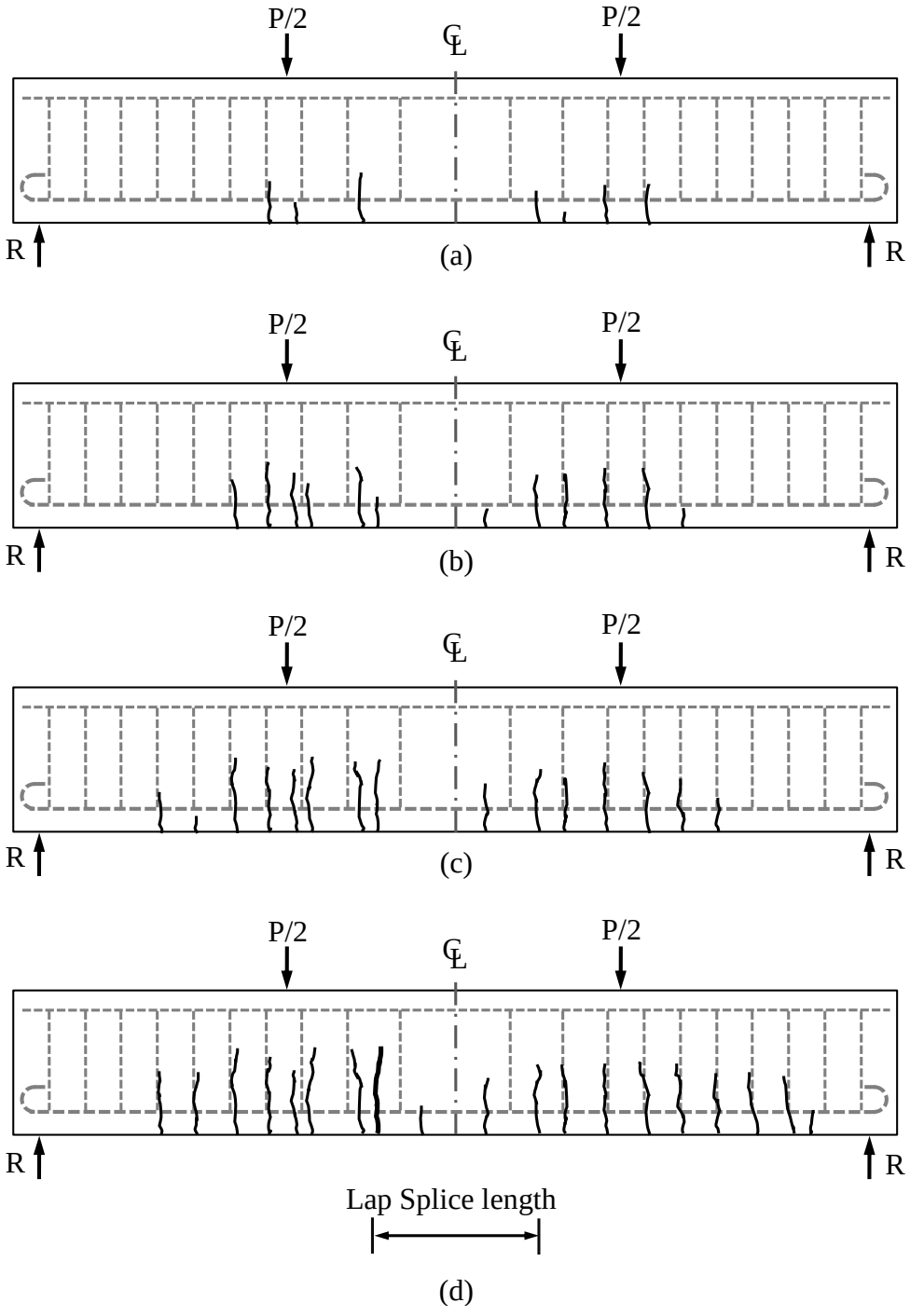

Figure 4C.8. Observed crack pattern - Specimen 32-910: (a) P = 0.3 P_{max}, (b) P = 0. 5 P_{max}, (c) P = 0.9 P_{max}, and (d) P = P_{max}

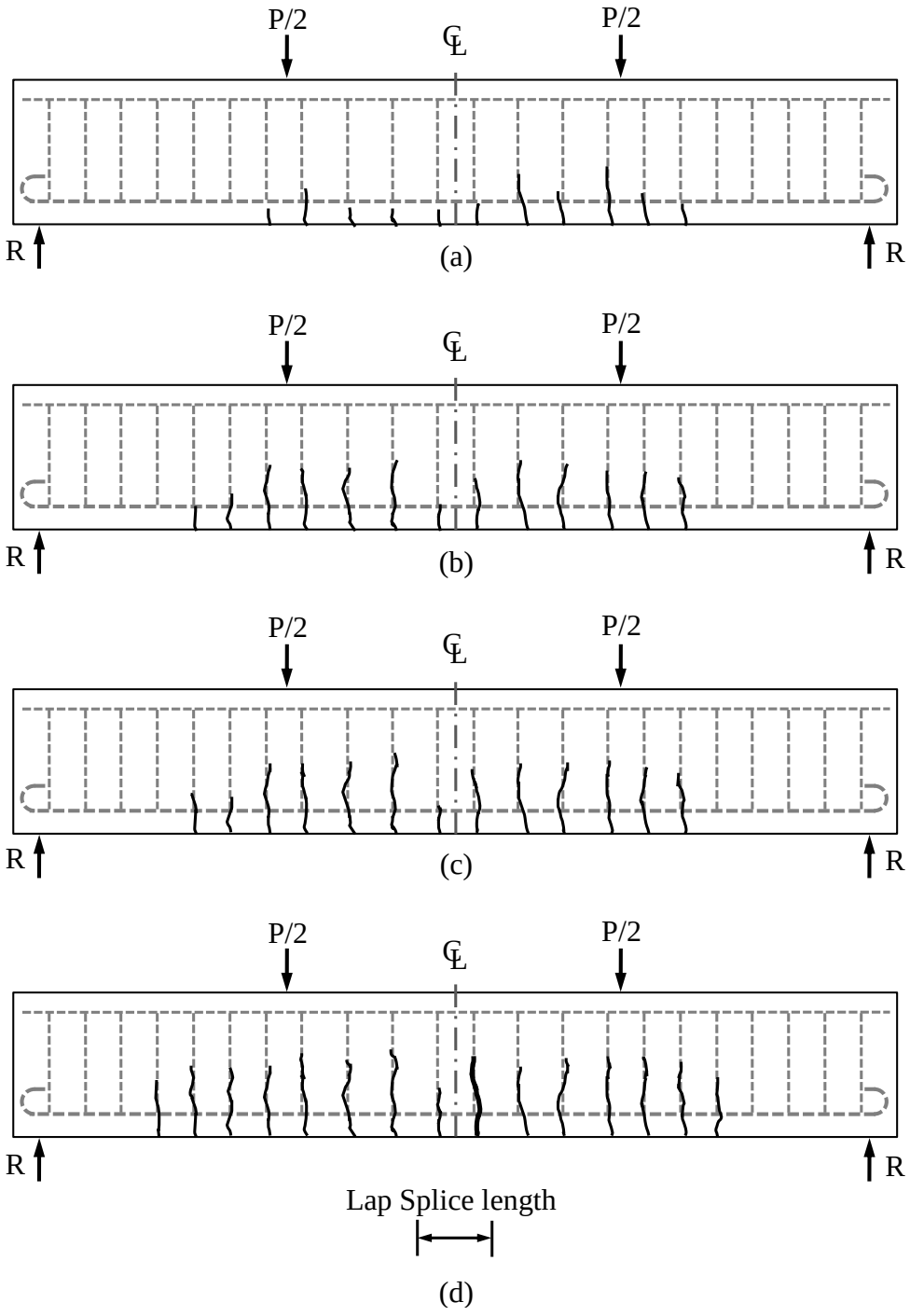

Figure 4C.9. Observed crack pattern - Specimen 25-410I: (a) P = 0.4 P_{max}, (b) P = 0.6 P_{max}, (c) P = 0.75 P_{max}, and (d) P = P_{max}

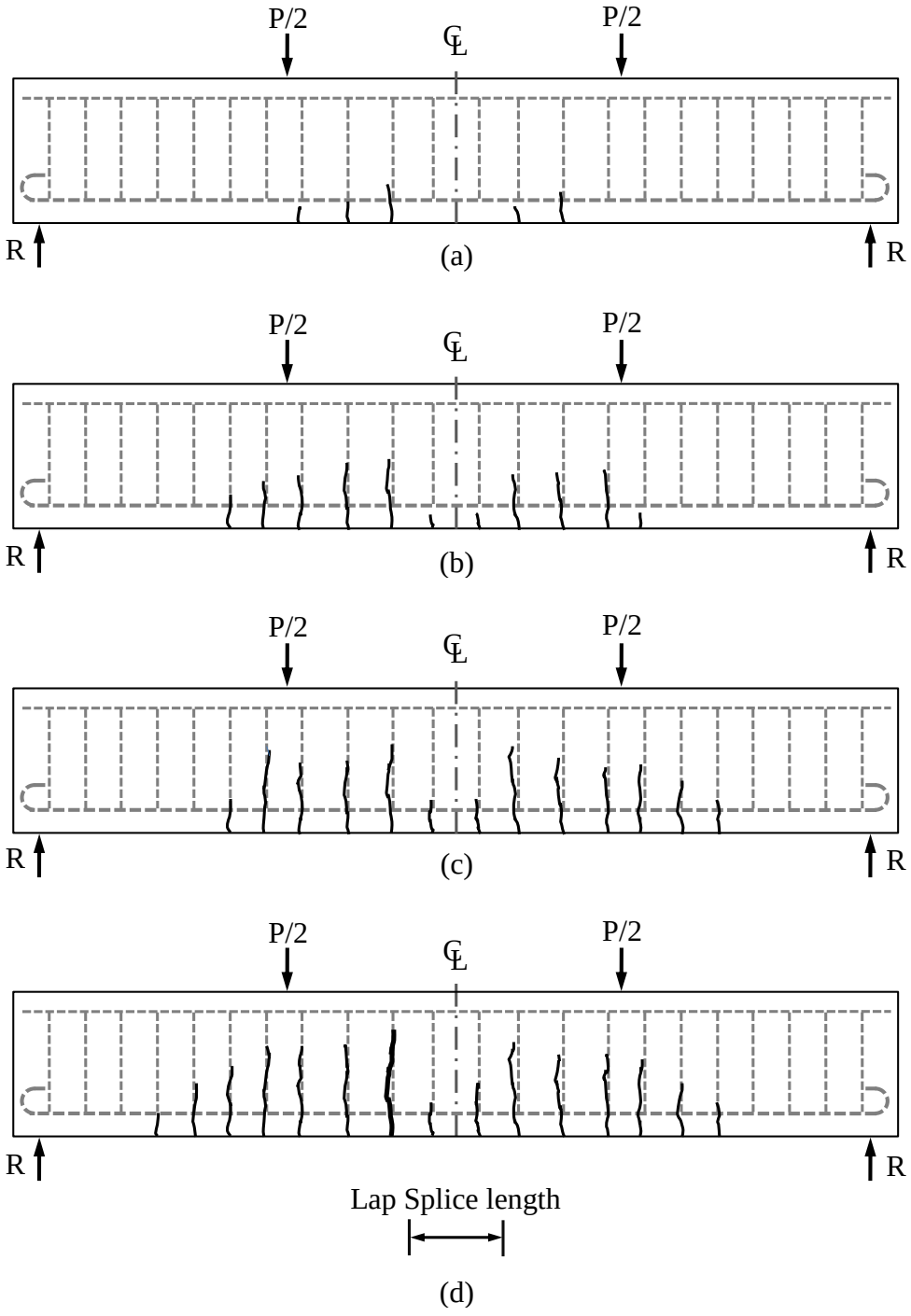

Figure 4C.10. Observed crack pattern - Specimen 25-510I: (a) P = 0.3 P_{max}, (b) P = 0.5 P_{max}, (c) P = 0.75 P_{max}, and (d) P = P_{max}

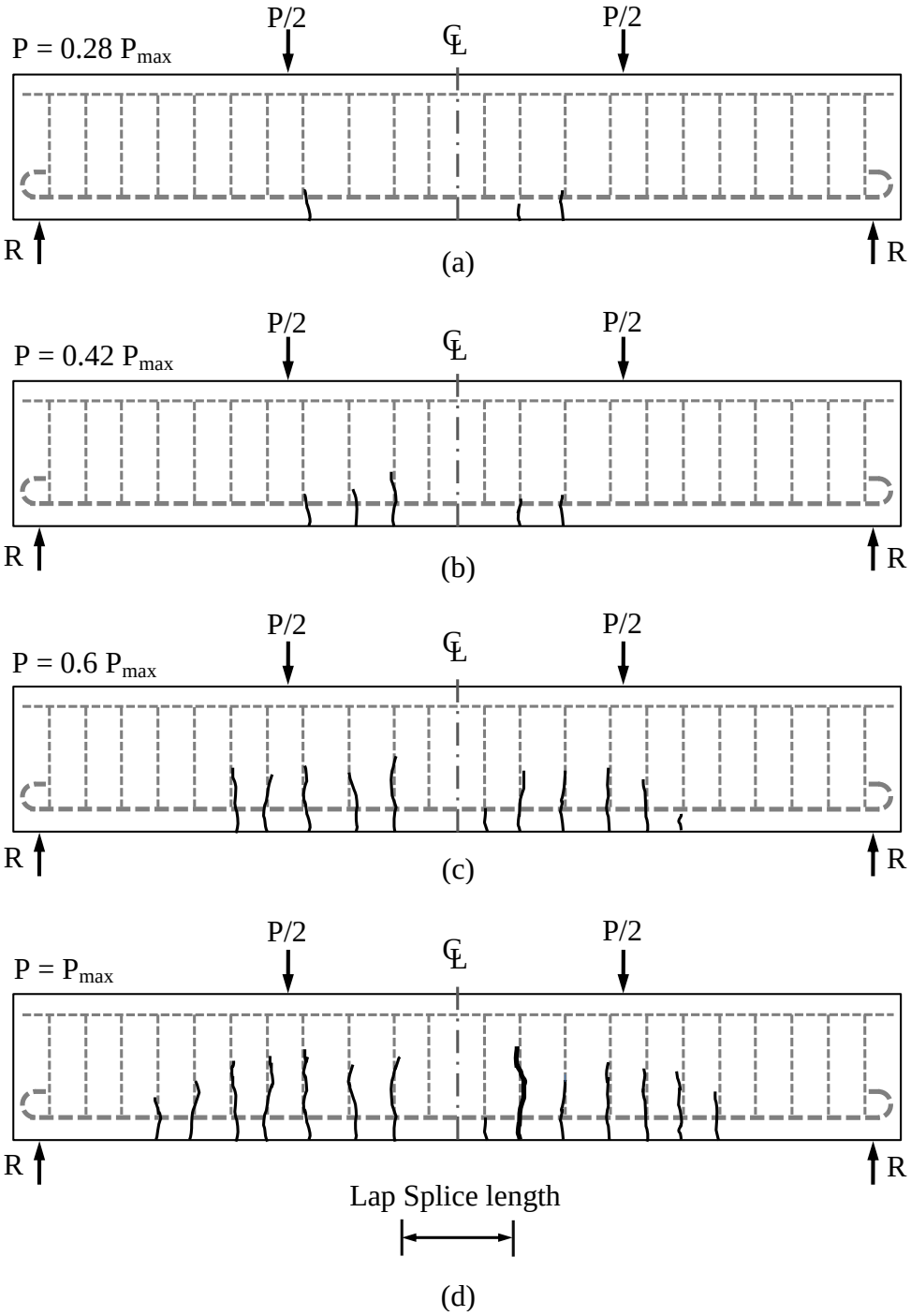

Figure 4C.11. Observed crack pattern - Specimen 25-610I: (a) P = 0.28 P_{max}, (b) P = 0.42 P_{max}, (c) P = 0.6 P_{max}, and (d) P = P_{max}

APPENDIX 4D: Observed Slip at the Ends of the Lapped Bars Following Testing

The concrete cover at the lap splice length ends was removed after testing of the specimens to expose the ends of the lapped longitudinal bars and determine whether any slip occurred during testing as discussed in Section 4.4. Slip of the unloaded (i.e. cut) end indicated that the failure of the specimen initiated by bond due to bar pullout. All of the specimens experienced slip at both ends of the lap splice length with exception of Specimens 19-610 and 25-510I where slip was observed at one end only.

Photographs of the end slip for Specimens 25-410, 25-610, 25-810 and 19-610 are presented in Section 4.4 while the photographs for the remainder specimens are presented here in Figures 4D.1 to 4D.4. All photographs were taken after testing was terminated.

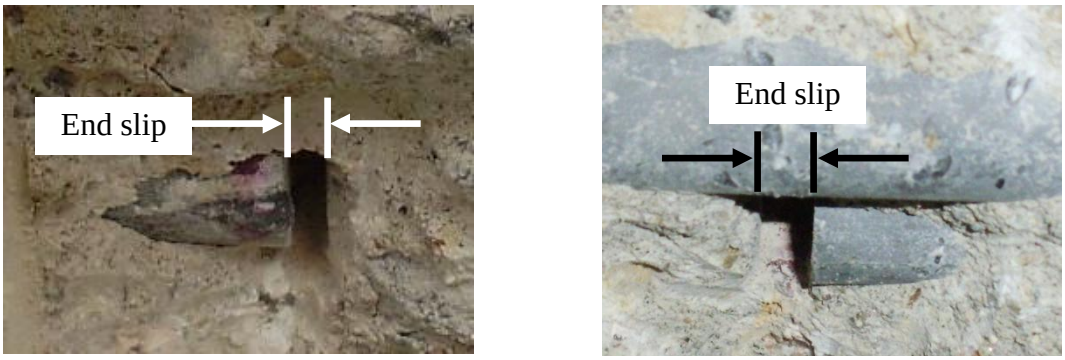

(a)

(b)

(c)

Figure 4D.1. End slip: (a) Specimen 19-305, (b) Specimen 19-410, and (c) Specimen 19-510

Figure 4D.2. Eng slip – Specimen 25-510.

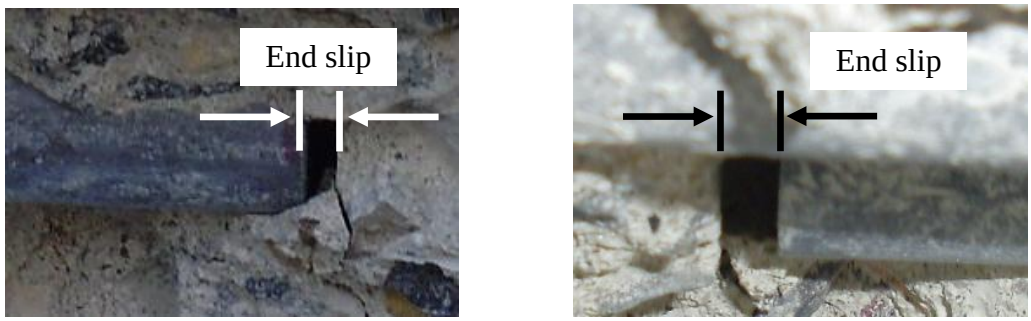

(a)

(b)

Figure 4D.3. End slip: (a) Specimen 32-410, and (b) Specimen 32-610.

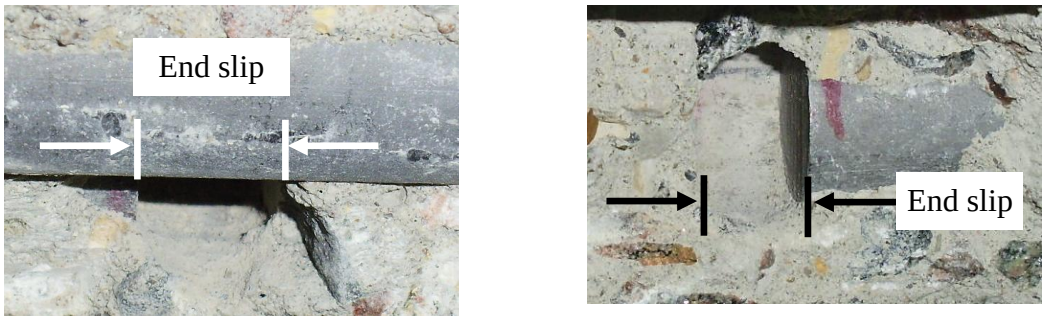

(c)

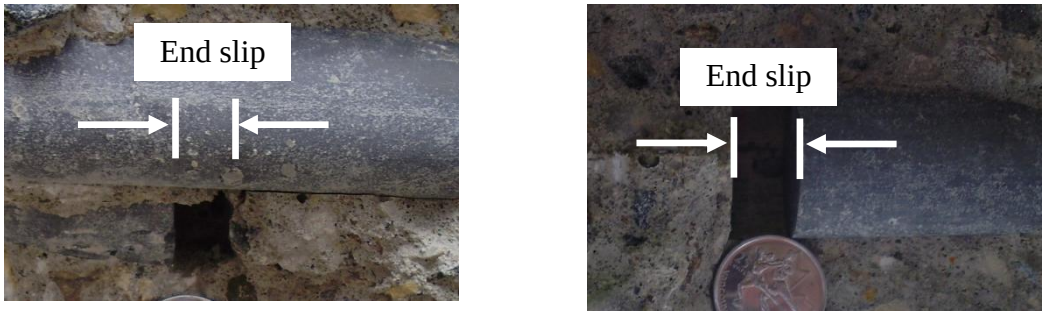

(d)

Figure 4D.3. (continued) End slip: (c) Specimen 32-810, and (d) Specimen 32-910.

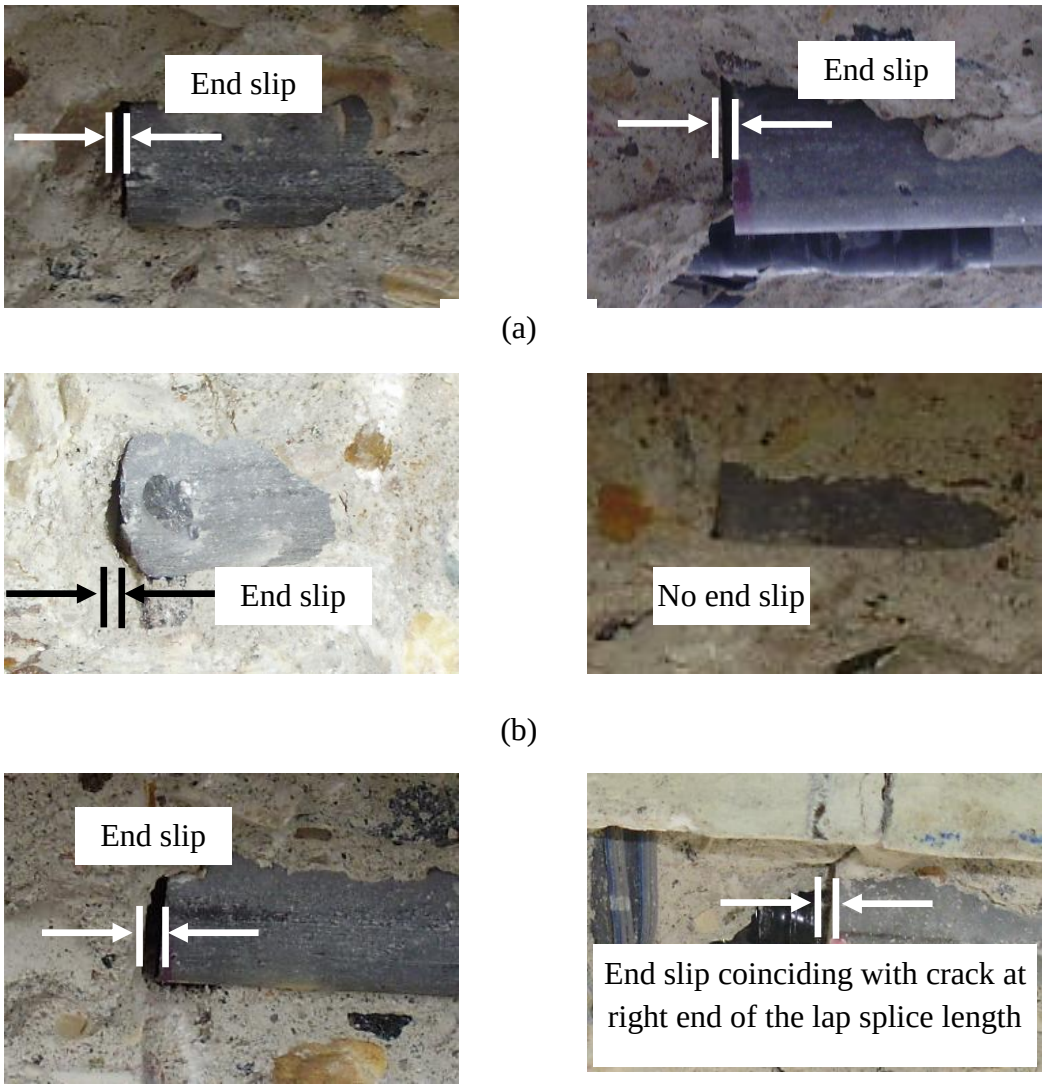

Figure 4D.4. End slip: (a) Specimen 25-410I, (b) Specimen 25-510I and (c) Specimen 25-610I.

APPENDIX 4E: Load versus Deflection

The load versus deflection behaviour of the specimens was obtained from the LVDT and load cell readings. Locations of the LVDTs are presented in Section 3.6. The theoretical load-deflection curves for the specimens were also derived to provide a comparison with the actual specimen behaviour as discussed in Section 4.5. Load versus deflection behaviour of Specimens 25-410, 25-610, 25-810, and 19-610 are discussed in Section 4.5 while the load-deflection behaviour of the remaining specimens are presented here in Figures 4E.1 to 4E.11.

The load versus deflection of Specimen 32-910, which has been identified as outlier, is shown in Figures 4E.8, and indicates that the specimen experienced large plastic deformations between subsequent load cycles. Loading and unloading likely affected the bond capacity of this specimen and therefore its test results are not compared with the other specimens which were tested under monotonically increasing static loading.

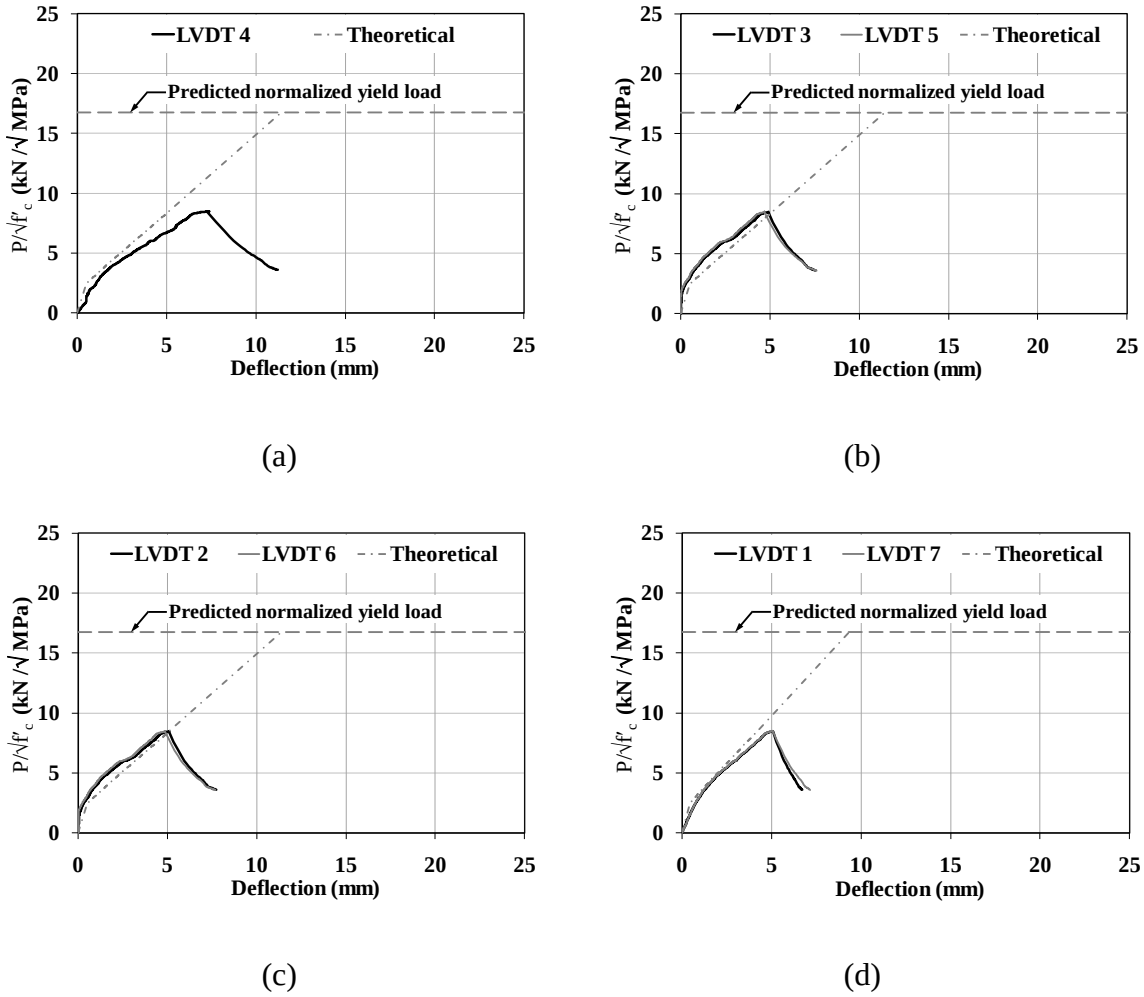

Figure 4E.1. Normalized applied load versus deflection - Specimen 19-305: (a) midspan, (b) quarter points along the lap splice length, (c) ends of the lap splice length, and (d) points of applied load.

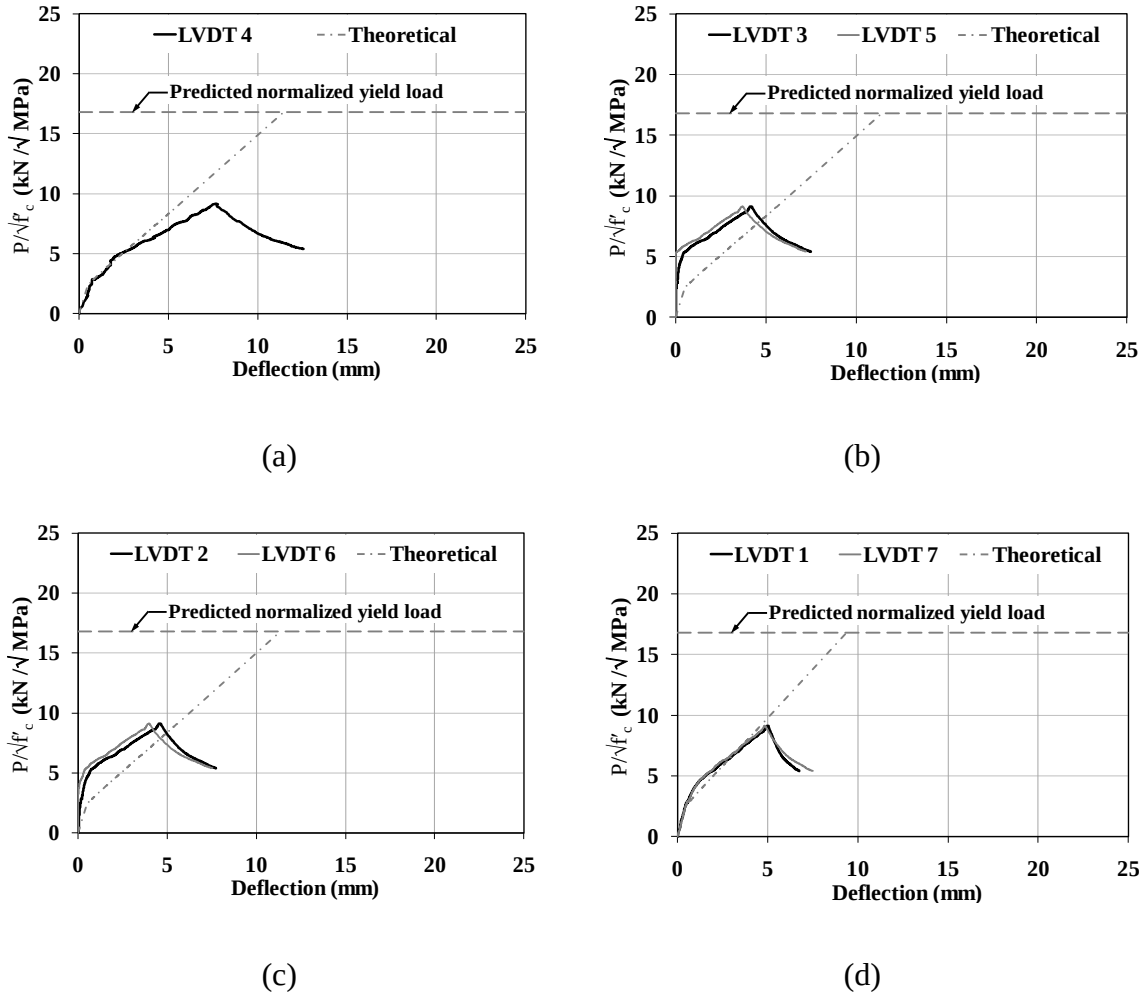

Figure 4E.2. Normalized applied load versus deflection - Specimen 19-410: (a) midspan, (b) quarter points along the lap splice length, (c) ends of the lap splice length, and (d) points of applied load.

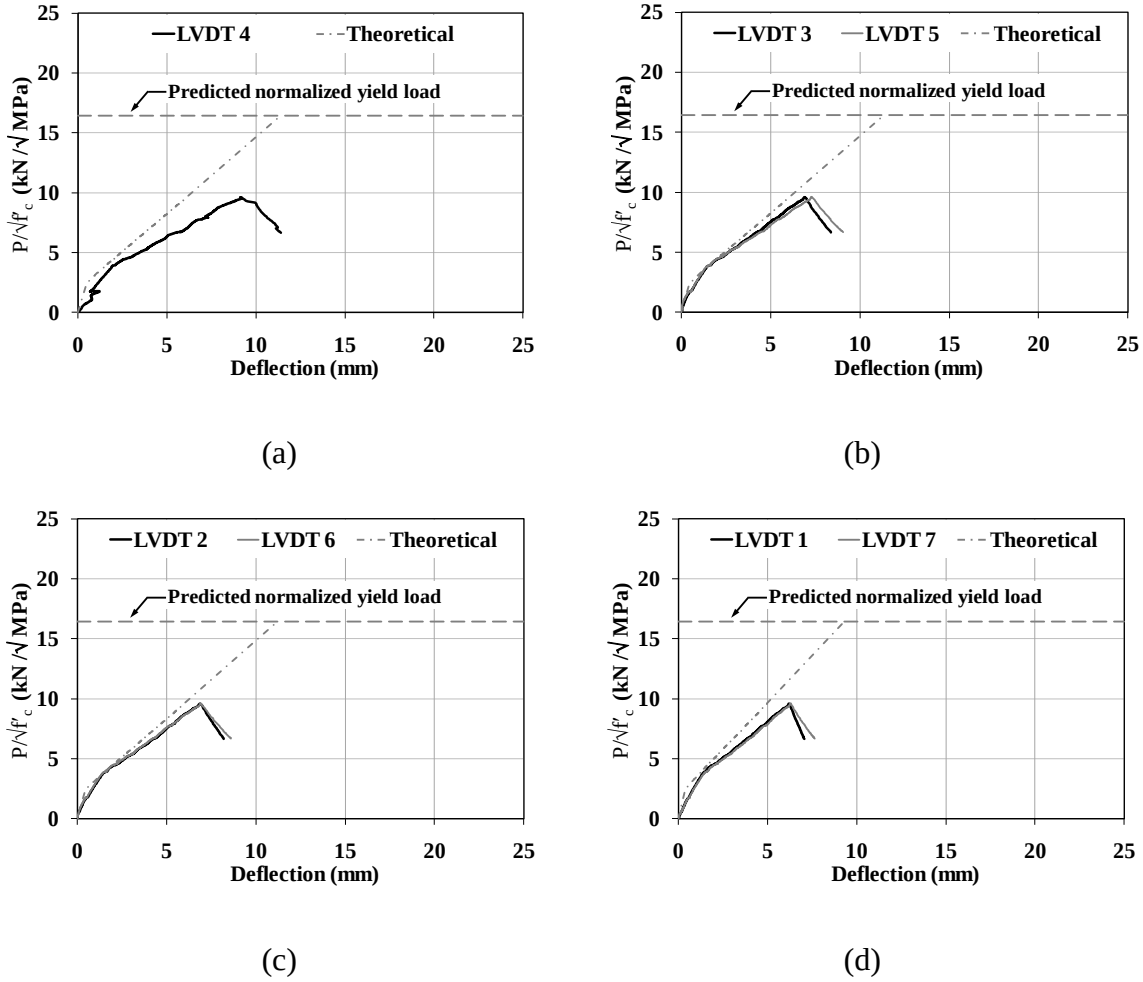

Figure 4E.3. Normalized applied load versus deflection - Specimen 19-510: (a) midspan, (b) quarter points along the lap splice length, (c) ends of the lap splice length, and (d) points of applied load.

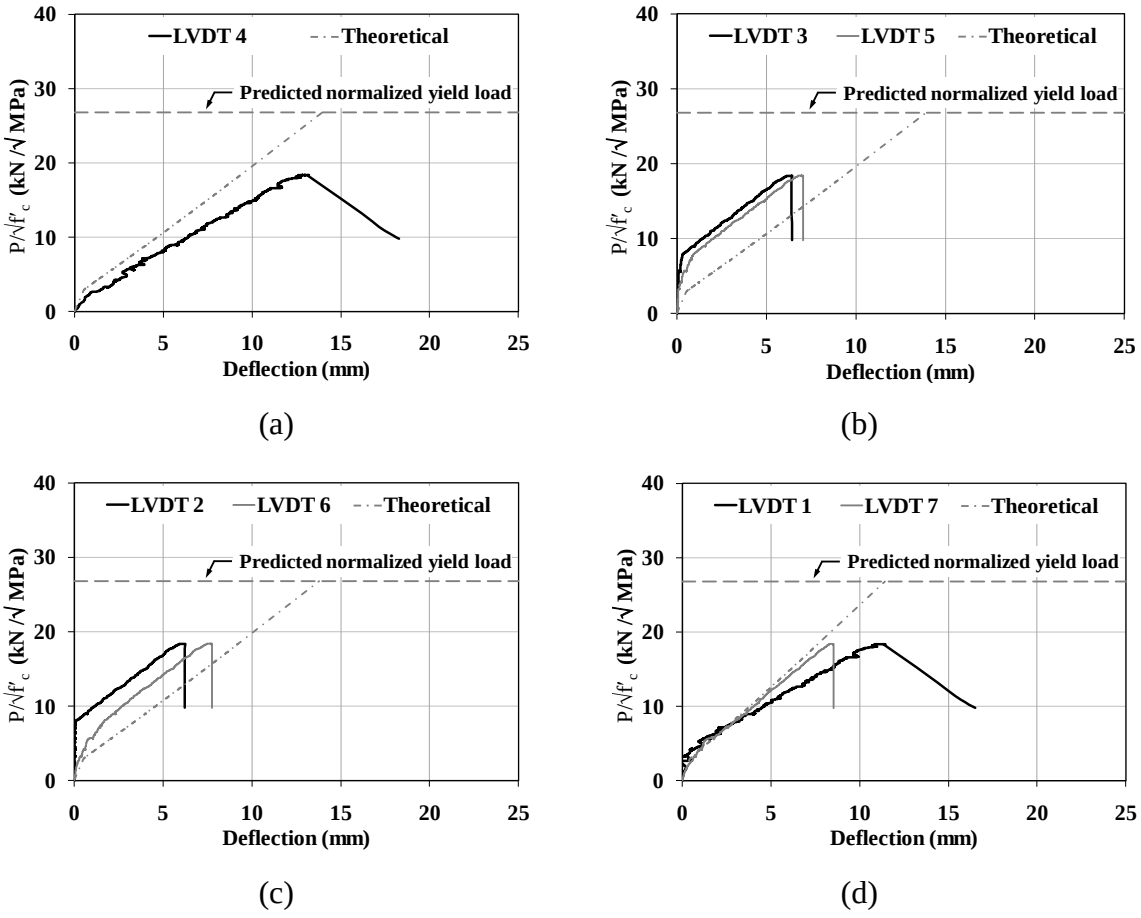

Figure 4E.4. Normalized applied load versus deflection - Specimen 25-510: (a) midspan, (b) quarter points along the lap splice length, (c) ends of the lap splice length, and (d) points of applied load.

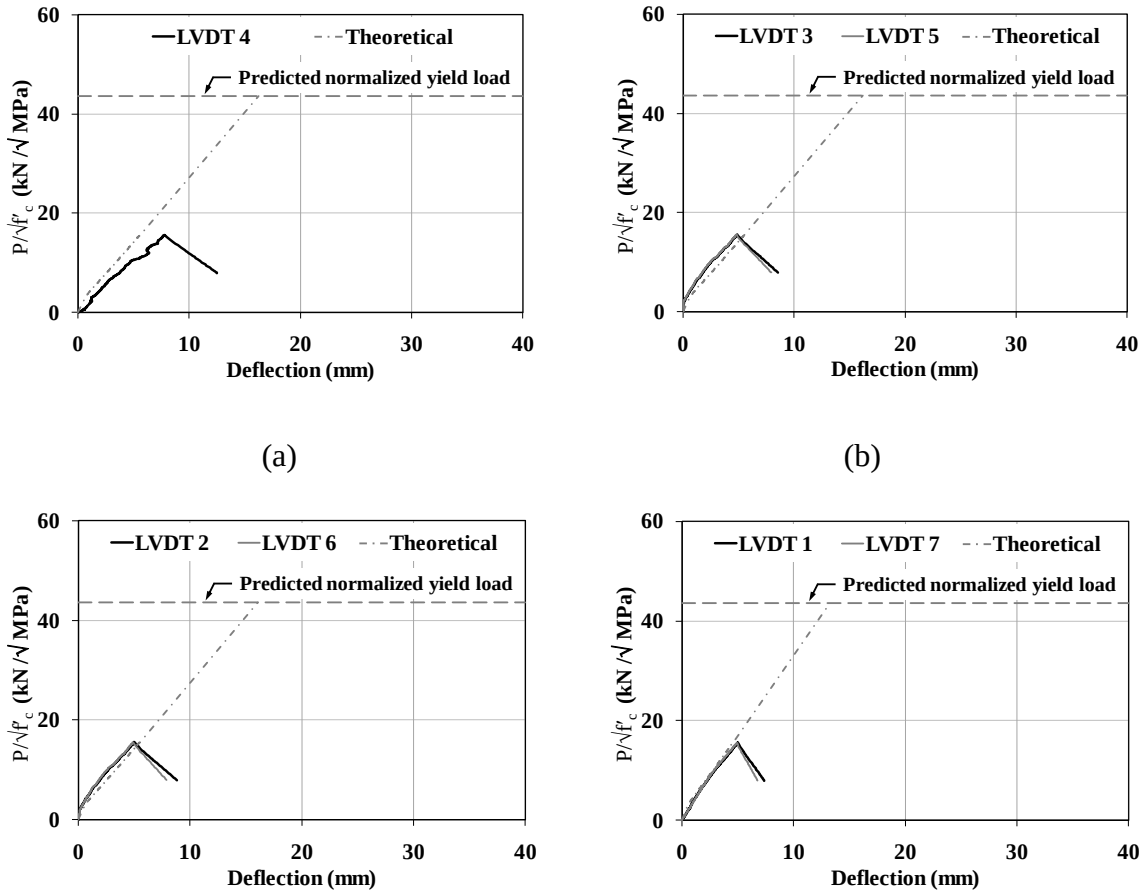

Figure 4E.5. Normalized applied load versus deflection - Specimen 32-410: (a) midspan, (b) quarter points along the lap splice length, (c) ends of the lap splice length, and (d) points of applied load.

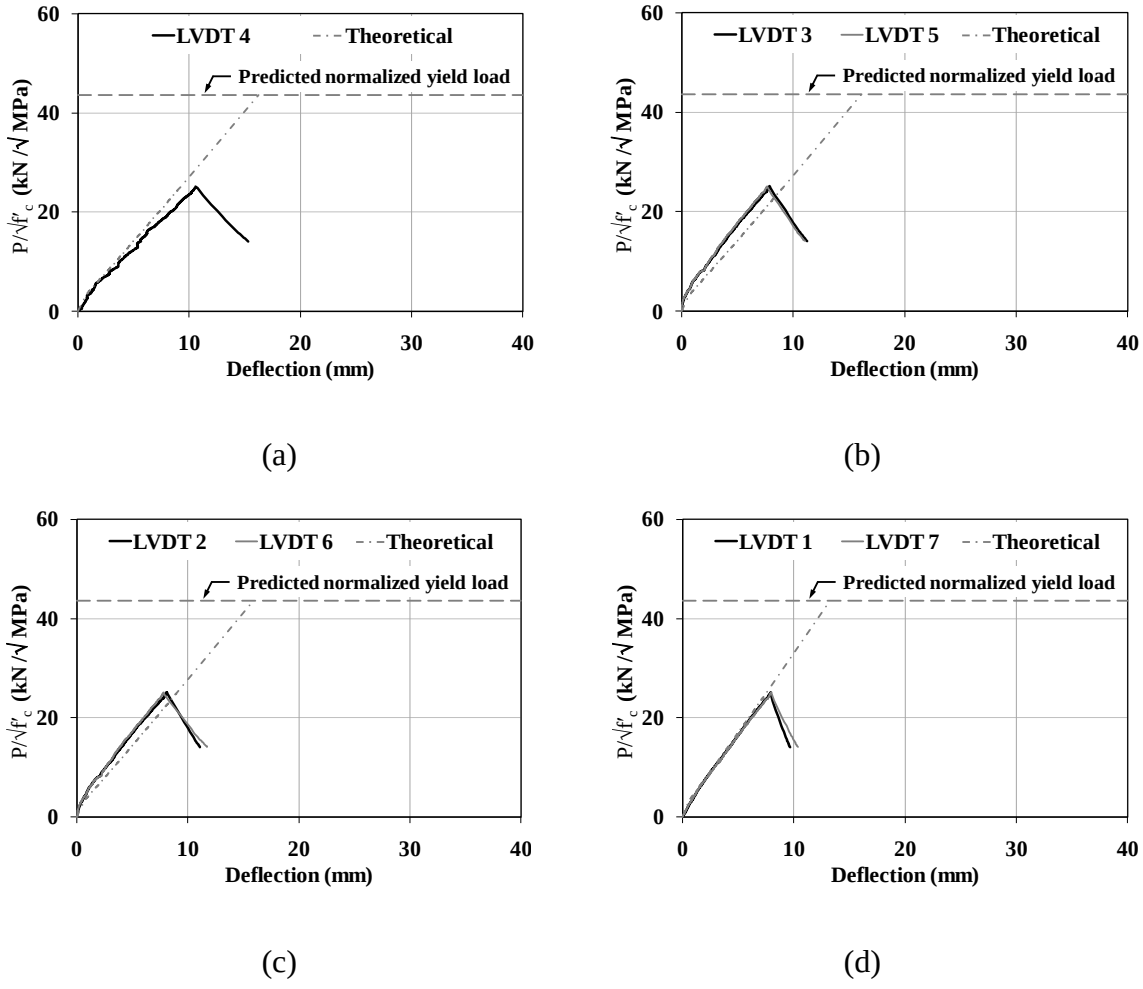

Figure 4E.6. Normalized applied load versus deflection - Specimen 32-610: (a) midspan, (b) quarter points along the lap splice length, (c) ends of the lap splice length, and (d) points of applied load.

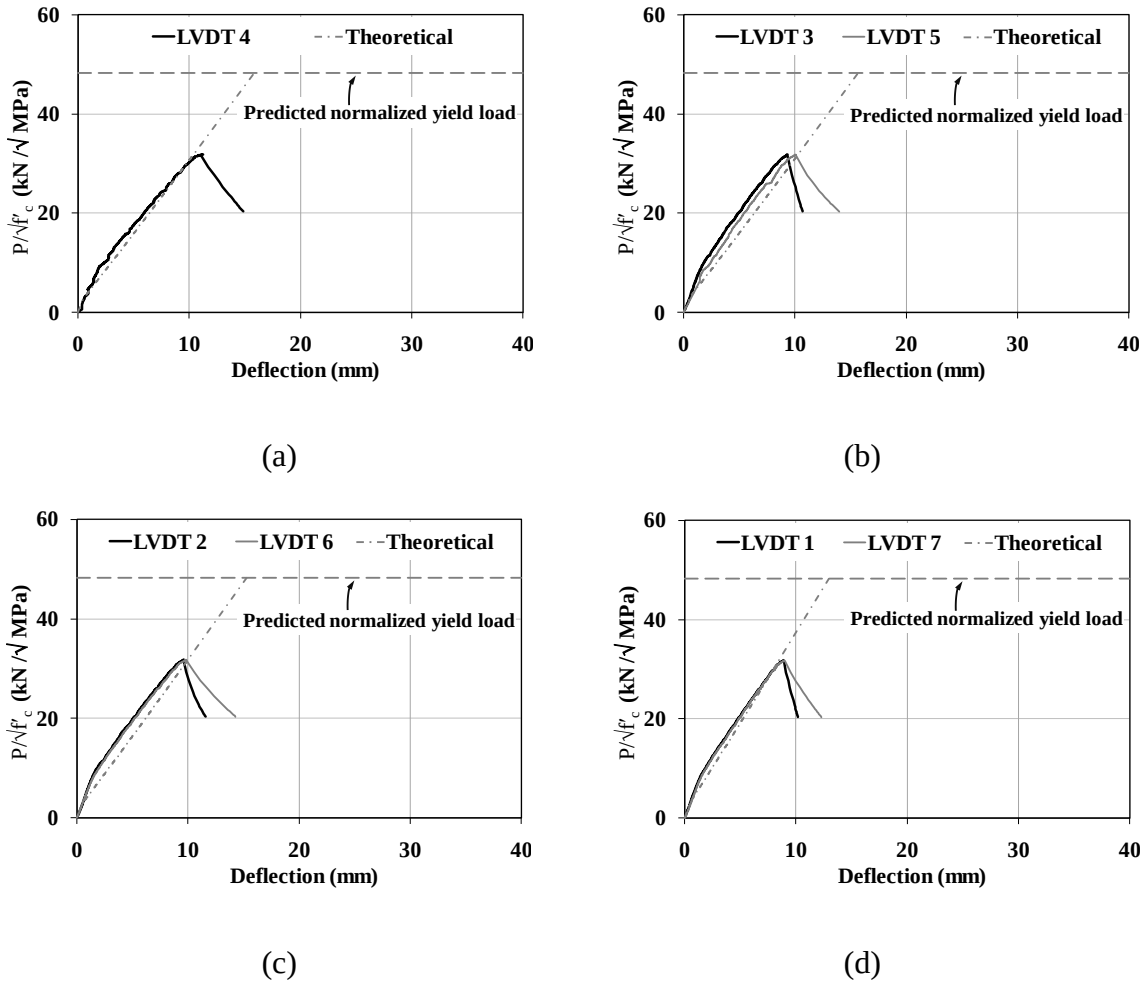

Figure 4E.7. Normalized applied load versus deflection - Specimen 32-810: (a) midspan, (b) quarter points along the lap splice length, (c) ends of the lap splice length, and (d) points of applied load.

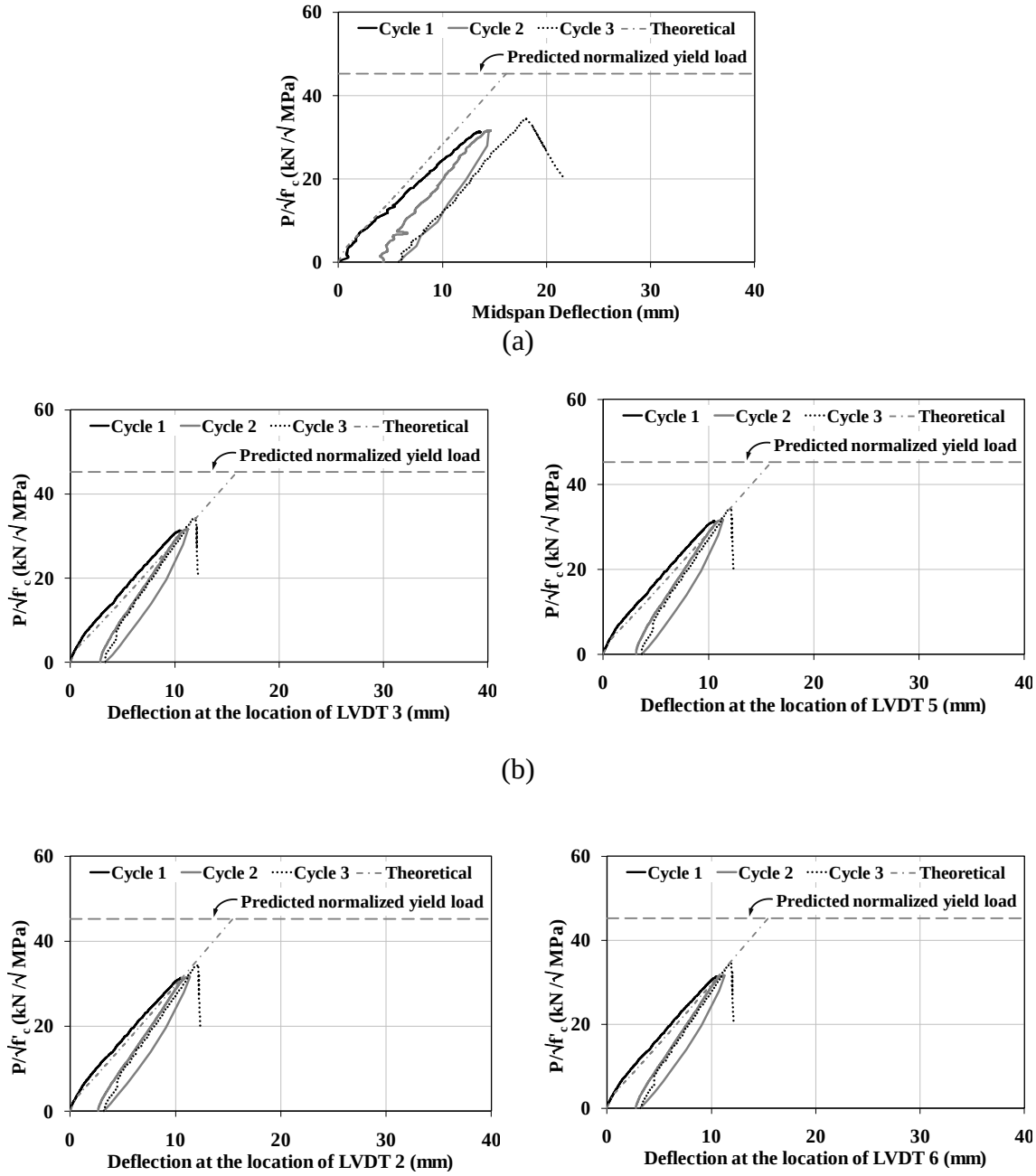

Figure 4E.8. Normalized applied load versus deflection - Specimen 32-910: (a) midspan, (b) quarter points along the lap splice length, and (c) ends of the lap splice length.

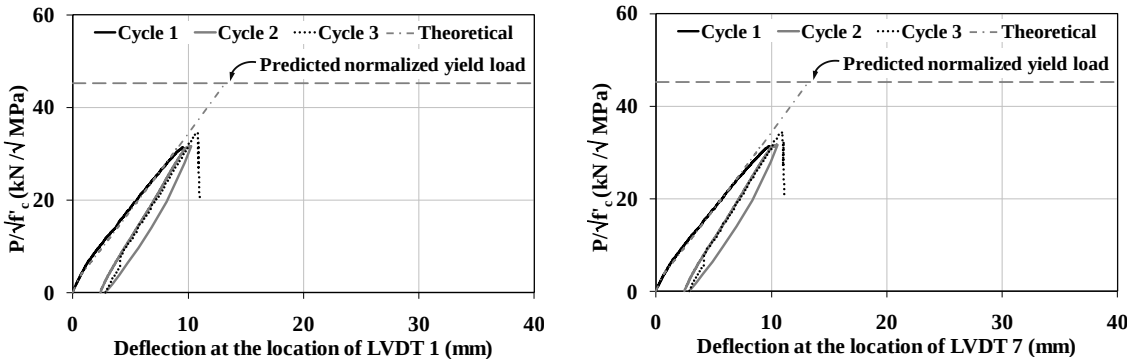

(d)

Figure 4E.8. (continued) Normalized applied load versus deflection - Specimen 32-910: (d) points of applied load.

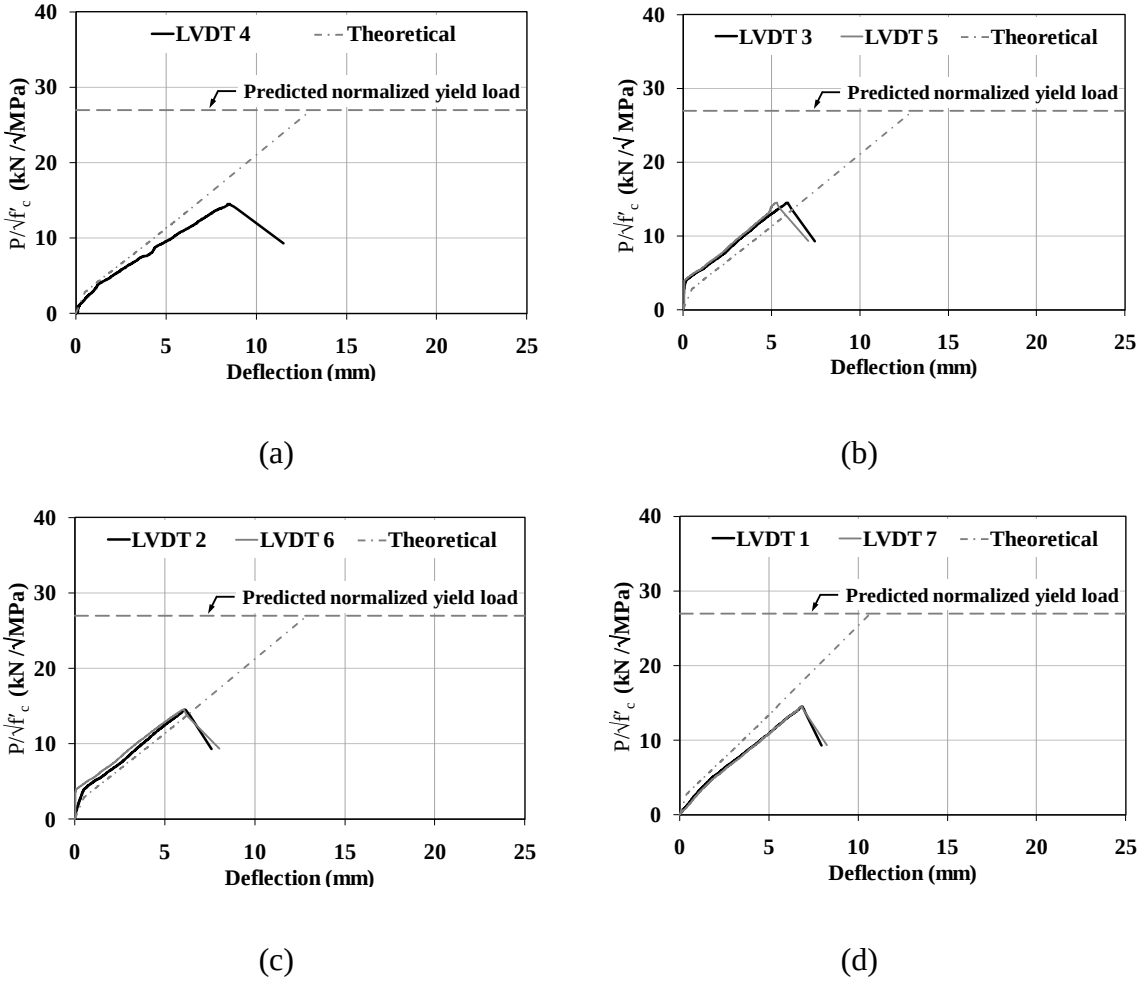

Figure 4E.9. Normalized applied load versus deflection - Specimen 25-410I: (a) midspan, (b) quarter points along the lap splice length, (c) ends of the lap splice length, and (d) points of applied load.

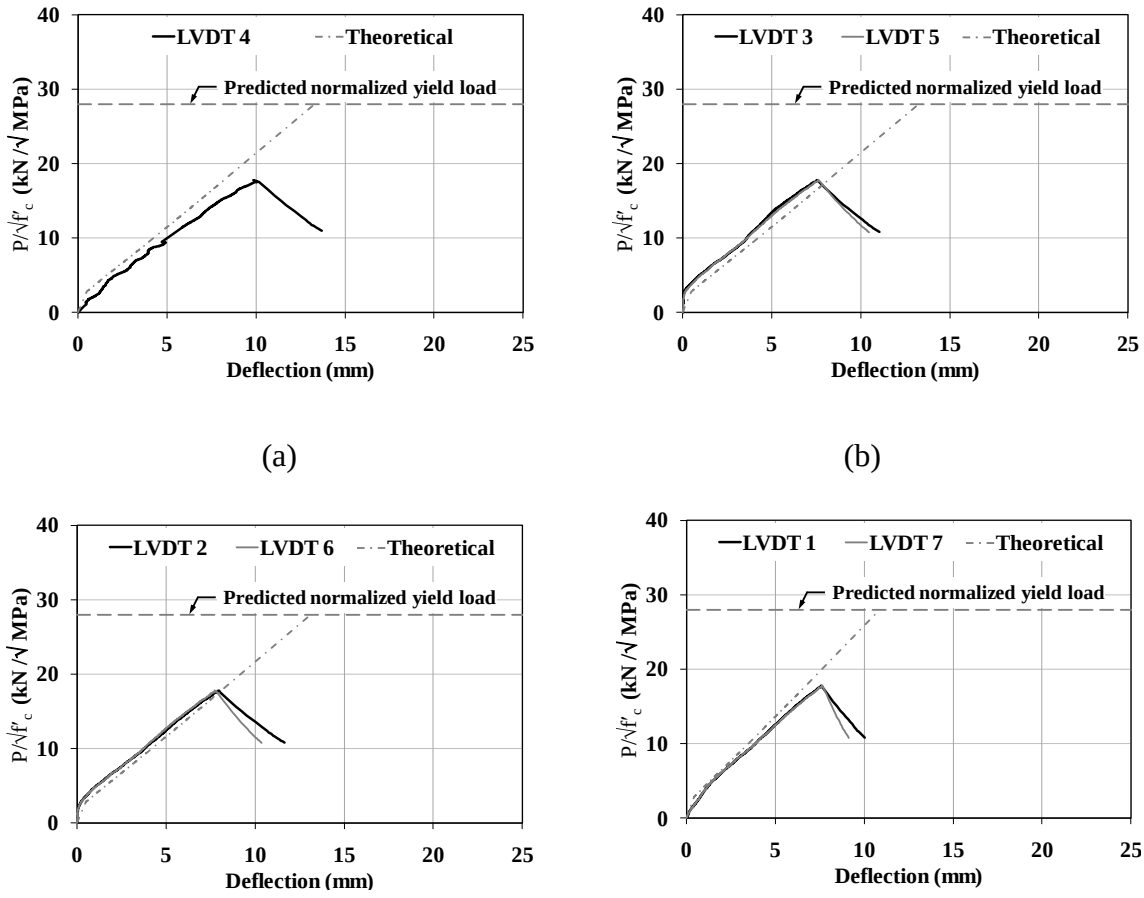

Figure 4E.10. Normalized applied load versus deflection - Specimen 25-510I: (a) midspan, (b) quarter points along the lap splice length, (c) ends of the lap splice length, and (d) points of applied load.

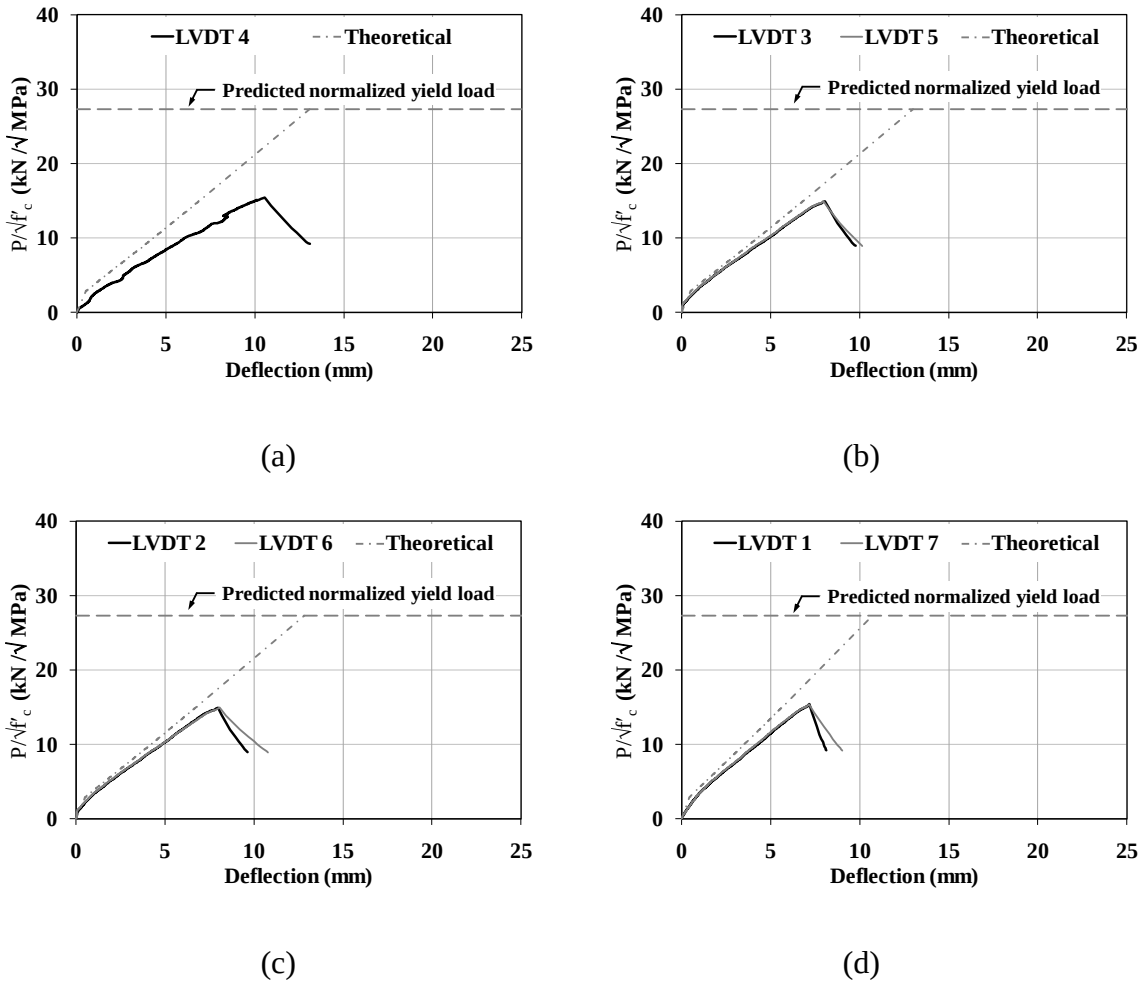

Figure 4E.11. Normalized applied load versus deflection - Specimen 25-610I: (a) midspan, (b) quarter points along the lap splice length, (c) ends of the lap splice length, and (d) points of applied load.

APPENDIX 4F: Deflection Profile

The specimens' deflection profiles at different load levels are derived from the LVDT readings and compared with their theoretical deflection profiles as discussed in Section 4.5. The deflection profile for Specimens 25-410, 25-610, 25-810, and 19-610 are discussed in Section 4.5 while the remainder specimens are presented here. The deflection profile for the theoretical first cracking load and the load levels for which crack patterns are presented in Appendix 4C are presented.

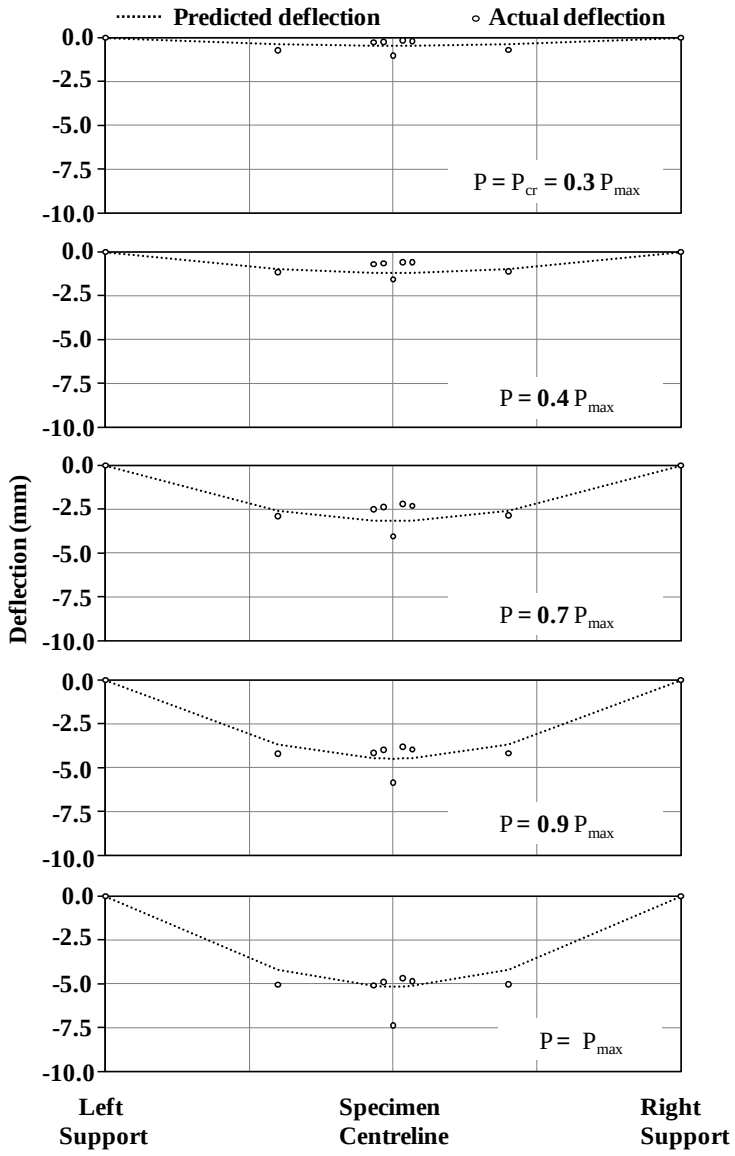

Figure 4F.1. Deflection profile at different load levels - Specimen 19-305

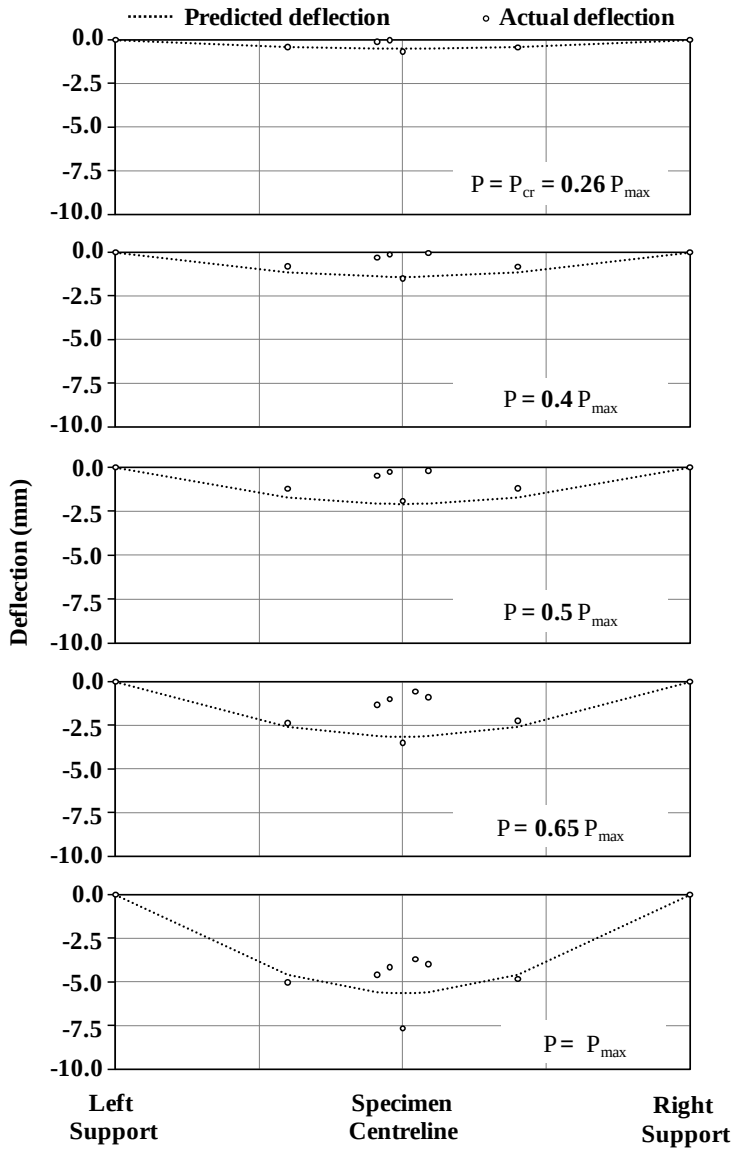

Figure 4F.2. Deflection profile at different load levels - Specimen 19-410

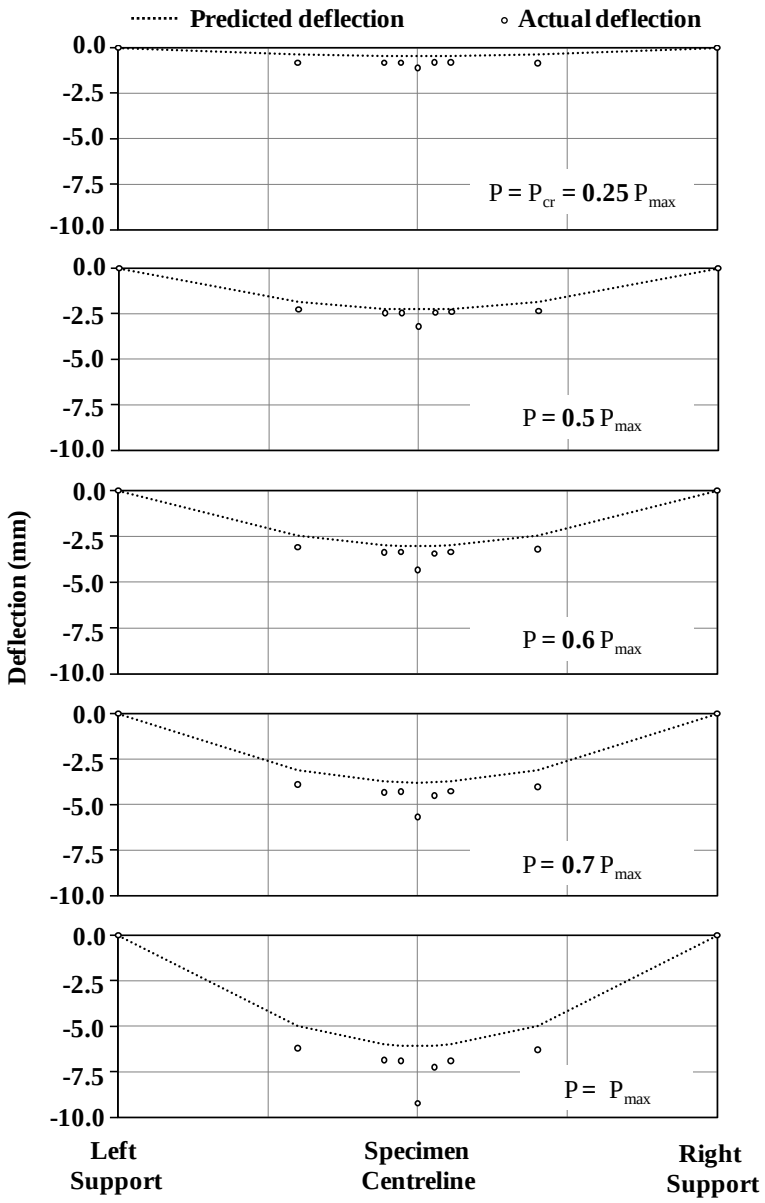

Figure 4F.3. Deflection profile at different load levels - Specimen 19-510

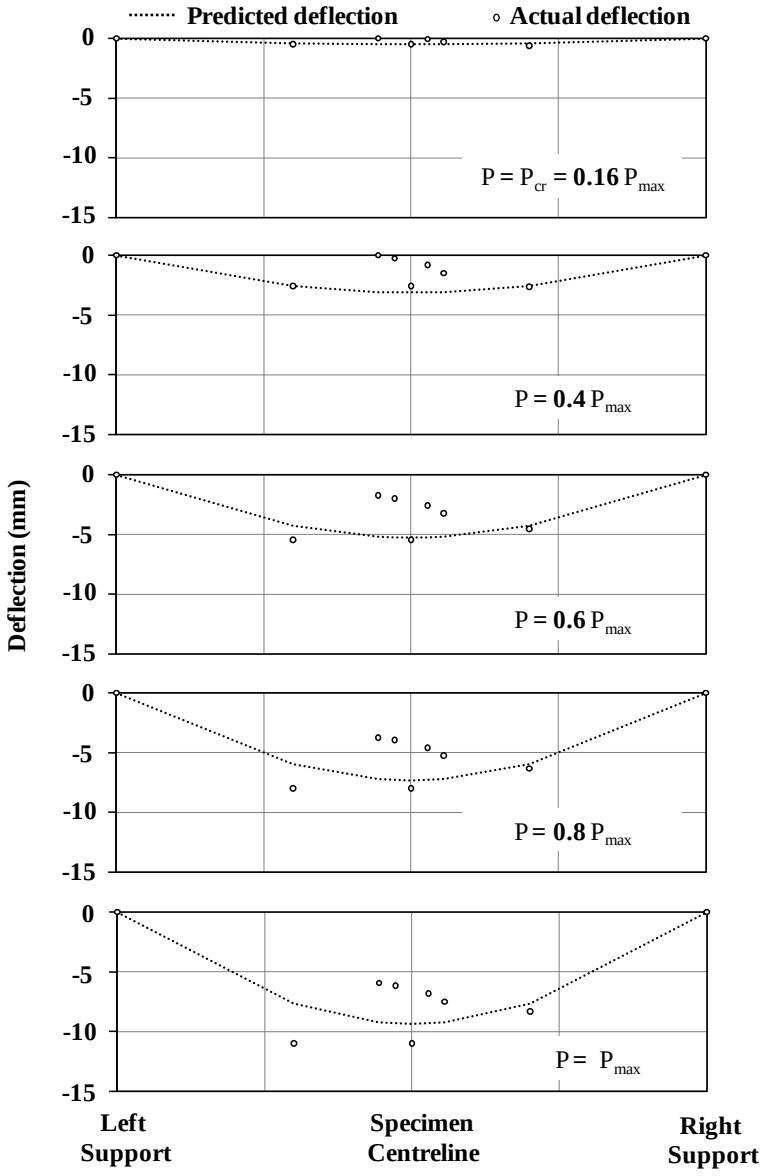

Figure 4F.4. Deflection profile at different load levels - Specimen 25-510

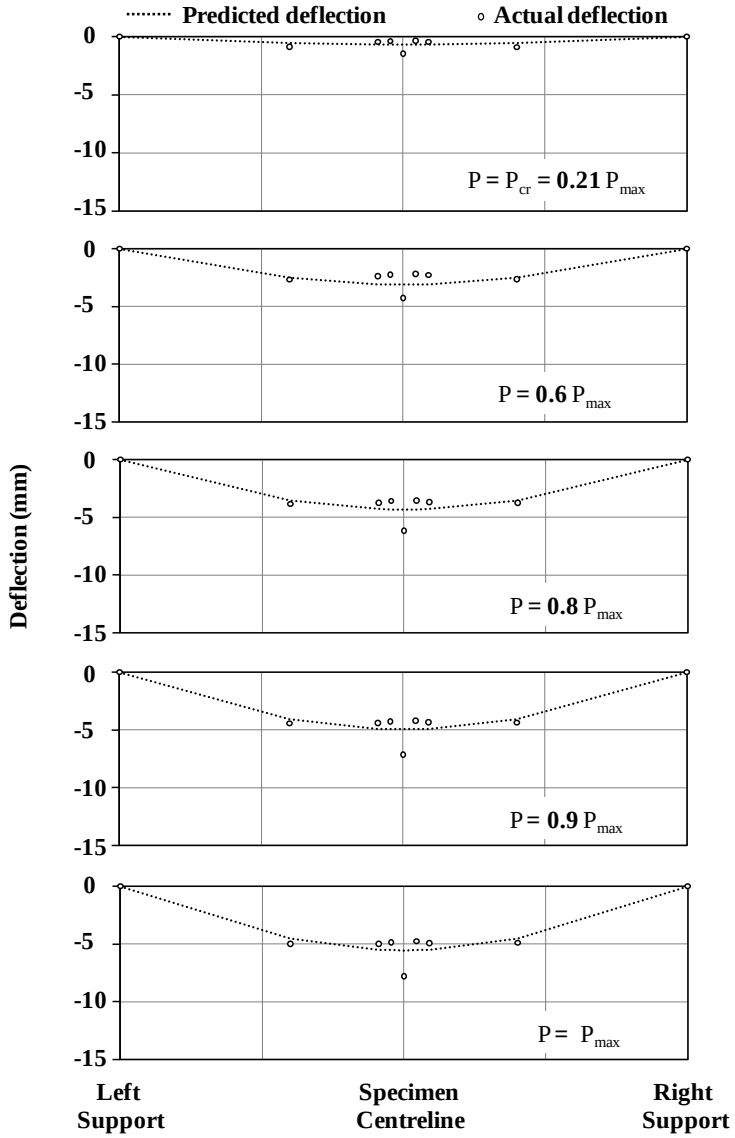

Figure 4F.5. Deflection profile at different load levels - Specimen 32-410

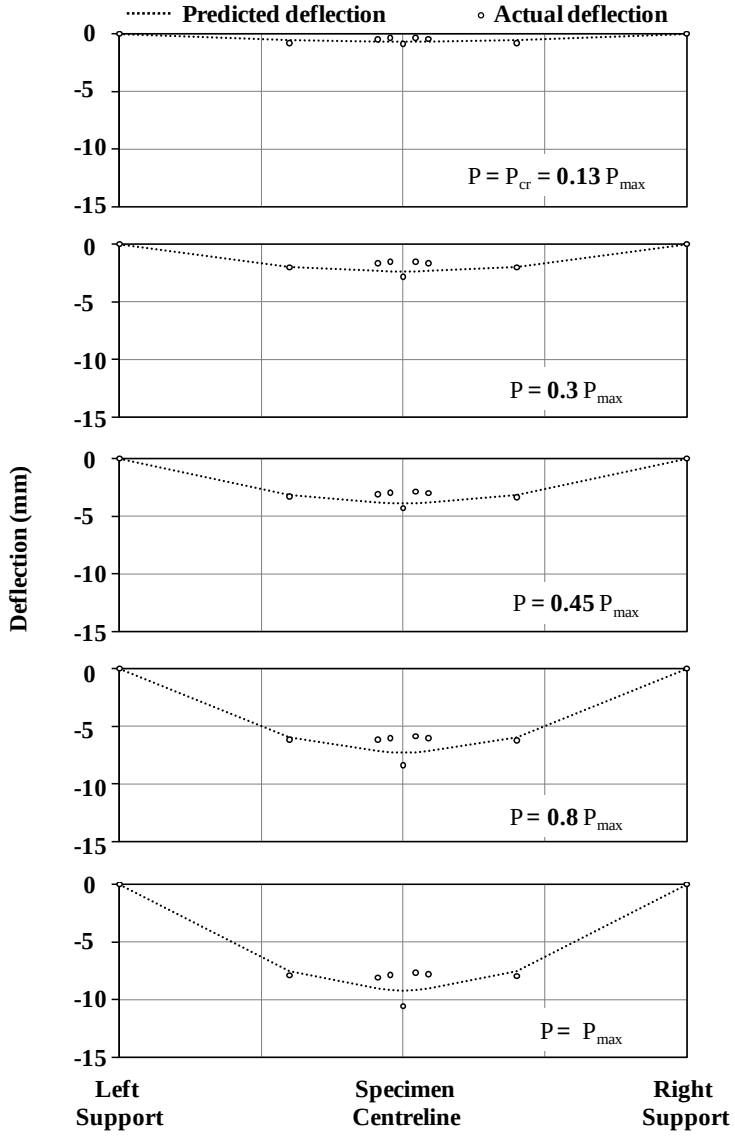

Figure 4F.6. Deflection profile at different load levels - Specimen 32-610

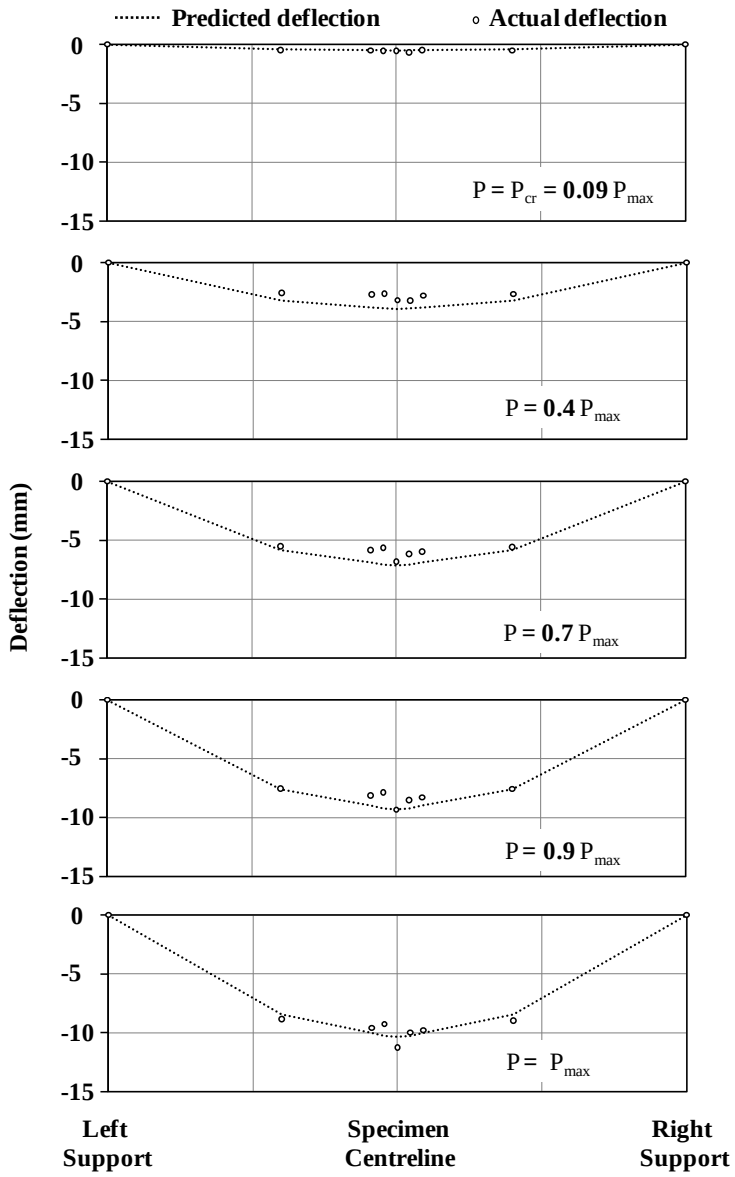

Figure 4F.7. Deflection profile at different load levels - Specimen 32-810

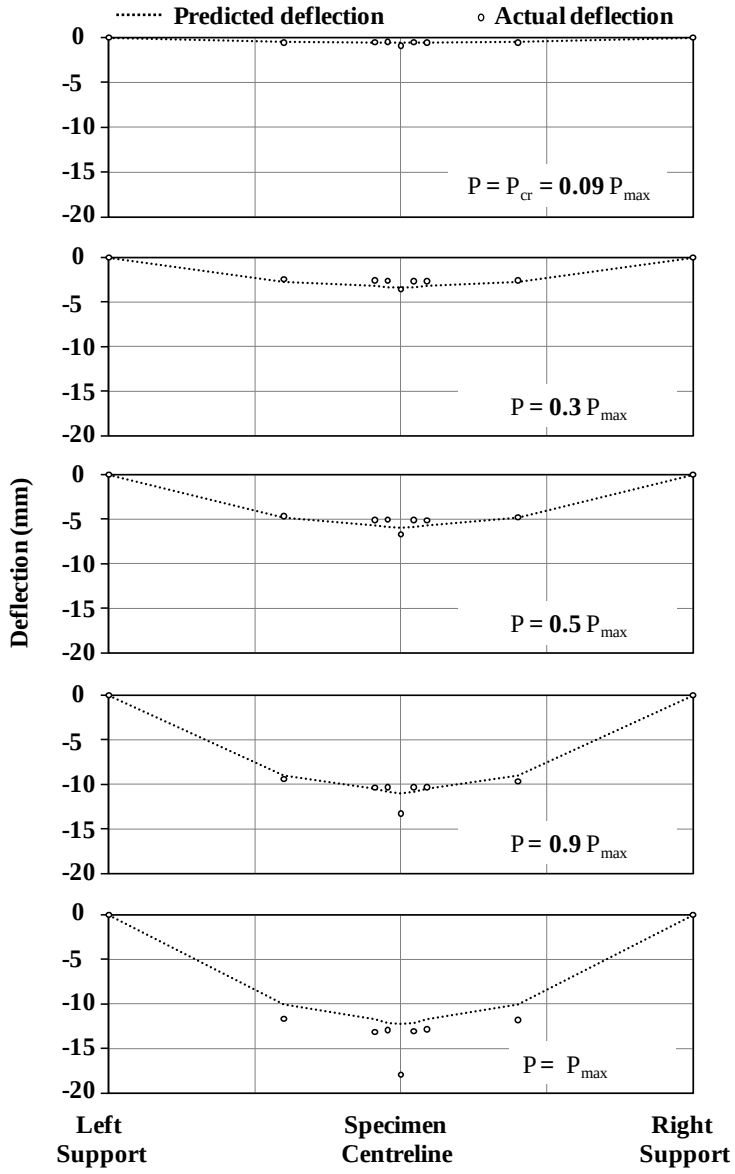

Figure 4F.8. Deflection profile at different load levels - Specimen 32-910

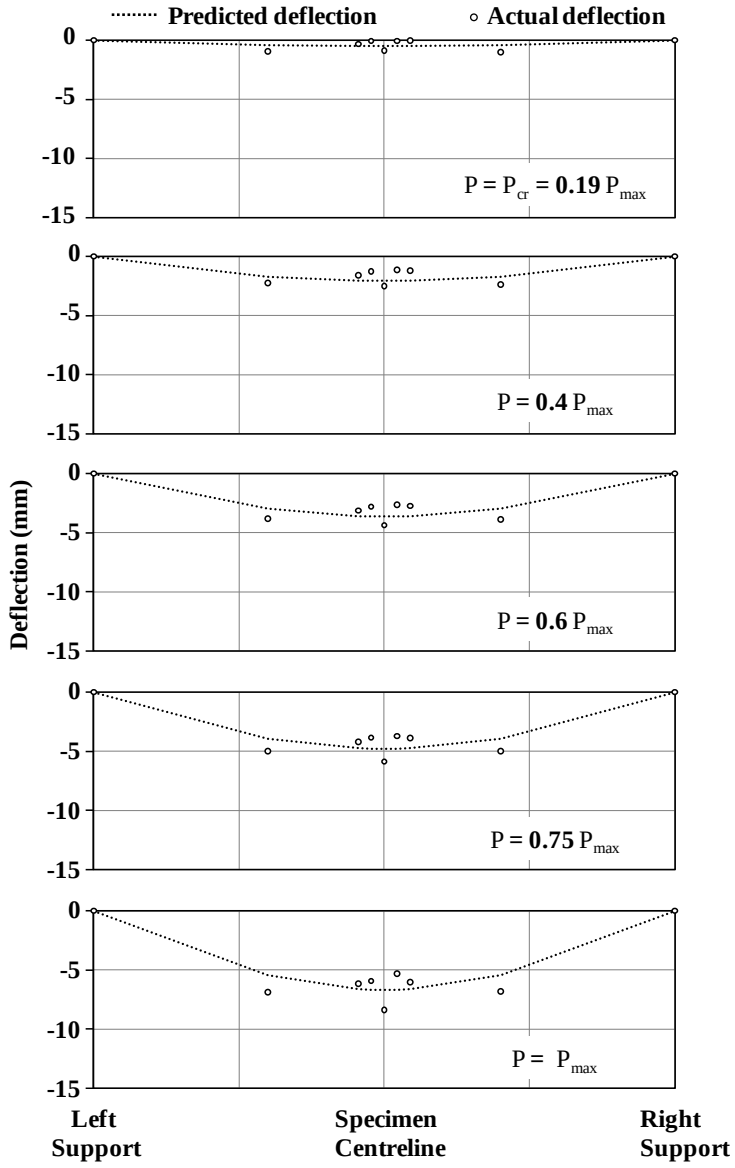

Figure 4F.9. Deflection profile at different load levels - Specimen 25-410I

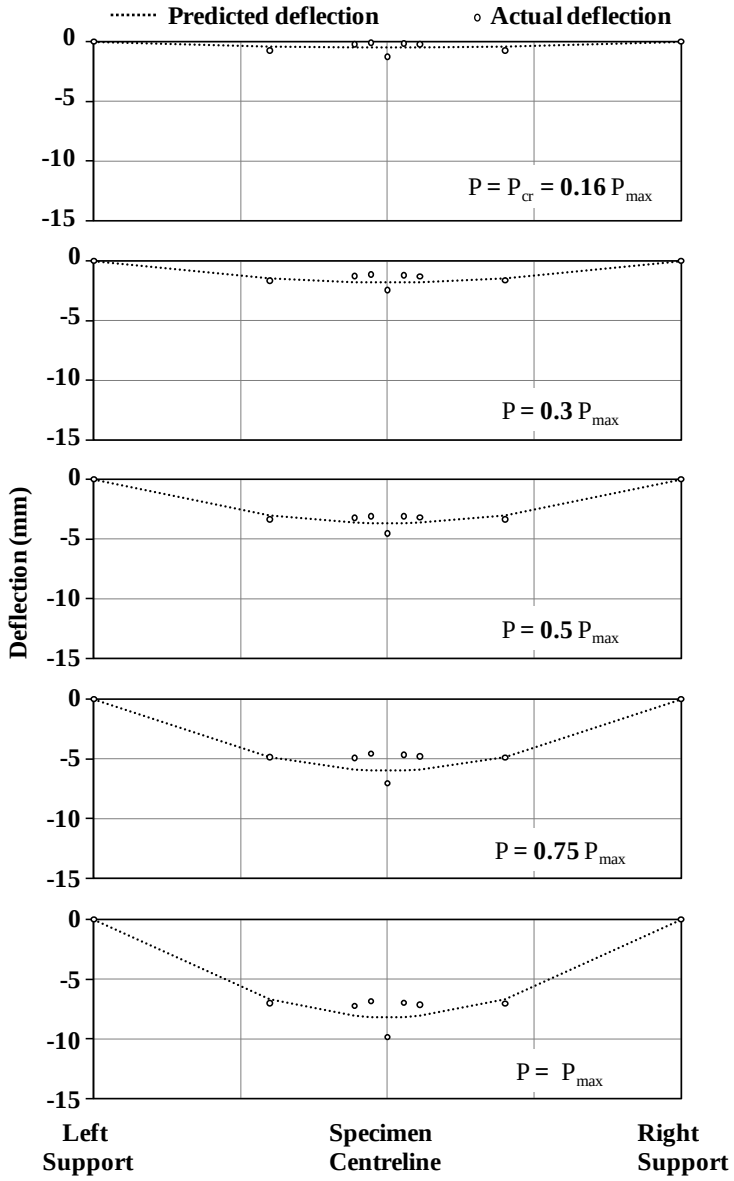

Figure 4F.10. Deflection profile at different load levels - Specimen 25-510I

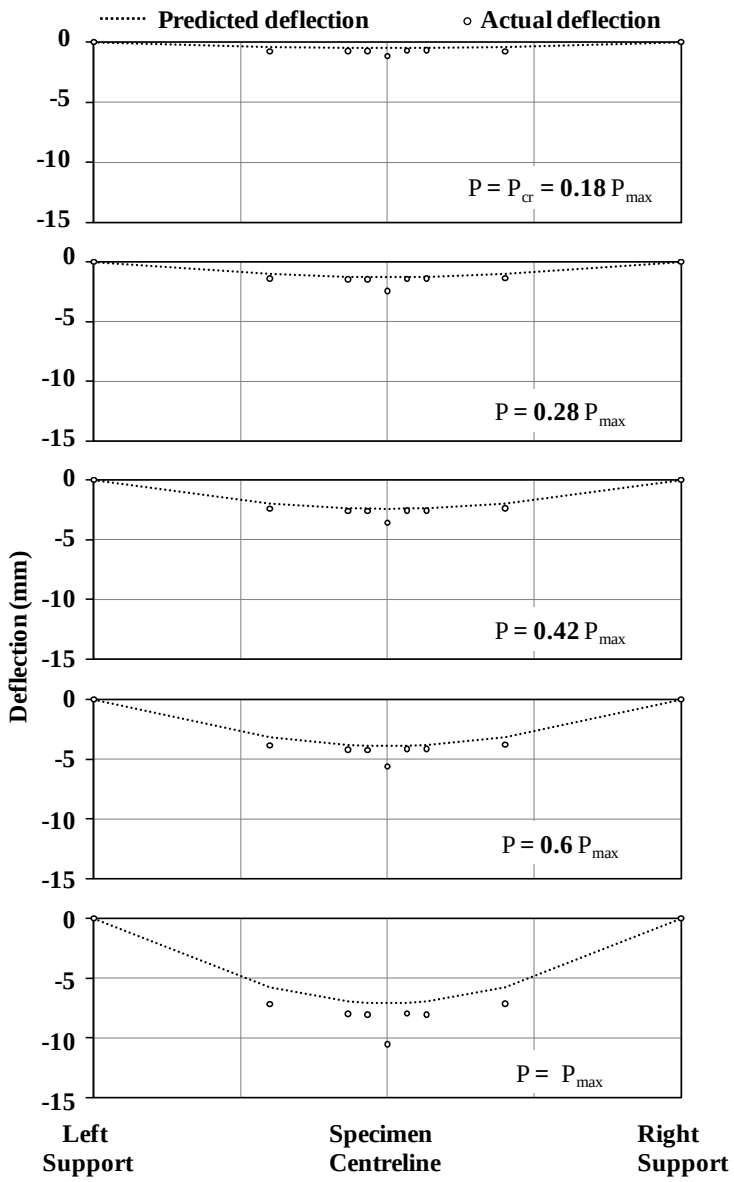

Figure 4F.11. Deflection profile at different load levels - Specimen 25-610I

APPENDIX 5A: Error Estimation: Strain Compatibility and Average Bond Stress

Strain gauge readings at $P/P_{max} = 0$ were recorded for several minutes as discussed in Section 3.6. The standard deviation of 250 strain readings at $P/P_{max} = 0$ for individual steel and concrete strain gauges for each specimen was determined. The maximum of the calculated standard deviations of steel and concrete readings obtained for each instrumented specimen is presented in Table 4F.1.

The standard deviation of the difference between steel and concrete strain, $S_{\varepsilon s-\varepsilon c}$ can be calculated from:

$$S_{\varepsilon s-\varepsilon c} = \sqrt{S_{\varepsilon s}^2 + S_{\varepsilon c}^2} \qquad [5A.1]$$

where $S_{\varepsilon s}$ and $S_{\varepsilon c}$ are the standard deviations of the steel and concrete strain gauge readings at $P/P_{max} = 0$. Similarly, the standard deviation of the difference of steel strain between two strain gauge locations of the lap splice length, $S_{\Delta\varepsilon s}$ can be calculated from the following equation:

$$S_{\Delta\varepsilon s} = \sqrt{2} S_{\varepsilon s} \qquad [5A.2]$$

The standard deviation of the strain difference calculated based on one steel strain gauge (i.e. from the cut end to the other location of the lap splice length) is equal to the standard deviation of the strain gauge readings at $P/P_{max} = 0$. The standard deviation of the average bond stress, S_u, was calculated from the following equation and presented in Table 4F.1:

$$S_u = \frac{S_{\Delta\varepsilon s} A_{sr} E_s}{\pi d_b \Delta x} \qquad [5A.3]$$

where E_s is the modulus of elasticity of the steel, A_{sr} is the reduced area of the reinforcing steel at the location of the steel strain gauges, d_b is the measured diameter of the longitudinal reinforcing steel bars and Δx is the distance between two adjacent steel strain gauges. The standard deviation of the average bond stress at the 95% confidence level (i.e. ± two times of the standard deviation) is also presented in Table 5A.1.

Table 5A.1: Errors in the strain gauge readings and average bond stress estimation

Specimen	Standard Deviation at $P/P_{max} = 0$		Standard deviation using 95% confidence level			
	Steel Strain $S_{\varepsilon s}$ μmm/mm	Concrete Strain $S_{\varepsilon c}$ μmm/mm	Steel Strain $2S_{\varepsilon s}$ μmm/mm	$2S_{\varepsilon s-\varepsilon c}$ μmm/mm	$2S_u$ MPa	
					Adjacent to the unloaded end	Other then unloaded end
25-410I	3.50	3.00	7.00	9.22	0.044	0.0622
25-510I	0.411	0.302	0.822	1.02	0.00417	0.0059
25-610I	3.10	5.80	6.20	13.2	0.0525	0.0742

APPENDIX 5B: Flexural Sectional Analysis - Description of Method

A flexural sectional analysis of the instrumented specimens within the lap splice length was determined assuming that plane section remains plane. A linear strain distribution was estimated for load increments of approximately P/P_{max} = 0.05 using a linear regression analysis of: (1) the concrete strains at 50 mm, 100 mm and the effective depth from the top of the section (Method 1), and (2) the concrete strains at the top two concrete strain gauges and the steel strain gauge on the longitudinal reinforcement (Method 2). The strain readings obtained from the concrete and steel strain gauges were adjusted to include the effect of the self weight of the specimen and that of the spreader beam and the bearing plate used in the test setup theoretically assuming perfect bond between reinforcing steel and concrete as discussed in Section 5.4.1.

Figure 5B.1 shows the established strain distribution in concrete at the different depths for a given instrumented. The vertical axis shows the height of a given strain gauge reading from the bottom fibre of the specimen and the horizontal axis shows the concrete strain. The coefficient of determination, R^2, for the established linear strain distributions at different applied load levels is presented in Tables 5B.1 to 5B.3. The dash-dotted line in Figure 5B.1 represents the linear relationship established for the concrete strain. The extreme fibre concrete compressive strain, ε_o, and depth of the neutral axis from the top of the section, c, were then determined from the established strain distribution.

The concrete compressive force and its line of action were determined in accordance with the ISIS Manual (2007), as it provides modified Whitney's stress block factors, α and β, for conditions other than the ultimate load level. However the concrete compressive force and its line of action for $\varepsilon_c / \varepsilon_o < 0.1$ were determined assuming an elastic stress-strain relationship for the concrete. The values for the concrete stress block parameters for each instrumented specimen are presented in Table 5B.4. Intermediate

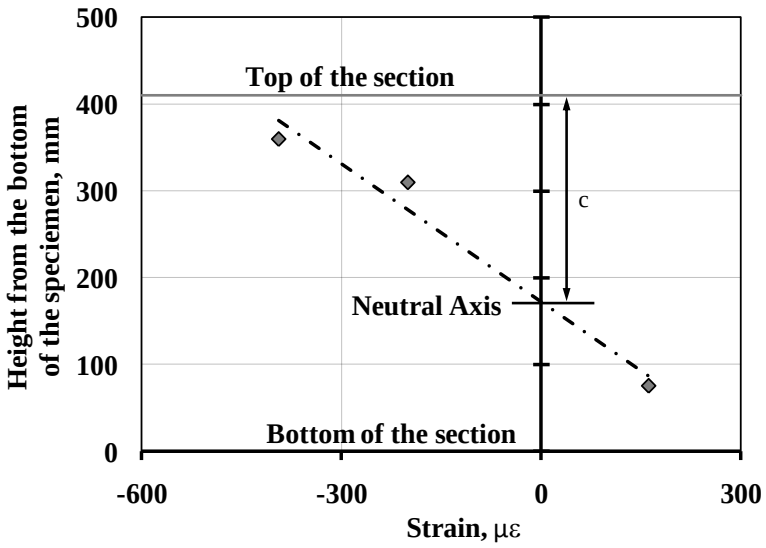

Figure 5B.1. Established strain distribution.

values of α and β were obtained by linear interpolation of the data presented. Calculated concrete compressive forces were adjusted to exclude the effects of self-weight of the specimen and the spreader beam and the bearing plates used in the test setup to provide a direct comparison with the normalized applied load as discussed in Section 5.4.1.

The stress in the reinforcing steel was calculated directly from the steel strain gauge data and the modulus of elasticity of the steel determined from the steel coupon tests. The cross-sectional area of the longitudinal reinforcing bars was reduced due to the installation of the steel strain gauges as discussed in Section 3.5 and presented in Appendix 4B. The tensile strength of the concrete was neglected in the calculation of total tension force at a given section. The strain compatibility analysis as presented in Section 5.2 indicates slip of the reinforcing steel bars from the surrounding concrete at low levels of applied loads. Tension carried by the concrete along the lap splice length would therefore be negligible and would not affect the flexural sectional analysis. The internal moment with respect to the plastic centroid of the section was calculated using the calculated internal forces.

Table 5B.1. Coefficient of determination, R^2 - Specimen 25-410I

P/P_{max} (%)	Coefficient of Determination, R^2					
	Left End of the Lap Splice Length		Centreline of the Lap Splice Length		Right End of the Lap Splice Length	
	Method 1	Method 2	Method 1	Method 2	Method 1	Method 2
5	1	1	0.9984	0.9984	0.9997	0.9999
10	0.9967	0.9999	0.9817	0.9916	0.9865	0.9994
15	0.9942	0.9998	0.9723	0.9896	0.9789	0.9988
19	0.9858	0.9993	0.9575	0.986	0.9621	0.9977
25	0.98	0.9991	0.9463	0.9836	0.9485	0.9973
30	0.9681	0.9987	0.934	0.982	0.9267	0.997
35	0.9505	0.9986	0.9208	0.9803	0.9079	0.9972
40	0.9419	0.9989	0.9131	0.9797	0.8893	0.9976
45	0.92	0.9993	0.9047	0.979	0.8709	0.9983
50	0.8954	0.9997	0.8942	0.9783	0.8514	0.9987
57	0.8808	0.9998	0.8893	0.9782	0.8549	0.9991
60	0.8408	0.9999	0.8829	0.9781	0.8639	0.9994
65	0.794	0.9999	0.8738	0.978	0.8938	0.9996
70	0.7813	0.9999	0.8733	0.9786	0.9054	0.9997
75	0.7492	0.9999	0.8627	0.9787	0.8959	0.9998
80	0.7327	0.9999	0.8497	0.9788	0.8586	0.9998
86	0.7098	0.9999	0.8309	0.9801	0.8102	0.9998
90	0.6777	0.9999	0.8123	0.9824	0.7741	0.9998
95	0.6457	0.9998	0.7807	0.9854	0.728	0.9998
100	0.635	0.9997	0.7462	0.9859	0.6633	0.9995

Table 5B.2. Coefficient of determination, R^2 - Specimen 25-510I

P/P_{max} (%)	Coefficient of Determination, R^2					
	Left End of the Lap Splice Length		Centreline of the Lap Splice Length		Right End of the Lap Splice Length	
	Method 1	Method 2	Method 1	Method 2	Method 1	Method 2
7	0.9999	0.9997	1	0.9999	0.9902	0.9943
10	0.9802	0.999	0.9985	1	0.9771	0.9877
15	0.9829	0.9978	0.9975	1	0.8901	0.9842
20	0.9779	0.9979	0.9977	1	0.782	0.9822
25	0.9674	0.9976	0.9976	1	0.6928	0.9833
30	0.952	0.998	0.9982	0.9999	0.6348	0.9848
35	0.897	0.9987	0.9978	0.9999	0.5734	0.9868
40	0.8285	0.9992	0.9983	0.9998	0.5211	0.989
45	0.7823	0.9994	0.9984	0.9997	0.4932	0.9904
50	0.7456	0.9996	0.9981	0.9997	0.4649	0.9911
56	0.719	0.9998	0.9983	0.9996	0.4533	0.9915
60	0.6767	0.9999	0.9985	0.9994	0.4307	0.9922
66	0.645	1	0.9986	0.9991	0.4203	0.9929
70	0.6258	1	0.9989	0.9988	0.4171	0.9935
75	0.6101	1	0.9991	0.9985	0.4124	0.9937
80	0.5787	0.9998	0.9995	0.9973	0.3979	0.9941
85	0.5595	0.9997	0.9995	0.9965	0.3912	0.9941
90	0.5461	0.9994	0.9992	0.9955	0.3785	0.9941
96	0.5354	0.9989	0.9988	0.9942	0.3613	0.994
100	0.5151	0.9977	0.9969	0.9935	0.3468	0.9937

Table 5B.3. Coefficient of determination, R^2 - Specimen 25-610I

P/P_{max} (%)	Coefficient of Determination, R^2				
	Left End of the Lap Splice Length		Centreline of the Lap Splice Length		Right End of the Lap Splice Length
	Method 1	Method 2	Method 1	Method 2	Method 2
5	0.9923	0.9917	0.9982	0.9953	1.0
10	0.9798	0.979	0.9939	0.9845	1.0
15	0.9641	0.967	0.9956	0.984	1.0
18	0.9268	0.9485	0.9953	0.9844	1.0
21	0.9129	0.951	0.9938	0.9845	1.0
25	0.8794	0.9454	0.9819	0.9827	1.0
30	0.8232	0.9583	0.976	0.9829	1.0
35	0.826	0.9616	0.9724	0.9829	1.0
40	0.8572	0.9669	0.9684	0.9835	1.0
45	0.9122	0.9712	0.9673	0.9848	1.0
50	0.9677	0.9748	0.9672	0.9857	1.0
55	0.997	0.9776	0.9695	0.9868	1.0
60	0.9992	0.9793	0.9701	0.9872	1.0
65	0.962	0.9823	0.9703	0.9884	1.0
70	0.9153	0.9842	0.9701	0.9872	1.0
75	0.8464	0.9864	0.9698	0.9905	1.0
80	0.7716	0.9883	0.9678	0.9916	1.0
85	0.7269	0.9899	0.9676	0.9928	1.0
90	0.652	0.9919	0.9574	0.9941	1.0
95	0.5868	0.9936	0.9561	0.9955	1.0
100	0.4555	0.9962	0.9429	0.9973	1.0

Table 5B.4. Stress block parameters used for the instrumented specimens

$\varepsilon_c / \varepsilon_o$	Specimen 25-510I f'_c = 20.8		Specimen 25-410I and 25-610I f'_c = 21.5	
	α	β	α	β
0.1	0.181	0.602	0.178	0.601
0.2	0.320	0.639	0.316	0.638
0.3	0.449	0.656	0.444	0.655
0.4	0.563	0.670	0.558	0.669
0.5	0.661	0.684	0.657	0.682
0.6	0.742	0.697	0.740	0.695
0.7	0.808	0.711	0.806	0.709
0.8	0.859	0.725	0.858	0.723
0.9	0.897	0.740	0.896	0.738
1	0.923	0.755	0.923	0.753